# FREEZE-THAW PERFORMANCE OF PRESTRESSED CONCRETE RAILROAD TIES

by

MOHAMMED T. ALBAHTTITI

B.S., American University of Sharjah, United Arab Emirates, 2010
M.S., Kansas State University, USA, KS, 2012

AN ABSTRACT OF A DISSERTATION

submitted in partial fulfillment of the requirements for the degree

DOCTOR OF PHILOSOPHY

Department of Civil Engineering
College of Engineering

KANSAS STATE UNIVERSITY
Manhattan, Kansas

2015

# Abstract

Air voids are purposefully entrained in concrete to provide freeze-thaw durability of prestressed concrete railroad ties. Durability assurance requires consistent provision of an air void system comprised of small, well-distributed bubbles in sufficient quantity for durability and a quality control method for testing tie freeze-thaw durability. Manufacturing processes at three concrete manufacturing plants were investigated in order to determine the effects of process variability on resulting concrete air void system variability. Variation in the concrete air void system and other rheological properties occurred as results of the manufacturing process and vibration. Freezing and thawing durability testing of prestressed concrete ties is currently performed by applying ASTM C666 on 3 x 4 x 11 to 16 in. specimens cut from the shoulders of concrete ties. However, excising these specimens from prestressed concrete could lead to stress changes in the sample and cracking, potentially causing false interpretations of results. Therefore, testing was undertaken to understand the effects of prestressing and sample extraction on freeze-thaw durability measured by ASTM C666. In order to assess the effects of sampling and testing procedures on freeze-thaw quality control testing results of prestressed concrete railroad ties, full ties, half ties, and 3 x 4 x 11 in. excised samples were tested. Freeze-thaw testing included determination of the optimal method to measure freeze-thaw deterioration in large sections, the effects of saw-cutting, and the presence of reinforcement. Results indicated that the Ultrasonic Pulse Velocity accurately represented deterioration in large sections. The presence of reinforcement in excised samples led to faster deterioration compared to cast ASTM C666 samples, while saw-cutting without reinforcement did not significantly affect freeze-thaw durability.

# FREEZE-THAW PERFORMANCE OF PRESTRESSED CONCRETE RAILROAD TIES

by

MOHAMMED T. ALBAHTTITI

B.S., American University of Sharjah, United Arab Emirates, 2010
M.S., Kansas State University, USA, KS, 2012

A DISSERTATION

submitted in partial fulfillment of the requirements for the degree

DOCTOR OF PHILOSOPHY

Department of Civil Engineering
College of Engineering

KANSAS STATE UNIVERSITY
Manhattan, Kansas

2015

Approved by:

Major Professor
Kyle A. Riding

# Copyright

# Abstract

Air voids are purposefully entrained in concrete to provide freeze-thaw durability of prestressed concrete railroad ties. Durability assurance requires consistent provision of an air void system comprised of small, well-distributed bubbles in sufficient quantity for durability and a quality control method for testing tie freeze-thaw durability. Manufacturing processes at three concrete manufacturing plants were investigated in order to determine the effects of process variability on resulting concrete air void system variability. Variation in the concrete air void system and other rheological properties occurred as results of the manufacturing process and vibration. Freezing and thawing durability testing of prestressed concrete ties is currently performed by applying ASTM C666 on 3 x 4 x 11 to 16 in. specimens cut from the shoulders of concrete ties. However, excising these specimens from prestressed concrete could lead to stress changes in the sample and cracking, potentially causing false interpretations of results. Therefore, testing was undertaken to understand the effects of prestressing and sample extraction on freeze-thaw durability measured by ASTM C666. In order to assess the effects of sampling and testing procedures on freeze-thaw quality control testing results of prestressed concrete railroad ties, full ties, half ties, and 3 x 4 x 11 in. excised samples were tested. Freeze-thaw testing included determination of the optimal method to measure freeze-thaw deterioration in large sections, the effects of saw-cutting, and the presence of reinforcement. Results indicated that the Ultrasonic Pulse Velocity accurately represented deterioration in large sections. The presence of reinforcement in excised samples led to faster deterioration compared to cast ASTM C666 samples, while saw-cutting without reinforcement did not significantly affect freeze-thaw durability.

# Table of Contents

# List of Figures

# List of Tables

# Acknowledgements

First of all I am thankful to Allah, the Creator, the Most Gracious and Most Merciful. I would like to thank my advisor, Dr. Kyle Riding, for his relentless support and for his guidance. I also would like to thank all the members of the Department of Civil Engineering, both staff and professors, at Kansas State University for their help and support; and likewise the Federal Railroad Administration (FRA) for their financial support and all those who helped me with this research.

# Dedication

*This dissertation is dedicated to **my family** who have always given me the encouragement to complete my graduate studies and continuously supporting me in any decision I make as well as for their love and sacrifice.*

# Chapter 1 - Introduction

## 1.1.Background

Concrete railroad ties are commonly exposed to very severe environments in track. As a result, they are expected to last approximately 50 years under harsh conditions that include extreme heat, cold, and wet conditions and cause premature deterioration of the concrete railroad tie. Potential tie failure mechanisms observed in track include cracking, rail seat deterioration, alkali-aggregate reaction, delayed ettringite formation, and freezing and thawing damage [1]. Concrete material and quality control methods required to ensure tie freeze-thaw durability have become subjects of interest to tie producers and track owners.

Repeated freezing and thawing of concrete under wet conditions may lead to damage ranging from minor spalling to complete deterioration. Freeze-thaw cycles can lead to a significant decrease in compressive and tensile strength due to micro-cracking in the concrete matrix [2]. Common modes of concrete tie deterioration due to freeze-thaw of concrete include pop-outs, cracking, and spalling from the concrete surface [3]. Micro-cracking near the surface allows additional water into the concrete, increases severity of freezing cycles and potentially accelerates freeze-thaw damage. Further deterioration may include structural cracking and total failure or crumbling of the ties. For concrete under freeze-thaw conditions, high volume-to-surface area ratios have led to low rates of concrete deterioration [3], possibly due to a change in the freezing rate, strains generated from the temperature change, and access to water. Although concrete ties have a low volume-to-surface area ratio compared to most civil structures, they are much larger in size and volume-to-surface area ratio than small prisms traditionally used for performance testing.

The concrete-entrained air void system is a primary microstructural characteristic that influences frost resistance. This system is developed by air entraining chemical admixtures during

mixing. Air is naturally added into the concrete through agitation and folding action during mixing. Without air entraining chemical admixtures, air bubbles are unstable and quickly leave the concrete. Air-entraining agents stabilize air that is mixed into the concrete during mixing. After placement in the forms, the concrete is typically subjected to vibration to ensure proper consolidation. However, concrete vibration can affect entrained air content, bubble size, bubble spacing, and frost resistance of hardened concrete. Variation in batch-to-batch concrete properties is expected as a result of small adjustments the operator makes to the mixture, variation in aggregate moisture content, and different air content.

Although concrete freezing and thawing durability testing is typically performed according to ASTM C666 on small specimens saw-cut from railroad ties or cast from the concrete mixture used in tie manufacturing, it is not subjected to the same placement and consolidation processes. For this project, freeze-thaw testing was performed on whole concrete railroad ties, half ties, small saw-cut specimens, and cast specimens in order to understand how saw-cutting and prestressing affect freeze-thaw durability of those ties. In addition, effects of the entrained air system and the manufacturing process on that system were investigated.

## 1.2. Objectives

This research sought to determine a) the effect of concrete rheology and fabrication process on air content in concrete railroad ties, and b) the effects of testing procedures on freeze-thaw quality control testing results of prestressed concrete railroad ties.

In order to assess the validity of the first objective, concrete air content was measured at various steps in the concrete railroad tie manufacturing process at three concrete manufacturing plants. The investigation included testing the following fresh concrete properties: air content, slump, temperature, vibration, and rheology. In addition, hardened concrete samples were

collected at the mixer, after handling and placement, and after vibration in order to quantify those effects on the concrete air void system using image analysis methods.

In order to achieve the second research objective, three sets of concrete railroad ties were constructed with small companion prisms made from one concrete batch according to ASTM C666. The three sets included two prestressed ties, two reinforced ties without prestressing, and two unreinforced ties. Each set consisted of a tie with air content of 7% and a tie with air content of 0.9%. Small prisms saw-cut to meet size requirements of ASTM C666 were excised from the concrete ties in order to determine the suitability of using prisms saw-cut from prestressed concrete railroad ties. The prisms were tested according to ASTM C666 in order to determine freeze-thaw durability of concrete railroad ties. In order to quantify strain due to saw-cutting, vibrating wire gages were embedded in these ties. Companion cast prisms were also tested according to ASTM C666 and compared to samples excised from the unreinforced concrete ties in order to determine deterioration caused by saw-cutting and isolate the effects of prestressing. In addition, prestressed half ties with sufficient transfer length were tested in freeze-thaw conditions in order to determine freeze-thaw durability of concrete ties tested for reference when sampling effects were removed.

## 1.3. Scope

**Chapter 2 - Literature Review:** Chapter 2 contains a review of freeze-thaw durability of concrete, methods to measure air systems in concrete, and test methods to measure freeze-thaw durability of concrete.

**Chapter 3 - Effects of the Manufacturing Process on Air Content:** This chapter presents changes and variability in entrained air systems that result from the concrete railroad tie manufacturing process at three manufacturing plants.

**Chapter 4 - Effect of Freezing and Thawing on Full-Scale Prestressed Concrete Railroad Ties:** This chapter presents the results of freeze-thaw tests performed on whole concrete ties supplied by the Illinois Department of Transportation (IDOT) as initial experiments of large concrete sample freeze-thaw testing.

**Chapter 5 - Effects of Prestressing and Saw-cutting on Freeze-Thaw Durability:** This chapter describes freeze-thaw tests performed on samples made from concrete railroad ties with prestressing, concrete ties with reinforcement but without prestressing, and unreinforced concrete ties. The objective of the testing was to determine the effects of prestressing and steel inclusion on freeze-thaw durability of concrete samples excised from concrete railroad ties.

**Chapter 6 - Comparison of Methods Used to Measure Freeze-Thaw Durability Prestressed Concrete Ties:** Freeze-thaw durability of concrete is currently determined using the change in relative dynamic modulus of elasticity (RDME) calculated from the fundamental transverse frequency. Although this method is applicable to small cast or saw-cut samples that satisfy the requirements of ASTM C666, its applicability for capturing deterioration in large-scale samples is still unproven. Several methods are investigated in this chapter in order to determine the most adequate forensic tool to investigate freeze-thaw durability of prestressed concrete ties.

**Chapter 7 - Bursting Strains in Samples Excised from Prestressed Concrete Railroad Ties:** Stress release caused by saw-cutting prestressed concrete railroad ties leads to bursting strains in the saw-cut samples. These bursting strains cause accelerated failure of saw-cut samples that undergo freeze-thaw testing. This chapter describes measurements of these strains using vibrating wire gauges in prestressed concrete ties.

**Chapter 8 - Conclusions and Recommendations:** This chapter presents a summary of the work performed and conclusions and recommendations for future work.

# Chapter 2 - Literature Review

In 1804, the first railway steam locomotive began service in the United Kingdom with a recorded speed of 5 mph (8 km/h). One hundred years later, German trains achieved speeds of 131 mph (210 km/h), which remained normative for rapid passenger trains until the 1970s. In 1955, however, the French National Railway Corporation tested an electric locomotive prototype (the BB 9004) that achieved a speed of 206 mph (331 km/h). Recent advancements in wheeled-rail technology have allowed a modified TGV POS train (designated V150) to register an unprecedented speed of 357 mph (575 km/h) in April 2007 [4]. However, high-speed trains require stronger, more reliable, and more durable railroad tracks, ties, and beds. Compared to conventional wooden ties, concrete crossties have proven their superiority in strength, reliability, and durability. High-speed train travel on tracks constructed with standard lightweight wooden ties can cause the ties to shift and occasionally fracture. Concrete ties, however, facilitate smoother, more stable operation of high-speed trains, thereby improving fuel efficiency [5]. Over the past 25 years, use of concrete railroad ties has increased in the United States because of the ties' economic and environmental advantages, particularly in heavy-haul and high-speed rail applications [6].

## 2.1. Prestressed Concrete Ties

P.H. Jackson, an engineer from California, initially developed the prestressing process in 1872 [9]. Sixteen years later, C.W. Doehring patented a process for prestressing a concrete slab with steel wires. However, these early prestressing attempts were unsuccessful due to prestressing loss caused by steel inadequacy. In 1926, Eugene Freyssinet used stronger steel with increased ductility in order to overcome prestress losses [9]. Use of high-strength steel, however, requires high-strength concrete to prevent excessive prestressing losses. In order for prestressed concrete railroad ties to be economically advantageous, the time between concrete placement and

prestressing release should be short enough to allow forms and stressing beds to be reused daily or even more frequently. Low water-cementitious material ratio (w/cm) concrete is typically used to increase early strength, allowing for decreased times to prestressing release and increased production rates.

Concrete crossties were first introduced in Europe in the early 1940s and tested in North America in the 1960s in order to advance high-speed rail systems [1]. In the mid-1970s, the Portland Cement Association (PCA) published a prestressed concrete tie design thought to be sufficient to withstand the heavy rail system in the United States [10]. That tie design has evolved to the current typical prestressed concrete crosstie shown in Figure 2.1. Current tie designs often have a small cross section in the mid-span region and a large cross section underneath the rails. This design was implemented to decrease material costs while maintaining adequate thickness and strength in essential locations. Scallops on the sides of the tie were added to provide additional friction with surrounding ballast in the field.

**Figure 2.1 Typical prestressed concrete crosstie**

Prestressed concrete ties, currently manufactured in the United States at precast plants, are designed to resist loading conditions suggested by the American Railway Engineering and Maintenance-of-Way Association (AREMA) [7]. These prestressed concrete ties use high early-strength concrete mixtures that reach approximately 80% or more of their specified 28-day strength after 24 hours [8].

### *2.1.1. Failure Mechanisms*

Railroad crosstie failures are characterized by two classifications. The first classification of failure is system-related and includes three primary causes of failure: support failure, stability failure, and electrical isolation failure. Support failure occurs when the system fails to transfer and distribute loads from the train wheels to the ground. This failure, manifested by crushing crossties, rail failure, or subgrade failure [1], can typically be avoided by proper strength, stiffness, spacing, and bearing of system crossties in the rail system. Stability failure is a consequence of leveling, surfacing, and subsurface issues. Any rail system displacement due to surface and subsurface deficiencies can lead to stability failure. Track geometry consistency also significantly contributes to stability failure prevention. Increased stability in rail systems is a direct result of ensuring that concrete ties are well-attached to the rail, contain consistent and accurate dimensions, and demonstrate good abrasion resistance [1]. Electrical isolation failure occurs when the rail fastener contacts prestressing wires in multiple locations or when the concrete tie contains high moisture while missing a tie pad.

The second classification of concrete crosstie failure is failure of the tie. In 2009, Russell H. Lutch identified three main failure mechanisms in prestressed concrete ties [8]. The first failure mechanism is rail-seat abrasion, which occurs as the cement gradually wears from the ties in the pad area [11]. The second failure mechanism is rail fastener failure caused by cyclic loading of the train. Flexural cracking was identified as the third type of failure in ties.

Rail fasteners are used in concrete ties to attach the steel rail to the ties and prevent rail movement. Fastener type typically depends on the railroad operator and the tie application [12]. The fastener system consists of three components: the steel shoulder, the spring clip, and the insulator. The steel shoulder can vary in size and depth of embedment in the concrete depending on tie type and fastener system.

Train loading, or cyclic loading, can cause rail fastener failure, the second failure mechanism. This loading causes either the spring clip or the ductile iron shoulder to fail [4]. Flexural cracking, the third failure mechanism, occurs when the tie cracks in the mid-top region due to negative moment resulting from rail loading on two sides of the tie [13]. Progressive deterioration due to environmental or chemical degradation is also a failure mechanism of concrete railroad ties that should be considered [1].

### *2.1.2. Durability of Prestressed Concrete Ties*

Progressive failure in concrete ties can occur as a result of insufficient durability of manufactured ties. Insufficient strength and prestressing, the presence of alkali-silica reaction (ASR), high moisture content, high curing temperature, low abrasion resistance, inadequate air void system, and pad issues all contribute to concrete progressive deterioration [1]. Insufficient strength can also lead to prestressing loss. Over time, high prestress force, poor bonding between prestress wires that causes a long transfer or development length, can result in insufficient moment or shear capacity [1]. Concrete railroad tie durability is a critical factor for determining whether or not concrete ties are economically competitive against wood ties.

## 2.2. Freeze-Thaw Damage

Repeated cycles of freezing and thawing may lead to damage varying from spalling to complete degradation of concrete. Observations and testing of construction material durability in freezing conditions have been conducted since the 1800s [14]. Freeze-thaw deterioration typically demonstrates two manifestations: surface scaling and internal or bulk damage [15]. Surface scaling occurs as result of exposure to salts such as de-icing salt or sea water during freeze-thaw cycles. Concrete surface scaling is defined as the progressive loss of cement or mortar particles only a few

millimeters in thickness [16]. The glue-spall mechanism is a current theory that describes surface scaling.

As result of de-icing salt or sea water, water accumulates on the surface of concrete and mechanically binds to the concrete when it freezes [17]. Frozen water tends to develop tensile stresses as the temperature decreases. Once the stresses increase beyond ice tensile capacity, the ice cracks; these cracks propagate through the surface of the concrete and cause scaling. Scaling occurs only if the water that created the ice contains salts in limited concentrations that provide pockets of unfrozen brine [17]. An adequate salt concentration is considered to be between 2 to 5% of salt by weight [17]. However, air-entraining agents can significantly reduce salt scaling damage as a result of the contraction of air-entrained concrete during freezing cycles [17].

Concrete mixtures susceptible to surface scaling are not necessarily susceptible to bulk freeze-thaw damage [18]. Although railroad operators do not use de-icing salts on the railroads, some railroad track exposure to de-icer salts may occur at highway crossings; however, these locations comprise only a small percentage of railroad track miles in the United States. This makes internal or bulk freeze-thaw damage the most significant cause of freeze-thaw deterioration for concrete ties.

### *2.2.1. Internal (bulk) Freeze-Thaw Damage*

Well-distributed air voids, achieved with an air-entraining admixture, provide good resistance to cracking and deterioration due to water freezing in concrete [19]. During the last fifty years, many theories have attempted to explain internal or bulk damage due to the freeze-thaw effect on concrete elements. Several mechanisms have been proposed to cause internal freeze-thaw damage: critical saturation, hydraulic pressure, and ice accretion and osmotic pressure [20]. Critical saturation refers to damage resulting from 9% expansion of freezing water. Damage occurs

when capillaries in the cement paste of the concrete are filled with more than 91.7% of water. Once water in the capillaries begins to freeze, the frozen water generates stresses in the concrete and causes internal damage. This damage occurs in localized zones of capillary saturation inside the cement paste. However, this damage can be mitigated if the capillaries are not completely filled with water.

The hydraulic pressure theory states that freeze-thaw damage is caused by buildup of hydraulic pressure caused by unfrozen water's resistance to flow in cement paste capillaries [21]. Because cement paste does not expand to accommodate water expansion in the capillaries, unfrozen water is forced to flow through the capillaries during a freezing event. Hydraulic pressure, the force that causes unfrozen water to move, is affected by permeability, flow rate, and fluid viscosity. Although permeability depends on cement paste microstructure, flow rate correlates to freezing rate. The faster the freezing rate, the faster the flow of water. For fluid viscosity, change in viscosity remains minimal for freezing water. The maximum length that water can flow is calculated based on equating the change in pressure to cement tensile strength and using fixed values for permeability, flow rate, and fluid viscosity [22]. Powers estimated this length to be 0.008 in. (0.2 mm) based on Vinsol resin air entrainer [22].

Flow resistance of unfrozen water through capillaries in concrete structures could result in accumulation of hydraulic pressure, thereby damaging the concrete. Ice accretion and osmotic pressure theory explain results unaccounted for by the previous two theories. During freezing, water in the gel pores travels to capillaries according to thermodynamics laws [20]. However, water in the gel pores cannot freeze at temperatures above -78 $^{o}$C due to the small size of these pores [22]. When the water temperature is less than 0 $^{o}$C, the water energy becomes higher than that of ice, causing water to flow from the gel pores to the capillaries. The energy gradient causes

this water to freeze once it reaches the capillaries. Water continues to flow from the gel pores to the capillaries until the water energy equalizes with the ice energy. Because water in the pores contains ions and the formed ice can only be pure water, these ions accumulate in the capillaries, causing continuation of water flow even when the capillaries are full. This continuation of water flow is a result of the system's attempt to equalize the solution concentration, consequently causing pressure buildup and internal damage [23].

According to Litvan's theory, water in the capillaries can freeze only in the outer surface of the structure and cannot freeze in its original position without movement [16]. Because of the difference between vapor pressure of the super-cooled water, frozen water, and unfrozen water in the concrete capillaries, water in the capillaries move to larger pores in order to freeze. Water movement and drying in the capillaries occur as results of rapid cooling in the capillaries during freezing cycles, leading to increased risk of damage to the cement paste. This damage is caused by the accumulation of water in the pores and cracks that cause expansion during freezing cycles. However, additional water introduced into the system causes more internal pressure and expansion due to freezing, consequently leading to further damage [24]. This damage becomes prominent when the system lacks a proper air system because the rate of freezing is too rapid and causes the water to freeze in the capillaries before reaching the air voids and the saturation level exceeds the level at which the air system can accommodate [24].

The hydraulic pressure theory explains the mechanism at which internal pressure is generated and the relationship between distances that water travels to reach the air voids and the freezing rate [16]. Ice crystal growth occurs when an increased freezing period causes increased damage. The osmotic pressure theory accurately describes this phenomenon, but it fails to explain the role of air voids in deteriorating frost action damage [16]. Litvan's theory lacks proper

description of the mechanism at which internal pressure is formed and commencement of the damage process. Although these theories contradict each other, they collectively explain frost action damage. However, even a combination of all these theories is unable to comprehensively explain the problems of frost action [16].

Pop-out occurs when saturated porous or weak aggregate splits as a result of frost action. This frost action exerts internal pressure inside the aggregate or when water is ejected from the aggregate due to the same pressure, thereby causing mortar or paste cover pop-out. These two types of pop-outs are referred to as Classical and Type II, as shown in Figure 2.2 redrawn from Pigeon and Pleau's book, *Durability of Concrete in Cold Climates* [16]. (See Appendix B for reprint authorization.)

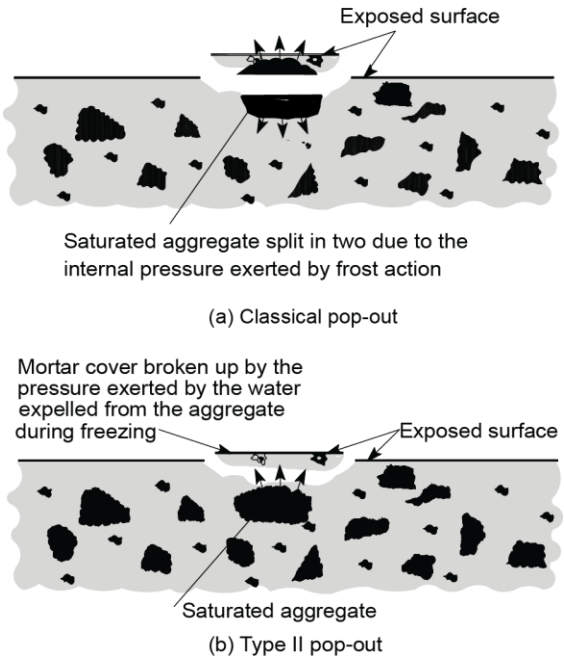


**Figure 2.2 Types of pop-outs: a) Classical pop-out, and b) Type II pop-out [16]**

## 2.3. Preventing Freeze-Thaw Damage

Three main concrete properties control freeze-thaw deterioration in concrete: aggregate characteristics, concrete permeability, and the air void system [25]. Sixty to eighty percent of the volume of a typical concrete is comprised of aggregates. Absorption and specific gravity are

important aggregate properties pertaining to freeze-thaw durability [24]. Similar to cement paste, freeze-thaw durability of aggregate depends primarily on its pore structure. Aggregate subjected to freezing while fully saturated must accommodate increased volume resulting from ice formation or be able to expel water from the aggregate to an air void in the cement paste before it freezes in the aggregate [24].

Aggregate freeze-thaw durability depends on aggregate type, size, absorption capacity, degree of saturation, pore size, and distribution [26]. Aggregate type can affect the strength of interfacial transition zones (ITZs) and development of micro-cracking [27]. When the weak transition zones suffer micro-cracking, permeability of the cement paste increases and the concrete becomes more susceptible to freeze-thaw damage [24]. Aggregate with low absorption produces air-entrained concrete with improved freeze-thaw durability compared to concretes with aggregates that have high absorption [28]. Instead of aggregate absorption, the aggregate pore structure tends to control freeze-thaw durability in air-entrained concrete [29]. In addition to aggregate type, aggregate size is an important factor for freeze-thaw durability. Small aggregate subjected to freeze-thaw cycles without the cement matrix were able to withstand freeze-thaw for longer periods than large aggregates following the internal hydraulic pressures mechanism [30]. For absorption, aggregates with high absorption capacities and very fine pore structures cause more freeze-thaw damage [31]. Water can be expelled from aggregates during the freezing cycle, resulting in increased hydraulic pressure and damage to the ITZ. The increased pressure and the freezing of the water cause aggregates to expand, thereby causing damage to the surrounding paste [32]. Aggregates with pores smaller than 5 μm tend to remain saturated in concrete for longer periods of time than aggregates with larger pores, and they tend to have low permeability that causes increased hydraulic pressure in the cement paste [16].

High-performance concrete with low permeability is typically made with a very low water to cement ratio and with the aid of water reducers. Low-permeability concrete has two main benefits: reduction of the amount of water that can enter the concrete and reduction of the amount of excess water in the hydrated cement [24]. Reduction in the amount of water absorbed lowers the concrete degree of saturation, consequently decreasing damage during freezing [24].

### *2.3.1. Air System*

Agitation and folding action during mixing naturally includes air into concrete. Without air-entraining chemical admixtures, air bubbles are unstable and quickly leave the concrete; however, air-entraining agents stabilize air mixed into the concrete. Air can be described as the foam that forms in the liquid state of the concrete and is retained in the solid state of the concrete. Powers described two main processes to generate air in concrete [33] [34]. The first process is the entrainment of air through folding during the vortex action of the mixing. The second process involves the flowing and falling mass of the fine aggregate onto itself, leading to air entrainment during mixing. Mielenz *et al.* [35] [34] stated that air is already in the system of materials and can be entrapped as a result of the mixing process. Air bubbles are naturally unstable in the concrete as a result of the thermodynamic behavior of the materials, at which the materials attempt to eliminate interfacial surface areas between the various materials [34]. Therefore, once air completes a life cycle, the air escapes, combines, or collapses. Air-entraining agents are used to entrain and stabilize air in the concrete. Typical air entrainers consist of various surfactants that are composed of hydrophilic heads and hydrophobic tails [34]. Although surfactants orient themselves randomly in bulk solutions, they tend to demonstrate a preferred orientation consisting of grouped hydrophobic tails of the surfactants, thereby causing the surfactants to form spheres

with hydrophilic heads on the outside, surrounded by the liquid, and hydrophobic tails on the inside, surrounded by air [34].

Air bubbles are locations to which water in concrete capillaries can travel in order to form ice crystals, thereby relieving stress resulting from freezing action [22]. A good distribution of air voids results in increased accessibility of air bubble sites and less freeze-thaw damage. The distance that water in concrete capillaries can travel without causing damage depends on factors such as rate of freezing, degree of saturation, porosity, permeability, water viscosity, degree of hydration, and tensile strength of the concrete [36] [37]. Critical thickness is the average maximum distance that water in the capillaries can travel without causing any damage. According to Powers' calculation, theoretical critical thickness in concrete is 0.2 mm (0.008 in.) [22] [37]. Based on this calculation, each air void would contain a spherical zone that was 0.2 mm (0.008 in.) beyond the radius of the bubble. These spheres are typically referred to as relief (protection) zones [22], as shown in Figure 2.3.

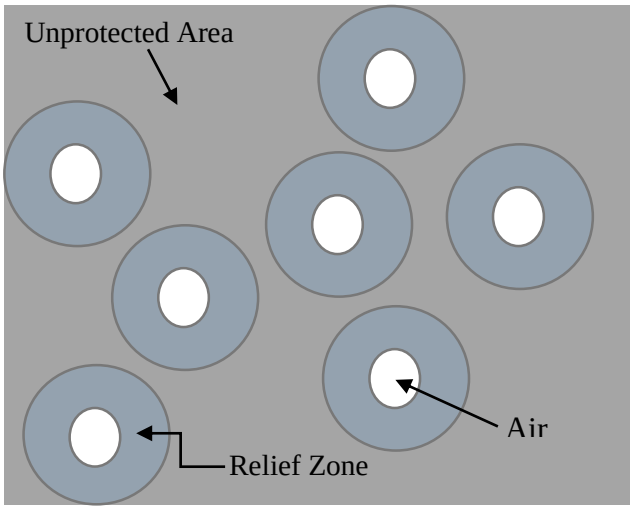


**Figure 2.3 Relief zones in air-entrained concrete [22]**

Buoyancy and consolidation of large buoyant bubbles causes air bubbles to be lost as they rise to the top of fluid concrete. Whether or not bubbles rise depends on concrete fluid properties

and bubble size. In order for a bubble to begin rising in concrete, applied shear stress attributed to upward buoyancy force and vibrational energy must be greater than the concrete's yield stress. Concrete yield stress is defined as the applied shearing stress needed to initiate the flow of concrete or cause the concrete to behave like a fluid. Applied shearing stress affects concrete viscosity, which consequently affects the speed at which bubbles rise. Viscosity is a measure of frictional forces between fluid layers. High viscosity causes increased frictional force between layers, resulting in higher resistance to bubble rising. Therefore, air bubbles rise slowly in concretes with high viscosity. Buoyancy force is proportional to bubble volume, whereas concrete resistance to bubble motion is proportional to surface area. Increased bubble size increases buoyancy related to the force's resisting motion and increases a bubble's tendency to rise in concrete. Stokes' law, shown in Equation 2.1, describes the motion of air bubbles in a viscous liquid [38].

$$v = \frac{\frac{2}{9}(\rho_{air} - \rho_{liquid})}{\mu_{liquid}} g R^2 \qquad \textbf{Equation 2.1}$$

where $v$ is air bubble velocity ($m/s$) (sinking if $\rho_{air} > \rho_{liquid}$ and rising if $\rho_{air} < \rho_{liquid}$), $\rho_{air}$ is mass density of the air bubble ($kg/m^3$), $\rho_{liquid}$ is mass density of the concrete ($kg/m^3$), $g$ is gravitational acceleration ($m/s^2$), and $\mu_{liquid}$ is dynamic viscosity of the concrete ($kg/m.s$).

Air volume required to accommodate water expansion is fairly small. A fully saturated concrete sample containing 30% paste requires approximately 1.3% air content in order to accommodate expansion [22]. Therefore, the number and distribution of air voids is more important than the total volume of air content. As shown in Figure 2.4, small air voids can produce large relief zone coverage and the same amount of air content with larger air voids can produce less relief coverage [22].

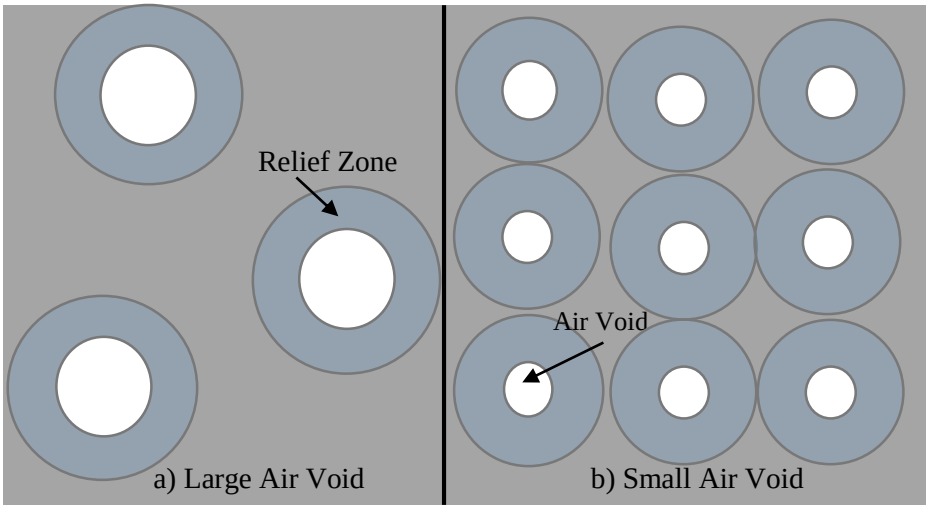


**Figure 2.4 Effect of air void size on relief zones (identical air content in both sides) [22]**

The spacing factor refers to average maximum distance that water must travel in order to reach the closest air void. Regardless of air void size, it can provide freeze-thaw protection to concrete within its relief zone [37]. The size of the relief zone depends on fluid viscosity, paste permeability, flow rate, and pressure gradient. According to Powers' calculations, an increase in flow rate and/or fluid viscosity causes the size of the relief zone to shrink [22]. Figure 2.5a illustrates the effect of proper spacing on freeze-thaw durability. As shown in the figure, water in concrete capillaries moves to the nearest air void without causing damage or cracking because these water capillaries are situated within a relief zone. However, when air voids are inadequately spaced, water freezes in the capillaries causing cracking and deterioration in the cement matrix, as shown in Figure 2.5b [22].

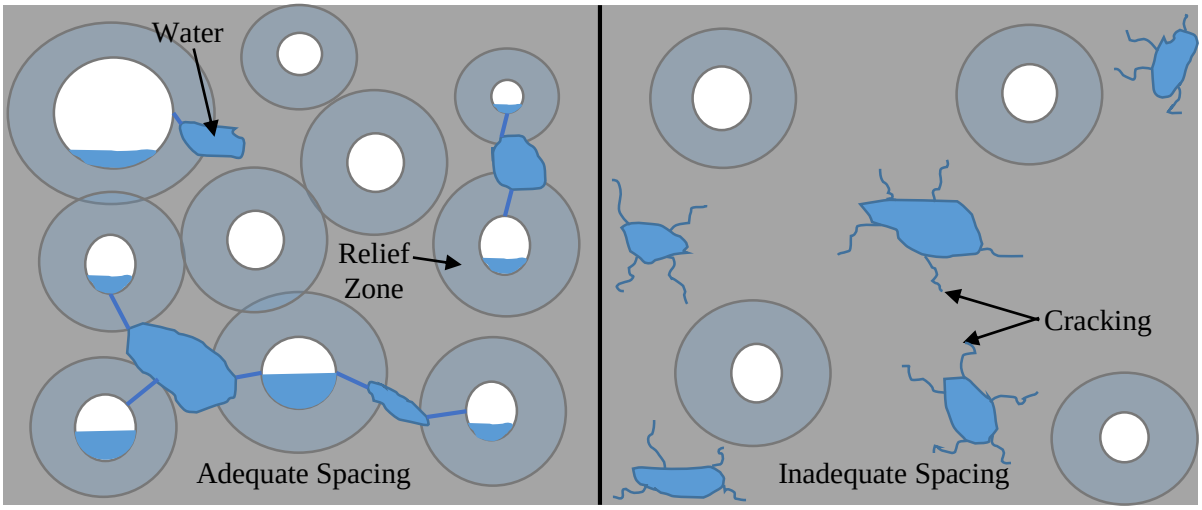


**Figure 2.5 Spacing factor effect**

### *2.3.2. Factors Affecting Air Void System*

Air void systems in concrete are influenced by factors such as cement, admixtures, rheology, mixing procedures, temperature, handling, and vibration. Research has shown that high cement alkali levels lead to a rise in air content, while an increase in the fineness of cement leads to a drop in air content [39] [40] [41]. As cement fineness increases, surface area also increases, requiring additional air-entraining agents to give the mix the desired air content [42]. Cementitious materials can affect air entrainment by affecting the air-entraining admixture. Carbon in fly ash works as an absorbent for surfactants used in the air-entraining admixture [43]. However, silica fume and slag cement negatively affect air content as a result of its high fineness and the presence of unburned carbon [41]. Metakaolin does not have any apparent effect on air content [41].

Admixtures' effects on the air system vary from normal to self-consolidating concrete (SCC). For normal concrete, admixtures containing lignin-based materials tend to increase the air content and the spacing factor [41]. The increase in air content is attributed to the nature of lignin, which is the base of some air-entraining agents. Retarders demonstrate similar effects as lignin-based materials, but accelerators have a negligible effect on air content [41]. SCC requires increased dosages of air-entraining agent in order to compensate for air loss [44] [45] [46]. In

highly fluid SCC, air bubbles experience more movement, causing ruptures and merging in the bubbles [44] [47]. In SCC with low fluidity, however, the air bubbles remain stable [34]. The addition of admixtures, such as viscosity modifying admixtures (VMAs) and superplasticizers, to the SCC disrupts the effect of air-entraining admixtures and causes less air entrainment [45]. When VMAs are used, increased dosages of superplasticizers are needed in order to maintain concrete workability. Cement particles absorb the superplasticizer as a result of this increase, thereby causing interference that prevents air bubbles from attaching to the cement [45]. The increase in concrete viscosity causes an increase in internal pressure of the air bubbles, resulting in air bubbles rupturing and escaping the concrete [48].

Rheology can be defined as the science of deformation and flow of bodies, including solids and fluids. Based on rheological properties, bodies can be categorized as solid, fluid, or plastic. A body is solid if it undergoes deformation under the application of any inhomogeneous force system without undergoing flow, regardless of large applied force. If the body is a fluid, it flows under the application of any inhomogeneous and anisotropic force system, regardless of small applied force. A plastic body, however, can behave like a solid or a fluid, depending on the value of the applied force. If the applied force exceeds a certain critical value, or yield stress, the body behaves like a fluid. If the applied force does not exceed the yield stress, however, the body acts like a solid. Two idealizations of this behavior that have been applied to concrete are Bingham plastics and Boltzmann plastics. Figure 2.6 shows a comparison between a Bingham plastic and a Newtonian fluid. As shown in the figure, any small application of a shear stress results in a shear rate that causes flow of a Newtonian fluid. Viscosity, or the ratio of applied shear stress to the rate of shearing strain, is constant for Newtonian fluids, but Bingham plastics have varying viscosities. The slope of the straight line that defines the relationship between the shearing stress and the rate

of shearing strain is referred to as the plastic viscosity for a Bingham plastic. For Newtonian fluids, the plastic viscosity is equal to the viscosity. In Bingham plastics, the lower the plastic viscosity, the higher the rate at which viscosity decreases with increasing shear stress. A Boltzmann plastic differs from a Bingham plastic in that its rheological characteristics depend on the shearing history of the material, meaning that the material exhibits changes in shearing stress with time even at a constant rate of shearing strain. This behavior is called thixotropy and antithixotropy. Thixotropy occurs when viscosity decreases with time, whereas antithixotropy occurs if viscosity increases with time. Some concrete mixtures exhibit strong thixotropy. Thixotropy could play an important role in concrete air void migration in concrete crossties that are vibrated for an extended period of time.

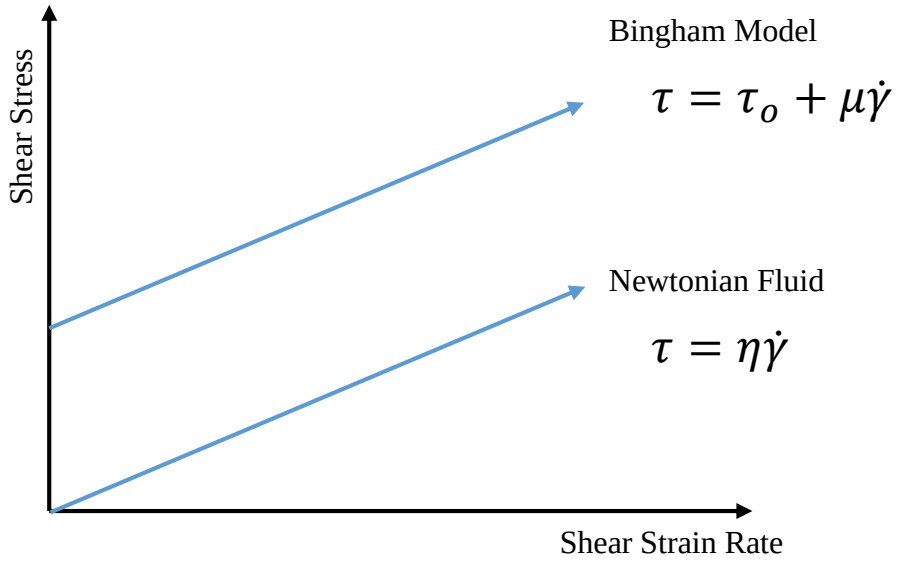


**Figure 2.6 Bingham plastic and Newtonian fluid rheological models**

Correlation of the effects of rheological properties on air content is very difficult because the addition of air alters rheological properties of any concrete [49]. Increased air content causes

a decrease in plastic viscosity and an increase in yield stress [49]. Increased mixing speed also results in increased air content [50]. Studies have shown that air content gradually increases with speeds up to 20 rpm and decreases at higher speeds [41]. The relationship between mixing time and air content was found to increase up to a certain mixing time, after which time the air content begins to destabilize [51]. Researchers have found that mixing for 60 seconds can achieve a good air void system, with air content increasing up to 90 seconds [52] [41]. Concrete with higher temperatures tends to have lower air content even when maintaining constant slump by adjusting the water [50]. For example, in order to achieve a constant 7 in. slump, the air content must drop 1% for every 15 $^{o}$C increase in temperature [50].

#### *2.3.2.1. Effects of Vibration on Concrete Air System*

During vibration, buoyancy causes air bubbles to be lost when they rise to the top of the fluid concrete or consolidate into large bubbles that readily rise to the concrete surface. Whether or not bubbles rise depends on concrete fluid properties and bubble size. In order for a bubble to begin rising in concrete, the applied shear stress provided by the upward buoyancy force and vibrational energy must be greater than the yield stress of the concrete. Concrete yield stress is defined as the applied shearing stress needed to initiate the flow of concrete (i.e., make the concrete behave like a fluid). The speed at which bubble rises is affected by the viscosity of concrete, which is consequently affected by the applied shearing stress. Viscosity is a measure of frictional forces between fluid layers. The higher the viscosity, the higher the frictional force between the layers, resulting in increased resistance to the rise of bubbles. This means that air bubbles rise more slowly in concretes with high viscosity as compared to concretes with low viscosity. Buoyancy force is proportional to bubble volume, whereas resistance to bubble motion by the concrete is proportional to the surface area. The larger the bubble, the larger the buoyancy relative to forces resisting motion

and the higher its tendency to rise in concrete. Vibration increases forces acting on the bubble, causing them to rise. However, researchers still do not fully understand exactly how these forces help bubbles. Vibration primarily eliminates large voids in the concrete and improve smoothness of the concrete finish on formed surfaces [53].

Similar to other congested concrete members, prestressed concrete ties are typically vibrated in order to consolidate the concrete and avoid honeycombing in the ties during placement. Vibration of concrete, however, can affect the entrained air content, bubble size, bubble spacing, and frost-resistance of hardened concrete. Excessive vibration results in loss of entrained air with 10 μm to 1 mm in diameter, thereby causing frost resistance in the concrete [54]. High vibration frequencies (maximum of 230 Hz) more significantly affect air content and spacing factor than frequencies lower than 130 Hz [55]. High frequencies disrupt air content by causing air bubbles to rupture or escape, and they increase spacing factors even when vibrated for as little as 20 seconds [56] [57]. At low frequencies (130 Hz), vibrators tend to locally affect the air content surrounding the vibrators [58]. Researchers have found that concrete loses the most air within the first few seconds of vibration; as vibration time increases, air loss decreases [59], indicating a proportionality between air loss and vibration time. Vibration tends to wield only a small sphere of influence since vibration in a small container leads to more air loss than vibration in a large container [59]. Regardless of initial air content, half of the air content could be removed from a 0.5 $ft^3$ of concrete in 50 seconds, while removal of the same amount of air would require only 12

seconds in 0.2 $ft^3$ of concrete when vibrated with a rod vibrator [60]. A correlation also exists between air loss and vibration of higher slump concrete [59].

## 2.4. Testing

### *2.4.1. Freeze-Thaw Testing*

Researchers such as Wray, Lichtefeld, Sweet, Lemish, Klieger, Stark, and Powers have studied freeze-thaw testing [61], and numerous standards are currently dedicated to the assessment of concrete resistance to freeze-thaw conditions [62], including ASTM C666 [63], UNE 12390-9 [64], JIS A 1148 [65], Rilem TC 176-IDC [66] [15], CEN/TR 15177 [67], and SS 137244 [68]. In his report, Makoto Kaneuji reported that the Highway Research Board Committee on Durability of Concrete-Physical Aspects investigated ASTM approaches for testing concrete resistance in freezing and thawing conditions [61]. They tested three concrete mixtures using four methods suggested by the ASTM. The first method, Rapid Freezing and Thawing in Water (ASTM C290), and the second method, Rapid Freezing in Air and Thawing in Water (ASTM C291), were withdrawn in 1971. The Slow Freezing and Thawing in Water or Brine (ASTM C292) method was withdrawn with no replacement in 1965, and the Slow Freezing in Air and Thawing in Water (ASTM C310) method was withdrawn with no replacement in 1964 [63]. Methods C292 and C310, both of which provided a single cycle every 24 h in order to cover tests that involve manual transfer of samples between freezing chambers and thawing tanks, were dropped from ASTM specifications as a result of their high cost and long time required for results [69]. In addition, ASTM C291, ASTM C292, and ASTM C310 were deemed too variable and required more consistent replacements [70]. As a result, they concluded that the Rapid Freezing and Thawing in Water (ASTM C290) method was the least variable and, therefore, the most reliable of the four

tests. This test is currently referred to as Resistance of Concrete to Rapid Freezing and Thawing (ASTM C666) Procedure A.

The ASTM C666 Standard consists of two tests: Procedure A and Procedure B. Procedure A involves rapid freezing and thawing in water, while Procedure B entails rapid freezing in air and thawing in water. Concrete specimens tested according to ASTM C666 were between 3 x 3 x 11 in. (75 x 75 x 279 mm) and 5 x 5 x 16 in. (125 x 125 x 405 mm). These specimens were saturated in a lime water bath for at least two days, and then conditioned at 40 °F (4 °C). The concrete was then frozen to 0 °F (-18 °C) and thawed to 40 °F (4 °C) 300 times. The freezing was rapid, with up to 12 cycles performed per day. As required, the freeze-thaw cycle was completed in not less than 2 hours and not more than 5 hours, with the thawing period requiring 25% of the cycle time for Procedure A and 20% for Procedure B [16], resulting in a cooling rate of 10.8 $^{o}$F/h (6 $^{o}$C/h) to 27 $^{o}$F/h (15 $^{o}$C/h). During testing, samples are were immersed in water or frozen in air and thawed by flooding the chamber that contained the concrete samples with water [63]. Damage was monitored by measuring the dynamic modulus of elasticity, length change, and mass loss after every 36 cycles or less. The freeze-thaw test was usually terminated once the 300 cycles were completed or the (RDME) dropped below 60%.

Although ASTM C666 was advantageously completed within two months, various issues arose as a result of subjecting concrete to such rates of freezing and thawing. The rates of freezing and thawing prevented ASTM C666 from replicating the natural exposure experienced in the field. Temperatures changes in nature rarely exceed 4 $^{o}$F (2 $^{o}$C) per hour, while in the rapid freeze-thaw test described in ASTM C666, temperature changes reached 27 $^{o}$F (15 $^{o}$C) per hour [16], indicating that deterioration caused by rapid freezing may not occur in nature. As a result of the variation of freezing rate allowed by ASTM C666, results of freeze-thaw durability varied depending on

freezing rates used by individual testing equipment. In addition to the freezing rate, the freezing time was significantly less in ASTM C666 than long freezing times observed in nature. Moreover, samples were kept fully saturated during the freeze-thaw test, which may not be an accurate replication of concrete in nature.

Three main European freeze-thaw resistance tests (CEN/TR 15177 and CEN/TS 12390-9) exist: the Slab-Test, the German and/or Cube Test, the CIF-Method. The Slab-Test, based on the Swedish freeze-thaw test (SS 137244) [71], requires four samples with 15 x 15 x 5 cm dimensions to be simultaneously tested. These slabs are obtained by saw-cutting four 15-$cm^3$ cubes. These cubes are demolded after 24 hours and then cured under water for 6 days at 20±2 °C. After curing, the samples are stored in a climatic chamber at 20±2 °C and 50±10% relative humidity for 21 days. After 14 days in the climatic chamber, the samples are sawn and then sealed from every surface except the top surface and then returned to the climatic chamber for 7 days. After a total of 28 days of age, the samples are subjected to de-ionized water (3 mm) on the top surface for 3 days [67]. Then the freeze-thaw testing is commenced on the samples with a cooling rate of 1.7 $^oC/h$ for a 12-hour freezing cycle and 12-hour thawing cycle (between +20±4 °C and -18±2 °C). The freeze-thaw rate is controlled by placing the sensor in the de-ionized water and on the top surface of the specimen. The specimens are measured in terms of RDME using Ultrasonic Pulse Transit Time or Fundamental Transverse Frequency after 7, 14, 28, 42, and 56 freeze-thaw cycles during the thaw cycle. The duration of the Slab-Test is 56 cycles, and criteria for failure is not defined as part of this standard method [67]. Therefore, flexibility of the Slab-Test method allows accommodation of criteria set by local authorities or clients. However, because the Slab-Test can test only one surface of the concrete, it is not an accurate representation of concrete elements that are consistently exposed to the environment. In addition, the Slab-Test method requires lengthy

storage in the climate chamber before testing, and the total length of the test may not be adequate to obtain an actual representation of freeze-thaw durability of the concrete. Although the Slab-Test is simple to perform and requires relatively low cost, sample preparation and accounting for the saw-cutting are difficult [74].

The second freeze-thaw method described in the European freeze-thaw resistance code is the German and/or Cube Test. As the name implies, test samples consist of 10 $cm^3$ concrete cubes that can be cast or excised from a larger structure. Similar to the Slab-Test method, the cubes are demolded after 24 hours and then cured under water for 6 days at 20±2 °C [71]. After curing, the samples are stored in a climatic chamber at 20±2 °C and 65±5% relative humidity for 20 days [72]. Then the samples are soaked for 1 day in water before the freeze-thaw testing commences. The procedure requires four cubes to be tested for each set, with two cubes in each frost chest. The samples are kept in water during the freeze-thaw cycles. Each freeze-thaw cycle runs for 24 hours, and testing is carried out during the thawing cycle. Freeze-thaw testing is performed by soaking the samples in a chest freezer with a cooling rate of 1.2 ºC/hour for 10 to 14 hours in the freezing cycle and 10 to 14 hours in the thawing cycle (between +20±2 °C and -15±2 °C) [73]. The freeze-thaw rate is controlled by placing the sensor in the center of one of the specimens. Testing includes RDME using Ultrasonic Pulse Transit Time or Fundamental Transverse Frequency in addition to a loss in weight after 7, 14, 28, 42, and 56 freeze-thaw cycles. Duration of the Cube method is 56 cycles, and the criteria for failure is not defined as part of this standard method [73]. Similar to the Slab-Test, the Cube method requires lengthy storage in the climate chamber before testing. In addition, the total length of the test may not be adequate to obtain actual representation of freeze-thaw durability of the concrete. Moreover, the test may not accurately replicate nature's severity in terms of freezing temperatures and freezing rate.

The third freeze-thaw method described in the European freeze-thaw resistance code is the CIF test (capillary suction, internal damage, and freeze-thaw). Test samples consist of five or more samples with 15 x 15 x 7 cm concrete dimensions. These samples can be cast samples or excised from a larger structure. Cast samples are cast in a 15-$cm^3$ mold with a vertical poly-tetra-fluor-ethylene (PTFE) plate in the center of the mold. Similar to the previous two methods, CIF samples are demolded after 24±2 hours and then cured under water for 6 days at 20±2 °C [15]. After curing, the samples are stored in a climatic chamber at 20±2 °C and 65±5% relative humidity for 21 days. After 7 days and before the completion of 21 days in the climatic chamber, the specimens are typically sealed on their lateral sides with aluminum foil using butyl rubber or a solvent-free epoxy resin [15]. Then the samples are placed on 5-mm spacers with the testing surface downward inside the testing container, followed by the addition of 10±1 mm of de-ionized water to the container. Capillary suction lasts for 7 days at a temperature of 20±2 °C. Each freeze-thaw cycle runs for 12 hours, and testing is carried out during the thawing cycle. Freeze-thaw testing is performed with a cooling rate of 10 $^{o}$C/h for a 4-hour freezing cycle and 4-hour thawing cycle (between +20±2 °C and -20±2 °C) [15]. In addition, the freezing cycle is kept constant at -20±2 °C for 3 hours, while the thawing cycle is kept at +20±2 °C for 1 hour. The freeze-thaw rate is controlled by placing the sensor underneath the testing container. Testing includes RDME using Ultrasonic Pulse Transit Time or Fundamental Transverse Frequency after 7, 14, 28, 42, and 56 freeze-thaw cycles. Duration of the CIF method is 56 cycles completed in 28 days. Failure criteria of the method are typically defined according to ISO 5725 [15]. The damage to concrete is slight if the RDME is greater than 90%, medium to extensive if the RDME is between 90% and 60%, and extensive to total if the RDME is below 60%. However, the simple preparation effect of the German Cube Method and the CIF Method is contradicted by the high cost of operation [74].

The primary goal of the critical degree of saturation test is to predict the duration that concrete can last in field under natural freeze-thaw cycles [16]. As part of this test, various degrees of saturation for a concrete specimen must be determined prior to freeze-thaw testing. In order to perform this test, 15 to 20 specimens are needed [75]. Samples' initial weights are recorded in order to obtain initial moisture conditions, and then the specimens are dried at 50 $^{o}$C for at least 2 days and reweighed [75]. The specimens are then vacuum-saturated for 2 days and weighed in water and air. Based on the degree of saturation and the two measurements of weight, the required specimen weight is calculated and the specimens are dried to that specific weight. When the specific weight is reached, the specimens are wrapped with thick plastic and sealed with tape [75]. After one day of sealing, the specimens' weights and fundamental frequencies are determined, and then freeze-thaw testing of the rewrapped specimen begins. Freezing and thawing occurs in air for 6 cycles. Freezing begins with the samples' center temperatures dropping to -10 $^{o}$C in 5 - 6 hours and then to -20 $^{o}$C after an additional 3 hours [75]. Thawing begins once specimen temperatures drop to -20 $^{o}$C, and thawing continues until specimen temperatures reach 5 $^{o}$C. After 6 cycles are completed, the specimens' fundamental frequencies and weights are recorded at room temperature. The critical degree of saturation ($S_{CR}$) is then determined, and the samples are dried at 105 $^{o}$C for at least 1 week [75]. The length of time required to reach critical saturation is determined by measuring absorption over a period of time. Unlike the ASTM C666, this test allows prediction of the service life prior to freeze-thaw damage. One disadvantage to the critical degree of saturation method is its inapplicability to test for salt scaling [16].

The critical dilation test measures the change in length of concrete specimens during freezing cycles. A concrete specimen that is sufficiently air-entrained experiences a decrease in length, while a frost-susceptible concrete specimen expands as the temperature drops below

freezing. ASTM C671 utilizes the critical dilation method to determine the duration that concrete can last under freeze-thaw cycles. Samples are made and cured to match exposed concrete in the field [16]. Specimens contain stainless steel gauge plugs at both ends in order to measure the change in length using a liner variable displacement transducer [16]. Freezing cycles begin when the specimens are placed in a water-saturated kerosene bath at 36 $^{o}$F (2 $^{o}$C) and then cooled at a rate of 5±1 $^{o}$F/h (2.8±0.5 °C/h). Once the temperature reaches 14 $^{o}$F (-10 $^{o}$C), the samples are removed from the freezing chamber and placed in water at 36 $^{o}$F (2 $^{o}$C) for 2 weeks until the next freezing cycle [16]. The length change measurement and temperature of the water-saturated kerosene bath are recorded regularly during the freezing cycle. In order to obtain dilation of the specimen, the maximum distance between the reduction curve (obtained from the change in length data) and a straight line that extrapolates pre-freezing data is measured [16]. For frost-susceptible concrete, the dilation continues to increase for each cycle. ASTM C671 set the failure criteria of the concrete to be an increase in dilation by two or more between consecutive cycles. Although this test reveals a very similar freezing rate to actual rates in nature, approximately 6 years would be required in order to perform 300 freeze-thaw cycles [16]. Moreover, this test cannot evaluate concrete specimens that have marginal freeze-thaw durability for which frost damage require longer periods in order to be more significant. This test also neglects the effect of lengthy freezing durations because the test requires only approximately 4 hours for completion, as is the case in nature [16]. This resulted in discontinuation of ASTM C671 in 2003.

#### *2.4.1.1. Method to Measure Freeze-Thaw Durability*

Powers first developed resonance frequency (RF) in 1938 [76]., RDME of the prismatic bar can be obtained using resonant frequency measurement of the bar's vibration [77]. Two methods are commonly used to determine resonant frequency of a concrete specimen: the forced

resonance method and the impact resonance method [78]. The forced resonance method uses an electromechanical driving unit to vibrate a supported specimen while measuring vibration of the surface of the specimen. The specimen is vibrated at various frequencies, and the frequency that corresponds to the maximum amplitude is the resonance frequency (RF) [78]. In the impact resonance method, a rounded impactor (rounded hammer) strikes the specimen, and an accelerometer records the impact wave. The recorded wave is analyzed using Fast Fourier transform (FFT) in order to obtain RF. RDME obtained by the resonant frequency method depends on specimen size and shape [79]. Wave induced by impact on the surface of the concrete causes the concrete to vibrate at its own natural frequencies [77], but amplitudes of these natural frequencies can be affected by cracking or air pockets. A drop in amplitude is known as damping capacity. This damping capacity increases significantly as a result of increased porosity, voids, a cracked location, or a weakness in the paste [69]. The damping effect tends to be more prominent in smaller sections because of their higher initial frequencies compared to low frequencies of large sections. In addition, the resonant frequency method can only be applied in laboratories with small dimension samples because variation in dynamic properties depends on sample size [79]. In addition, the damping effect of the surrounding can reduce the frequency measurement in the field.

Ultrasonic Pulse Velocity (UPV) can be used to evaluate the condition of concrete specimens with various shapes and sizes. In UPV, a transmitting transducer (electro-acoustical transducer) is used to generate mechanical wave bursts from voltage pulses [80]. A receiving transducer is placed at a known distance from the transmitting transducer in order to measure the time interval between the transmission and reception of the pulse. These two transducers should be coupled to the concrete surface using a proper medium (grease or cellulose paste) [80]. The generated pulse can travel through the concrete but not through air, causing the pulse to travel

around cracks, thereby increasing travel time and lowering velocity. These transducers are typically arranged in one of three configurations: direct transmission, semi-direct transmission or diagonal transmission, and indirect or surface transmission. Direct transmission results in maximum sensitivity because the two transducers face each other and they do not require any wave reflection [80]. As concrete deterioration develops, changes are reflected as a decrease in pulse velocity [80].

Impact Echo (IE) has been used to detect structure thickness, internal delamination, honeycombing, and cracking parallel to the surface [81]. During an IE test, a solenoid impactor is used to induce a displacement wave (P-Wave) in the concrete that is picked by an accelerometer [81]. Wave energy is reflected when the medium for wave travel changes, usually from concrete to air or water as a result of cracking, delamination, or the end of the section or depth. In order to identify resonant echoes, the frequency domain is utilized instead of the time domain. FFT analysis is then performed on the collected data in order to obtain the resonant echo peak and concrete depth [81].

#### *2.4.1.2. Post-tensioning and Prestressing Effect on Freeze-Thaw Durability*

In 1959, Fouad E. Musleh studied the effect of post-tensioning on freeze-thaw durability of concrete [82]. He attempted to compare the performance of ordinary concrete and post-tensioned concrete under repeated cycles of freezing and thawing. Ordinary concrete had an ultimate strength of 3000 psi, while the post-tensioned concrete had an ultimate strength of 5000 psi [82]. Two identical sets of specimens were made with different curing times: Specimens in Set 1 cured for 28 days, and specimens in Set 2 cured for 14 days. Each set consisted of four concrete batches made according to two concrete design mixes. Three batches were made with a mix design, resulting in an ultimate strength of 5000 psi, and one batch was made with a mix design that

resulted in an ultimate strength of 3000 psi. Six specimens were made in each of the batches, resulting in a total of 24 specimens in each of the two sets, totaling 48 specimens [82]. In addition, 6-in. by 12-in. compression test cylinders were made in order to test the ultimate strength of the batch. All 48 specimens were beams with dimensions of 3 x 4 x 16 in. The testing chamber achieved freezing at 0 $^{o}$F and thawing at 40 $^{o}$F in accordance with ASTM C291-52T. Sample freezing was monitored at the center of a dummy sample, requiring 2.5 hrs to reach freezing. Thawing required approximately 0.5 hrs to reach 40 $^{o}$F. When the samples completed 20 cycles, the freeze-thaw chamber was turned off and specimens were tested for changes in weight and dynamic modulus of elasticity. Musleh concluded that post-tensioning concrete improves its durability against freeze-thaw conditions. In addition, continuously post-tensioned concrete specimens were more durable than intermittently-stressed concrete specimens, but both proved to be more resilient against freeze-thaw than unstressed concrete samples [82].

In 1979, the Canadian Rail Research Center performed freeze-thaw testing on large samples saw-cut from eight prestressed concrete railroad ties, two ties from each prestressed concrete railroad tie used in the Canadian rail system [3]. Three samples were collected from each two-tie set, as shown in Figure 2.7. The first two samples (A and B) were cut from a tie that cracked under static loading; the third sample (C) was cut from a tie that failed in fatigue under dynamic loading. Completion of one freeze-thaw cycle took 24 hours, with temperatures increasing from -17.8 $^{o}$C (0 $^{o}$F) to 4.4 $^{o}$C (40 $^{o}$F). Freezing and thawing cycles were performed in water. Researchers discontinued testing on the largest sample (B) after 100 cycles in order to avoid handling-induced damage of the large and heavy samples. After 98 cycles, investigators noticed spalling and chipping on some samples with initial indications of rust at the wires' ends. In addition, weight loss was less than 0.35% of the original weight. After 305 cycles, one of the samples from Set A

was completely destroyed, and any hand pressure caused crumpling of the remaining structure. Two of the samples from Set A did not suffer any deterioration after 305 cycles, and the fourth sample exhibited only light spalling, pop-outs, and fine cracking. The only observed deteriorations of samples in Set C were light pop-outs and spalling after 340 cycles. Researchers concluded that samples that did not suffer deterioration were air-entrained. Therefore, they stated that air entrainment is necessary to ensure freeze-thaw durability.

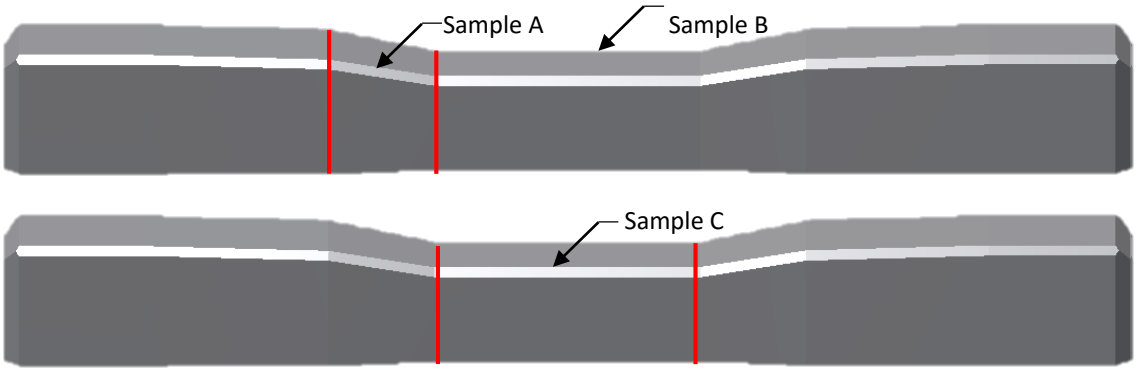


**Figure 2.7 Freeze-thaw saw-cut samples**

### *2.4.2. Air Measurements*

#### *2.4.2.1. Methods to Measure Air Voids in Fresh Concrete*

Three main methods are typically used to measure air voids in fresh concrete: the Gravimetric method, the Volumetric method, and the Pressure method. The Gravimetric method compares the theoretical unit weight of concrete and the measured unit weight. According to ASTM C138 [83], air content (A) can be computed according to the Gravimetric method using Equation 2.2 and Equation 2.3.

$$A = \frac{U_t - U}{U_t} x100 \qquad \textbf{Equation 2.2}$$

$$A = \frac{V - V_i}{V} x100 \qquad \textbf{Equation 2.3}$$

where $V = Volume\ of\ concrete\ produced\ per\ batch, m^3 [yd^3]$

$V_i = Total\ volume\ of\ batch\ ingredients, m^3\ [ft^3]$

$U = Unit\ weight\ of\ concrete, kg/m^3\ [lb/ft^3]$

$U_t = Theoretical\ unit\ weight\ of\ concrete\ excluding\ the\ air, kg/m^3\ [lb/ft^3]$.

Unfortunately, a minor error in calculation can lead to a significant error in calculated air content. This method is typically used as a comparison baseline for air content of a concrete batch, but it lacks precision provided by other methods [16].

The Volumetric method compares concrete volume to the volume of the same concrete after expelling air by agitating the concrete under water. Figure 2.8 shows the volumetric air meter (roller meter) used in ASTM C173 [84]. The volumetric air meter has two sections. The top section of the meter must be larger than the bottom section by at least 20%, and the bottom section must have a minimum volume of 0.002 $m^3$ (0.075 $ft^3$). In addition, both sections must be watertight when assembled with the concrete sample inside. After the bottom section is filled with concrete, the two sections are assembled using clamps. Then, using a funnel inserted in the nick of the top section, water is poured slowly in order to reduce disturbance until the specific calibration mark is reached. The vessel is sealed from the top using the screw cap. Finally, the concrete is agitated in order to force air out. When the air is stabilized and remains constant at the top of the vessel, the difference in water level and air content (A) are calculated using Equation 2.4.

$$A = \frac{(h_i - h_f)A_{top}}{V_{bottom}} x100 \qquad \textbf{Equation 2.4}$$

where $h_i = Initial\ water\ height\ before\ agitiation, mm\ [in]$

$h_f$ = $Final\ water\ height\ when\ air\ became\ constant\ and\ stable, mm\ [in]$

$A_{top} = Cross - sectional\ area\ of\ the\ top\ section\ of\ the\ vessel, mm^2\ [in^2]$

$V_{bottom} = Volume\ of\ the\ bottom\ section, mm^3\ [in^3]$.

Although this method is not affected by aggregate type and properties such as moisture content and absorption, measurements are difficult to make in the field and require significant physical effort, leading to results with decreased accuracy [16].

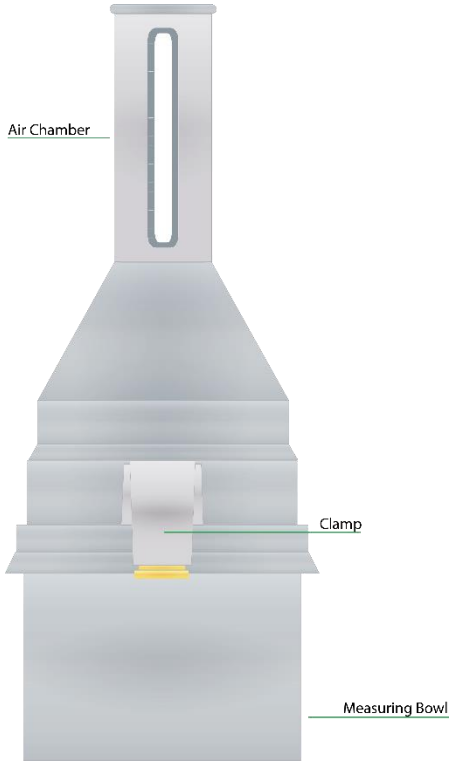


**Figure 2.8 Air meter for ASTM C 173 volumetric test [85]**

The Pressure method measures volume change or pressure change of a concrete sample because air in the concrete, both in the cement and the aggregate, is compressed by applied pressure. According to ASTM C231 [86], two types of air meters measure air content. A Type A air meter employs differences in volume measurement. Similar to the volumetric vessel, the Type A air meter utilizes a watertight seal in addition to water filled to a fixed level in order to measure

air content, as shown in Figure 2.9. Implementation of Boyle's law, which states that multiplication of the pressure and volume of an ideal gas at a given temperature is constant, allows calculation of concrete sample air content [16]. Because water is an incompressible substance, air is identified as the only material that changes volume, as shown in Equation 2.5.

$$A = \frac{(h_i - h_f)A_{top}}{V_{bottom}} x \left(\frac{P}{P - P_{atm}}\right) x100 \qquad \textbf{Equation 2.5}$$

where $P_{atm}$ is the atmospheric pressure and $P$ is the pressure of the air meter that can be checked using Equation 2.6.

$$P = \frac{V_{bottom}P_{atm}}{V_{bottom} - A_{top}(h_i - h_f)} \qquad \textbf{Equation 2.6}$$

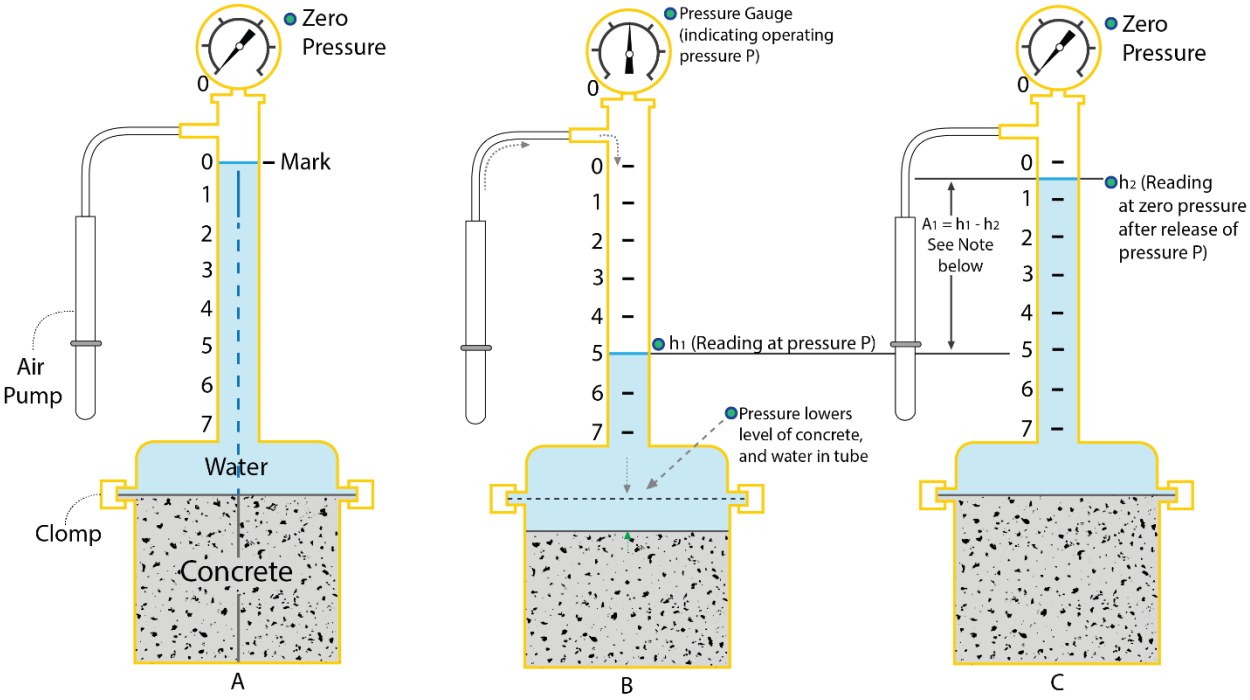


Note: $A_1 = h_1 - h_2$ when measuring bowl contains conrete as shown in this figure; when measuring bowl contains only aggregate and water , $h_1 - h_2 = G$ (aggregate correction factor ).
$A_1 - G = A$ (entrained air content of concrete)

**Figure 2.9 Type A air meter to measure air content using the pressure method [86] (Reprinted with permission from C231/C231-10 Standard Test Method for Air Content of Freshly Mixed Concrete by the Pressure Method, copyright ASTM International, 100 Barr**

**Harbor Drive, West Conshohocken, PA 19428. A copy of the complete standard may be obtained from ASTM International, www.astm.org.)**

Type B air meters measure the pressure difference in order to calculate the air content of a concrete sample. Although predominantly similar to the previous two vessels, this apparatus also contains two parts joined by clamps to form a watertight seal. Once the bottom pot is filled with concrete in three layers and ASTM standard 25 rodding has been performed, the two parts are clamped together. Water is introduced through one of two petcocks in order to fill the remaining void between the concrete sample and top section of the apparatus, as shown in Figure 2.10. Once the pressure gauge is zeroed out, the air pump is pumped until the pressure gauge aligns with the calibrated pressure value. Then the two petcocks are closed, and the sample is pressurized by releasing air pressure from the top section of the vessel to the concrete sample using the main air valve, thereby allowing the pressure gauge to record the decrease in air pressure in the top section of the apparatus. Application of Boyle's law allows use of Equation 2.7 to calculate air content.

$$A = \frac{V_i}{V_{bottom}} x \left( \frac{P_i - P_f}{P_f - P_{atm}} \right) x100 - G \qquad \textbf{Equation 2.7}$$

where $V_i$ is the initial volume of air in the top section and $P_i$, $P_f$ are the initial and final pressures of the air meter, respectively. $G$ is the aggregate correction factor measured using the method described in ASTM C231 [86].

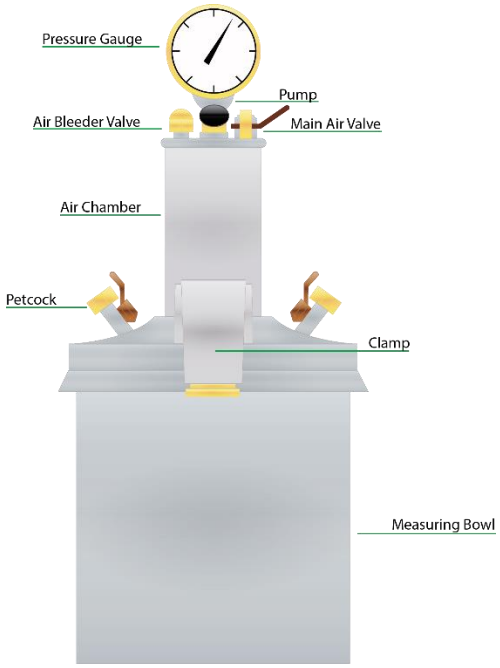


**Figure 2.10 Type B air meter to measure air content using the pressure method**

### *2.4.2.2. Hardened Air Void Measurements*

Adequate air content with proper spacing between air voids is essential in order for concrete to resist freezing and thawing in the field. This increases in importance when the element in question is installed in the rail tracks under the effects of the environment. Unfortunately, however, concrete air content varies immediately upon completion of concrete mixing until concrete delivery, placement, and vibration. Therefore, actual air content and spacing in the actual elements must be known. Several methods are available for quantifying the air void system in hardened concrete. Three-dimensional (3D) scanning of a concrete sample is now possible using X-ray microtomography, but this method cannot be used on large concrete samples to measure air voids and it is slow and expensive. However, advancements in current microscopic analysis methods, in which samples are saw-cut and air void is counted, have allowed more time and cost-efficient analyses. Quantitative stereology has been used to determine air void characteristics in

3D volumes from two-dimensional (2D) surfaces [87]. Quantitative analysis is usually done by taking a plane section, with enough area to estimate the total volume, from the analyzed 3D volume [88]. When a saw-cut plane intersects air void spheres, it creates circles, but these circles may not be good representations of the spheres' radii. This misrepresentation can yield useful information regarding variation in the spheres' radii distribution [88]. Two assumptions are typically made for air void systems: a) air void microstructural sphere systems do not overlap, and b) air voids are distinct spheres [88]. A concrete petrographer can choose between several probes when performing stereological analysis. These probes include points, lines, surfaces, or volumes. A concrete petrographer must choose a probe based on the amount of data required for the test. For example, point probes are used to determine volume fractions, while line probes characterize the size and spacing of air voids [88]. Although the number of air voids can be calculated from surface probe data, it can only be approximated in line probe data. Two methods for quantifying air void system quality are described in ASTM C457 [89]: the linear traverse and modified point count methods [90].

#### *2.4.2.2.1. Linear Traverse*

The linear traverse method records individual and cumulative chord length of the paste, aggregate, and air voids across predefined parallel and equally spaced lines across the specimen surface [89]. Air content is calculated by dividing the cumulative chord length crossing air voids by the total length of chords multiplied by 100. Figure 2.11 shows chord distribution on a concrete sample used to measure air content in the linear traverse method.

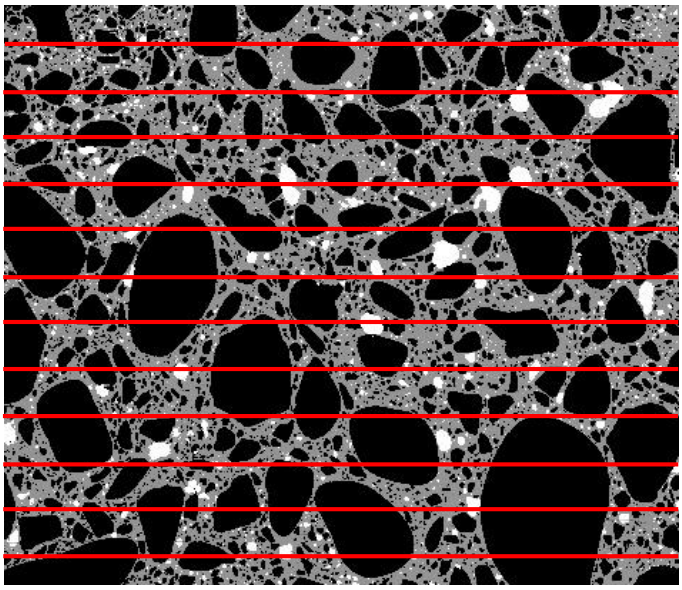

**Figure 2.11 Linear traverse method on a concrete sample**

Two main concrete properties, air content ($A$) and paste content ($p$), can be calculated using Equation 2.8 and Equation 2.9 [89]. The spacing factor ($\overline{L}$), calculated using Equation 2.10 [89], depends on the paste-air ratio ($p/A$). In order to solve these equations, the total number of air voids intersected ($N$), total length of traverse ($T_t$), traverse length through air ($T_a$), and traverse length through paste ($T_p$) must be measured and recorded.

$$A = 100\left(\frac{T_a}{T_t}\right) \qquad \textbf{Equation 2.8}$$

$$p = 100\left(\frac{T_p}{T_t}\right) \qquad \textbf{Equation 2.9}$$

$$\overline{L} = \begin{cases} \dfrac{T_p}{17.368\ \mathrm{N}} & if\ p/A < 4.342 \\ \dfrac{3\ T_a}{17.368\ \mathrm{N}}\left[1.4\left(1+\dfrac{p}{A}\right)^{\frac{1}{3}} - 1\right] & if\ p/A > 4.342 \end{cases}$$ **Equation 2.10**

The linear transverse method gives air content 10 to 20% less than what is recorded for fresh concrete using the pressure method and volumetric method [91], especially when air content exceeds 4%. Therefore, 0.5 to 1.5% higher air content is typically reported by fresh concrete testing methods [91]. Therefore, Khayat and Nasser recommended use of Equation 2.11 and Equation 2.12 to predict linear transverse results from air content measured using a fresh concrete air content test [91].

$$LT_{Predicted\ Air\ Content} = 1.10 + 0.58x(Air\ measured\ by\ Pressure) \quad \textbf{Equation 2.11}$$

$$LT_{Predicted\ Air\ Content} = 0.42 + 0.78x(Air\ measured\ by\ Volumetric) \quad \textbf{Equation 2.12}$$

However, Celik Ozyildirim [92] reported no significant difference between air content measured by the pressure method and air content measured by the linear transverse method using untampered concrete from the same batch. He also attributed that difference to the admixture used to entrain air in the concrete [92].

#### *2.4.2.2.2. Modified Point Count*

In the modified point count method, a grid of lines is used as a testing reference for which the constituent under each point on the grid is identified. Figure 2.12 shows a grid drawn on a concrete sample. Concrete characteristics can be identified by recording the total number of air voids intersected ($N$), total number of points on the grid ($N_t$), total number of paste points ($N_p$), and total number of air points ($N_a$). Equation 2.13 and Equation 2.14 are used to calculate the paste

and air content of the sample, respectively [89]. Depending on the paste-air ratio (*p/A*), Equation 2.15 is used to calculate the spacing factor of air in the concrete sample [89].

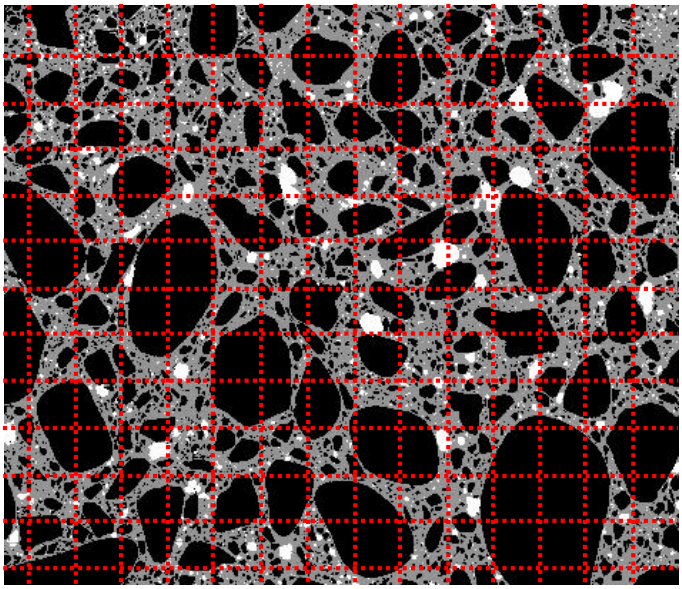

**Figure 2.12 Modified point count method on a concrete sample**

$$p = 100\left(\frac{N_p}{N_t}\right) \qquad \textbf{Equation 2.13}$$

$$A = 100\left(\frac{N_a}{N_t}\right) \qquad \textbf{Equation 2.14}$$

$$\overline{L} = \begin{cases} \dfrac{p\,N_t}{1736.8\,N} & if\ p/A < 4.342 \\ \dfrac{3\,N_t A}{1736.8\,N}\left[1.4\left(1+\dfrac{p}{A}\right)^{\frac{1}{3}} - 1\right] & if\ p/A > 4.342 \end{cases} \qquad \textbf{Equation 2.15}$$

#### *2.4.2.2.3. Image Analysis*

Image analysis is a process in which an algorithm is used to separate out air voids from the paste and aggregate in a cross-section of the concrete using an image of the concrete surface instead of manual examination of the surface. Image analysis follows the same sample preparation as ASTM C457 [89] methods: Samples are polished before scanning. Image analysis performed on

scanned images utilizes either of the two methods in ASTM C457 [89] [93]. Image analysis involve separating scanned images based on color or other features into cross-sectional images of the cement paste, air content and aggregate. Several methods are available to perform image analysis in order to obtain various air parameters. One of the main methods involves analyzing black and white enhanced samples using a microscope, a camera, and a computer [94]. A commercial system known as the RapidAir 457 utilizes that method with the help of computer image processing software. Results obtained from the RapidAir 457 have shown excellent correlation with air void parameters obtained using ASTM C457 [94].

The image analysis method can also be used in conjunction with a flatbed scanner and image processing software. In 2001, Karl Peterson developed a novel procedure to study hardened concrete samples using a flatbed scanner [95]. This method consisted of three stages: non-stained scanned sample, phenolphthalein-stained scanned sample, and black and white-treated scanned sample. A computer program that uses an automated modified point count method to determine air content properties is utilized. In his study, Peterson conducted four analyses on each image while changing sampling point locations for each analysis in order to optimize results throughout the entire sample. His tests of 570 microscopic images yielded 90.2% accuracy using an automated modified point count compared to a modified point count method manually performed on the same samples. In addition, air void frequencies and specific surfaces were lower than those calculated and measured according to the manual modified point count method. Spacing factors were also slightly higher than spacing factors measured using the manual modified point count method. According to Peterson, these differences could be attributed to poor detection of small air voids or the scanner's tendency to lump air voids in close proximity to each other. These two discrepancies

could be overcome using a higher resolution scanner. However, Peterson proved that this method works with anticipated increased accuracy with higher resolution scanners.

Although the automated modified point count method successfully measured air content parameters, small variations occurred when changing sampling points [95]. Similar to the linear traverse method in which every pixel line can be analyzed, as shown in Figure 2.13, utilization of computational capabilities of current computers can achieve better results by sampling every pixel as a point in the image. Peterson *et. al.* (2002) concluded that standard deviations calculated for samples analyzed by the modified point count method were consistently larger than that of identical standard deviations calculated for samples analyzed by the linear traverse method [96].

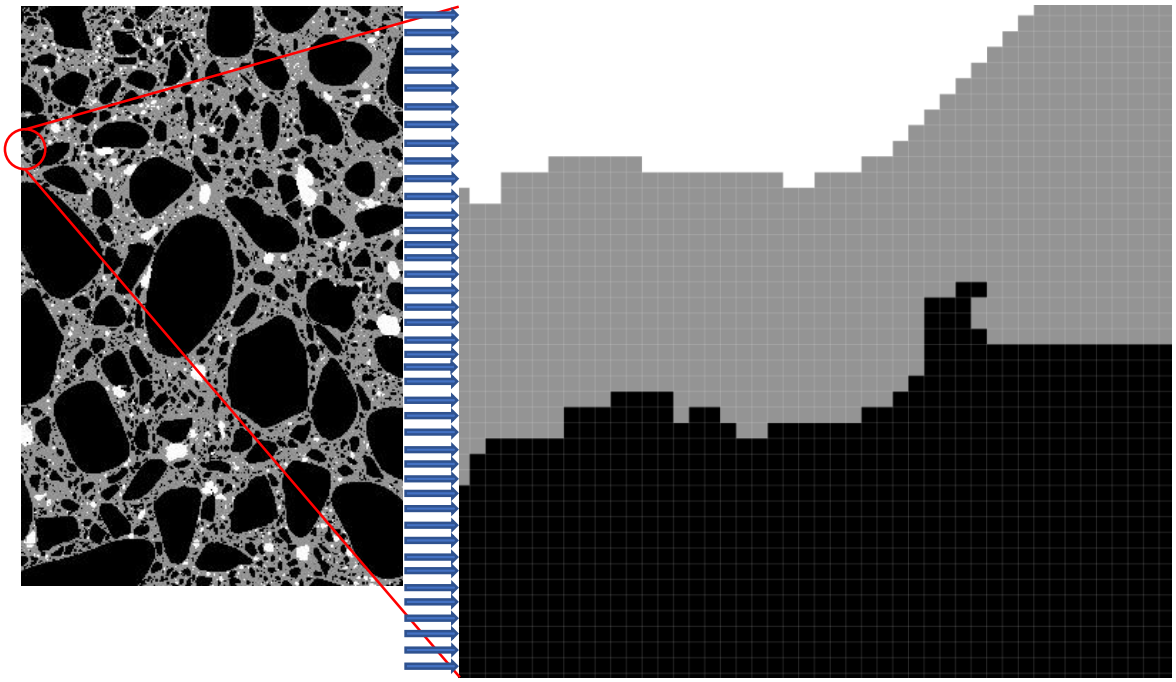

**Figure 2.13 Pixel line analysis performed on scanned concrete sample**

Ramezanianpour and Hooton (2010) compared two image analysis methods of measuring air content in hardened concrete and concluded that lack of knowledge of concrete paste content leads to less accurate air content reading with a flatbed scanner and RapidAir 547 [97]. They also

stated that results obtained using the flatbed scanner were in better agreement with the manual method from ASTM C457 as compared to RapidAir 457. They reported that the RapidAir 457 detected very small air voids (30 μm) compared to ASTM C457 methods. Radlinski *et. al.* (2010) [98] compared air analysis performed on hardened concrete samples using the modified point count method and the flatbed scanner method. They concluded that air content measurements were higher for the modified point count method compared to flatbed scanner results, but the estimated specific surface of the air was higher for the flatbed scanner compared to results of the modified point count method [98]. They also stated that air contents measured by the flatbed scanner method were closer to the air content in fresh concrete measured by the pressure method than that from the modified point count method [98].

# Chapter 3 - Effects of the Manufacturing Process on Air Content

The manufacturing process can significantly affect the air content of prestressed concrete railroad ties. In order to understand and quantify these effects, measurements of concrete material properties and vibration exposure during placement were made at two concrete tie manufacturing plants. Plants with unique placement and vibration mechanisms were observed in order to determine how differences in materials and fabrication techniques affect entrained air. Testing in both plants included fresh concrete air content test, slump, unit weight, temperature, vibration measurements, rheology, and hardened air void sampling. Obtained results showed a correlation between rheological parameters and air reduction during handling. Vibration testing conducted at Plant B showed high complexity of wave propagation and interference induced by form-based vibrators.

The manufacturing process in both plants began with cleaning and oiling the formwork, and then the identification tag and rail shoulders were placed in the form cavities for each tie as shown in Figure 3.1. Precast concrete factories usually have several lines of production in order to increase productivity. Each form that spans the entire bed length is called a cavity. A collection of adjacent cavities is called a casting bed, as shown in Figure 3.2 for Plant A and Figure 3.3 for Plant B. The final step in the manufacturing process before placing the concrete was to install reinforcing steel wires in the cavities of the casting bed, as shown in Figure 3.4. This installation process included running the wires through each cavity, applying initial stress in order to enforce the design pattern of the wires, and applying full design stress to the wires. Prestressed wires for one bed were tensioned together using the same hydraulic jack. After bed and wire preparation, the concrete was mixed and placed in the crosstie cavities. Concrete mixed at both plants included the addition of chemical admixtures such as high range water reducer and air-entraining admixtures. After mixing,

the batch operator sampled concrete to perform slump, fresh concrete air content, unit weight, and temperature tests to ensure that the concrete met specification. Upon completion of these tests, the operator dispensed the concrete into the delivery bucket, as shown in Figure 3.5. During observation for this study, at Plant A, the delivery bucket brought the concrete to the casting machine and dispensed the concrete into the casting machine hopper (Figure 3.5). At Plant B, the delivery bucket traveled the length of the plant and delivered the concrete to a secondary bucket used to transport the concrete the width of the plant to the casting machine.

**Figure 3.1 a) Forms cleaning and oiling, and b) shoulder installation in Plant A**


**Figure 3.2 Casting beds in Plant A**


**Figure 3.3 Casting beds in Plant B**

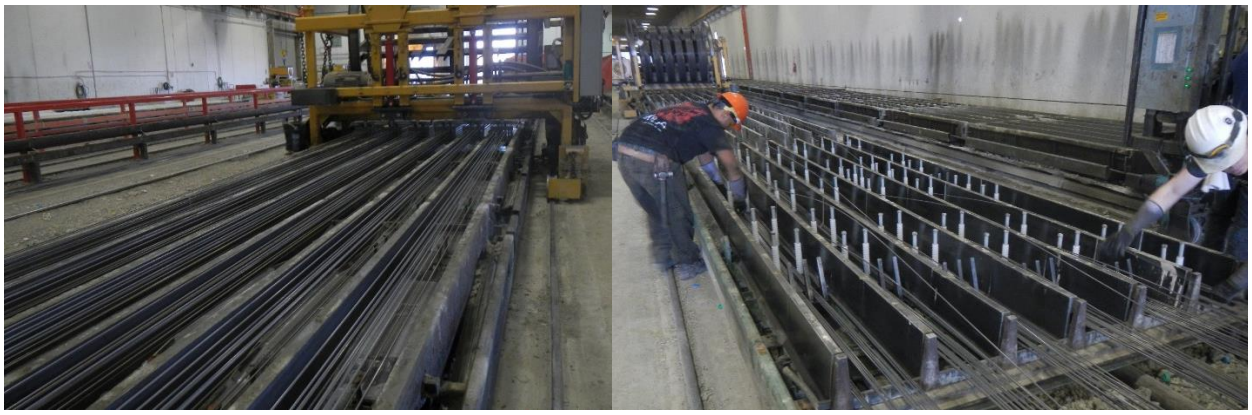

**Figure 3.4 a) Reinforcing steel wires during installation, and b) enforcing the wire spacing pattern in Plant A**

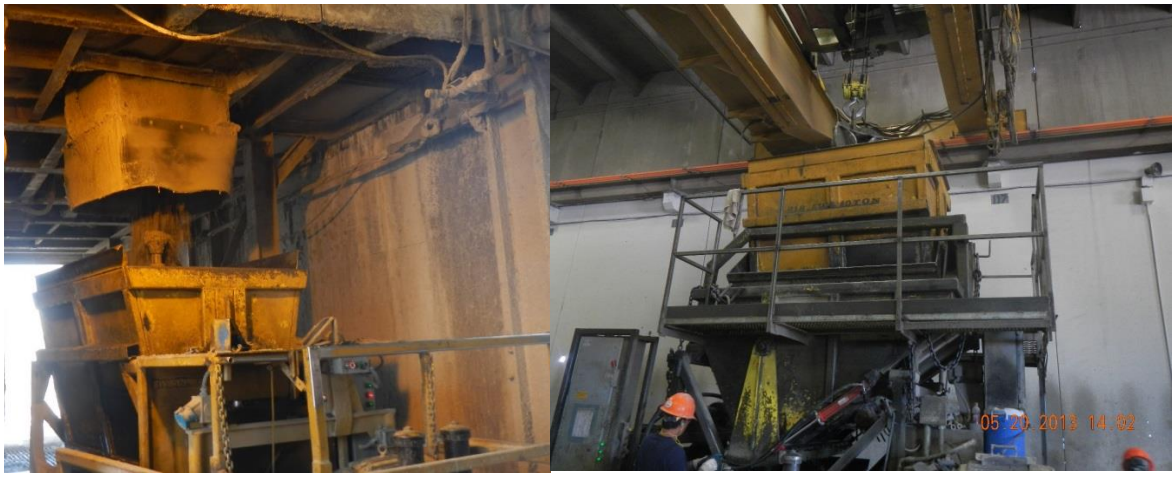

**Figure 3.5 a) Dispensing concrete in the delivery bucket, and b) dropping concrete in the casting machine hopper in Plant A**

The casting machine placed the concrete into the forms, and an operator sitting behind the casting machine controlled the rate to ensure even filling of all forms. In Plant A, the concrete was vibrated as it was placed into the six cavities of the bed using six tilted rod vibrators built into the casting machine, as shown in Figure 3.6. At Plant B, four tie cavities adjacent to one another were vibrated by a form vibrator attached to the bottom of the middle section of the cavities, located in the middle of the ties lengthwise, as shown in Figure 3.7.

**Figure 3.6 Plant A vibration rods attached to the casting machine**

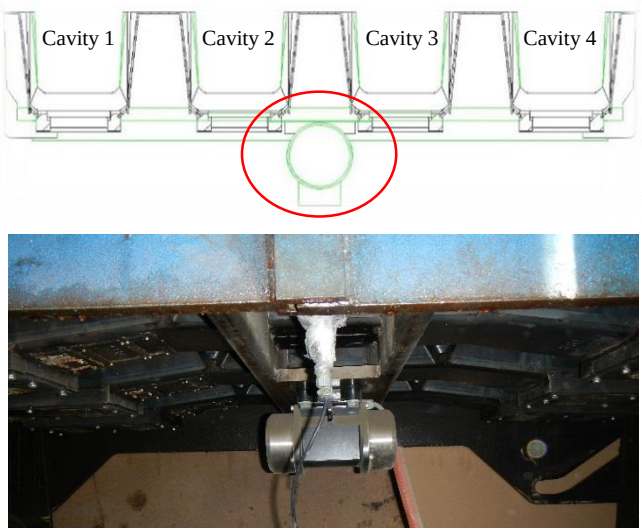


**Figure 3.7 a) Plant B vibrator schematics with labeled cavities, and b) actual vibrator in position**

Quality control samples for strength testing, slump, air content, unit weight, and temperature were taken once at the end of each bed. During the placing and vibration, the placing

crew followed the casting machine and finished the concrete surface. Because the concrete ties were placed upside down, the finished side became the bottom side of the tie. In Plant A, workers applied texturing to the surface for roughness. After finishing, the concrete was left to cure under nylon sheets until the concrete compressive strength met the required strength for detensioning the steel wires. Once the samples for compressive strength reached required strength, the bed was detensioned slowly. The concrete ties were cast continuously in the longitudinal direction and saw-cut after detensioning into individual crossties. Figure 3.8 summarizes the crosstie manufacturing process in both plants with the difference highlighted.

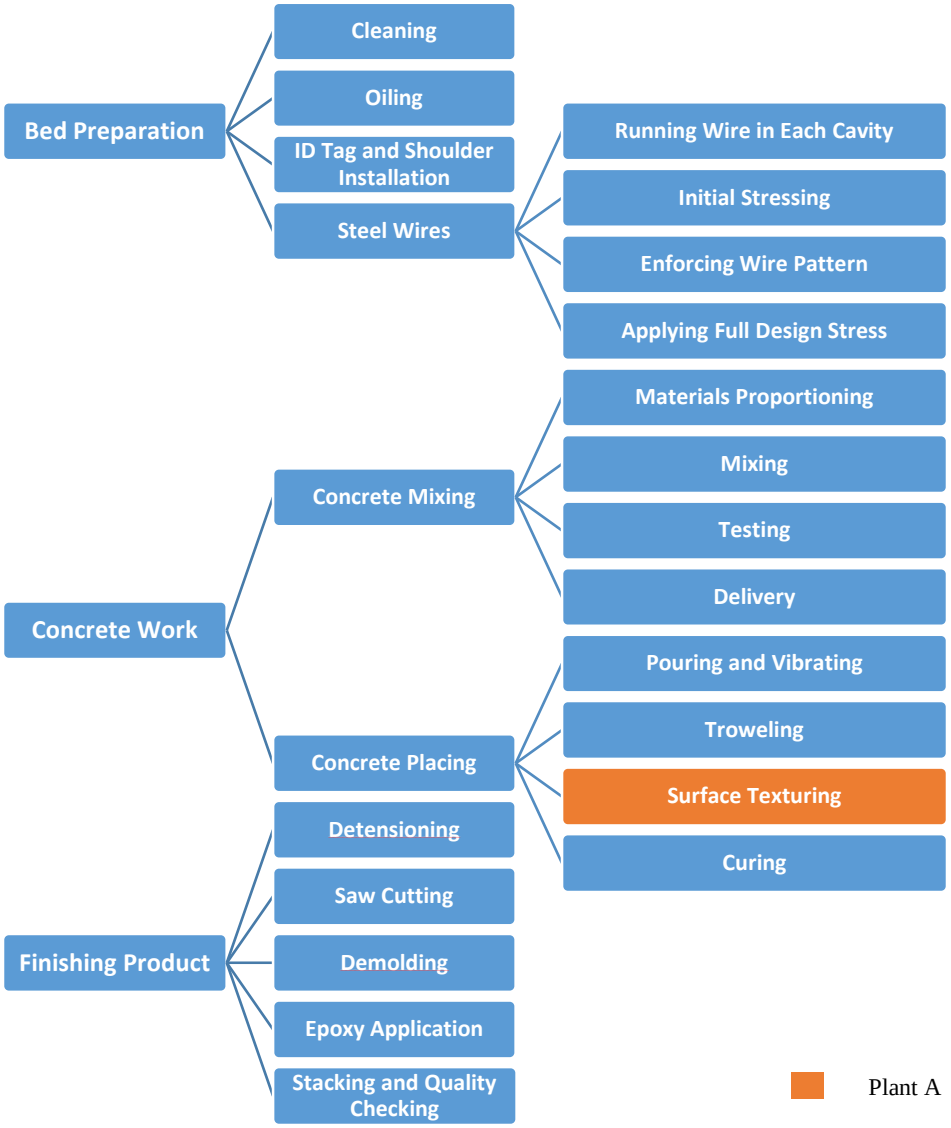

**Figure 3.8 Summary of the entire manufacturing process of two plants**

## 3.1. Plant A Testing

### *3.1.1. Sampling*

Concrete was sampled for slump, air content, unit weight, and temperature tests twice per casting bed. The first sample was collected from the second concrete batch directly from the mixer. The second sample was collected from the 14$^{th}$, 15$^{th}$, or 17$^{th}$ concrete batch made per bed after concrete delivery to the casting machine. The exact batch number sampled depended on the total number of batches made per bed. In addition to these tests, hardened air void samples were collected nine times per casting bed: three from the mixer (one from the 2$^{nd}$ batch, one from the 9$^{th}$ batch, and one from the 14$^{th}$, 15$^{th}$, or 17$^{th}$ batch), three from the casting machine before vibration (one from the 2$^{nd}$ batch, one from the 9$^{th}$ batch, and one from the 14$^{th}$, 15$^{th}$, or 17$^{th}$ batch), and three from the casting machine after vibration (one from the 2$^{nd}$ batch, one from the 9$^{th}$ batch, and one from the 14$^{th}$, 15$^{th}$, or 17$^{th}$ batch). All samples were collected between April 22, 2013, and May 17, 2013.

### *3.1.2. Slump, Temperature, Unit Weight, and Air Content*

Slump, fresh air content, unit weight, and temperature were measured for concrete sampled from the mixer after transporting to the casting machine. The slump test was performed according to ASTM C 143 (2012) [99] by filling a truncated metal cone (open from both sides) with fresh concrete and then lifting the cone within a 5-second period. The drop in concrete was then measured and reported as the slump value of the concrete. This test gives an indirect indication of concrete yield stress since the concrete height stabilizes the moment its stress from gravity becomes less than the yield stress necessary for flow. A large drop in concrete height results in a high slump value and indicates a low yield stress. Concrete temperature and unit weight were

measured according to ASTM C 1064 [100] and ASTM C 138 [83], respectively. Air content was measured using the pressure method according to Method B in ASTM C 231 [86]. In this method, air content was measured by compressing the concrete using a known volume of pressurized gas, causing air bubbles to be the only phase in the concrete that compresses, changing the available volume in which the pressurized gas can expand. The pressure drop in the portion of the container that holds the pressurized gas was calibrated to the percent air in the pressurized concrete.

### *3.1.3. Rheology*

An ICAR Rheometer was used to measure the concrete rheological properties as shown Figure 3.9. The ICAR rheometer works by shearing the concrete via a rotating vane and measuring the torque developed by the resistance of concrete to the rotational motion of the vane. There are two different tests that can be performed using the ICAR rheometer, the stress growth test and the flow curve test. The stress growth test is used to obtain the static yield stress while the flow curve test is used to obtain the dynamic yield stress and plastic viscosity. The dynamic yield stress is the yield stress after the effects of thixotropy.

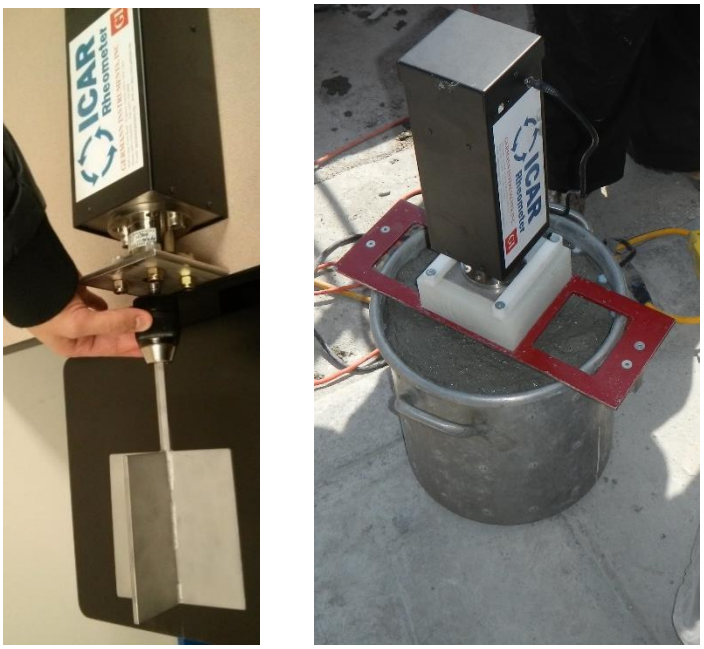


**Figure 3.9 ICAR rheometer a) with the vane, and b) in use**

The stress growth test rotates the vane using a slow constant speed while recording the increase in torque with time. Once the torque value begins to decrease, the maximum torque is reached; the concrete ceases to be a solid and begins to flow like a fluid. Yield stress obtained from measured maximum torque is called static yield stress of the concrete because it was measured under quasi-static conditions. The flow curve test begins with a pre-shear period before taking measurements. This period involves rotating the vane at maximum speed in order to minimize the effects of thixotropy and to provide a consistent shearing history. After completing the pre-shear period, the rheometer applies a series of vane rotations at various rotational speeds while measuring the corresponding developed torque at each speed. Fitting the data with a straight line results in an equation that gives the yield value measured by torque and the viscosity value measured by torque/speed. Figure 3.10 shows flow curve test measurements taken with a relative

yield value of 2.4561 N·m and a relative viscosity value of 1.8671 N·m·s. Dynamic yield stress and plastic viscosity can be obtained from these values.

In Plant A, rheology tests were performed on concrete sampled from the mixer because the concrete mixture was designed to have high yield stress that increased during the handling process due to mixing water being absorbed by the aggregates. Once the concrete reached the casting machine, the concrete was too stiff to measure using the ICAR rheometer.

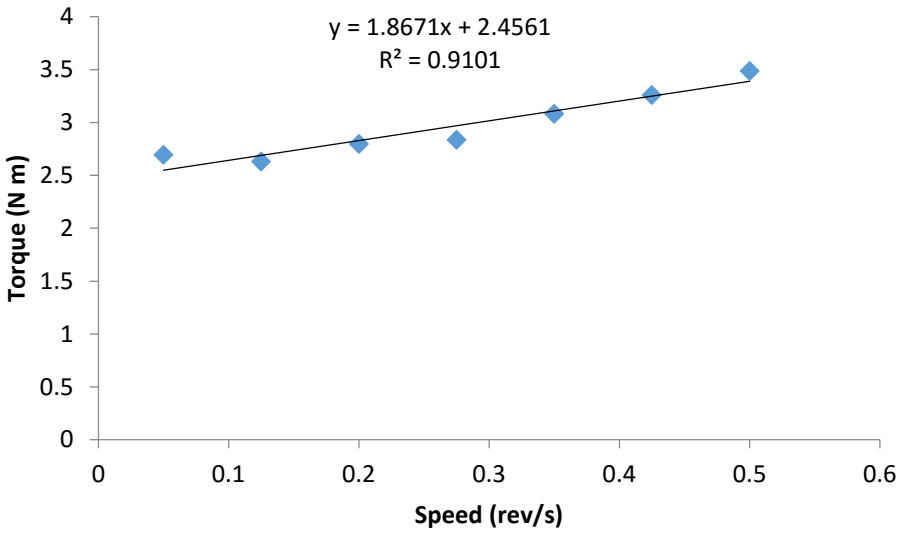


**Figure 3.10 Sample flow curve test for the ICAR rheometer**

### *3.1.4. Vibration*

Plant A used moving immersion vibrators in the casting process in order to consolidate low slump concrete. Because the submersible accelerometer could become entangled with the placing equipment, only surface-mounted accelerometers were used to measure concrete vibration. An accelerometer was fixed to the form and casting machine surface using a magnetic base in order to measure the frequency and amplitude of vibrators attached to the casting machine. Measurements taken on the casting machine gave a composite acceleration of the six immersion

vibrators used in each tie cavity. Figure 3.11 shows the accelerometer attached to the casting machine in one of the locations before the test began.

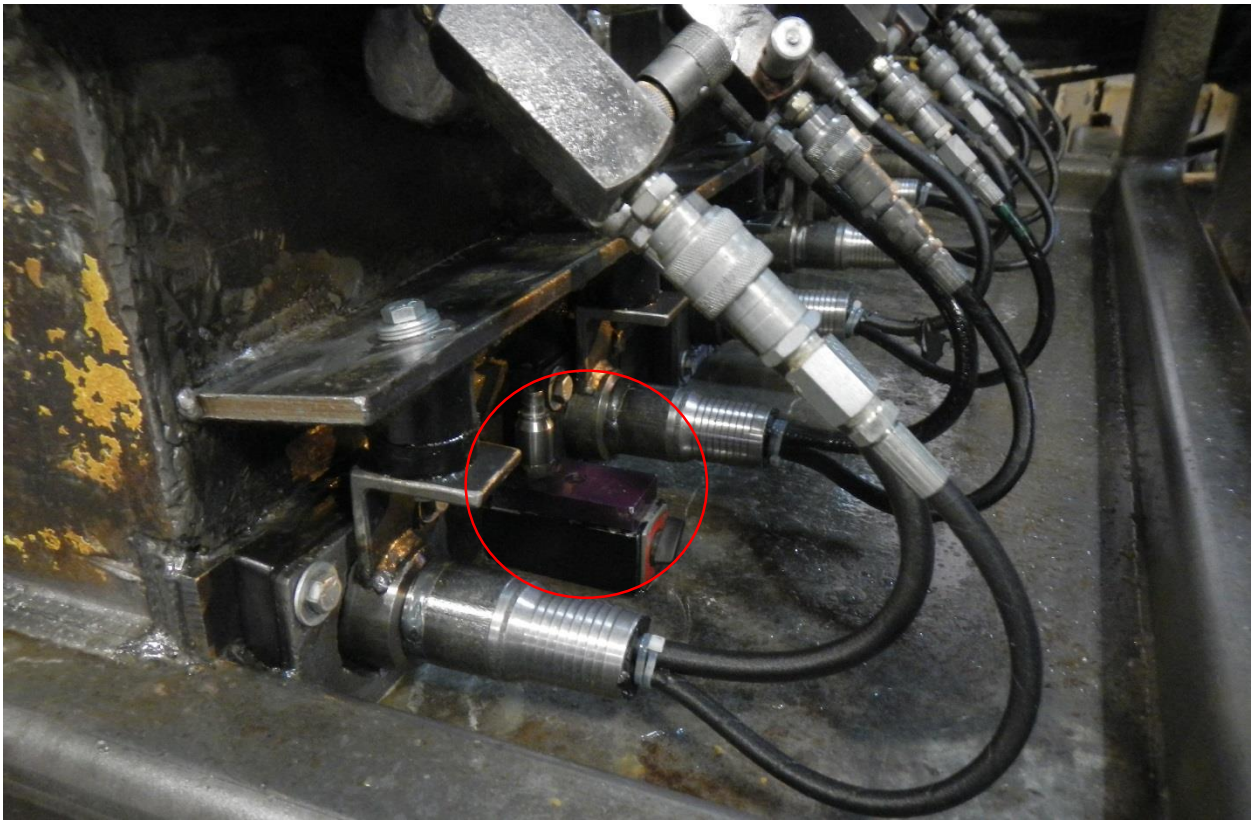

**Figure 3.11 Accelerometer attached to the casting machine between two embedded vibrators**

## 3.2. Plant B Testing

### *3.2.1. Sampling*

Concrete was sampled three times each time a casting bed was measured. The first sample was collected from the first concrete batch directly from the mixer. The second sample was taken from the fourth concrete batch at the casting machine level (before vibration). The third sample was also taken from the mixer, but it was sampled from the thirteenth concrete batch. The concrete fresh air content was measured each time the concrete was sampled. The concrete slump, unit weight, and temperature were measured on concrete sampled from the fourth batch and the thirteenth concrete batch from concrete collected from the casting machine.

In addition to these tests, hardened air void samples were collected six times per casting bed: two from the mixer (one from the first batch and one from the thirteenth batch), two from the casting machine before vibration (one from the fourth batch and one from the thirteenth batch), and two from the casting machine after vibration (one from the fourth batch and one from the thirteenth batch). Hardened air void samples were made from concrete collected from the casting machine and placed on top of the bed to vibrate for the entire period of casting for that bed in order to capture the effects of vibration on air content. Concrete samples at Plant B were collected between May 28, 2013, and June 21, 2013.

### *3.2.2. Slump, Air Content, Unit Weight, and Temperature*

Concrete fresh air content, slump, temperature, and unit weight were measured at Plant B. Tests were performed on concrete sampled during discharge from the mixer into the conveyance bucket and from the concrete casting machine.

### *3.2.3. Rheology*

Rheology measurements were performed on concrete sampled from the mixer before delivery and after delivery to the casting machine at Plant B. Measurements with the ICAR rheometer included the stress growth test and the flow curve test.

### *3.2.4. Vibration*

Form vibration was recorded using an accelerometer attached to the bed form, and concrete vibration was measured using a submersible accelerometer. The two accelerometers were set to record data at 20,000 Hz to ensure that sampling frequency was sufficiently higher than the concrete vibration frequency in order to obtain accurate measurements of concrete acceleration during the full range of a vibration cycle. The submerged accelerometer was installed on a setup that could be adjusted in order to measure various depths and widths. The depth of the submersible

accelerometer was always measured from the bottom of the form upwards to the tip of the accelerometer. This setup included a magnet block attached to the top of the bed to ensure that the manufacturing process was not disturbed or affected by testing. Data were recorded at points along the bed at various depths in order to quantify vibration attenuation throughout the length of the crosstie. **Error! Reference source not found.** shows the two accelerometers in position to record ibration.


**Figure 3.12 Two accelerometers in position for recording**

Vibration recording lasted for approximately 10 seconds in most locations. Figure 3.13 shows the locations for recording vibration along the depths of the ties in their molds. Figure 3.14 and Figure 3.15 show the locations along the length, width and depth of the crosstie when measurements were taken. Only half of the tie is shown in Figure 3.13 because measurements were recorded only at the three locations presented.

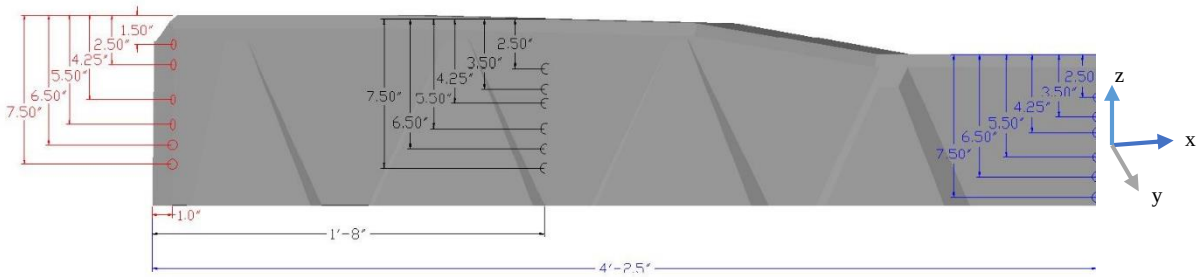


**Figure 3.13 Vibration measurement depth location**

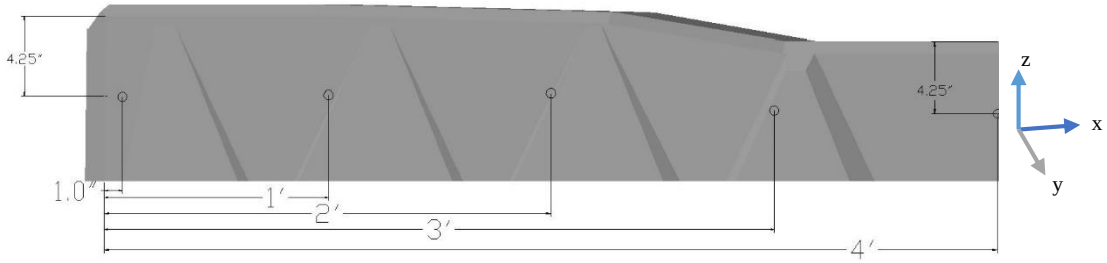


**Figure 3.14 Half-tie representation for vibration measurement locations for 1-ft intervals (Measurements were taken on the other end of the tie.)**

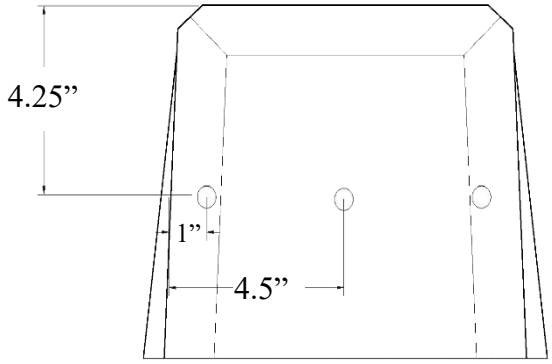


**Figure 3.15 Vibration measurement locations for width of tie**

Vibration measurements were taken along the length of the tie with two different intervals fixed at a depth of 4.25 in. Vibration measurements were recorded in the crosstie width direction, as shown in Figure 3.15. In addition to these sets, vibration was recorded for the entire bed vibration period using the exterior accelerometer (form accelerometer) and for 15 minutes using the submersible accelerometer. The submersible accelerometer was removed after 15 minutes of

immersion in the concrete because of low measured acceleration and because additional time in the concrete would cause difficulty in removing the sensors from the rapidly stiffening concrete or prevent reconsolidation of the concrete after sensor removal. Both accelerometers were installed at the beginning of the bed at 1in. from the beginning of the tie in Cavity 1.

## 3.3. Hardened Air Void Analysis

Hardened air void samples were made by placing the concrete in boxes with dimension of 3.5 x 4.5 x 6 in. and allowing them to harden in-place, undisturbed. Samples were saw-cut and polished before scanning on a flatbed scanner. The saw-cut samples had a trapezoidal shape with parallel side dimensions between 4.5 and 5.5 in. The sample cut cross-section height was typically 6 in., as shown in Figure 3.16. Thickness of the saw-cut samples averaged 1 in. Before polishing, samples were painted with a solution comprised of 80% acetone and 20% lacquer, and then dried for 15 minutes. The lacquer was applied in order to strengthen the cement paste matrix during polishing, thereby preventing damage to the air voids. After the solution on the samples dried, the samples were attached to a 7.5-in. diameter rotation cylinder using hot glue, as shown in Figure 3.17, in order to allow a motor to turn the sample in the opposite direction of the polishing wheel, assuring even and random polishing. Four samples were polished on the polishing wheel at a time. On the polishing wheel, the samples were attached to two motors in which rubber belts were used to turn them in the opposite direction of the polishing wheel, as shown in Figure 3.18. Samples were first polished using nickel-plated diamond discs with a grit of 80 for approximately 10 to 15 minutes in order to level the sample and remove any large scratches. After polishing with the 80-grit disc, the samples were cleaned and checked to ensure that they were flat and level without any large undulations. A synthetic diamond-resin 1200-grit disc then replaced the 80-grit for polishing for one additional hour without the addition of acetone lacquer solution to the cleaned

sample. The additional hour on the 1200-grit disc ensured that all scratches were removed from the sample, especially the paste. Finally, the samples were placed on a synthetic diamond-resin 2200-grit disc for 10 minutes in order to remove micro-scratches.

**Figure 3.16 Hardened air void sample after cutting**

**Figure 3.17 Side view of hardened air void sample attached to the rotation cylinder**

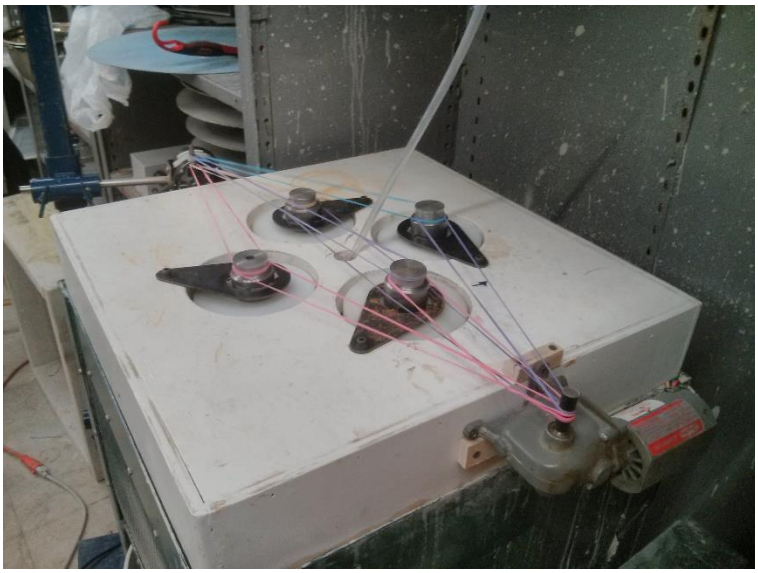

**Figure 3.18 Turning four samples using two motors**

After polishing, the samples were scanned in three steps using a modified procedure developed by Peterson (2001) [95]. Figure 3.19 presents an example of the three different scans taken of a sample. The original polished, untreated sample was scanned using a high-resolution desktop scanner, as shown in Figure 3.19a. After scanning the polished samples, the samples were treated with a phenolphthalein solution (1% w/v phenolphthalein indicator in 95% v/v alcohol) in order to stain the cement matrix pink or purple, as shown in Figure 3.19b. Phenolphthalein turns color in a pH above 10, and uncarbonated cement pastes typically have a pH above 13. The stain helped distinguish the cement matrix from the aggregates during image processing. After scanning the phenolphthalein-treated sample, the sample was covered with fluorescent orange chalk powder, and a rubber stopper was used to force the powder into the air voids. Finally, the orange powdered polished sample was wiped in order to remove any powder residue not in an air void on the sample before scanning. Due to the high cost and lengthy process of scanning and analyzing an entire concrete sample, utilization of a 3D sample to scan a slice or a section of a concrete sample and to use as a base in order to generalize the entire sample is more efficient and can achieve a good level

of generalization of air properties. Tested samples had a minimum area of 12 $in^2$, which met the ASTM C457 requirement for 2D image analysis results to approach 3D results. Testing performed by Peterson in 2001 [95] showed that the resolution of scanned images affected the results in term of spacing factor and size distribution of air voids, but it had only a limited effect on air content. Scans were taken using a resolution of 4800 dpi, resulting in a pixel length of 5.5 micrometers.

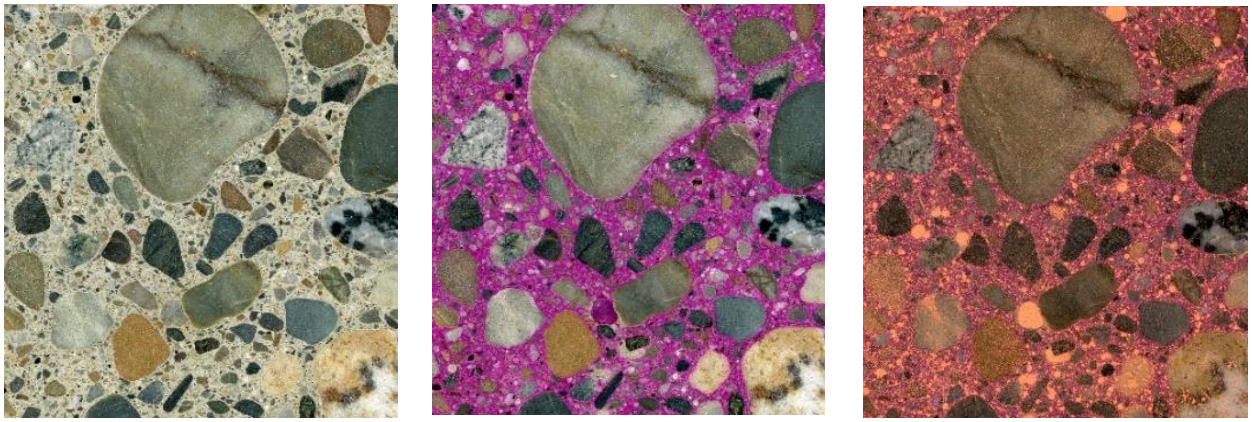

a) b) c)

**Figure 3.19 Scans of a) polished sample untreated, b) polished sample treated (with phenolphthalein), and c) polished sample powdered with orange chalk**

Image processing software was used to separate the three main elements of the image: the paste, aggregate, and air voids. An example of this image classification is shown in Figure 3.20 for sample scans in Figure 3.19. Figure 3.20a shows the sample after detection of the aggregate, and Figure 3.20b shows air voids after detection. The paste is the area not defined as an aggregate or air void. Separated images were assigned unique colors and laid on top of each other in order to form the three-color simplified image shown in Figure 3.21.

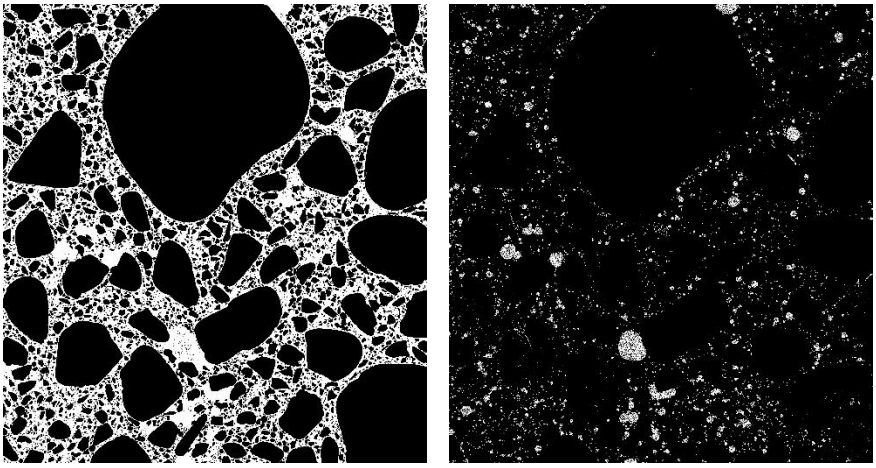

a) b)

**Figure 3.20 a) Aggregate image, and b) Air void image**

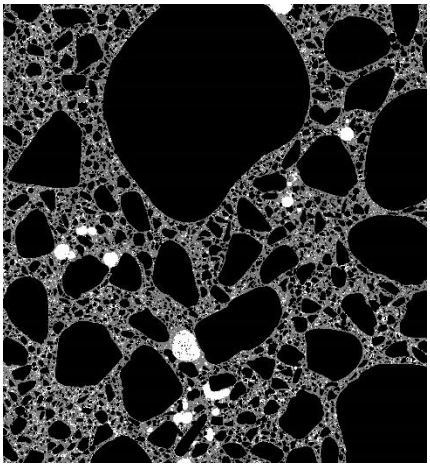

**Figure 3.21 Three-color simplified image (black: aggregate; gray: paste; white: air)**

A software used principles from the linear traverse method and calculations described in ASTM C457 in order to calculate the air void spacing factor in every sample. Every pixel across the height of the specimen was counted as a line in order to measure various cord lengths of the paste, aggregate, and air. This resulted in more reliable and adequate results. White pixels in Figure 3.21 were counted and divided by the entire number of pixels in the image in order to calculate air content ($A$). Paste content ($p$) was also calculated by dividing the number of gray pixels by the entire number of pixels in the image. Equation 3.1 represents the linear traverse method for calculating the spacing factor according to ASTM C457 [89].

$$Spacing\ Factor\ (\bar{L}) = \begin{cases} \dfrac{T_p}{17.368N} & for \quad {}^{p}/_{A} < 4.342 \\ \dfrac{3T_a}{17.368N}\left[1.4\left(1+\dfrac{p}{A}\right)^{\frac{1}{3}} - 1\right] & for \quad {}^{p}/_{A} > 4.342 \end{cases}$$ **Equation 3.1**

where $T_p$ is the traverse length through paste (*pixels*), $T_a$ is the traverse length through air (*pixels*), and $N$ is the total number of air voids intersected.

## 3.4. Results and Analysis

Concrete fresh air content, slump, unit weight, temperature, and rheological parameters were measured. Table 3.1 summarizes the average fresh concrete parameters at Plant A and Plant B. Plant B had, on average, higher fresh concrete air content than Plant A, but also higher air loss during handling. The stiff concrete of Plant A lost an average of 0.6% air during handling compared to 3.0% air lost from the concrete from Plant B. The increased air content loss corresponded to the low concrete yield stress of concrete used in Plant B as measured by the static yield stress and slump test. The high viscosity measured for concrete from Plant B confirmed visual observations of the stickiness of concrete from Plant B. The average concrete static yield stress and plastic viscosity increase at Plant B between the mixing and the casting machine was most likely from the aggregate-absorbing mixing water. Table 3.2 summarizes the hardened air average and standard deviations for samples collected at both plants and the average fresh air content associated with these specimens.

**Table 3.1 Experimental results at Plant A and Plant B**

| **Plant** | | **A** | | **B** | |
|---|---|---|---|---|---|
| Calculation | | Average | Standard Deviation | Average | Standard Deviation |
| Temperature, $^{o}$C ($^{o}$F) | | 21.1 (70) | 2.1 (3.74) | 31.94 (89.5) | 1.8 (3.24) |
| Unit Weight, N/m$^3$ (lb/ft$^3$) | | 22481 (143.1) | 210.51 (1.34) | 22151.1 (141) | 208.9 (1.33) |
| Slump, mm (in) | At Mixer | 101.6 (4) | 14.99 (0.59) | - | - |

| | | | | | | |
|---|---|---|---|---|---|---|
| | | At QC | 48.26 (1.9) | 12.19 (0.48) | 226.06 (8.9) | 11.43 (0.45) |
| | | Loss | 50.8 (2) | 14.22 (0.56) | - | - |
| Static Yield Stress, Pa (lb/ft$^2$) | | At Mixer | 1499 (29.24) | 640 (13.37) | 752 (15.71) | 303 (6.33) |
| | | At QC | - | - | 715 (14.93) | 467 (9.75) |
| Bingham Parameters | Dynamic Yield Stress, Pa (lb/ft$^2$) | At Mixer | 825 (17.23) | 604 (12.61) | 208 (4.34) | 144 (3.01) |
| | | At QC | - | - | 143 (2.99) | 148 (3.09) |
| | Plastic Viscosity, Pa·s (lb·s/ft$^2$) | At Mixer | 145 (3.03) | 48 (1.003) | 192 (4.01) | 37 (0.77) |
| | | At QC | - | - | 345 (7.21) | 102 (2.13) |

**Table 3.2 Measured air void systems for Plant A and Plant B**

| **Plant** | | **A** | | **B** | |
|---|---|---|---|---|---|
| **Calculation** | | **Average** | **Standard Deviation** | **Average** | **Standard Deviation** |
| **After Vibration (AV)** | **Air Content (%)** | 5.5 | 1.8 | 6.2 | 2.1 |
| | **Spacing Factor (in)** | 0.0065 | 0.0041 | 0.0086 | 0.0026 |
| **Before Vibration (BV)** | **Air Content (%)** | 7.6 | 2.3 | 8.4 | 1.5 |
| | **Spacing Factor (in)** | 0.0047 | 0.0029 | 0.0058 | 0.0012 |
| **Mixer (M)** | **Air Content (%)** | 9.5 | 2.4 | 9.6 | 1.5 |
| | **Spacing Factor (in)** | 0.0043 | 0.0021 | 0.0048 | 0.0009 |
| **Mixer Fresh Air (%)** | | 7.5 | 0.6 | 10.3 | 1.0 |
| **Placing Machine Fresh Air (%)** | | 6.7 | 0.7 | 7.2 | 1.2 |
| **Gravimetric Air content (%) (ASTM C138)** | | 5.1 | 0.18 | 8.1 | 0.64 |

The concrete-hardened air content for Plant A was 2% higher when sampled from the mixer compared to the fresh concrete air content. The concrete in the stiff concrete mixture used in Plant A possibly contained higher amounts of entrapped air that were easily removed during rodding in order to consolidate the concrete in the pressure-based fresh air content test ASTM C231. However, samples made to measure the hardened air content were not consolidated.

Fresh concrete air content measurements were taken for both plants at two separate times in the manufacturing process: one sample from the mixer and one sample from the placing machine. At Plant A, the concrete air content measured from concrete sampled from the mixer varied from 5.8 to 8.8% with an average of 7.1% and a standard deviation of 0.65%. The air content at the placing machine ranged from 5.3 to 7.3% with an average of 6.5% and a standard deviation of 0.64%. The reduction in air content between the mixer level and the Quality Control laboratory (QC lab) was very low, typically less than 1%. The calculated gravimetric air content varied between 4.14% and 8.5% with an average of 6.96% and a standard deviation of 1.04%. Figure 3.24 shows air content by the gravimetric method (ASTM C 138) as compared to air content measured using the pressure method (ASTM C 143).

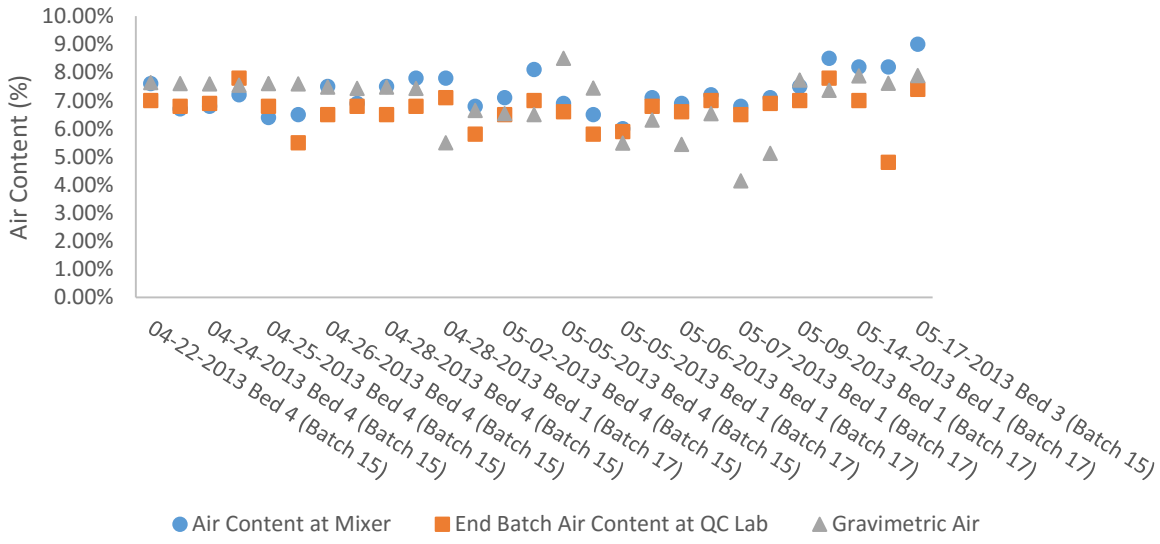


**Figure 3.22 Air content of fresh concrete at Plant A**

Figure 3.23 shows air content measured for Plant B from May 28, 2013, to June 21, 2013. The air content at the mixer level varied from 7.8 to 11.8% with an average of 9.7% and a standard deviation of 1.18%. The air content at the placing machine ranged from 5.3 to 8.3% with an

average of 6.8% and a standard deviation of 0.94%. This higher reduction was likely due to the lower yield stress that creates less resistance to bubbles rising and exiting the concrete during handling. The calculated Gravimetric air content varied between 6.5% and 8.4% with an average of 8.1% and a standard deviation of 0.64%. The decreased air content could be attributed to a high initial air content once air loss is known. The solution of high air content is only applicable when air loss is known and all other parameters remain unaffected. Once a parameter is affected, reinvestigation of the air loss may be necessary.

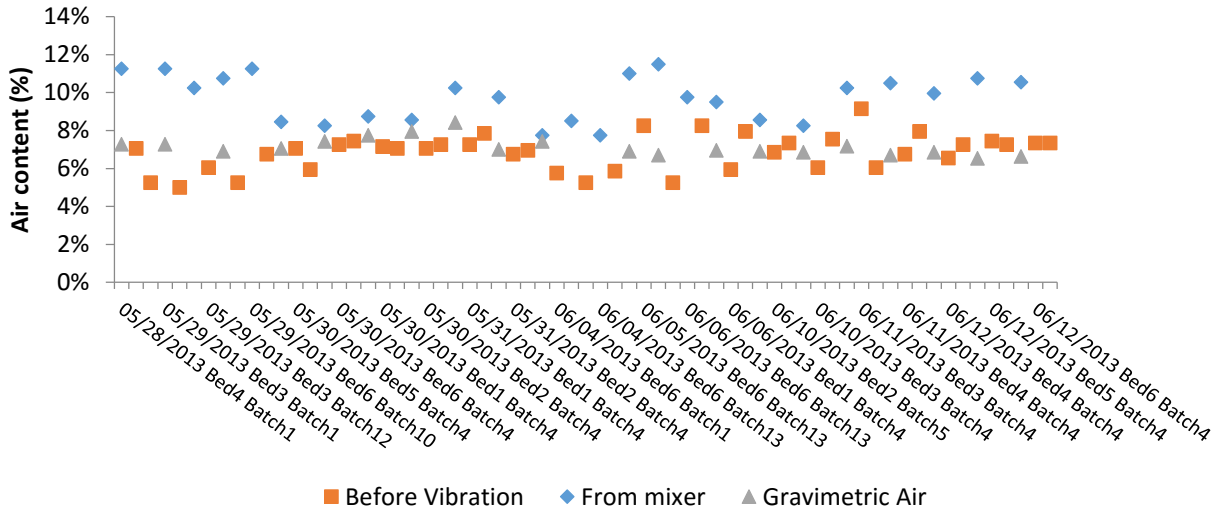


**Figure 3.23 Air content of fresh concrete at Plant B**

The concrete air content decreased significantly during the handling and consolidation operations. The hardened air content decreased from 9.5% to 5.5 % (4% difference) for Plant A and from 9.6% to 6.2% (3.4% difference) for Plant B during the placement and consolidation operations. Figure 3.24 shows a comparison of concrete-hardened air content versus fresh air content for companion samples taken at various stages in the manufacturing process at Plant A. Spacing factors of companion concrete-hardened air void samples are shown in Figure 3.25. On average, spacing factors increased with additional handling and processing; however, the material

standard deviation increased. The average spacing factor for the concrete remained below the commonly cited threshold of 0.008 in. required for good freeze-thaw performance [22]. For each group, the average of all samples based on the location in the manufacturing process was calculated. Figure 3.26 shows the hardened air voids distribution from each manufacturing stage at Plant A.

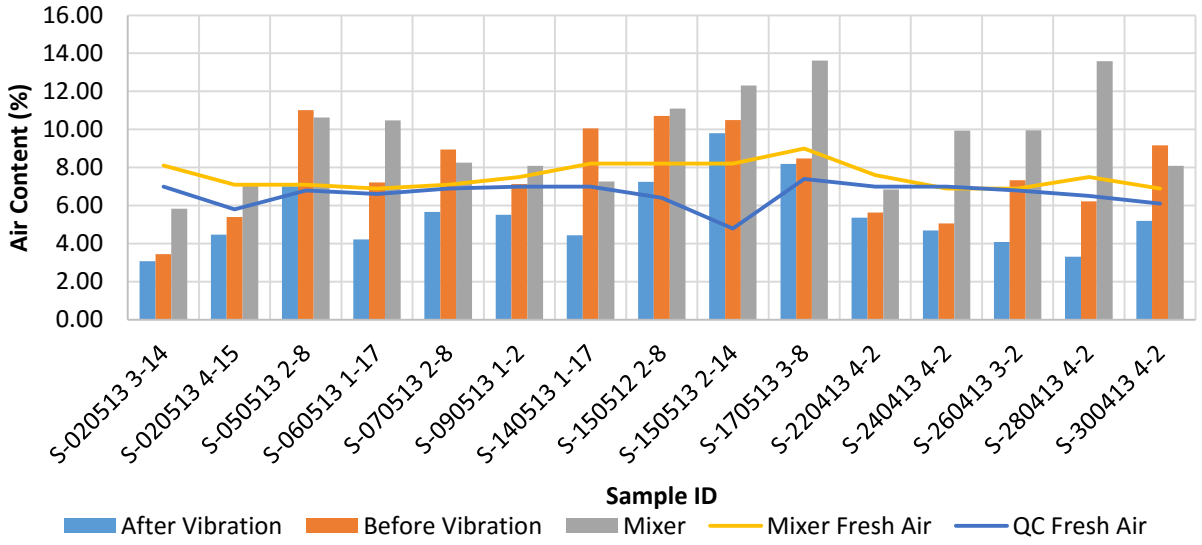


**Figure 3.24 Concrete-hardened air content versus fresh air content at various stages of manufacturing process at Plant A**

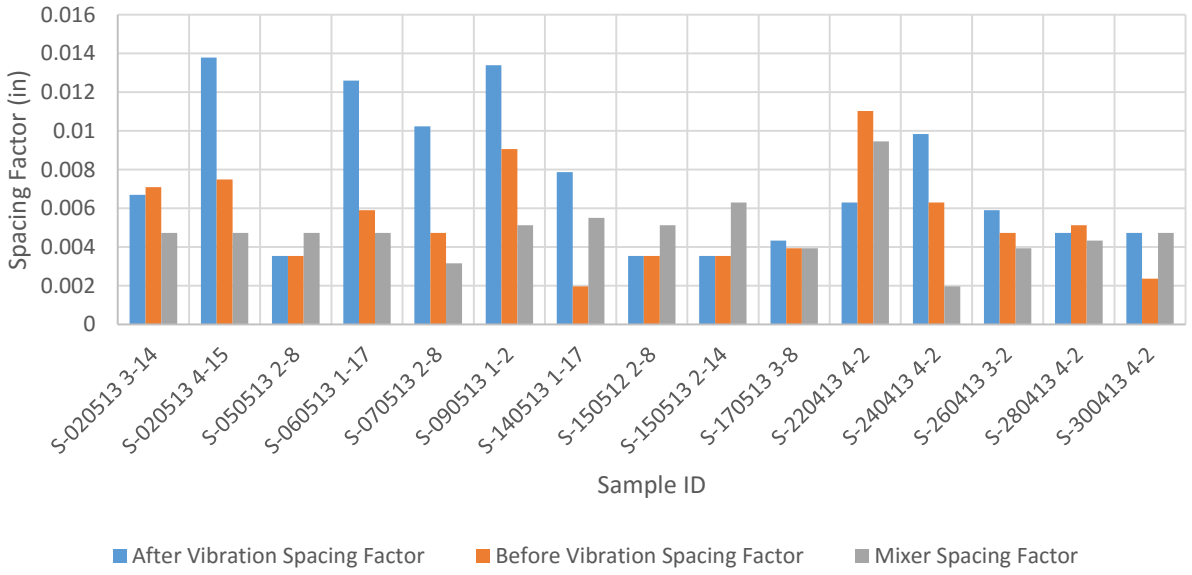

**Figure 3.25 Air spacing factor at various stages of manufacturing process at Plant A**

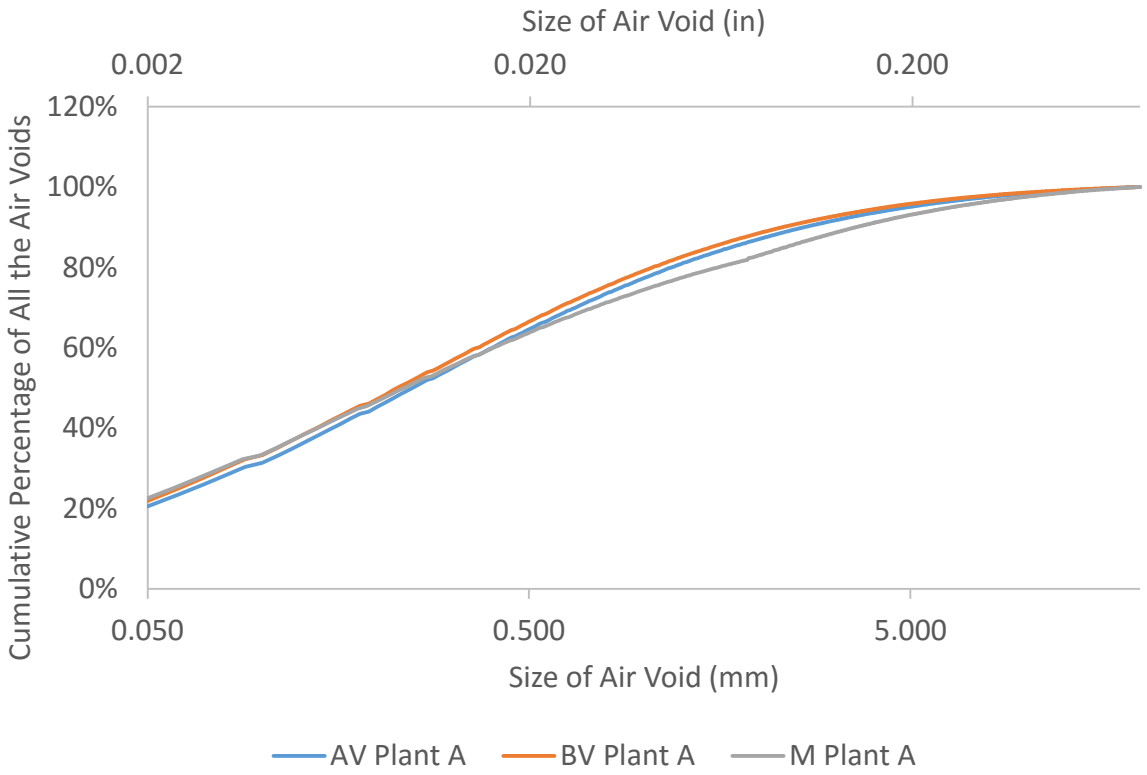


**Figure 3.26 Average air void size distribution after vibration (AV), before vibration (BV), and mixer (M) samples collected at Plant A**

Figure 3.27 shows concrete-hardened air content versus fresh air content for companion specimens at various manufacturing stages at Plant B. Spacing factors increased more from vibration in Plant B than Plant A, as shown in Figure 3.28, potentially due to the low concrete yield stress and the use of form vibrators instead of immersion vibrators. Form vibrators imparted vibration to the concrete over a longer period of time and at a higher frequency of vibration than immersion vibrators used in Plant A. Figure 3.29 shows the hardened air voids distribution from each manufacturing stage at Plant B. Figure 3.30 shows the difference in air void distribution between Plant A and Plant B. Plant A produced concrete with 50% of the air voids smaller than 0.009 in. (0.23 mm) compared to concrete from Plant B that contained only 36% of the voids

smaller than 0.009 in. (0.23 mm). This difference between the two plants can be the result of the different chemicals used and concrete rheological properties between both plants.

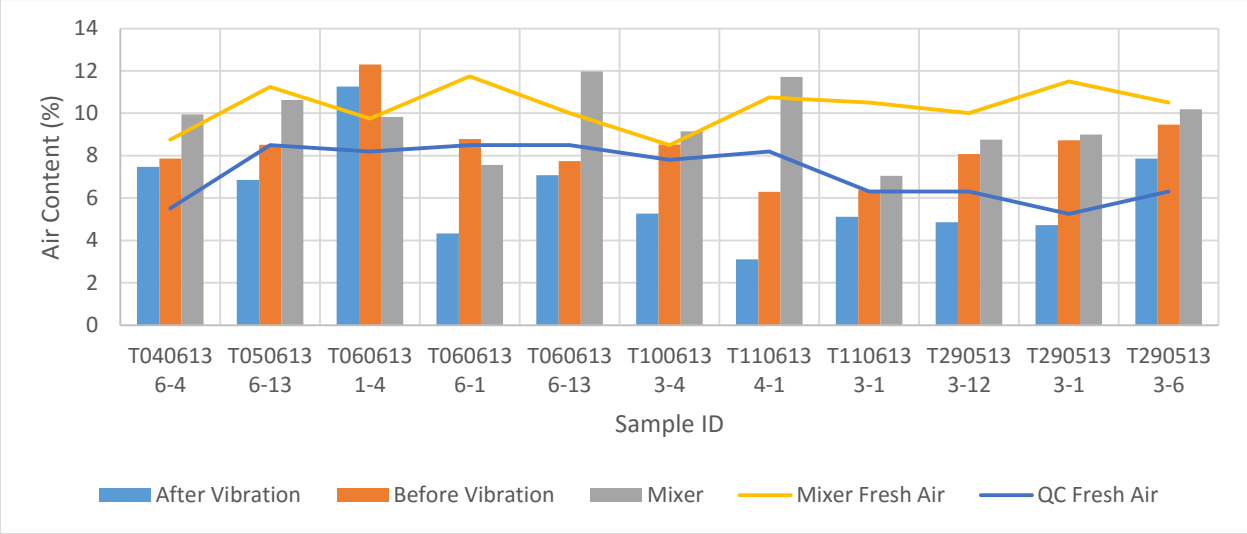


**Figure 3.27 Concrete-hardened air content versus fresh air content at various stages of the manufacturing process at Plant B**

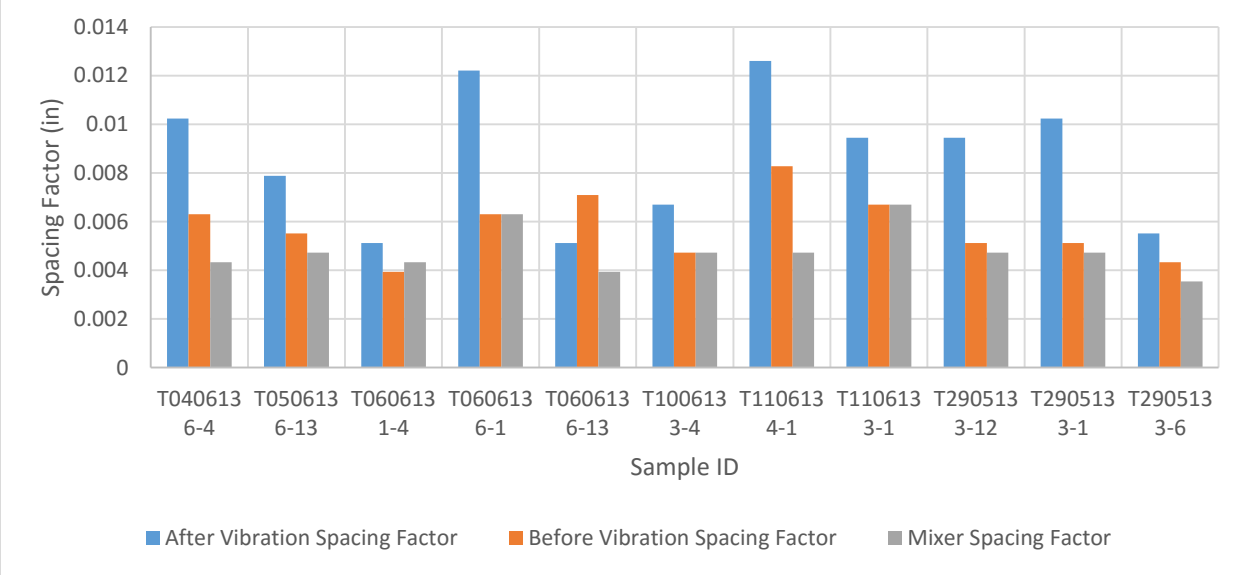


**Figure 3.28 Air spacing factor at various stages of the manufacturing process at Plant B**

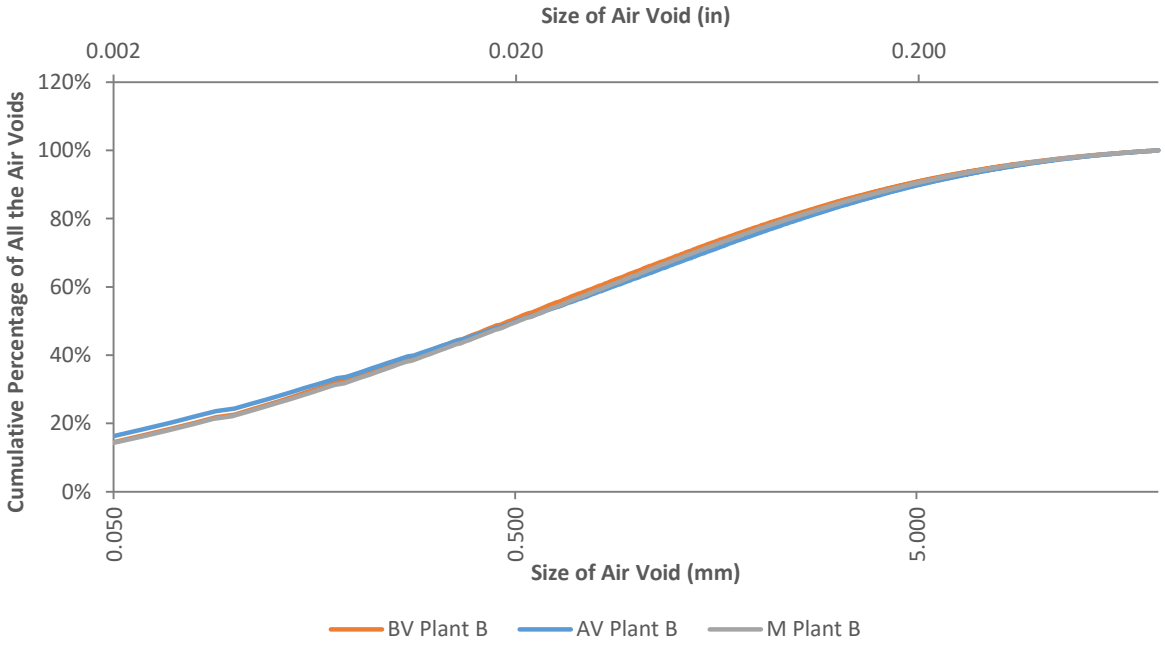


**Figure 3.29 Average air void size distribution after vibration (AV), before vibration (BV), and mixer (M) samples collected at Plant B**

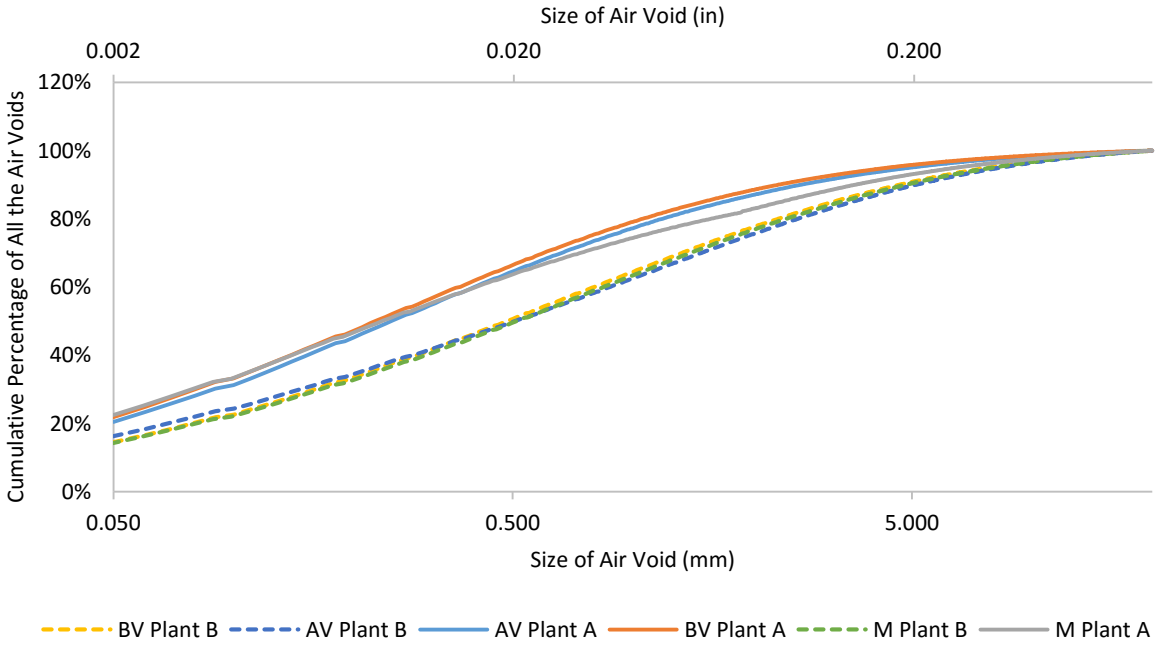


**Figure 3.30 Average air void size distribution after vibration (AV), before vibration (BV), and mixer (M) samples for both plants**

Figure 3.31 shows variation in the fresh concrete unit weight measured at Plant A. The range of measured unit weights during the testing period was 140 to 145.3 lb/ft$^3$ (2242 to 2327 kg/m$^3$). Variation in the fresh concrete temperature is shown in Figure 3.32 with values ranging from 65 to 80 $^o$F (18.3 $^o$C to 26.7 $^o$C). Figure 3.33 shows measured slump values. The reduction ranged from 3 in. to 0.5 in. with an average reduction of 2 in. (50.8 mm) and a standard deviation of 0.56 in. (14.2 mm).

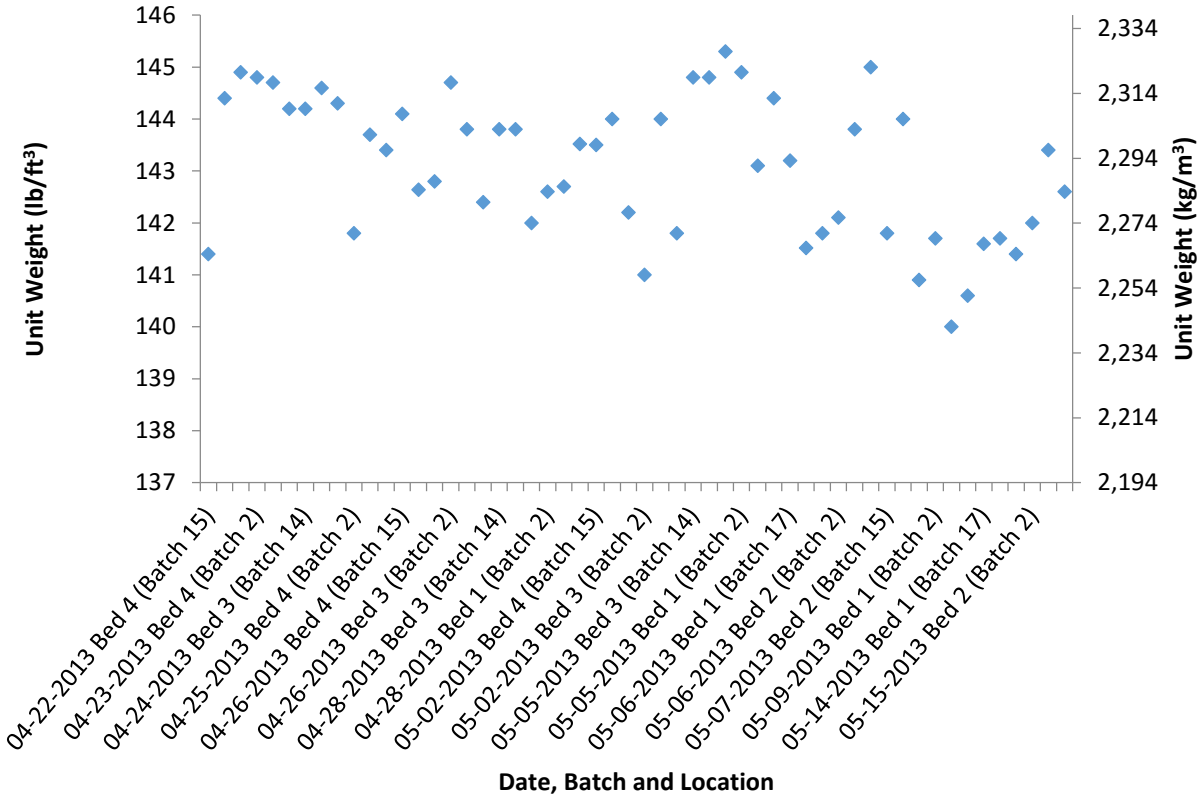


**Figure 3.31 Concrete unit weight at Plant A**

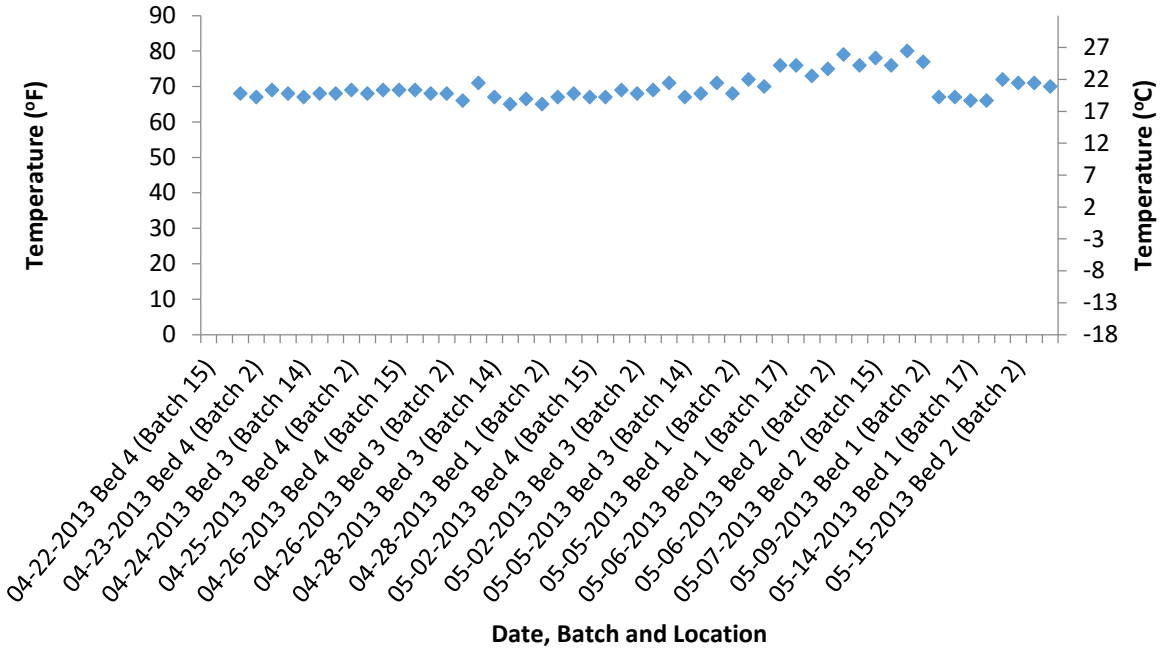


**Figure 3.32 Temperature of fresh concrete at Plant A**

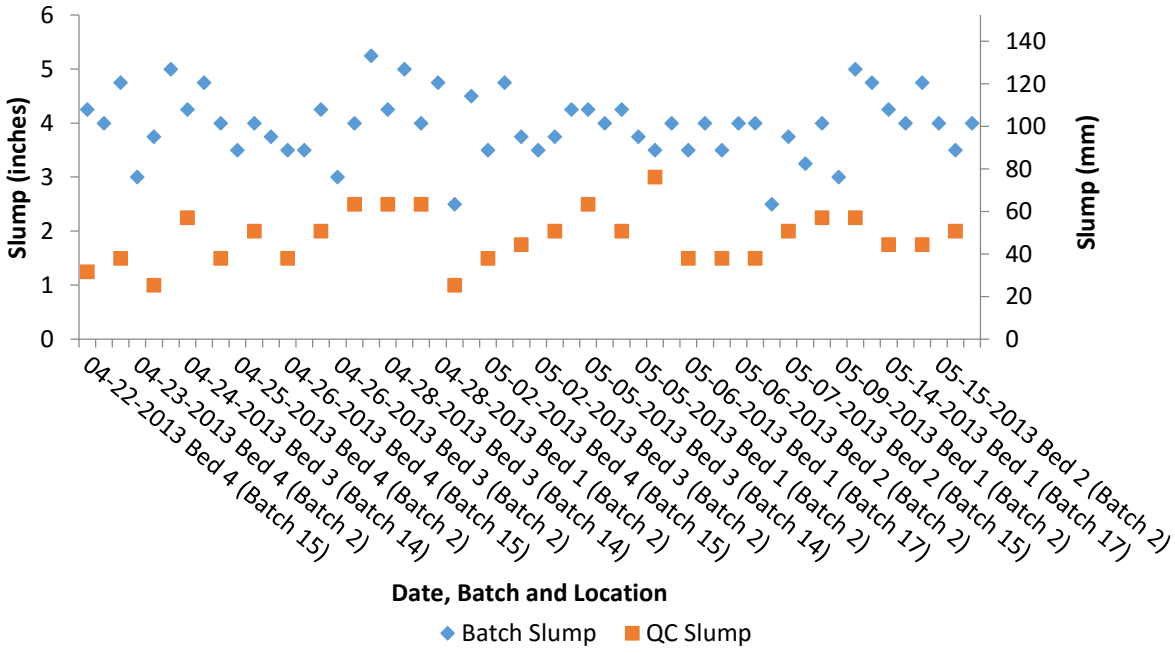


**Figure 3.33 Slump of fresh concrete at Plant A**

Figure 3.34 shows variation in the fresh concrete unit weight measured at Plant B. The measured unit weight range during the testing period was 136.8 to144.8 lb/ft$^3$ (21.5 to 22.8 kN/m$^3$). The range in the fresh concrete temperature ranged from 80 to 95.8 $^o$F (26.7 to 35.4 $^o$C), as shown in Figure 3.35. Figure 3.36 shows measured slump values. The reduction was most likely due to water absorption by aggregates and cement particle flocculation/aggregation that trap water. Meanwhile, slump at the mixer level was not performed due to high fluidity of the concrete. Very fluid concrete mixtures spread enough during the slump test to leave a concrete patty, with the patty maximum height determined by maximum aggregate size, rendering the concrete slump test unable to differentiate the yield stress of very fluid mixtures.

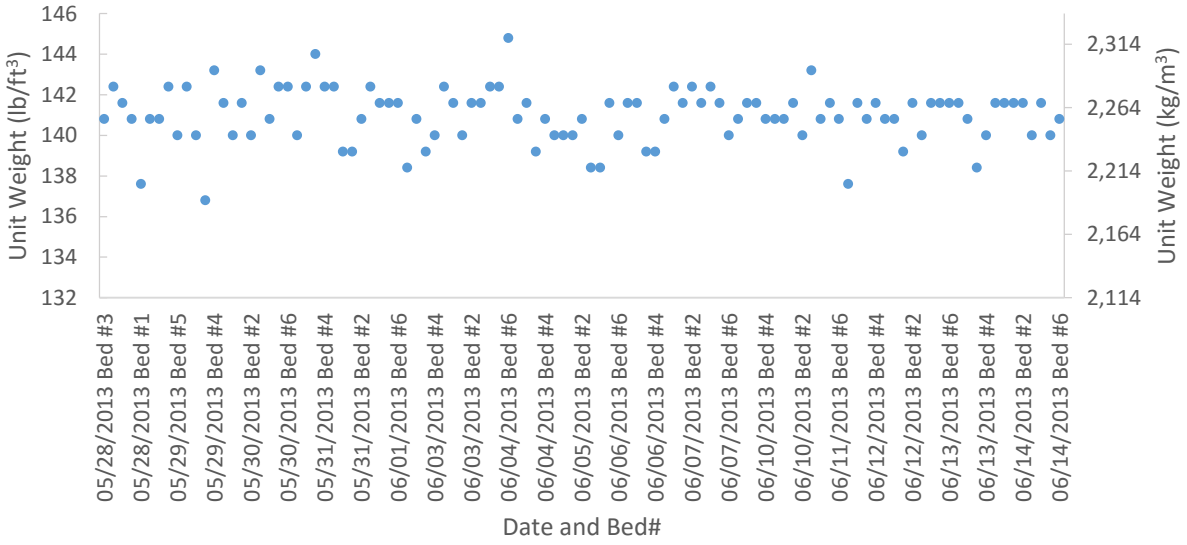


**Figure 3.34 Concrete unit weight at Plant B**

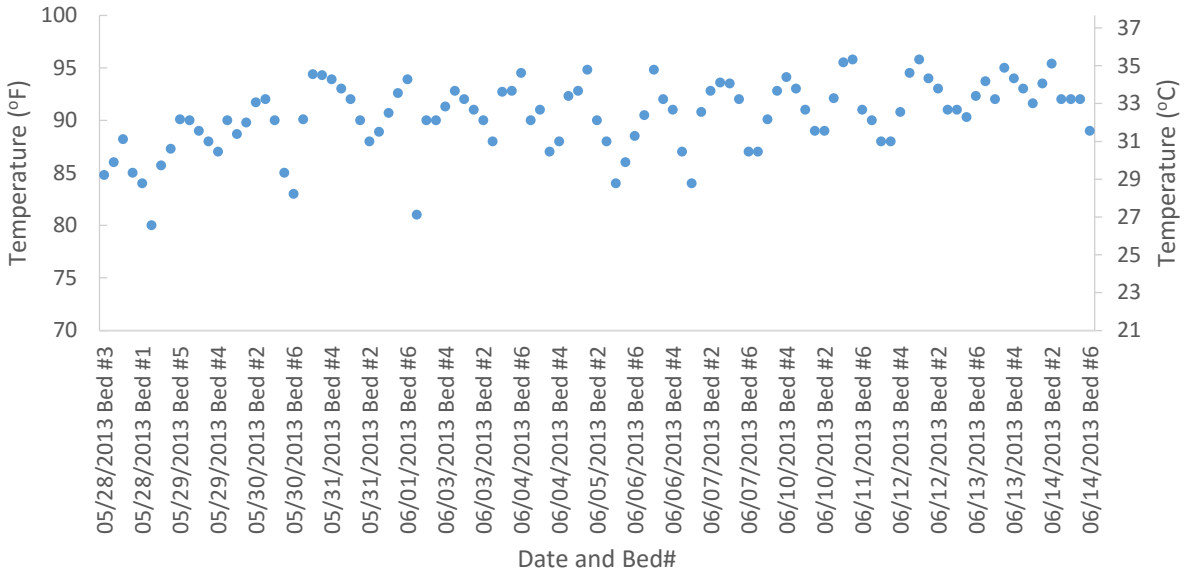


**Figure 3.35 Temperature of fresh concrete at Plant B**

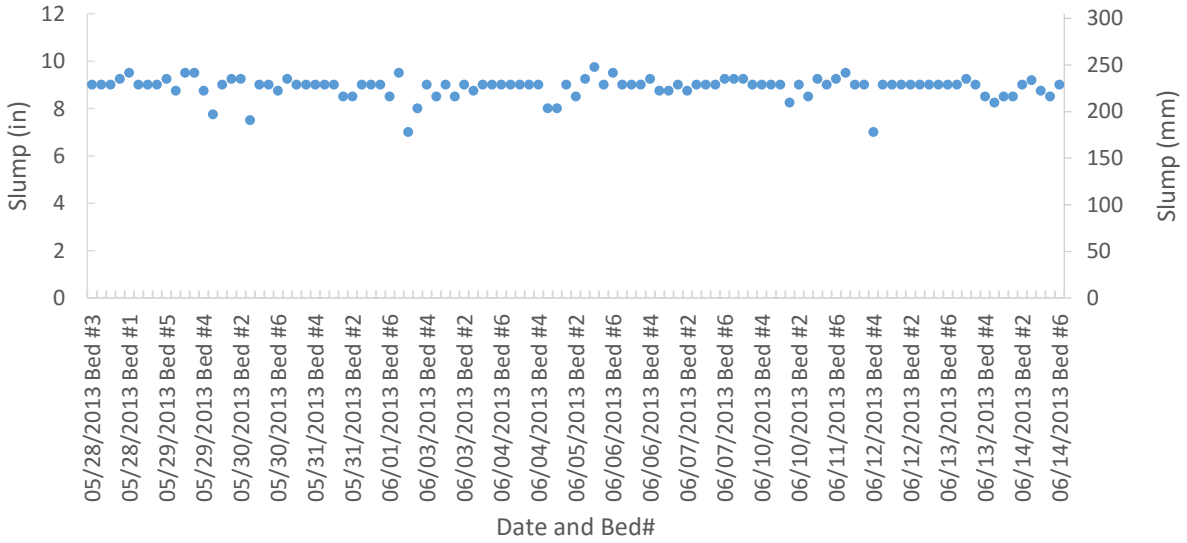


**Figure 3.36 Slump of fresh concrete at Plant B**

Various concrete rheological parameters could affect the rate of entrained air void loss during handling and vibration. Rheological parameters are also needed in order to understand the attenuation of shear waves in fresh concrete caused by vibration. Figure 3.37 shows the variation in measurements of static yield stress and dynamic yield stress (i.e., Bingham yield stress)

measured at Plant A. As expected, measured dynamic yield stress was always lower than static yield stress because the material is easier to shear while it is flowing rather than shearing from a static position. Figure 3.38 shows variation in plastic viscosity of concrete throughout the period of study at Plant A. Figure 3.37 and Figure 3.38 show a large standard deviation of yield stress and plastic viscosity values. The static yield stress varied between 303.5 and 3027.4 Pa with an average of 1499.2 Pa and a standard deviation of 640 Pa, while plastic viscosity varied between 45.4 and 217.9 Pa·s with an average of 145.1 Pa·s and a standard deviation of 47.8 Pa·s. This shows that rheological properties can vary daily in concrete batch plants, based on factors such as temperature, slight variations in aggregate moisture content, and slightly different air. This fluctuation in rheology may also be due to the fact that the batch operator was given some tolerance in regards to modifying batch proportions during mixing in order to meet certain objectives. These small modifications could significantly affect rheological properties of the concrete mixture.

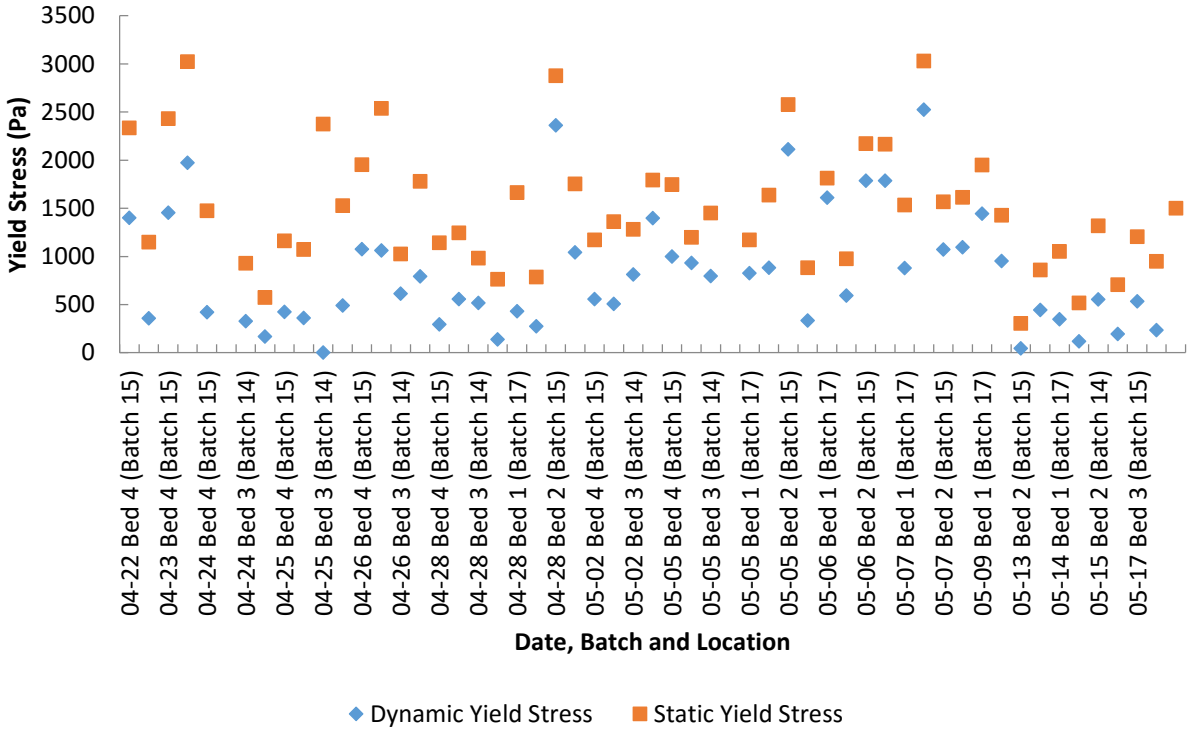


**Figure 3.37 Yield stress of fresh concrete at the mixer level in Plant A**

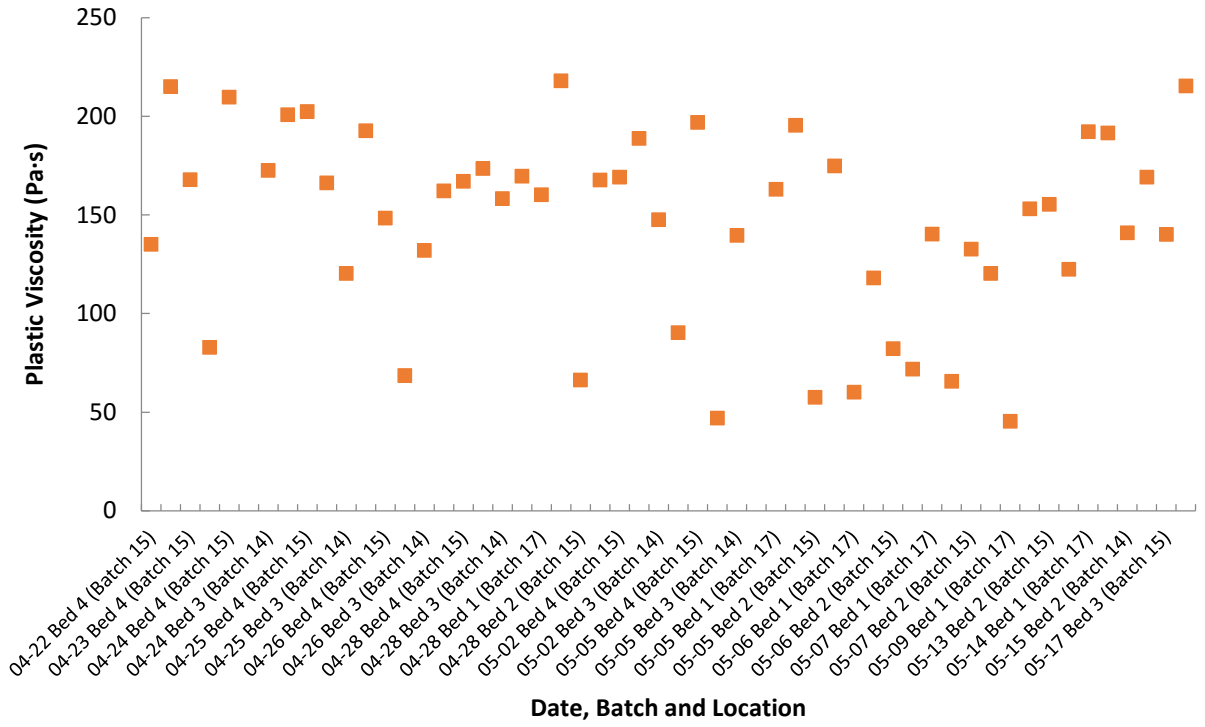


**Figure 3.38 Plastic viscosity of fresh concrete at the mixer level in Plant A**

Figure 3.39 presents variation in the measurements of static yield stress and dynamic yield stress throughout the study period at Plant B. Similar to Plant A observations, Figure 3.39 shows that dynamic yield stress was always lower than static yield stress at mixer and QC levels. Figure 3.40 shows variation in plastic viscosity of concrete throughout the period of study at Plant B. The static yield stress varied between 160.4 and 1148.7 Pa with an average of 751.8 Pa and a standard deviation of 303.4 Pa, while plastic viscosity varied between 128.8 and 263.3 Pa·s with an average of 192 Pa·s and a standard deviation of 37.1 Pa·s. The overall trend shown in Figure 3.40 indicates higher plastic viscosity in concrete sampled from the casting machine. Figure 3.41 shows the change of rheological parameters with time for a single batch of concrete at Plant B. All rheological parameters increased with time possibly as a result of water absorption by aggregate and cement particle aggregation/ flocculation.


**Figure 3.39 Yield stress of fresh concrete at Plant B**

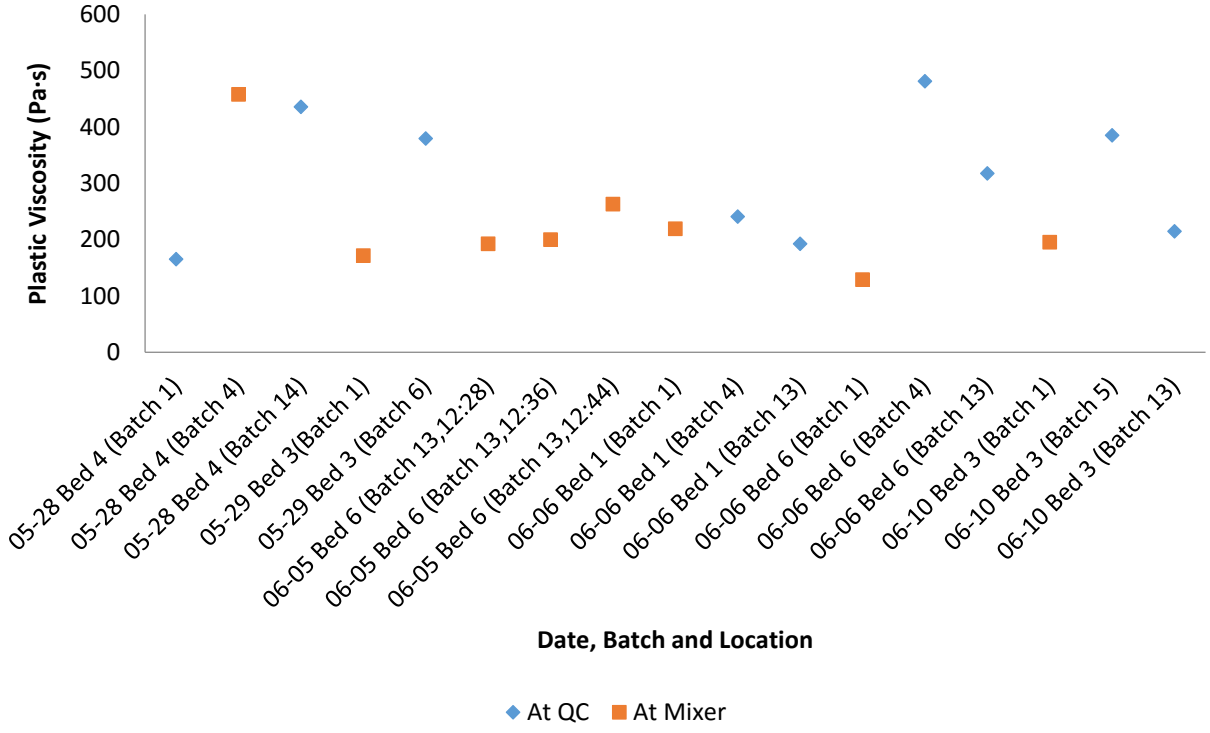


**Figure 3.40 Plastic viscosity of fresh concrete at Plant B**

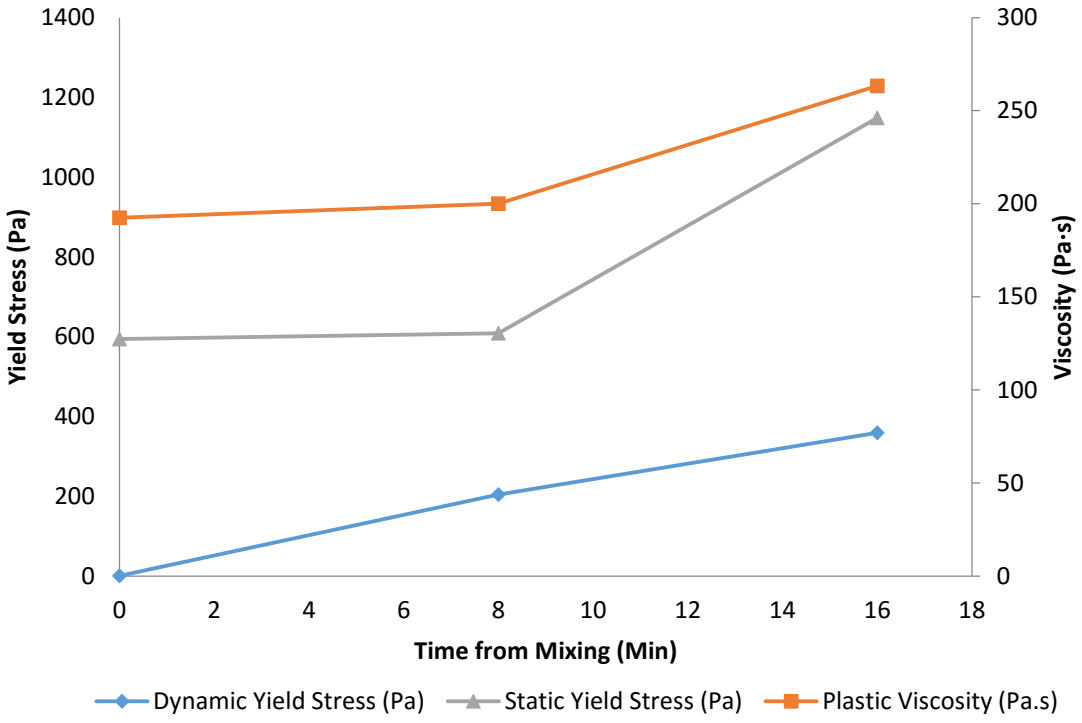


**Figure 3.41 Rheological parameters versus time for a single batch at Plant B**

Figure 3.42 shows variation in vibration frequency with time during the vibration of Bed 4 at Plant A. Immersion vibrator frequency was 110 Hz. Short-term frequency increases shown in Figure 3.42 were likely caused by the surrounding environment, such as workers and other machinery that impacted the casting bed or machine. Figure 3.43 presents a zoomed-in portion of the frequency curve obtained from the end of Bed 2 at Plant A.

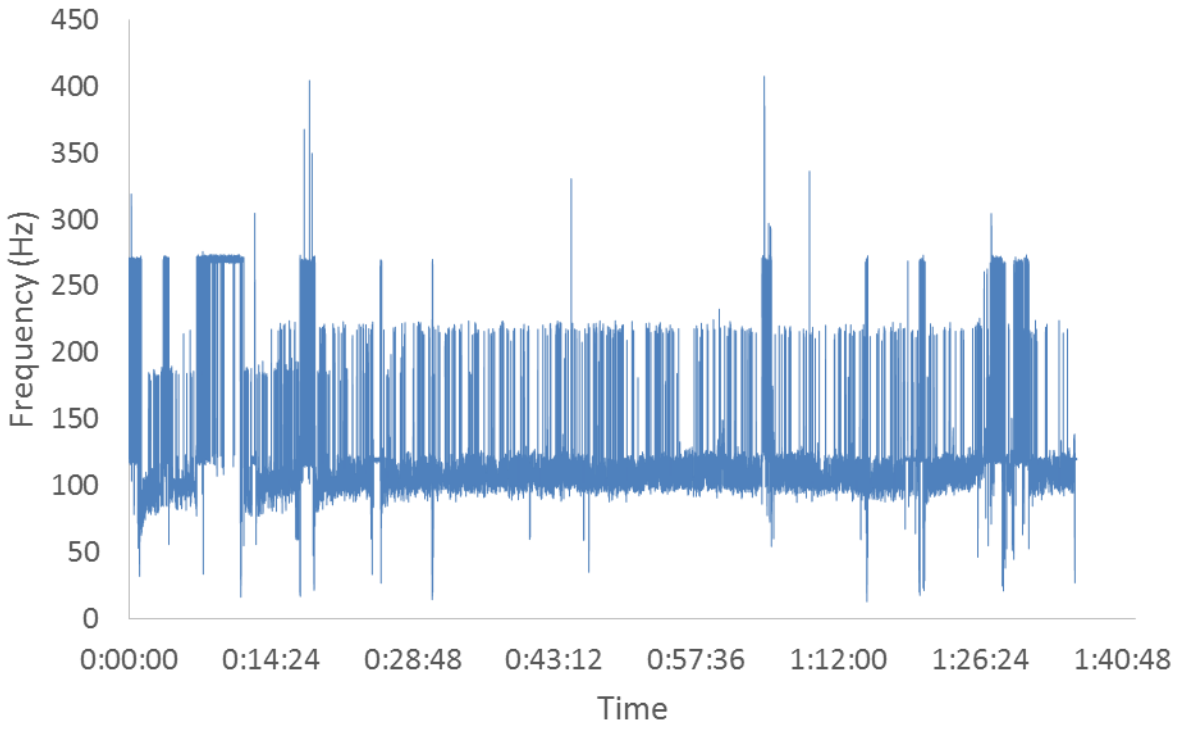


**Figure 3.42 Frequency variation of vibration of Bed 4 at Plant A for 1 hour and 40 minutes**

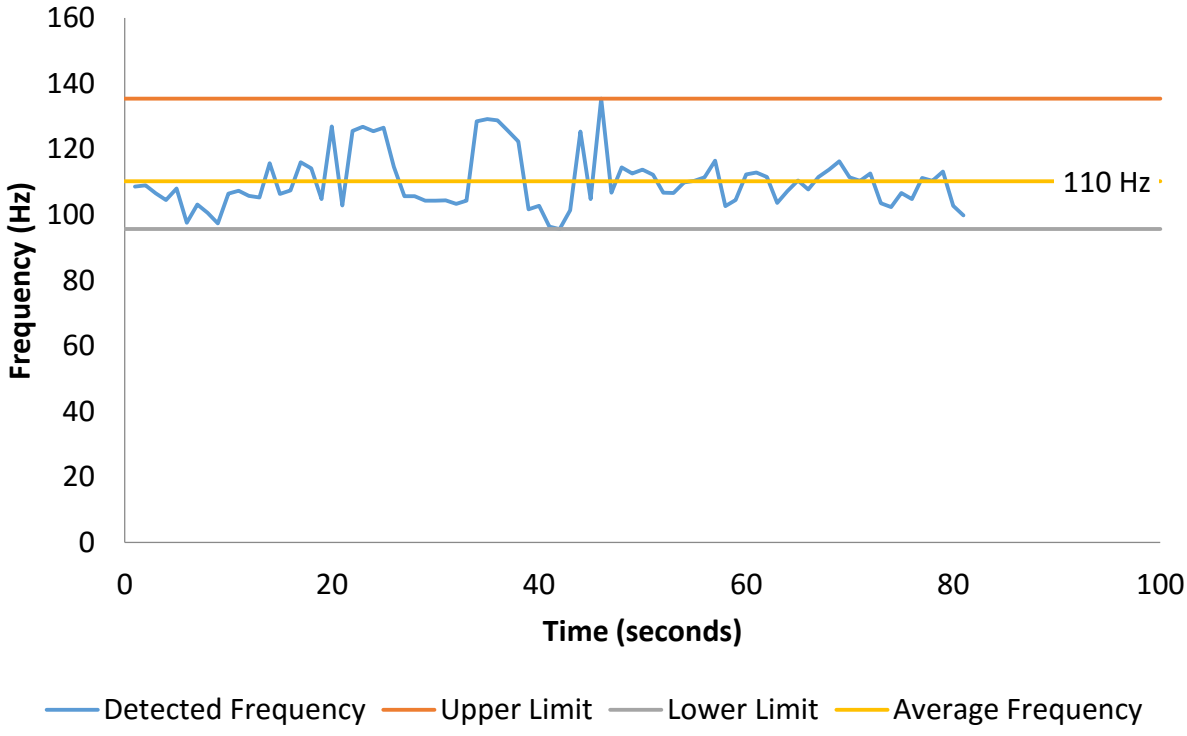


**Figure 3.43 Average frequency in an 80-second interval at the end of Bed 2 of Plant A**

Data envelopes were found for maximum acceleration in the positive and negative direction, as shown in Figure 3.44. The average recoded maximum acceleration in Plant A was 2.5 g at the casting machine. The accelerometer measured an average acceleration of 0.5 g when attached to the forms at a distance of 1ft from the casting machine, as shown in Figure 3.45.

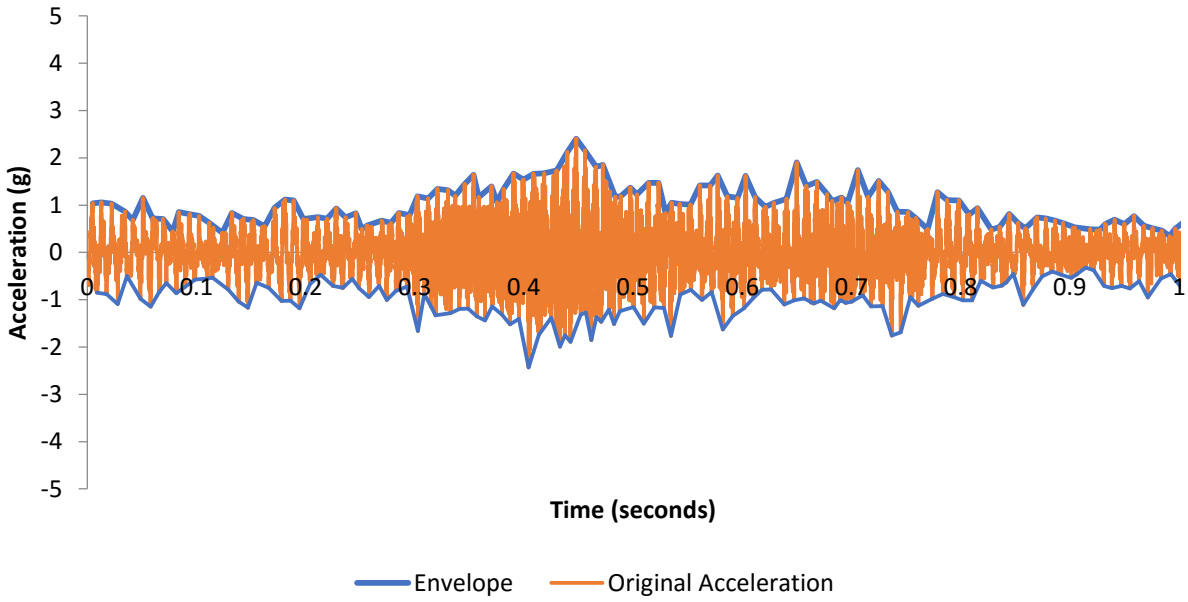


**Figure 3.44 Acceleration with maximum acceleration envelope recorded over 1 second at the end of Bed 2 with an accelerometer attached to the casting machine of Plant A**

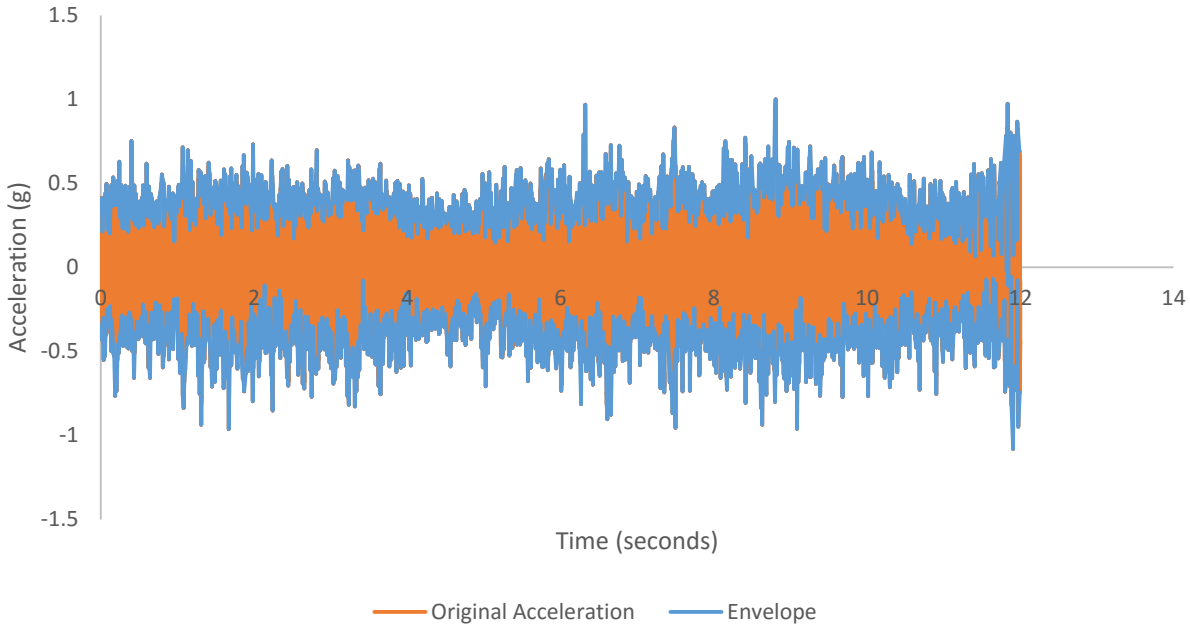


**Figure 3.45 Acceleration with the envelope recorded over 12 seconds at the end of Bed 2 with the accelerometer attached to the forms of Plant A**

Unlike Plant A, Plant B used a form-based vibration system in which the interior of the concrete was easily accessible. Vibration provided by the bed vibrator in this plant had an average frequency 75 Hz. Short-term frequency increases shown in Figure 3.46 were likely caused by the surrounding environment for the form accelerometer readings. Short-term increases in concrete vibration measured by the submersible accelerometer could have been caused by the environment or the accelerometer contacting a wire during vibration. The average recorded acceleration in Plant B was 5 g.

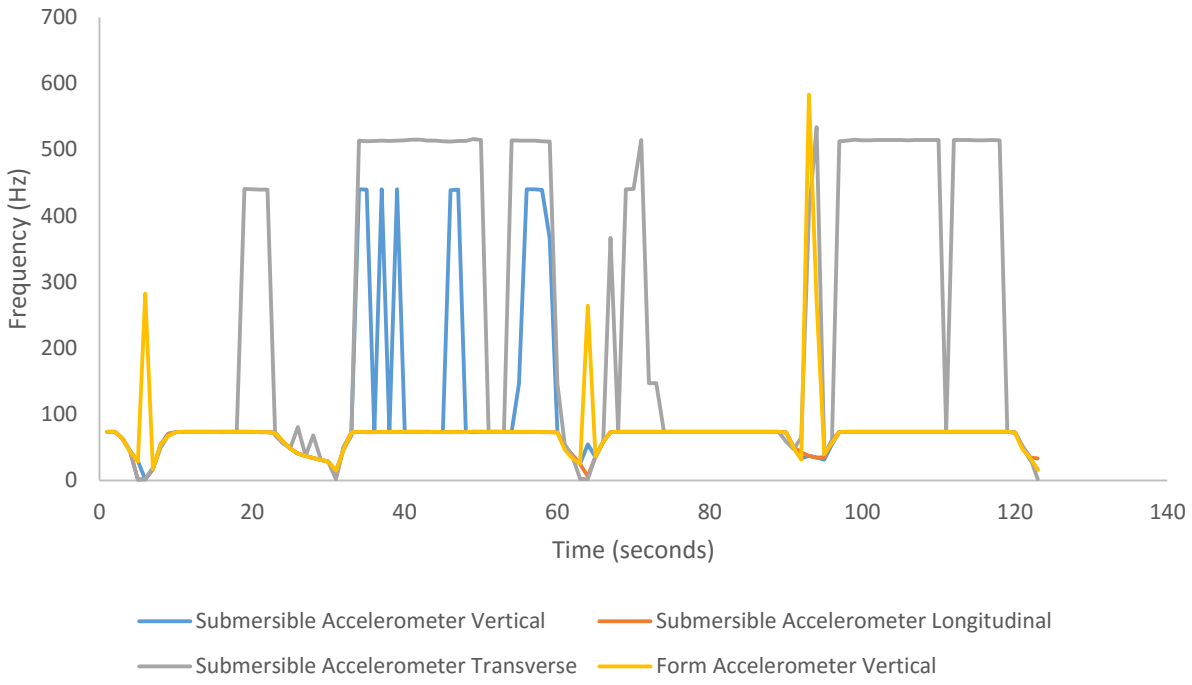


**Figure 3.46 Average frequency in a 123-second interval at the end of Bed 2 in Cavity 1 of Plant B with the immersed accelerometer at a depth of 3.5 in.**

Acceleration measurements inside the concrete were taken during vibration of the beds. Interior and exterior cavities were examined to identify differences in vibration acceleration induced into concrete at different cavities. Measurements of concrete acceleration were taken across the depth, along the length, and across the width of the cavity. Figure 3.47 shows the vertical acceleration envelope (i.e., peak accelerations for each cycle in the vertical direction versus time) along the length of Cavity 1 at 4.25 in. deep at 2-ft intervals. As shown, variations occurred in the peak accelerations at various locations along the crosstie cavity. At some durations, peak acceleration experienced a sudden drop or rise due to switching on/off the vibrator and reversing rotation direction of the vibrator. The measured acceleration can be better understood by averaging the peak acceleration at each location without including the off periods, and plotting them versus location, as shown in Figure 3.48. Acceleration was higher near the vibrator in the midspan of the

cavity compared to the edges; acceleration in all directions ranged between 1.3g and 7.6g. Such vibration, however, results in the reflection of waves from boundaries of the cavities, leading to complicated constructive and destructive interferences.

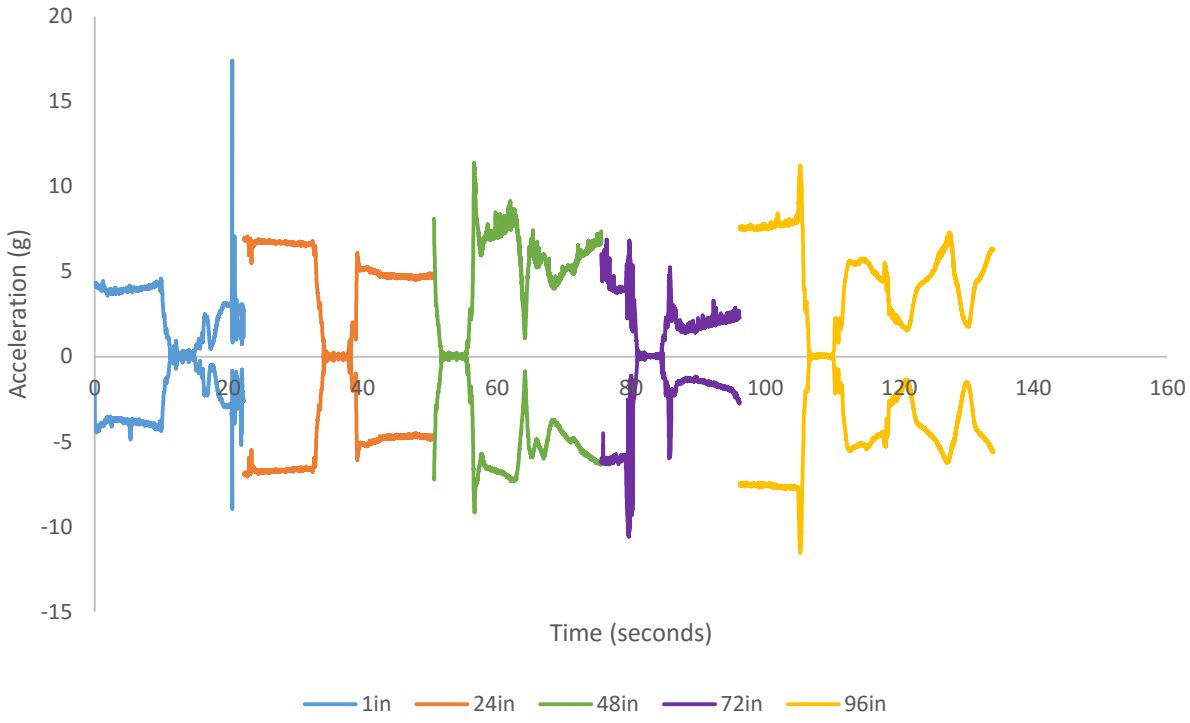


**Figure 3.47 Vertical acceleration envelope along the length of Cavity 1 at a depth of 4.25 in. with 2-ft intervals**

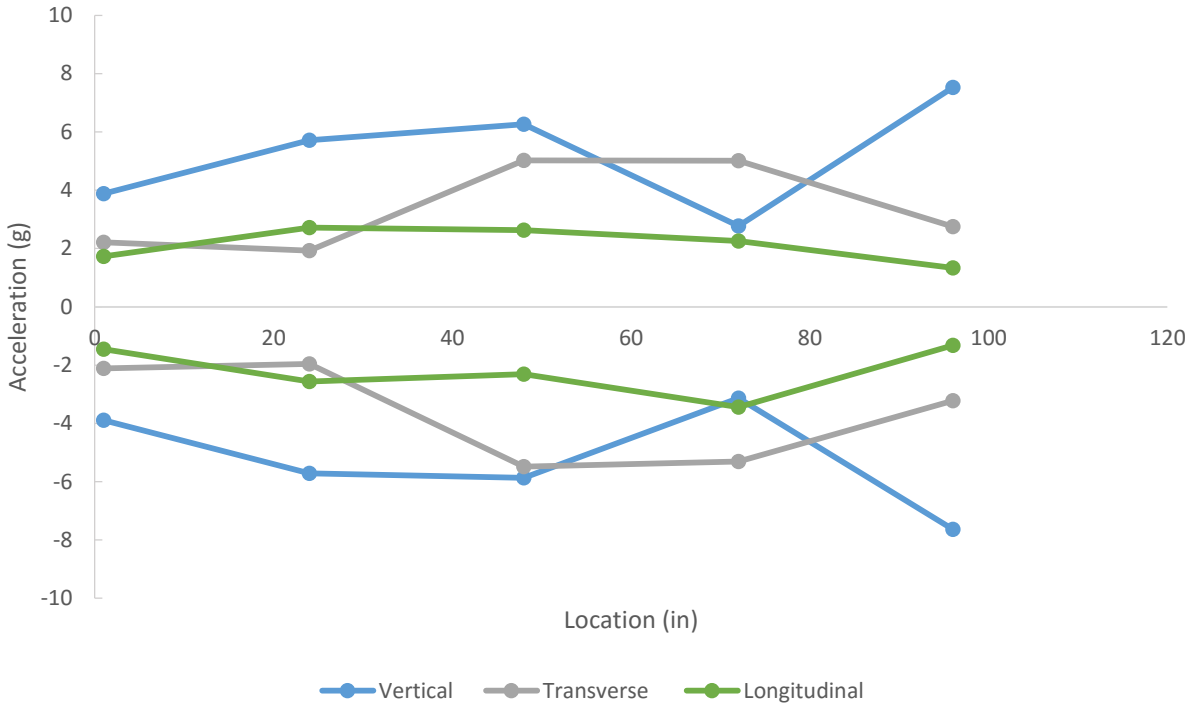


**Figure 3.48 Average peak acceleration versus location along the length of Cavity 1 at a depth of 4.25 in. with 2-ft intervals without off periods**

Figure 3.49 shows average peak acceleration along the length of Cavity 2 at a distance of 4.25 in. from the concrete top surface and at 1-ft intervals. For this cavity, the behavior was non-uniform as compared to the previous case, although both cavities had the same vibrator. This could be due to vibration wave interference in the formwork or local vibration. The three vibrators used may have had small variation in acceleration and frequency that caused increased turbulence in the measurements. Nevertheless, the range of acceleration in this case was much larger, with 0.6 g as the lower bound and 9.7 g as the upper bound. This increase in the upper bound could be because Cavity 2 was closer to the vibrator than Cavity 1, resulting in higher vibration energy transmitted to the concrete in Cavity 2.

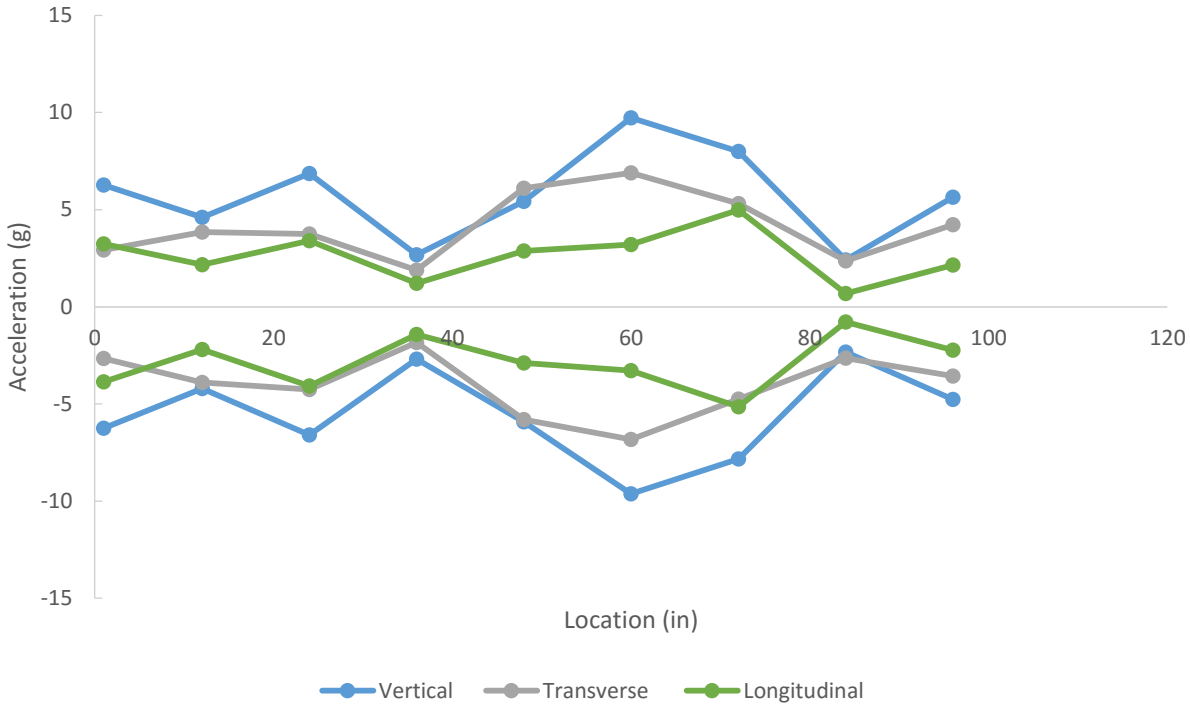


**Figure 3.49 Average peak acceleration versus location along the length of Cavity 2 at a depth of 4.25 in. with 1-ft intervals**

Acceleration measurements shown in Figure 3.50 through Figure 3.52 indicate that maximum acceleration occurred in the middle of the cavity slightly away from the surface of the vibrating form as seen in Figure 3.13. The edges of the cavity also experienced increased acceleration compared to under the rail seats. Overall, the behavior showed non-uniformity, with the middle and edges of the cavity experiencing more acceleration closer to the vibrator compared to under the rail seat.

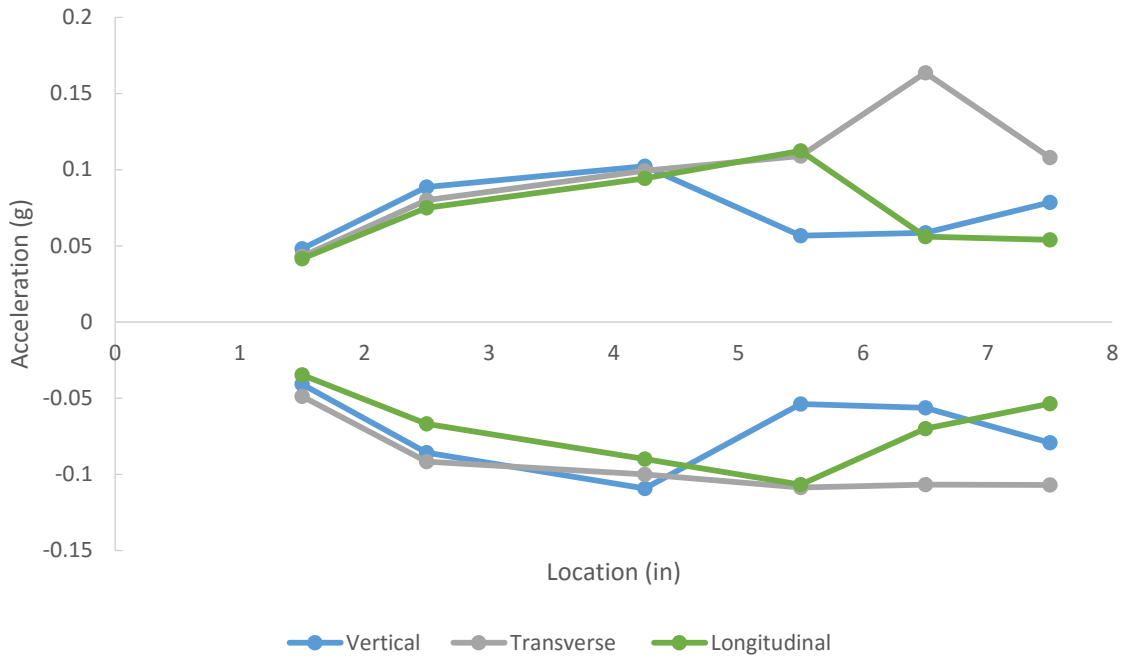


**Figure 3.50 Average peak acceleration versus location across the depth of Cavity 2 at the middle of the crosstie cavity**

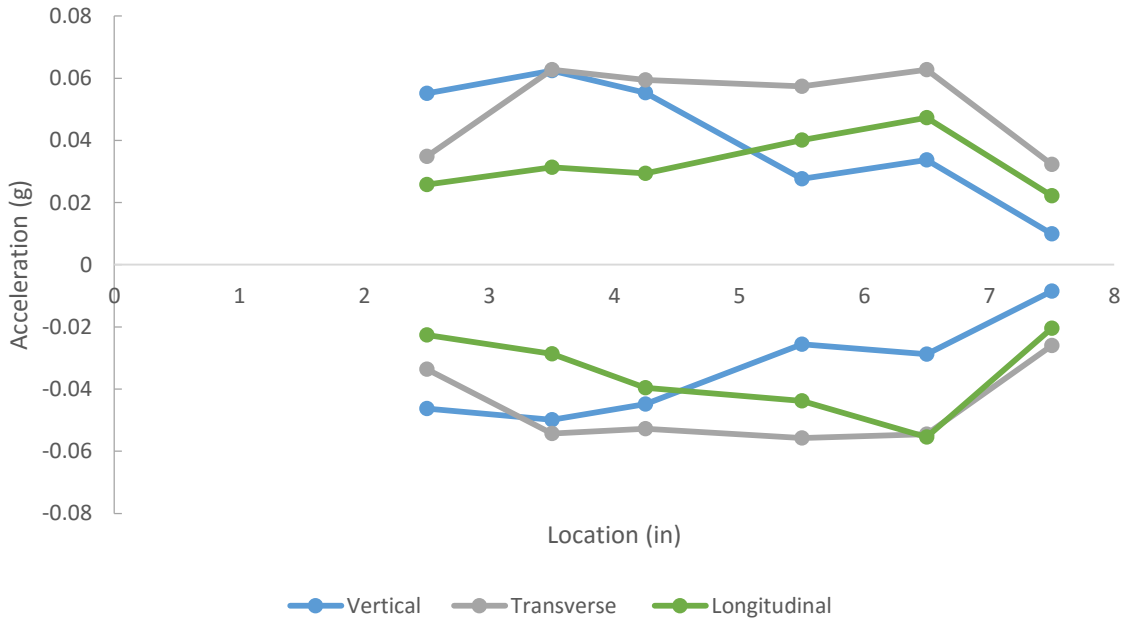


**Figure 3.51 Average peak acceleration versus location across the depth of Cavity 2 1 in. from the edge of the crosstie cavity**

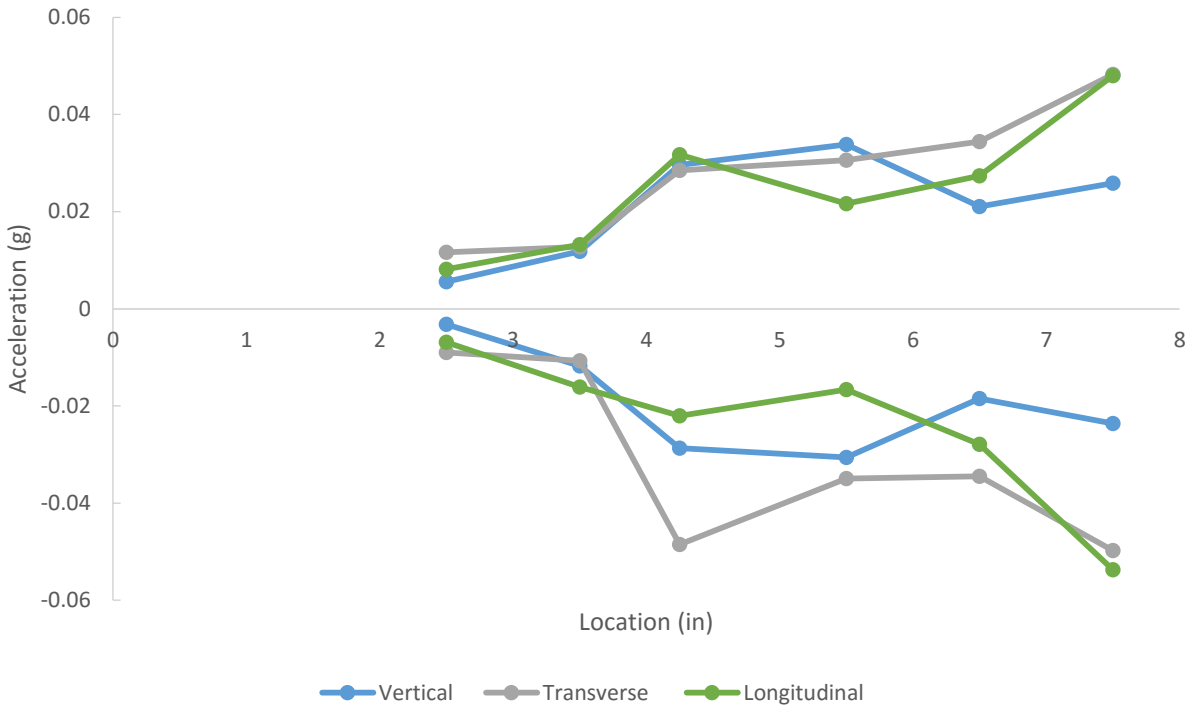


**Figure 3.52 Average peak acceleration versus location across the depth of Cavity 2 under the rail seat**

Figure 3.53 shows average peak acceleration across the width of Cavity 2 measured at a distance of 1 in. from the edges and the middle of the cavity. The two figures show that maximum acceleration occurred in the middle across the width of the cavity, whereas the edge closest to the vibrator experienced more acceleration compared to the edge farthest from the vibrator. A boundary condition effect occurred with the vibration. During vibration, the concrete moved separately from the formwork and air bubbles traveled to the concrete surface, possibly because the middle section received vibration waves from the three directions and these waves caused a buildup in acceleration.

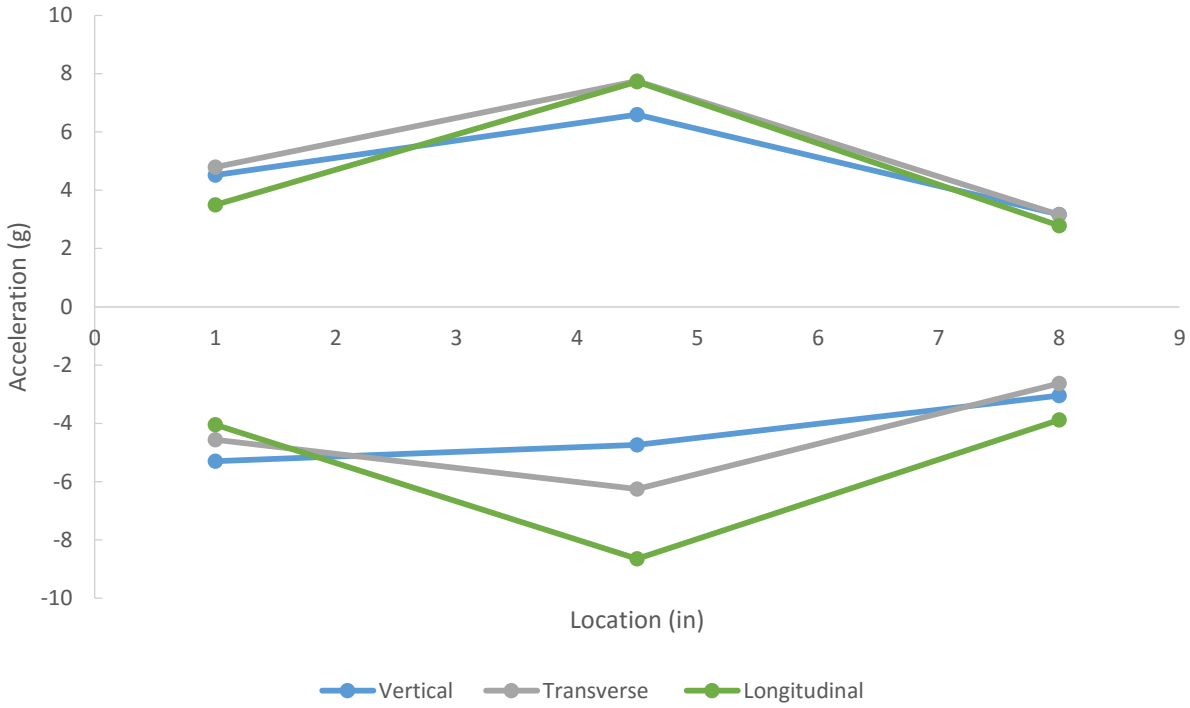


**Figure 3.53 Average peak acceleration versus location across the width of Cavity 2 1 in. from the edge of the cavity**

Concrete crossties in a cavity were cast as a continuous concrete element with other crossties that were saw-cut after strand detensioning in order to separate individual ties. Because the concrete crossties were continuous, the concrete in a previously cast location experienced vibration from a form vibrator a considerable distance away. Vibration acceleration was recorded using the submersible accelerometer to measure vibration energy as a function of distance from the active vibrators, as shown in Figure 3.54. This was achieved by recording vibration as it moved away from the accelerometer and measuring the distance every time the vibration moved further away. The submersible accelerometer recorded vibration for approximately 15 minutes until the vibration had moved 30 ft away from the accelerometer. The accelerometer mounted on the form recorded form vibration for the entire period of casting, as shown in Figure 3.55.

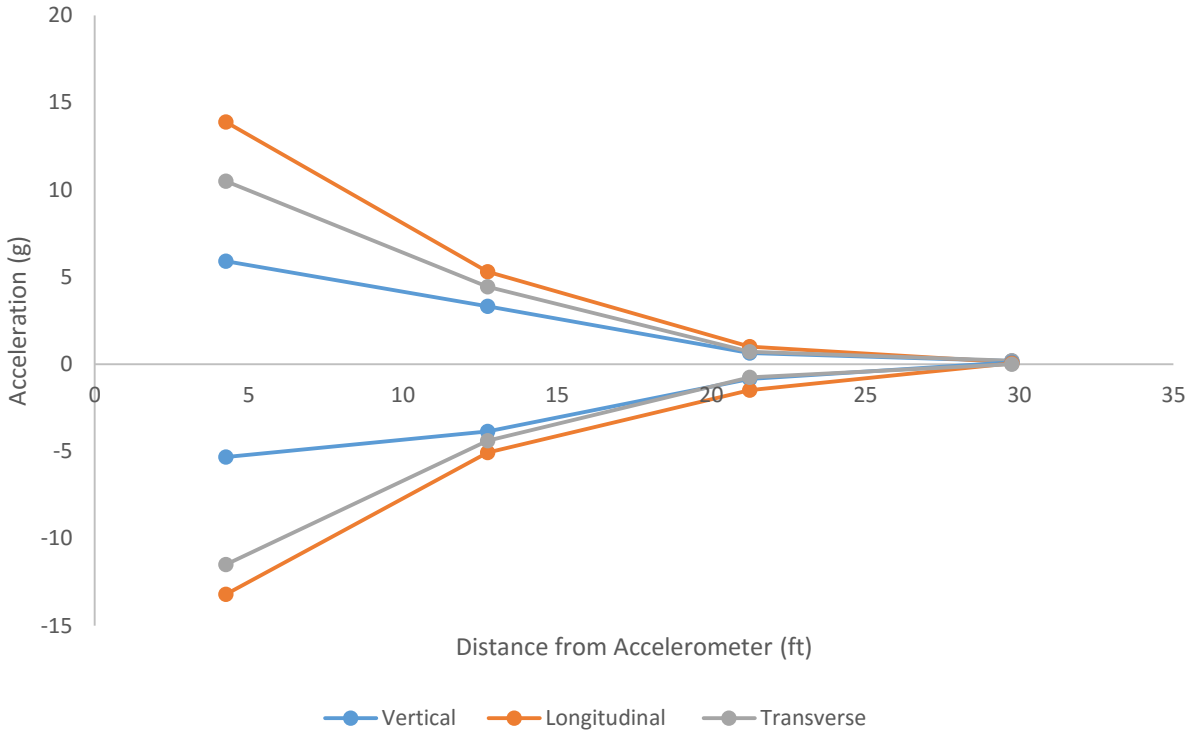


**Figure 3.54 Average peak concrete acceleration versus location across 30 ft of length of the bed in Cavity 1 1 in. from the start of the bed**

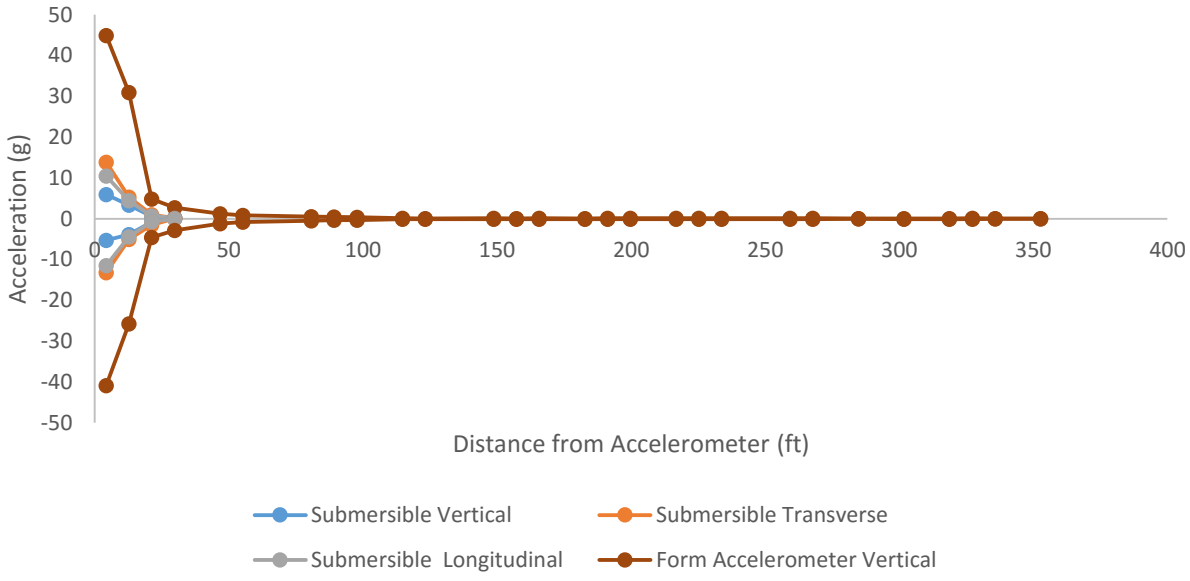


**Figure 3.55 Average peak concrete and form acceleration versus location across the length of the entire bed in Cavity 1 1 in. from the start of the bed**

Vibration in the concrete was substantially less than vibration in the form, thus confirming visual observations that the form tended to move quite rapidly. However, some sloshing of the concrete could have dampened some of the concrete acceleration. In addition, concrete acceleration remained high for some time after the form vibrator immediately underneath had been turned off. Vibration was another important factor. Form vibrators (Plant B) affected concrete for great distances after casting, as shown in Figure 3.54 and Figure 3.55, while immersion vibrators had smaller regions of influence. Immersion vibrators typically apply vibration for shorter but more effective intervals.

## 3.5. Conclusions

Slump, air content, temperature, rheology, and vibration of fresh concrete were measured at two concrete railroad tie plants. Concrete vibration at Plant A was performed using internal vibrators operating at 110 Hz. At Plant B, concrete was vibrated using form vibrators at 75 Hz. Results showed a correlation between concrete yield stresses and air loss from the fresh concrete during handling. Variations in batch-to-batch concrete rheology were also observed. These variations could be due to minor adjustments made to the mixture, variation in aggregate moisture content, and different air content. Vibration testing was also conducted at Plant B, thereby demonstrating the high complexity of wave propagation induced by form-based vibrators. Vibration also occurred for a longer period of time than needed to just consolidate the concrete. Immersion vibrators vibrated the concrete for a shorter, more concentrated, and more effective period of time with less unwanted ongoing vibration from neighboring crossties.

Hardened air content samples were made in order to quantify how handling and consolidation processes typical of prestressed concrete railroad tie manufacturing operations affect concrete air void systems used for freeze-thaw protection. On average, the hardened air content

decreased by 4% and 3.4% between leaving the mixer and finishing vibration for Plant A and Plant B, respectively. On average, concrete spacing factors increased from 0.1092 to 0.1651 mm (0.0043 to 0.0065 in) for Plant A and 0.1219 to 0.2184 mm (0.0048 to 0.0086 in) for Plant B. Once the concrete left the mixer, each stage in the process decreased the air content. The concrete air void spacing factor was found to increase more during handling with a more workable mixture and extended vibration. These results will be used to guide and validate laboratory testing in order to optimize vibration for specific air content.

# Chapter 4 - Effect of Freezing and Thawing on Full-Scale Prestressed Concrete Railroad Ties

This chapter describes the test of whole concrete ties using procedures based on ASTM C666 [63] specifications in order to estimate their construction quality with respect to freeze-thaw durability. ASTM C666 specifies how to test small concrete prisms in order to measure their ability to withstand freezing and thawing cycles. According to those specifications, specimens were subjected to 300 cycles of freezing and thawing or until dynamic modulus of elasticity was reduced to less than 60% of the original, whichever occurs first unless otherwise specified. This test method also allows for optional testing of concrete expansion and mass loss. Some state departments of transportation (DOTs) use a length change measurement criteria instead of dynamic modulus of elasticity, while other DOTs require that concrete be tested with dynamic modulus of elasticity and length change measurements. When using the optional length change criteria, 0.1% expansion is often used as the end of test, although agencies such as the Illinois Department of Transportation (IDOT) use an expansion threshold of 0.06% [101]. Concrete is typically said to fail the test when the concrete dynamic modulus of elasticity is lower than 60% of the original, or when the concrete reaches an expansion of 0.1%.

Concrete samples for testing concrete resistance to freezing and thawing are usually saw-cut from a prestressed concrete tie. However, saw-cutting prestressed concrete railroad ties may damage the samples, giving results that may not be representative of the entire tie. Potential damage could include micro-cracking that would allow water to quickly penetrate the sample and accelerate damage, bursting stresses caused by steel's proximity to the surface, and various stress states and micro-cracking-caused eccentricities from cutting prestressed concrete. When the close proximity of prestressing wires or strands prevent a specimen without steel from being saw-cut,

samples are cast from the same concrete but not subjected to the same consolidation and finishing operations as the ties, potentially making them non-representative of concrete tie behavior during freezing and thawing.

For this study, whole concrete railroad ties were tested using procedures based on ASTM C666. Testing whole railroad ties eliminates potential saw-cutting problems previously mentioned and may provide a more realistic evaluation of concrete tie durability in the field instead of only that of the original concrete material. However, some modifications were made to the ASTM C666 test method in order to accommodate the large sample size for this study. First, freezing and thawing cycling time was extended because of the large thermal mass. Second, the concrete ties being tested were wrapped in burlap and sealed in plastic tubes instead of in water containers. (Rigid water containers prevent ice and concrete from expanding during freezing, thereby causing damage that is not representative of field concrete that is not retrained from expanding.)

IDOT sampled 16 prestressed concrete railroad ties and sent the ties to Kansas State University (KSU) for freeze-thaw testing. Table 4.1 shows tie identification numbers, location of sampling, sampling dates, casting plant, and tie condition when sampled. Seven whole ties were tested in 300 cycles of freezing and thawing using a modified version of ASTM C666. Because of specimen size, a few procedure modifications were made based on procedures used in a previous research study performed by CN Rail [3].

**Table 4.1 Tie samples**

| Tie # | Mile Post Sampled | Date Tie Was Sampled | Tie ID # | Casting Plant | Tie Condition | Tie Tested in Freeze-Thaw |
|---|---|---|---|---|---|---|
| 1 | 217 | 10/4/2010 | #2-042-C | Plant B | Good | ● |
| 2 | 202 | 10/21/2010 | #1-092-B | Plant B | Good | |
| 3 | 171 | 12/3/2010 | #1-109-C | Plant B | Good | |
| 4 | 114 | 6/4/2011 | #2-134-A | Plant B | Good | |

| | | | | | | |
|---|---|---|---|---|---|---|
| 5 | 104 | 6/18/2011 | #2-05103-2 | Plant C | Good | ● |
| 6 | 96 | 6/23/2011 | #2-034-B | Plant B | Good | |
| 7 | 90 | 7/5/2011 | #1-05075-3 | Plant C | Good | |
| 8 | 83 | 7/16/2011 | #1-05009-3 | Plant C | Good | ● |
| 9 | 73 | 7/21/2011 | #1-05035-4 | Plant C | Good | |
| 10 | 273 | 8/7/2011 | #1-06037-5 | Plant C | Good | |
| 11 | 269 | 8/17/2011 | #1-053-C | Plant B | Good | ● |
| 12 | 266 | 8/19/2011 | #2-05029-2 | Plant C | Good | ● |
| 13 | 83 | 8/1/2012 | #1-4397-F | Plant A | Good | ● |
| 14 | 84 | 8/1/2012 | #2-4386-B | Plant A | Good | ● |
| 15 | 247 | 4/21/2012 | #1-F-4299 | Plant A | Good | |
| 16 | 242 | 5/1/2012 | #2-4397-D | Plant A | Good | |

The most common method used to measure concrete susceptibility to freeze-thaw deterioration is ASTM C666 in which concrete specimens between 3 x 3 x 11 in. (75 x 75 x 279 mm) and 5 x 5 x 16 in. (125 x 125 x 405 mm) are saturated in a lime water bath for at least two days and then conditioned at 40 °F (4 °C). The concrete is then frozen to 0 °F (-18 °C) and thawed to 40 °F (4 °C) 300 times. The freezing is rapid, with up to 12 cycles performed per day. During testing, samples are immersed in water or frozen in air and thawed by flooding the chamber containing the concrete samples with water [63]. Damage is monitored by dynamic modulus of elasticity, length change, and mass loss. Seven concrete railroad ties from a high-speed rail line were tested under freeze-thaw conditions to determine their expected freeze-thaw durability in track. Differences between ASTM C666 test procedures and procedures used for this experiment [63] are presented in Table 4.2.

**Table 4.2 Differences between ASTM C666 and KSU whole-concrete tie testing**

| | **ASTM C666** [63] | **Full Scale Ties Modifications** |
|---|---|---|
| ***Freezing-and-Thawing Apparatus*** | The apparatus must be in compliance with the following:<br>(*1*) For Procedure A: the specimen must be completely surrounded by not less than 1⁄32 in. (1 mm) nor more than 1⁄8 in. (3 mm) of water at all times.<br>(*2*) For Procedure B, the specimen must be completely surrounded by air during the freezing period and by water during the thawing period. | Tie was kept wet by wrapping in wet burlap and vacuum-sealed with plastic tubing. |
| | Rigid containers are not allowed. | None |
| | The temperature of the specimen or specimen container surface shall be uniform to within 6 °F (3 °C), except during the transition period between freezing and thawing. | None |
| ***Temperature-Measuring Equipment*** | The measuring device must be capable of measuring the temperature at several points within the chamber and at the centers of the control specimen to within 2 °F (1 °C) | Concrete temperature was monitored at the same depth from the concrete surface as specified by ASTM C666 or 1.5 in. (38 mm) from the concrete surface. |
| ***Scales*** | The scale must have a capacity at least 50% greater than the mass of the specimens and accurate to at least 0.01 lb (5gm) within the range of ± 10% of the specimen mass. | Used Scale Capacity 1000 lb (454 kg) with 0.1 lb (0.05 kg) accuracy. |
| ***Freezing and Thawing Cycle*** | The freezing and thawing cycle temperature shall be controlled by measurements of temperature from the control specimen. | None |
| | Changing the location of control specimen frequently to account for extremes of temperature variation. | The control tie was kept in a fixed location because of limitations on wire access to the data logger. |
| ***Freezing and Thawing Cycle Sampling*** | The nominal freezing and thawing cycle for Methods A and B requires lowering the temperature of the specimens from 40 to 0 °F (4 to -18 °C) and raising it from 0 to 40 °F (-18 to 4 °C) between 2 to 5 h. | The cycle alternated from 40 °F (4 °C) to 12 °F (-11 °C). The freeze cycle time was 11 hours. The thaw time was 2.8 hours. Although the higher freezing temperature used in |

| | | |
|---|---|---|
| | The tolerance of temperatures at the centers of the specimens shall be 0 ± 3 °F (-18 ± 2 °C) for the cooling period and 40 ± 3 °F (4 ± 2 °C) for the heating period. | whole-tie testing may be slightly less severe than ASTM, it is still below the freezing point of water in the tie and low enough for damage to be evident in poor quality concrete. |
| | The variation of temperature from the center of a specimen to its surface shall not exceed 50 °F (28 °C). | None |
| | The transition time between the freezing and thawing periods cannot exceed 10 min, except when specimens are being tested. | None |
| | Saw-cut samples from hardened concrete must be acquired according to ASTM C823. | The whole tie was tested. |
| ***Test Specimens*** | The specimens used must be prisms or cylinders made and cured according to ASTM C192/C192M and ASTM C490. | The whole tie had a non-uniform prismatic shape. |
| ***Test Specimens*** | Specimen width, depth, or diameter must be within 3 in. (75 mm) to 5 in. (125 mm), and specimen length within 11 in. (275 mm) and 16 in. (405 mm). | Ties tested in this program were 8.5 ft (2.6 m) long, with a trapezoidal cross section (9 in. [230 mm] top, 11 in. [280 mm] bottom. and 9.5 in. [240 mm] height at its largest cross section). |
| | Control the temperature of the specimen immediately after the specified curing period. The temperature should be -2 °F and +4 °F (-1 °C and +2 °C) of the thaw temperature. Take readings of the fundamental transverse frequency, mass, average length, and cross section dimensions of the concrete specimen within the tolerance required in ASTM C215. Moisture loss should be prevented between the end of curing period and initiation of freezing and thawing cycles. | Not applicable since ties were collected from the field. |
| | Test for fundamental transverse frequency, mass, and length (optional) change at least every 36 cycles. | None |

| | | |
|---|---|---|
| | Keep the specimens moist when they are out of the freeze-thaw machine. When returning the specimens, return them either to random positions or to predetermined positions according to a rotation arrangement that would ensure each specimen is subjected to all conditions in the freezing machine. | None |
| | Freeze-thaw cycling continues for 300 cycles or until the concrete RDME reaches 60% of the initial modulus, whichever happens first. An additional optional length change test can be used to end the test when the expansion reaches 0.10% of the original length. | None |
| | If a specimen is removed due to failure, a replacement "dummy specimen" must be added for the remainder of the test. | None |

Figure 4.1 represents the entire testing process following the modified ASTM C666 for whole concrete ties described in Table 4.2.

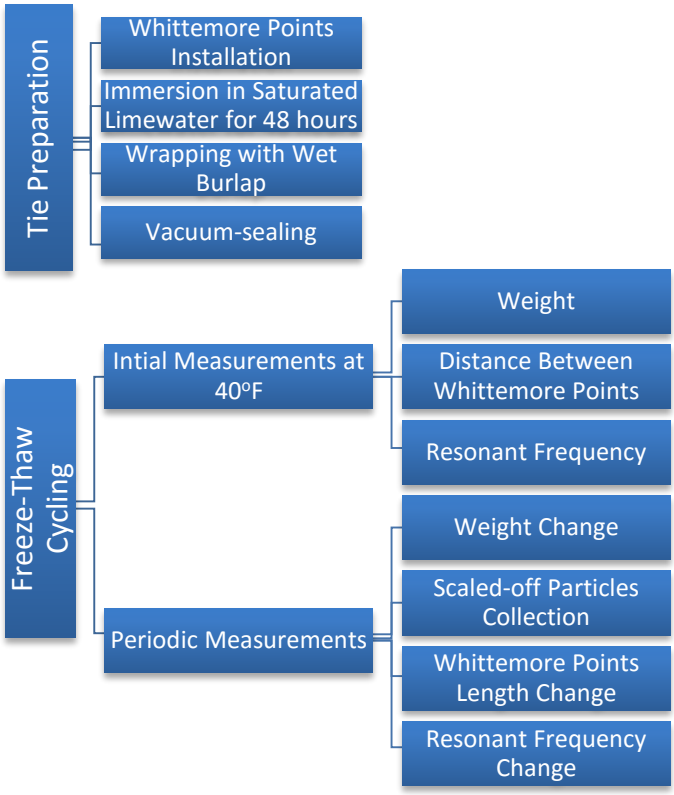


**Figure 4.1 Summary of whole-tie freezing and thawing test procedures**

## 4.1. Tie Preparation

In order to measure length change of concrete ties, 10 Whittemore mechanical strain gauge points were installed in four locations on two sides of the tie using Devcon Precision Brushable Ceramic Epoxy, as shown in Figure 4.2. A Whittemore mechanical strain gauge used these points as a reference to measure any length change in the concrete. In order to install these points at exact locations on ties with eight in-between points on each side, as shown in Figure 4.2, triangular templates were used to control point location during attachment. The locations selected are also shown in Figure 4.2. Although length-change measurements are not on the whole tie, strain measurements should match those seen in the overall tie. Any local differences in strain at other

locations, such as geometrical transitions, would likely result in surface damage or pop outs and would be noticed in visual observations.

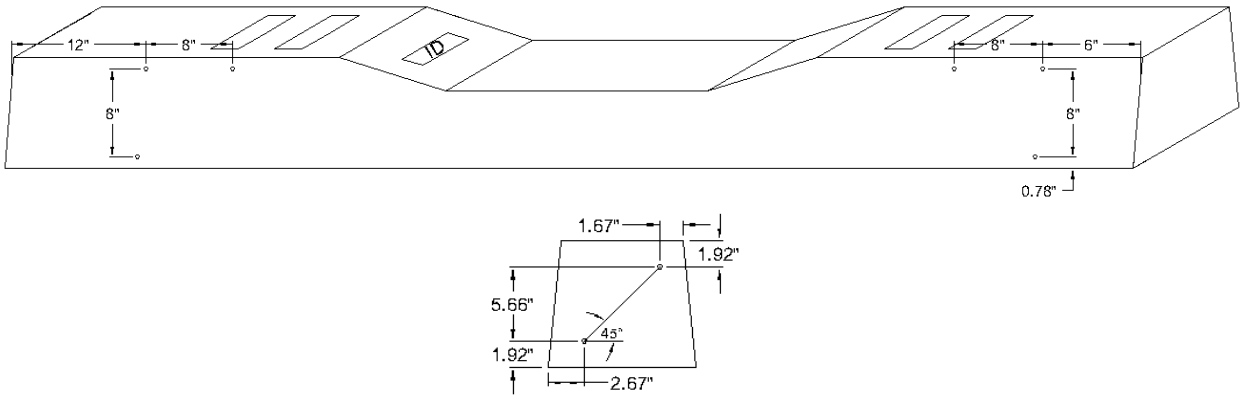


**Figure 4.2 Railroad tie with Whittemore points on front (both ends with identical configuration)**

In order to begin freeze-thaw testing, concrete railroad ties were soaked in saturated limewater at 73.4 ± 3 °F (23 ± 1.7 °C) for 48 hours. The ties were immersed in two large water tanks, with up to four ties stacked two deep per tank, as shown in Figure 4.3.


**Figure 4.3 Railroad tie with Whittemore points on front (both ends with identical configuration)**

After the soaking period, the ties were removed from the lime water tanks and wrapped with wet burlap sheets. The wet burlap was placed around the tie to ensure that free water was present all around the tie for the duration of the test instead of collecting underneath the tie. The wrapped ties were covered with plastic tubing with one end of the tubing sealed. A wet and dry vacuum was used to remove air from the tubing through the open end, as shown in Figure 4.4. After removing the air, the open end of the tube was sealed, and the tie was wrapped with packing tape to ensure that the plastic tubing was held tightly around the tie. Wrapping the burlap and plastic close to the tie surface limited the insulating effects of the burlap and tubing.

**Figure 4.4 Railroad tie vacuum-sealed and wrapped with packing tape**

## 4.2. Freeze-Thaw Cycling

After preparation, eight ties were placed in the freeze-thaw chamber for 300 cycles of freezing and thawing. These eight ties included seven ties from Illinois and one dummy tie used to monitor and control the chamber temperature. Researchers were concerned that drilling into test specimens to insert thermocouples could cause micro-cracking of the ties or allow additional water into the ties. Use of a dummy tie allowed the concrete temperature to be measured without having

to drill into test specimens to control the temperature. The dummy tie temperature was measured using thermocouples installed 1.5 in. (38 mm) deep in the tie center; the thermocouples were installed by drilling a narrow hole into the tie, inserting them, and then filling the hole with epoxy. A thermocouple was also placed in the center of the tie using the same procedure. A schematic of the chamber built to house the ties during freeze-thaw testing is shown in Figure 4.5. Figure 4.6 shows the ties in the assembled chamber. Locations of ties in the chamber were rotated each time measurements were taken in order to prevent bias from tie location.

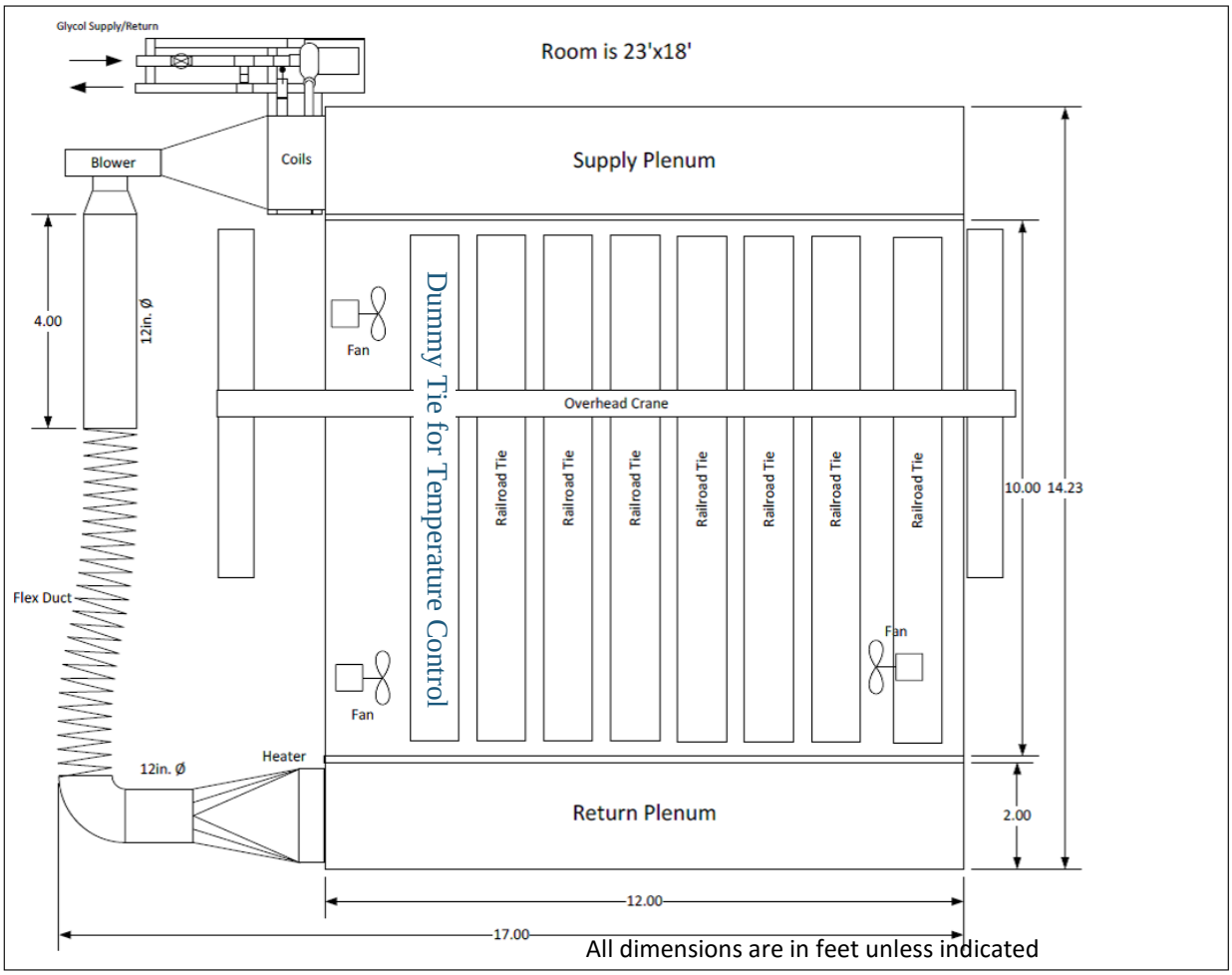


**Figure 4.5 Chamber layout**

**Figure 4.6 Railroad ties in the testing chamber**

A 2,000-gallon glycol tank attached to a chiller was used to freeze the chamber. The chamber temperature during cooling reached 3 °F (-16 °C). The chamber was designed to hold eight ties and to perform freezing and thawing cycles from 12 °F (-11 °C) to 40 °F (4 °C) while maintaining these temperatures 1.5 in. (38 mm) from the top surface of the ties. A depth of 1.5 in. (38 mm) was selected to match the depth below the concrete surface at which the concrete temperature is modified, as specified in ASTM C666. A heater was placed in the supply plenum in order to increase the thawing rate during the thawing cycle. Fans were placed in the chamber to ensure uniform air temperatures and accelerate cycling through increased convection at the tie surface. Figure 4.7 shows typical temperatures measured by the thermocouple inserted 1.5 in. (38 mm) from the concrete dummy tie surface during freeze-thaw cycles.

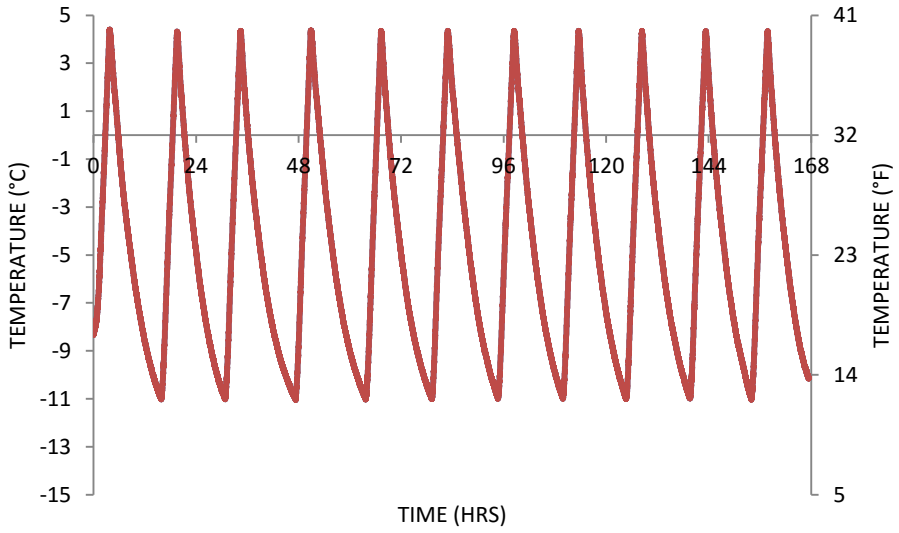


**Figure 4.7 Typical freeze-thaw cycle temperatures measured 1.5 in. (38 mm) from the concrete dummy tie surface**

### *4.2.1. Measurements*

After placing the ties in the chamber, initial readings of tie weight, distance between Whittemore points, and resonant frequency were taken after the ties reached 40 °F (4 °C) and before commencing freeze-thaw cycles. Once the cycling commenced, length change, weight, and resonant frequency measurements were taken every 20 to 36 cycles. ASTM C666 specifies that measurements should be taken at least every 36 cycles, but more frequent measurements are permitted in order to accommodate standard Monday through Friday work schedules. For testing, tubes were unsealed, as shown in Figure 4.8, and burlap was collected in individual bags to gather concrete particles stuck to the fabric in order to measure mass loss. After measurements were completed, the ties were wrapped in wet burlap and sealed in plastic for additional freeze-thaw cycling.

**Figure 4.8 Unwrapping railroad ties**

The ties were weighed using a 1,000-lb (454 kg) crane scale with a resolution of 0.1 lb (0.05 kg). The crane scale was attached to a 2-ton gantry crane with a 14.5-ft (4.4 m) span. During the testing period, the ties were kept wet using a sponge. Concrete expansion was measured using a Whittemore mechanical strain gauge at four locations on the tie, as shown in Figure 4.9.

**Figure 4.9 Whittemore point length measurements**

Concrete resonant frequency typically is measured in order to detect concrete deterioration from freezing and thawing cycles. Cracking and other forms of damage slow down waves that travel through the concrete. These internal damages are not apparent in visual observations, but they are indicated by a decrease in concrete resonant frequency. In this test program, resonant frequency change in ties was measured using the impact resonance method shown in Figure 4.10, in which the concrete at one location was impacted with a light hammer. Waves transmitted through the concrete from the impact were detected using an accelerometer at another location. The resonant frequency of the concrete was then calculated from the measured waves. This process was repeated for the points shown in Figure 4.11 and Figure 4.12. Values equivalent to the RDME were calculated at each resonant frequency location using Equation 4.1 [63].

$$P_c = \left(\frac{n_c^2}{n^2}\right) x100 \qquad \textbf{Equation 4.1}$$

where $P_c$ is the RDME after $c$ cycles of freezing and thawing (%), $n$ is the resonant frequency at 0 cycles of freezing and thawing, and $n_c$ is the resonant frequency after $c$ cycles of freezing and thawing.

**Figure 4.10 Resonant frequency measurements**

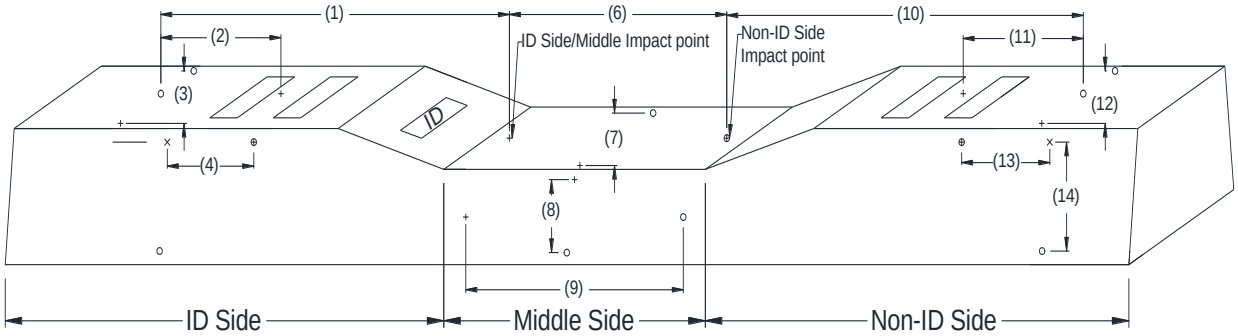


+Impact Point

○Accelerometer Point

⊕Horizontal Impact /Accelerometer Point

×Vertical Impact /Accelerometer Point

(1) ID Top/Long 2
(2) ID Top/Long 1
(3) ID Top/Short
(4) ID Side/Horizontal
(5) ID Side/Vertical
(6) Middle Top/Long
(7) Middle Top/Short
(8) Middle Side/Vertical
(9) Middle Side/Horizontal
(10) Non-ID Top/Long 2
(11) Non-ID Top/Long 1
(12) Non-ID Top/Short
(13) Non-ID Side/Horizontal
(14) Non-ID Side/Vertical

**Figure 4.11 Resonant frequency reading locations**

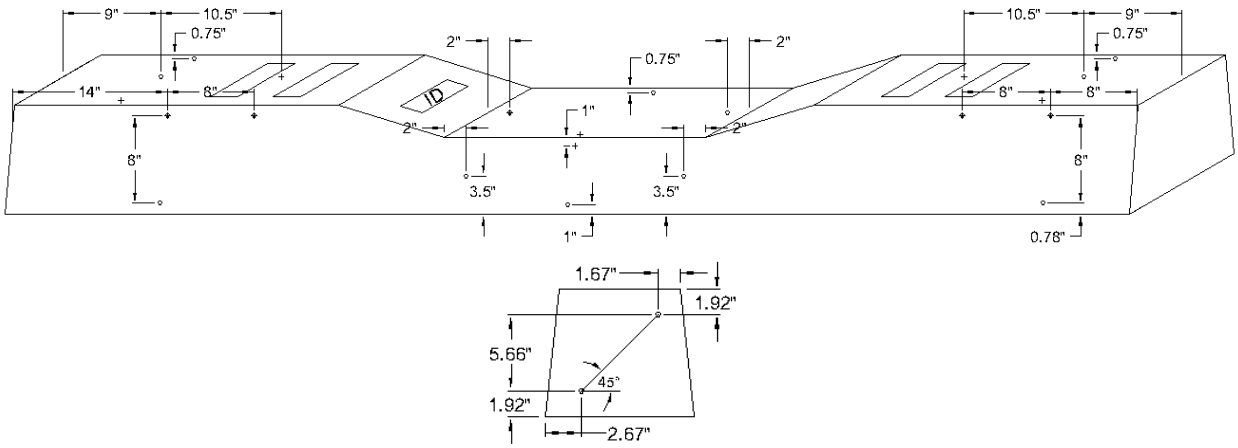


**Figure 4.12 Geometrical locations for resonant frequency readings**

Whole-tie resonant frequencies were induced with a hammer and recorded using an accelerometer in two locations on each tie, as shown in Figure 4.13. Time series data for each

pulse were extracted from the accelerometer and converted to corresponding frequency domains using an FFT algorithm, and then resonant frequencies were obtained from the frequency domain. After completing these measurements, the ties were wrapped and vacuum-sealed in the chamber.

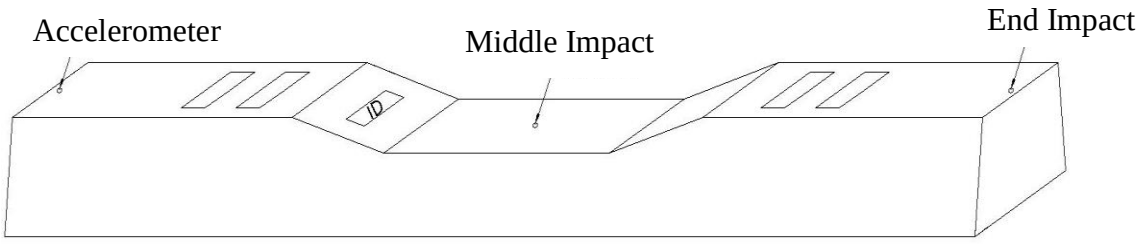


**Figure 4.13 Impact and accelerometer locations on tie top surface**

## 4.3. Results and Analysis

Seven concrete ties were subjected to 300 cycles of freezing and thawing. Concrete tie expansion, weight change, and resonant frequency measurements were taken before, during, and after freezing and thawing cycles. Table 4.3 summarizes measurements after 300 cycles of freezing and thawing and typical failure criteria. Maximum length change at 300 cycles listed below was the greatest percent change in length measured on a given tie at 300 cycles. The RDME provided was from the whole-tie resonant frequency testing.

**Table 4.3 Summary of experimental results at 300 cycles**

| Tie # | Tie ID # | Length Change at 300 Cycles (%) | Particle Loss Weight (%) | RDME (%) |
|---|---|---|---|---|
| Failure Criteria | | 0.1 | - | 60 |
| 1 | 2-042-C | 0.041% | 0.004% | 100 |
| 5 | 2-05103-2 | 0.034% | 0.009% | 100 |
| 8 | 1-05009-3 | 0.016% | 0.004% | 109 |
| 11 | 1-053-C | 0.016% | 0.007% | 97.5 |
| 12 | 2-05029-2 | 0.004% | 0.005% | 102 |

| | | | | |
|---|---|---|---|---|
| 13 | 1-4397-F | -0.040% | 0.008% | 104.5 |
| 14 | 2-4386-B | -0.004% | 0.019% | 95.5 |

### *4.3.1. Concrete Expansion*

Concrete that deteriorates during freezing and thawing cycles typically expands due to the growth of internal micro-cracking. Concrete tie length change showed similar trends regardless of location. Figure 4.14 shows fluctuations of the percentage length change for all ties; however, length change did not consistently increase beyond ±0.05% throughout the testing period. This is significantly less than the commonly used failure criteria of 0.1%. Some brass points popped off the surface of the ties, possibly due to weakening of the epoxy-concrete bond caused by freezing and thawing cycles and different coefficients of thermal expansion for the epoxy and the concrete. Length change measurements from the other gauge locations are shown in Appendix A. Observed length changes remained below the 0.1% limit specified in ASTM C666 for the entire 300 cycles. This consistency indicates that the concrete ties did not experience significant amounts of internal cracking.

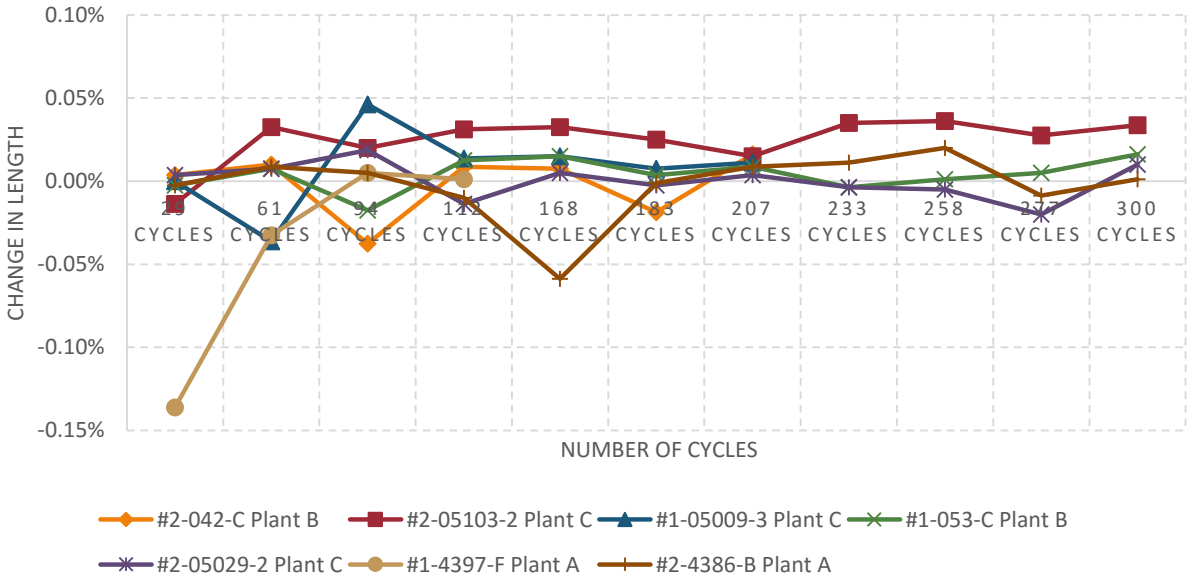


**Figure 4.14 Length change in diagonal direction at the non-ID side**

### *4.3.2. Weight Change*

Concrete weight loss from scaling, pop-outs, or crumbling is a common result of freeze-thaw damage. However, no commonly accepted limit for weight loss exists because a lack of weight loss does not necessarily equal good performance. (The concrete can develop internal micro-cracking without losing any weight). A large amount of weight loss, however, is an indicator of damage. Measurements of concrete weight throughout the testing period showed that concrete ties did not lose a significant amount of weight from freeze-thaw testing, as shown in Figure 4.15. Small fluctuations in weight values could be attributed to slight changes in water content on the surface of the specimens.

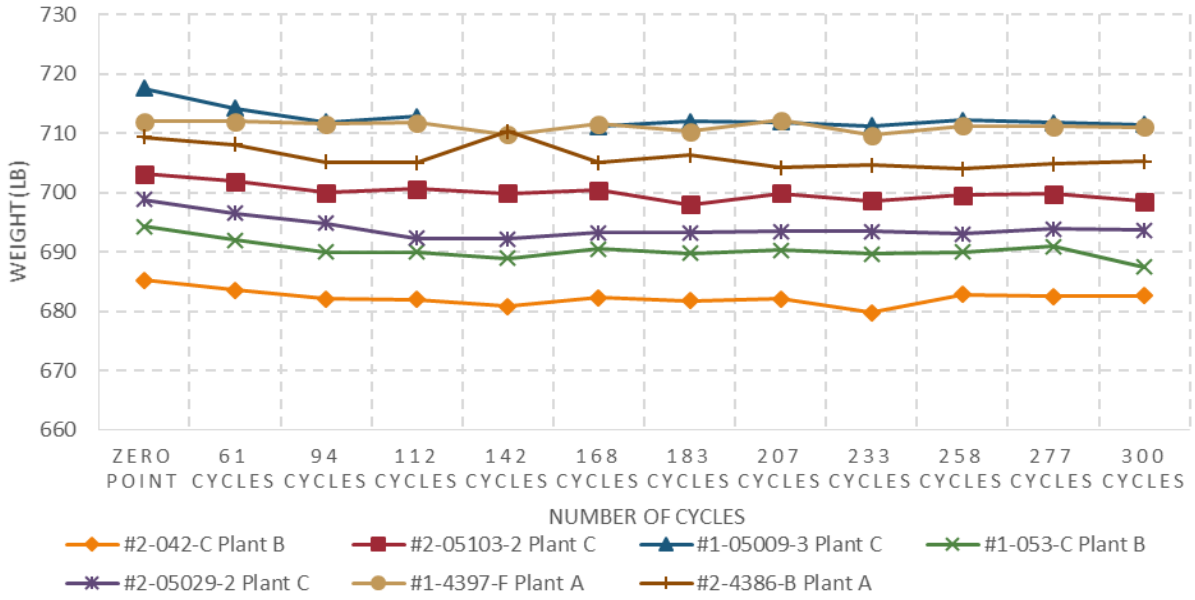


**Figure 4.15 Concrete tie weight**

Measurements of weights of scaled-off particles showed a small amount of weight loss, although less than 0.1%. Most weight loss was caused by surface pop-outs or slight scaling. Figure 4.16 shows that the cumulative weight of scaled-off particles did not exceed 25 gm for most ties, even after 300 cycles of freezing and thawing. Tie #2-4386-B experienced mass loss from a

piece of concrete that came off one of its bottom corners (approximately 1.4 oz (40 gm)) after 168 cycles of freezing and thawing. Tie #1-4397-F developed cracking between cycles 258 and 277, developing into a section loss of 0.3 oz (9 gm). This small weight loss was considered minor. Surface problems were expected to cause problems only if the entire region at the rail seat deteriorated, which was not seen in testing.

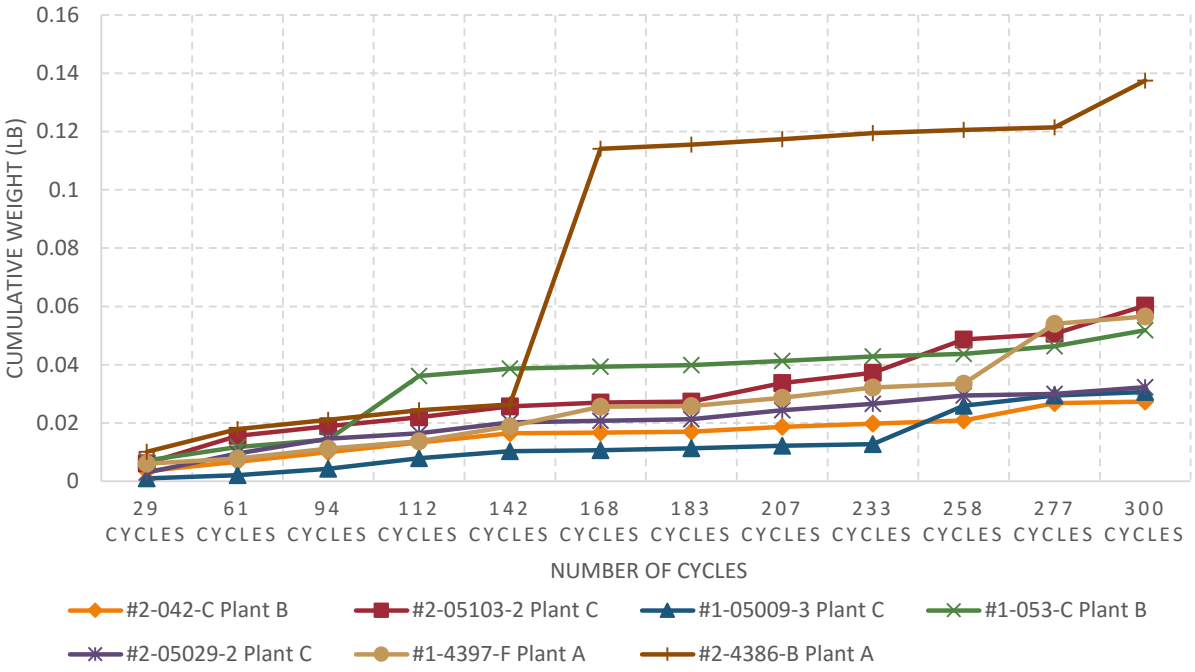


**Figure 4.16 Concrete ties cumulative mass loss**

### *4.3.3. Resonant Frequency Results*

Figure 4.17 shows results for Tie #1-05009-3 along the top longitudinal direction where the RDME stayed constant until cycle number 142. At cycle 207, the tie exhibited a large increase in RDME, followed by a large decrease in RDME at cycle 277. This sudden increase or decrease in RDME values may be attributed to the fact that, unlike small specimens, whole ties are not supported along their entire length during testing. They are instead simply supported. As a result,

changes in the locations of simple supports may affect resonant frequency readings based on changes in wave energy dissipation. Therefore, results for RDME values at each local resonant frequency location were deemed inconsistent and inconclusive. Because local RDME measurements did not provide consistent results, acquisition of resonant frequency measurements over the length of the tie was recommended for future testing to ensure that the induced wave passes through the supports regardless of their locations, guaranteeing more consistent results. If local resonant frequency measurements are desired, tie support jigs can be used to ensure consistent support locations.

Whole-tie resonant frequency testing was not originally planned but was implemented after the observation of inconsistencies in RDME results. Whole-tie resonant frequency was measured at cycles 258, 277, and 300 in order to detect the presence of concrete deterioration and unseen internal micro-cracking in the ties. In general, resonant frequency measurements are based on physics similar to other nondestructive tests such as pulse velocity, and resonant frequency is a measure of wave speed in the concrete, similar to the pulse velocity test. They are based on the principle that internal damage and micro-cracking in the concrete slow down waves transmitted through the concrete, consequently decreasing the pulse velocity and resonant frequency. An increase in resonant frequency is indicative of an increased concrete modulus from continued cement hydration and concrete strengthening during the testing period. Resonant frequency is commonly used on small prismatic concrete specimens, whereas pulse velocity is commonly used on large structural members with highly irregular geometries (i.e., not simply supported, not connected to other structural members). Steel in the prestressed concrete tie should not prevent the resonant frequency test from detecting internal damage because the pulse velocity through the steel

does not change from freezing and thawing. Any differences in resonant frequency would be from a change (likely from cracking) in the speed of the waves through the concrete.

Whole-tie resonant frequency measurements gave consistent impact pulse measurements. Figure 4.18 shows time series data obtained from the accelerometer for one of the ties at the 258$^{th}$ cycle. The first impact pulse is the end pulse and the second impact pulse represents a pulse delivered in the middle of the tie. The frequency domain of the two pulses for one tie is shown in Figure 4.19. A small peak in all frequency domains is shown at the beginning of each graph, but that peak was not counted as the first peak since such a peak is produced inherently from environmental vibrations measured by the accelerometer without applying any pulse. The two pulses produced peaks at almost the same frequency. Figure 4.20 through Figure 4.22 show the end pulse frequency domain at the 258$^{th}$ cycle for Plant A, Plant B, and Plant C ties plotted against the end pulse frequency for their corresponding control ties. Similar graphs for the 277$^{th}$ and 300$^{th}$ cycles are shown in the Appendix. The range for the first resonant frequency of all ties was 105 - 120 Hz, indicating that the ties had similar internal states. Table 4.4 shows initial resonant frequency for ties at the 258$^{th}$, 277$^{th}$, and 300$^{th}$ cycles. Because this test was not conducted at the 0 cycle, the control for this case was taken to be the companion ties not subjected to freeze-thaw damage. Observed differences in whole-tie resonant frequency testing was within expected experimental error. The nearly-constant whole-tie resonant frequency values indicated that the ties did not incur any internal structural damage during freezing and thawing cycles.

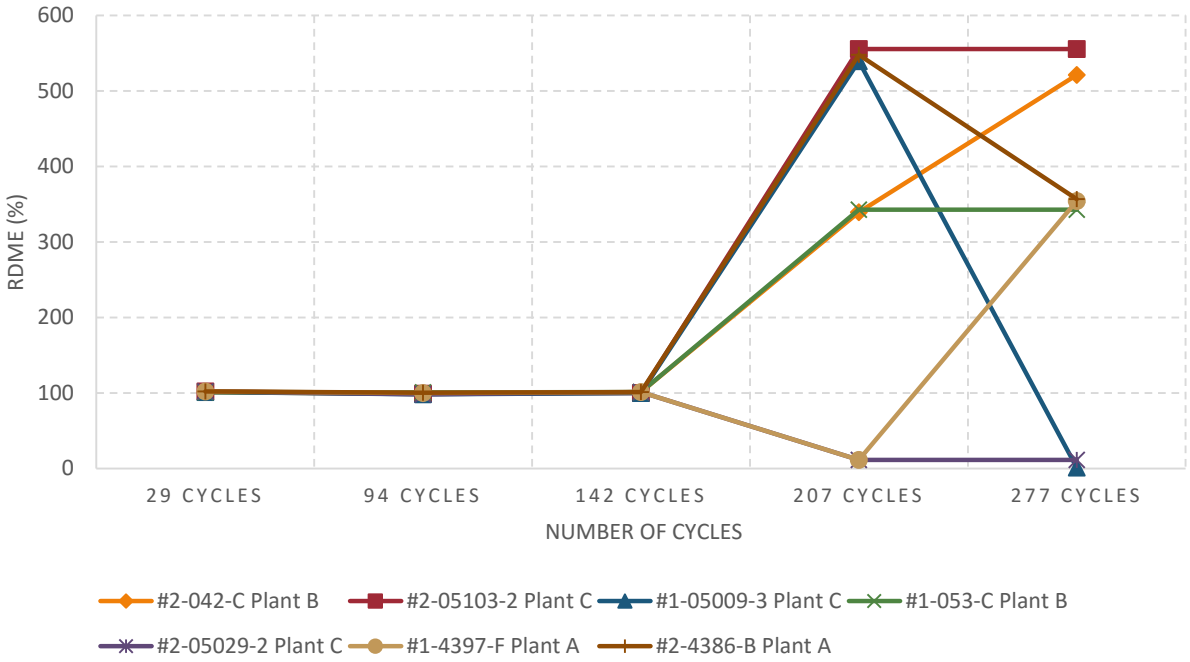


**Figure 4.17 RDME values at the ID side for the long top longitudinal direction of the tie**

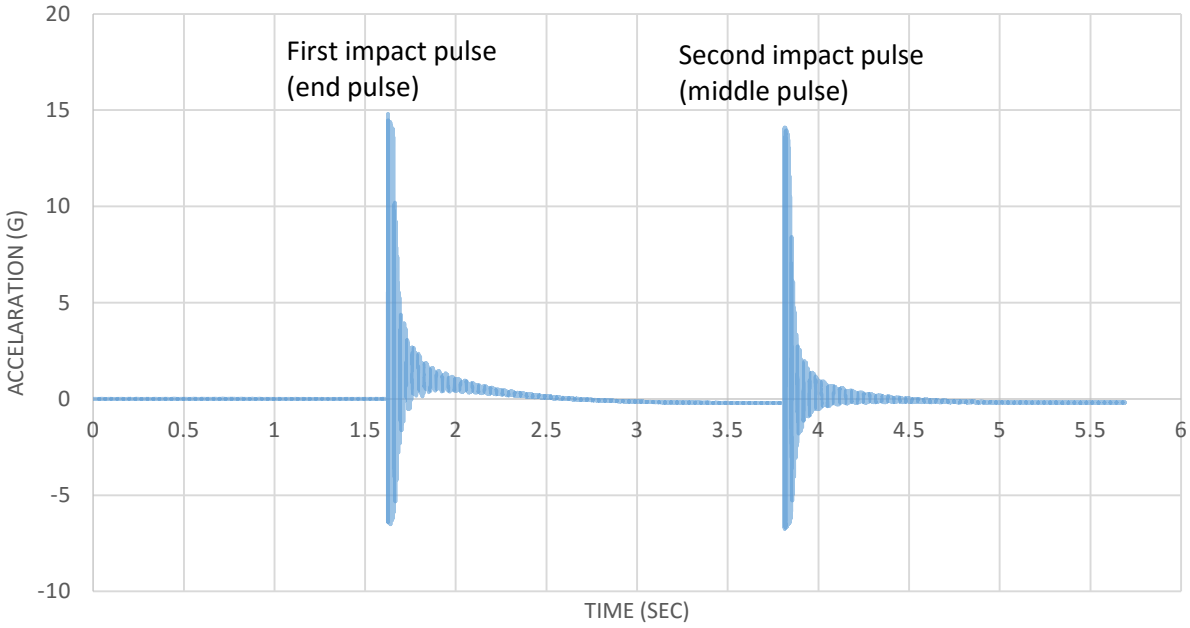


**Figure 4.18 Pulse vibration for Tie #2-05103-2 Plant C at the 258$^{th}$ cycle**

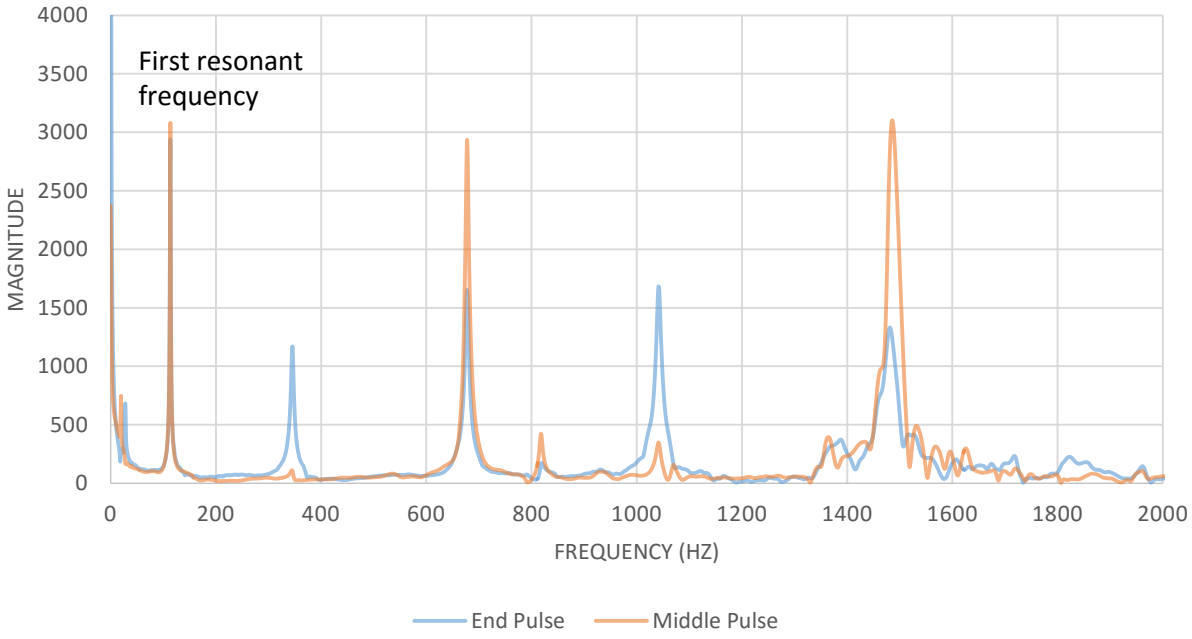


**Figure 4.19 Frequency domain for Tie #2-05103-2 Plant C at the 258th cycle**

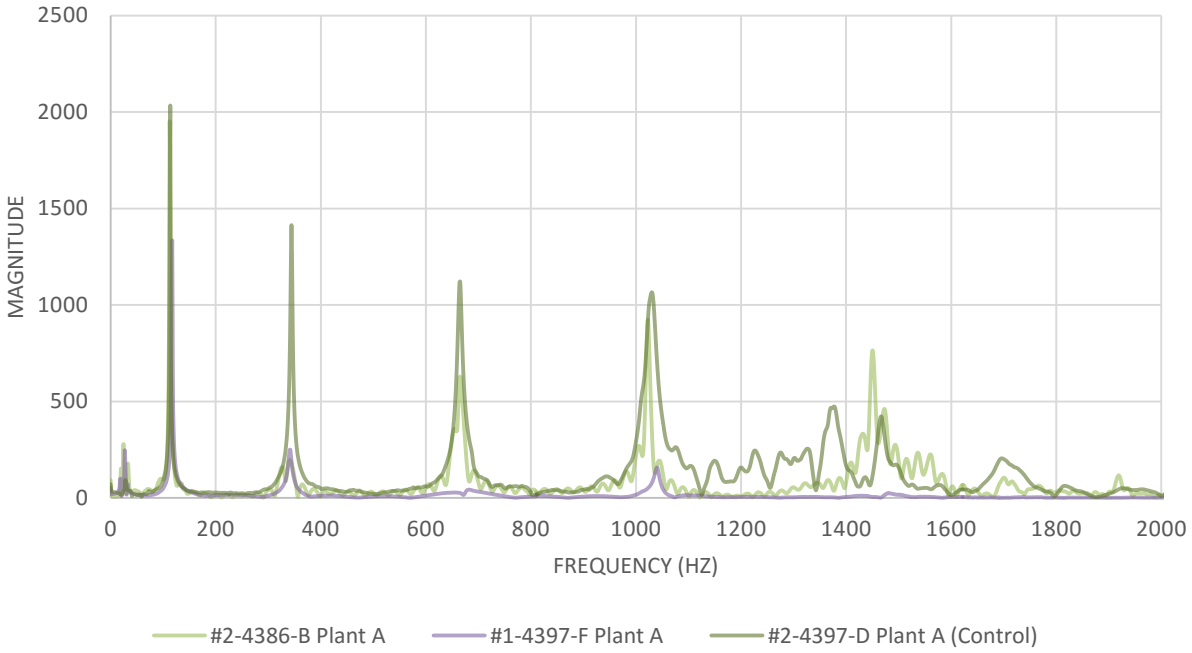


**Figure 4.20 End impact frequency domain for Plant A ties at the 258th cycle**

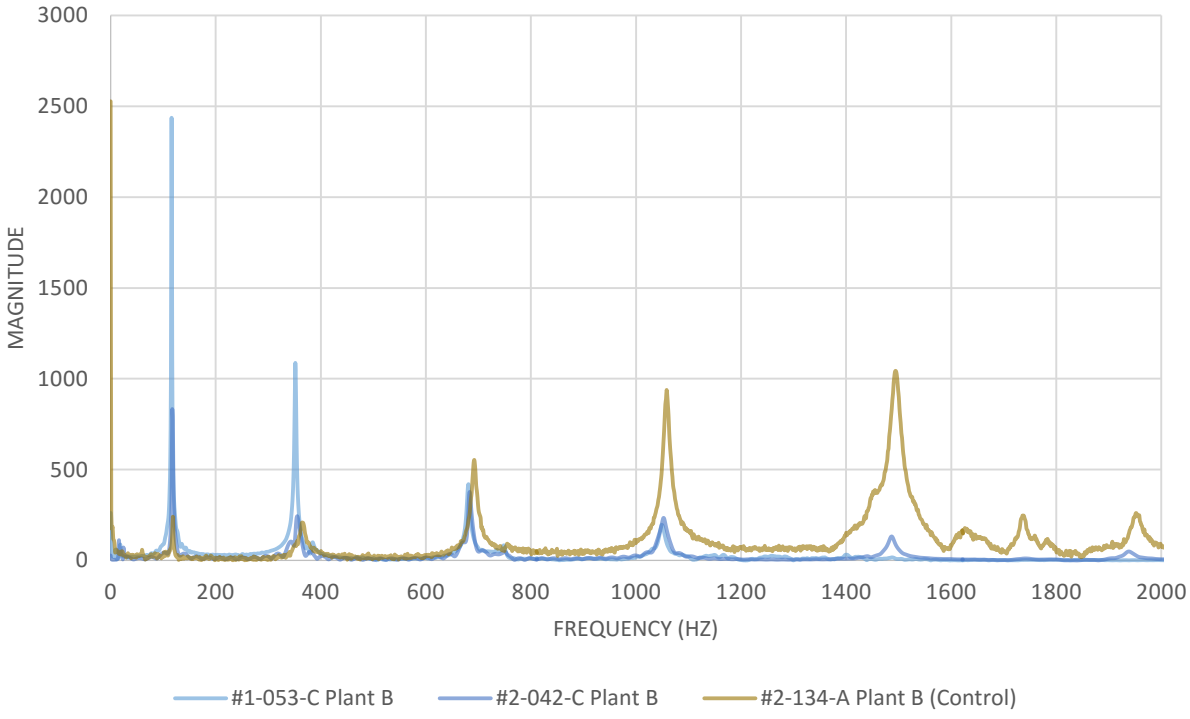


**Figure 4.21 End impact frequency domain for Plant B ties at the 258th cycle**

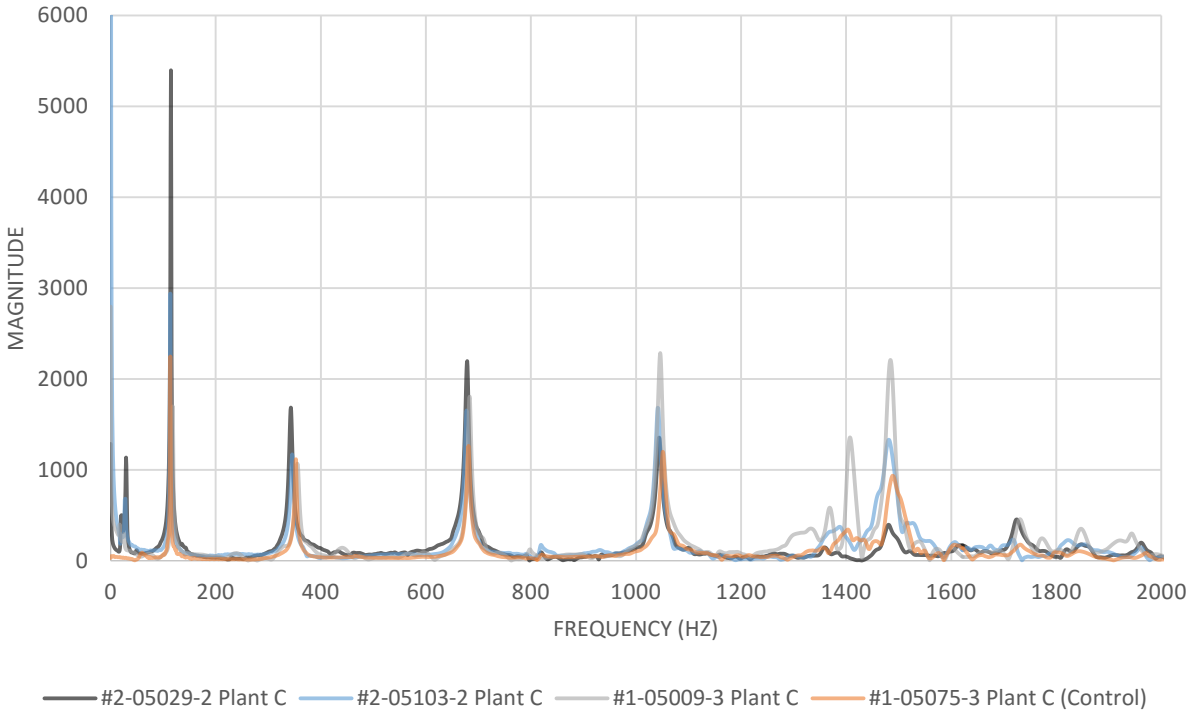


**Figure 4.22 Impact frequency domain for Plant C ties at the 258th cycle**

**Table 4.4 Resonant frequencies for all ties**

| Type | Tie | First Resonant Frequency (Hz) | | |
|---|---|---|---|---|
| | | 258th Cycle | 277th Cycle | 300th Cycle |
| Freeze-Thaw | #1-053-C Plant B | 116 | 117 | 117 |
| | #2-05029-2 Plant C | 114.5 | 112.5 | 114.5 |
| | #2-4386-B Plant A | 112.5 | 113.5 | 111 |
| | #1-4397-F Plant A | 117 | 117 | 116 |
| | #2-042-C Plant B | 117 | 118.5 | 118.5 |
| | #2-05103-2 Plant C | 113.5 | 113.5 | 113.5 |
| | #1-05009-3 Plant C | 118.5 | 118.5 | 118.5 |
| Companion Control Ties | #1-05075-3 Plant C | | 113.5 | |
| | #1-05035-4 Plant C | | 106 | |
| | #2-4397-D Plant A | | 113.5 | |
| | #1-F-4299 Plant A | | 113.5 | |
| | #1-092-B Plant B | | 118.5 | |
| | #1-109-C Plant B | | 118.5 | |
| | #2-134-A Plant B | | 118.5 | |

The ties suffered some surface damage represented by pop-outs and small, shallow surface cracking that occasionally resulted in pop-outs. The shallow surface damage was typically not deeper than 0.25 in. (6 mm) and did not affect strength capacity of the ties. Tie #2-4386-B, which came from Plant A, suffered pop-outs and the loss of a piece of a corner weighing approximately 1.4 oz (40 gm), as shown in Figure 4.23 and Figure 4.24.


**Figure 4.23 Tie #2-4386-B pop-outs and surface scaling**


**Figure 4.24 Tie #2-4386-B corner piece after fracture**

Tie #1-4397-F experienced a shallow crack several inches in length between cycles 258 and 277. Figure 4.25 shows this crack that was expected to result in a pop-out. A smaller pop-out on top of the same tie is shown in Figure 4.26.


**Figure 4.25 Tie #1-4397-F shallow cracking**

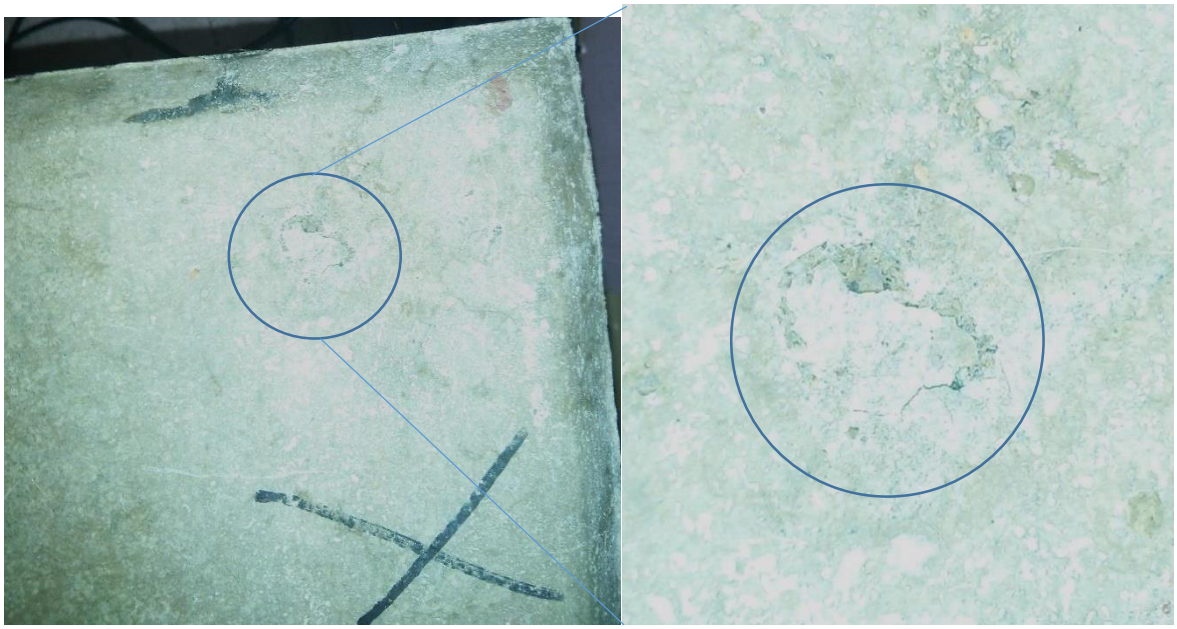

**Figure 4.26 Small pop-out/crack in Tie #1-4397-F**

## 4.4. Conclusions

Seven whole concrete railroad ties were subjected to 300 cycles of freezing and thawing in order to determine their performance against industry criteria given by ASTM C666. Test procedures were modified slightly to account for differences between small specimens and whole-tie testing. Test results showed that these concrete railroad ties did not experience significant deterioration as a result of freeze-thaw testing.

# Chapter 5 - Effects of Prestressing and Saw-Cutting on Freeze-Thaw Durability

Although saw-cutting of concrete for freeze-thaw testing remains an acceptable method according to ASTM C666, its effects are unknown on prestressed concrete samples. Limited research has been conducted on the effects of saw-cutting and stress release caused by saw-cutting in prestressed concrete members. This chapter addresses the effects of saw-cutting and the existence of reinforcement, prestressed or not, in saw-cut samples on freeze-thaw durability of concrete elements.

## 5.1. Large-Scale Samples

Six prestressed concrete railroad ties were saw-cut in half and soaked in a lime water bath at 73.4 ± 3 °F (23 ± 1.7 °C) for 7 days, as shown in Figure 5.1. The saw-cut ends of the ties were epoxied in order to eliminate absorption from that end and simulate the presence of a full tie. One of the ties was made with non-air-entrained concrete to ensure failure and to validate testing methods and criteria. Samples were tested at various stages of initial preparation. The tested half ties were 8.5 ft (2.6 m) long with a trapezoidal cross section (10 in. (254 mm) top, 11 in. (280 mm) bottom, and 10.5 in. (267 mm) height). Initial testing was performed after the samples were soaked for 2 days and 7 days and after the samples were cooled to 40 $^{o}$F following the 7-day soaking. After the soaking period, the half ties were removed from the lime water bath and wrapped with a wet burlap sheet. The wet burlap was placed around the ties to ensure that free water was present all around the half ties for the duration of the test. In addition, the samples were wrapped with plastic wrap to avoid evaporation during freezing stage. UPV measurements were conducted over the top surface of the half ties, as shown in Figure 5.2. Sensors of the UPV were placed 38 in. apart.

**Figure 5.1 Soaked half ties covered with burlap**

UPV readings were performed using an Olson Instruments NDE 360. Half ties were weighed using a 1,000-lb (454 kg) crane scale with a resolution of 0.1 lb (0.05 kg). The crane scale was attached to a 2-ton gantry crane with a 14.5-ft (4.4 m) span. During the testing period, the half ties were kept wet using a sponge.

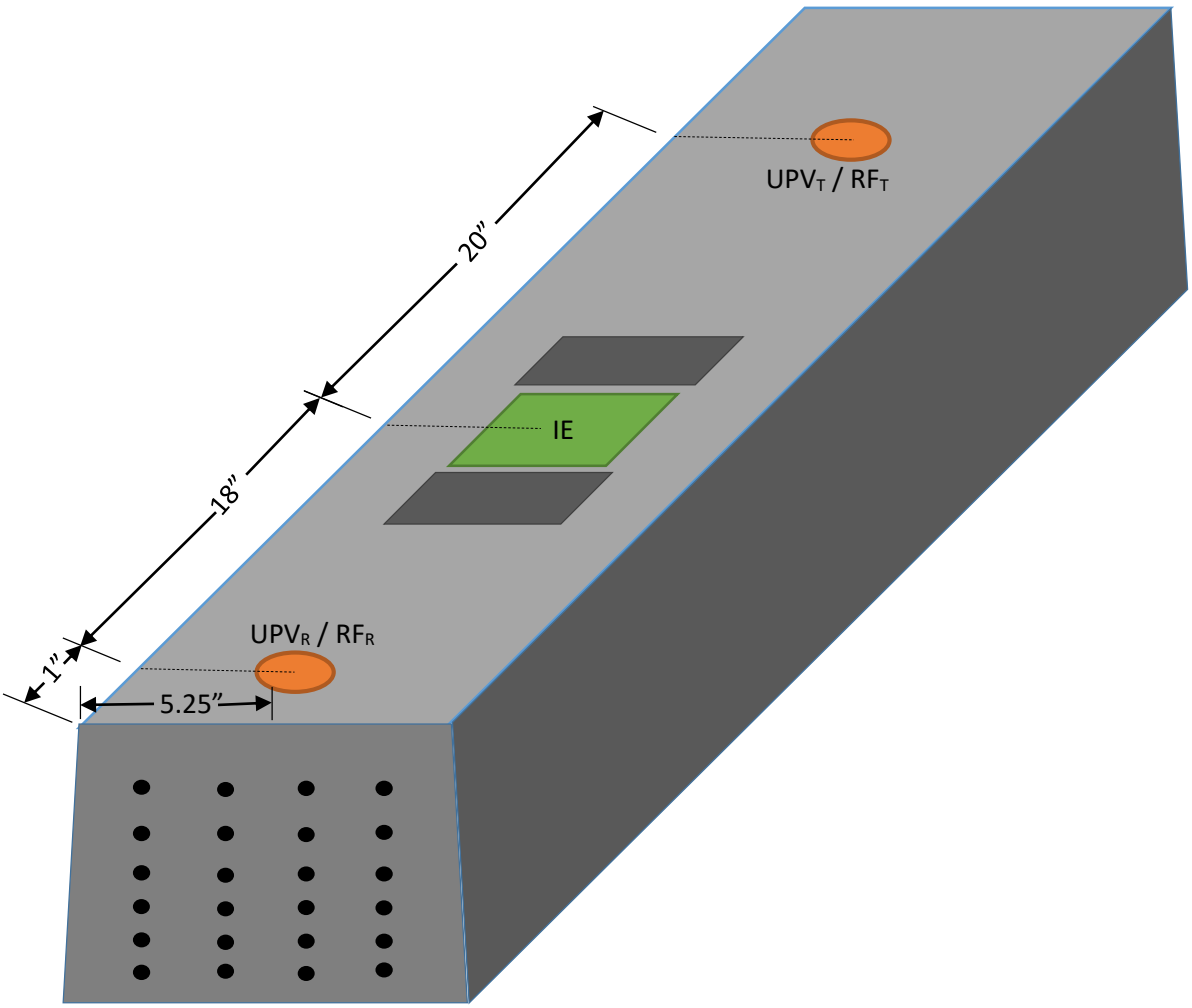


**Figure 5.2 Measurement locations on half ties (R represents the receiver and T represents the transmitter)**

After completing initial testing, the sample was subjected to 300 freeze-thaw cycles using a large freeze-thaw chamber. The chamber was designed to hold three whole ties and perform freeze-thaw cycles from 0 ± 3 °F (-18 ± 1.7 °C) to 40 ± 3 °F (4 ± 1.7 °C). The temperatures were maintained at a distance of 4.5 in. (114.3 mm) from the top surface of the ties, thereby allowing 3.13 cycles every day with cycle lengths of 460 minutes. Figure 5.3 shows typical temperatures measured by thermocouples from the center of the half tie during freeze-thaw cycles. Half ties

were tested every 36 cycles or less. Testing included the same tests performed during initial testing.

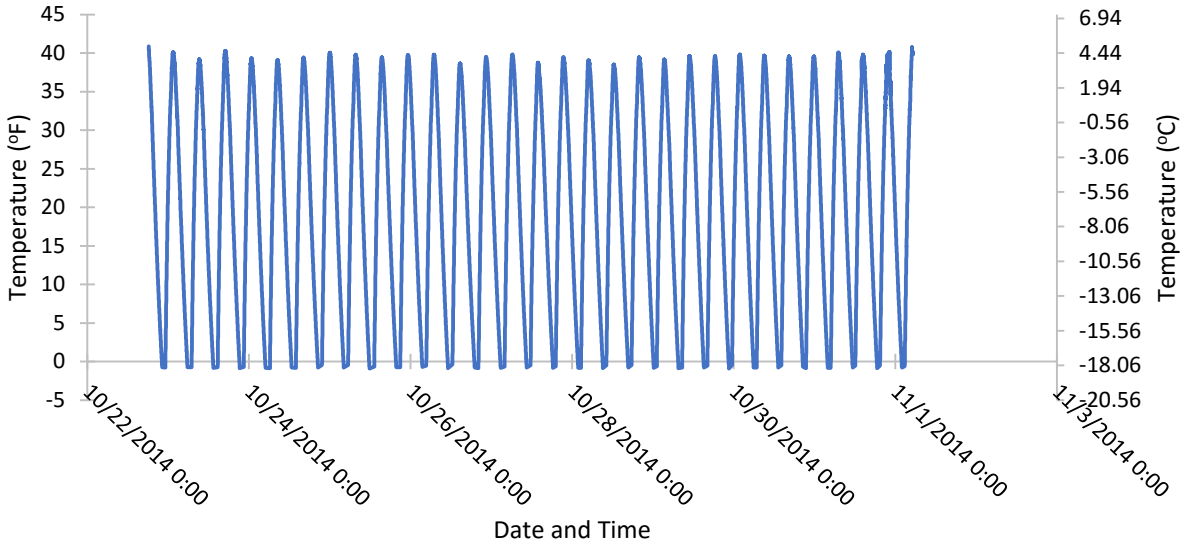


**Figure 5.3 Typical freeze-thaw cycle temperatures measured 4.5 in. (114 mm) from the concrete tie surface**

## 5.2. Saw-Cut Samples

In order to understand the effects of saw-cutting and reinforcement, prestressing or not, concrete ties were cast with prestressing wires and un-prestressed wires and without steel reinforcement. Each type of reinforcement consisted of two ties, one air-entrained and one non-air-entrained, resulting in a total of six ties. In addition to these ties, four additional air-entrained prestressed concrete ties were obtained from prestressed concrete manufacturing facilities. Three samples were excised from each tie and tested in freeze-thaw conditions. The other halves of the prestressed ties were used in the freeze-thaw testing described in the previous section. Three samples were exerted from the end of each tie, as shown in Figure 5.4. The samples had dimensions of 3 x 4 x 11 in. (76.2 x 101.6 x 279.4 mm), as shown in Figure 5.5. End pins were then installed

on the saw-cut samples in order to measure change in length resulting from freeze-thaw testing. Finally, the samples were soaked in lime water for 2 days at 40 ± 3 °F (4 ± 1.7 °C) in order to satisfy ASTM C666.

**Figure 5.4 Saw-cutting samples from the tie end**

Initial testing was performed on the samples after they reached 40 ± 3 °F (4 ± 1.7 °C). Initial testing included change in weight, change in length, and transverse RF. In order to satisfy requirements of ASTM C666 Method A, the samples were tested at least every 36 freeze-thaw cycles. Two chambers were used in this testing: the same chamber used to test the half ties and a smaller chamber. Temperature was controlled using a dummy cast sample with a thermocouple 1.5 in. (38.1 mm) from the top surface of the sample. The samples were tested according to ASTM C666 with at least 5 cycles per day. A typical saw-cut sample is presented in Figure 5.6.

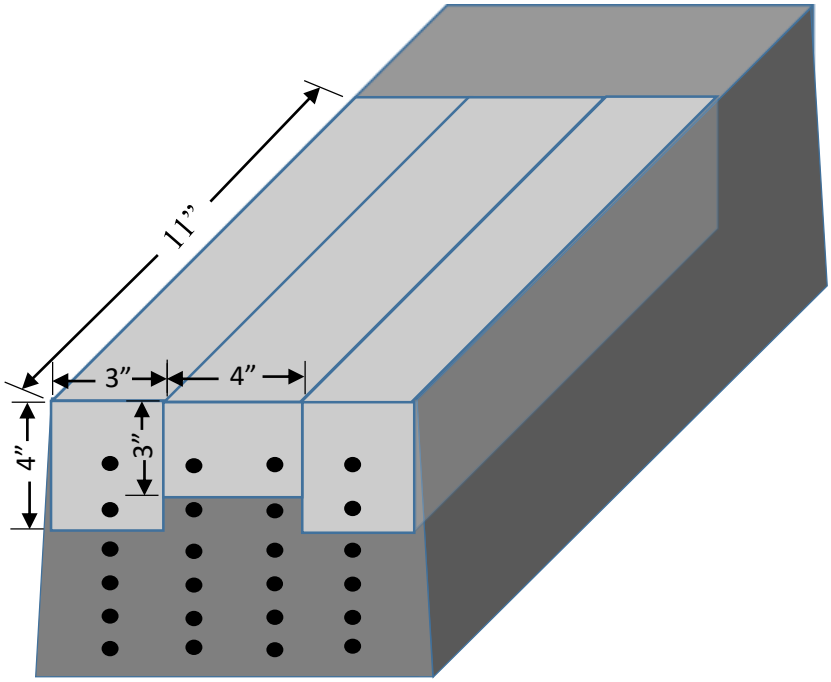


**Figure 5.5 Three saw-cut samples from the tie end**

**Figure 5.6 Typical 4 x 3 x 11 in. saw-cut freeze-thaw sample**

For the excised samples, results of the three samples were averaged for each tie. The half ties were given the designation HT#, followed by the tie number. The excised set of samples were given the designation SHT#, where HT# corresponds to the other half of the same tie used in the half tie testing. Excised samples were given an individual ID in addition to the set ID, including material properties and sample number. Some samples were assigned the letter W instead of a

number in order to represent samples with embedded vibrating wire gauge sensors. Samples without half ties tested in freeze-thaw conditions were given additional designation that represented the material and structural properties of the tie.

## 5.3. Cast Samples

In addition to the half ties and saw-cut samples, four cast samples were made from the same concrete used to make the ties. Two of the samples were made with air-entrained concrete and two without air entrainment. The samples had embedded pins in order to measure change in length. The cast samples were larger than the saw-cut samples, with dimensions of 3 x 4 x 16 in. (76.2 x 101.6 x 406.4 mm), but they still satisfied ASTM C666 requirements. All testing was done in accordance with ASTM C666 similarly to the saw-cut samples. Initial preparation and testing of these samples was done after the samples cured for 14 days. In addition, the samples were tested in the small chamber used to test some of the saw-cut samples.

Table 5.1 represents all samples used in this part of the study and testing done on each sample. The half ties were given the designation HT#, followed by the tie number, and the excised set of samples were given the designation SHT#, where HT# corresponded to the other half of the same tie used in the half tie testing. Samples without half ties tested in freeze-thaw conditions were given other designation that represented material and structural properties of the tie.

**Table 5.1 Resonant frequencies for all ties**

| Set | Sample | Air Entrained | Type | | | | | Tests Performed | | | |
|---|---|---|---|---|---|---|---|---|---|---|---|
| | | | Half Tie | Saw-cut | | | Cast | Weight | Length Change | Fundamental Frequency | Ultrasonic Pulse Velocity |
| | | | | Prestressed | Not Prestressed | No Wire | | | | | |
| **HT1** | | ● | ● | | | | | ● | | | ● |
| **HT2** | | ● | ● | | | | | ● | | | ● |
| **HT3** | | ● | ● | | | | | ● | | | ● |
| **HT4** | | ● | ● | | | | | ● | | | ● |
| **HT5** | | ● | ● | | | | | ● | | | ● |
| **HT6** | | | ● | | | | | ● | | | ● |
| **SHT1** | 06-M1 | ● | | ● | | | | ● | ● | ● | |
| | 06-M2 | ● | | ● | | | | ● | ● | ● | |
| | 06-B | ● | | ● | | | | ● | ● | ● | |
| **SHT2** | F-M1 | ● | | ● | | | | ● | ● | ● | |
| | F-M2 | ● | | ● | | | | ● | ● | ● | |
| | F-B | ● | | ● | | | | ● | ● | ● | |
| **SHT3** | 1-M1 | ● | | ● | | | | ● | ● | ● | |
| | 1-M2 | ● | | ● | | | | ● | ● | ● | |
| | 1-B | ● | | ● | | | | ● | ● | ● | |
| **SHT4** | 09-M1 | ● | | ● | | | | ● | ● | ● | |
| | 09-M2 | ● | | ● | | | | ● | ● | ● | |
| | 09-B | ● | | ● | | | | ● | ● | ● | |
| **SHT5** | PA-1 | ● | | ● | | | | ● | ● | ● | |

| | | | | | | | | | | | |
|---|---|---|---|---|---|---|---|---|---|---|---|
| | PA-2 | ● | | ● | | | | ● | ● | ● | |
| | PA-W | ● | | ● | | | | ● | ● | ● | |
| **SHT6** | PNA-1 | | | ● | | | | ● | ● | ● | |
| | PNA-2 | | | ● | | | | ● | ● | ● | |
| | PNA-W | | | ● | | | | ● | ● | ● | |
| **NPA** | NPA-1 | ● | | | ● | | | ● | ● | ● | |
| | NPA-2 | ● | | | ● | | | ● | ● | ● | |
| | NPA-W | ● | | | ● | | | ● | ● | ● | |
| **NPNA** | NPNA-1 | | | | ● | | | ● | ● | ● | |
| | NPNA-2 | | | | ● | | | ● | ● | ● | |
| | NPNA-W | | | | ● | | | ● | ● | ● | |
| **NWA** | NWA-1 | ● | | | | ● | | ● | ● | ● | |
| | NWA-2 | ● | | | | ● | | ● | ● | ● | |
| | NWA-W | ● | | | | ● | | ● | ● | ● | |
| **NWNA** | NWNA-1 | | | | | ● | | ● | ● | ● | |
| | NWNA-2 | | | | | ● | | ● | ● | ● | |
| | NWNA-W | | | | | ● | | ● | ● | ● | |
| **Cast Prism** | C1-A | ● | | | | | ● | ● | ● | ● | |
| | C4-A | ● | | | | | ● | ● | ● | ● | |
| **Cast Prism/No Air** | C1-NA | | | | | | ● | ● | ● | ● | |
| | C4-NA | | | | | | ● | ● | ● | ● | |

## 5.4. Failure Criteria

ASTM C666 failure criteria were followed in order to determine the failure for saw-cut and cast samples. The samples were declared to be failures once the RDME dropped to 60% or less or sample length changed more than 0.1%. For the half tie, failure criterion was established as a drop in RDME beyond 60% or when sample testing was not possible due to excessive surface damage. RDME for the half tie was calculated based on UPV. Equation 5.1 was followed while calculating the RDME for the half tie ($R_{UPV}$).

$$R_{UPV} = \left(\frac{UPV_f}{UPV_o}\right)^2 x\ 100 \qquad \textbf{Equation 5.1}$$

where $UPV_f$ is the UPV at failure or at 300 cycles, whichever comes first, and $UPV_o$ is the initial UPV at 40 $^oF$ and after soaking in lime water for 7 days.

## 5.5. Results and Analysis

Initial fresh air content when available and hardened air void analysis are shown in Table 5.2.

**Table 5.2 Fresh and hardened air content of all tested samples**

| Sample | Fresh Air Content (%) | Hardened Air Content (%) | Spacing Factor (in) |
|---|---|---|---|
| HT1 | - | 3.6 | 0.0117 |
| 1-M1 | | | |
| 1-M2 | | | |
| 1-B | | | |
| HT2 | - | 2.5 | 0.0131 |
| F-M1 | | | |
| F-M2 | | | |
| F-B | | | |
| HT3 | 8.5 | 4 | 0.0098 |
| 09-M1 | | | |
| 09-M2 | | | |
| 09-B | | | |
| HT4 | - | 4 | 0.0133 |
| 06-M1 | | | |
| 06-M2 | | | |
| 06-B | | | |
| HT5 | 7 | 6.1 | 0.0049 |

| | | | |
|---|---|---|---|
| **PA-1** | | | |
| **PA-2** | | | |
| **PA-W** | | | |
| **C1-A** | | | |
| **C4-A** | | | |
| **HT6** | 0.9 | 2.3 | 0.0083 |
| **PNA-1** | | | |
| **PNA-2** | | | |
| **PNA-W** | | | |
| **C1-NA** | | | |
| **C4-NA** | | | |
| **NPA-1** | 7 | 4.9 | 0.0030 |
| **NPA-2** | | | |
| **NPA-W** | | | |
| **NPNA-1** | 0.9 | 3.5 | 0.0090 |
| **NPNA-2** | | | |
| **NPNA-W** | | | |
| **NWA-1** | 7 | 3.5 | 0.0088 |
| **NWA-2** | | | |
| **NWA-W** | | | |
| **NWNA-1** | 0.9 | 3.2 | 0.0033 |
| **NWNA-2** | | | |
| **NWNA-W** | | | |

Out of the six excised sample sets, three sets failed after 70 cycles or less, one set failed after 121 cycles, and two sets did not fail according to RDME measurements, as shown in Figure 5.7. Failure in the excised samples began as cracking between the prestressing wires parallel to wires on the surfaces of the samples, as shown in Figure 5.8. This cracking could have developed as a result of three main parameters: thermal diffusivity differences between the concrete and steel, prestress release due to saw-cutting, and higher absorption rates caused by damage from saw-cutting near the reinforcement. Because thermal diffusivity is the rate at which a material conducts thermal energy relative to storing that energy, the difference between concrete and steel thermal diffusivity rates can lead to deterioration. The difference in thermal diffusivity between the steel (11.72 $mm^2/s$) and concrete (0.76 to 1.97 $mm^2/s$) typically causes the steel to drop in temperature at much faster rates than the concrete [102], causing the concrete surrounding the steel to be subjected to more severe freeze-thaw cycles, thereby cooling at faster rates and resulting in

cracking and deterioration. As a result of deterioration and cracking, some samples lost some mass surrounding the prestressing wires, as indicated in Figure 5.9 and Figure 5.10. This mass loss was accompanied by concrete expansion as result of cracking and water freezing in the cracks. Figure 5.11 shows the sample expansion in the excised samples from the six ties. For samples SHT2 and SHT3, the tests conducted on these excised samples gave a false sense of durability, an indication that the samples from set SHT2 and SHT3 did not suffer failure. However, visual inspection revealed cracks, as shown in Figure 5.8.

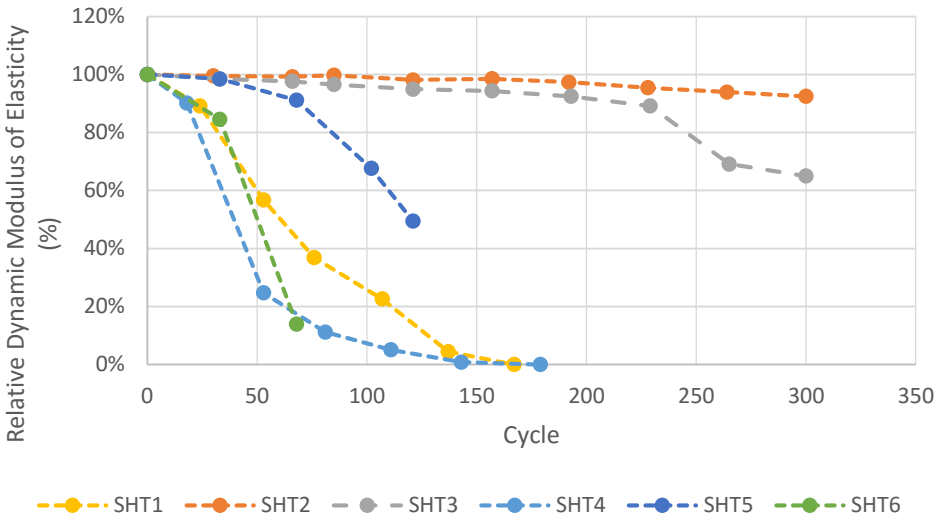


**Figure 5.7 Average RDME results of the six sets of excised samples**

**Figure 5.8 Cracking pattern in saw-cut samples in freeze-thaw testing (SHT3)**

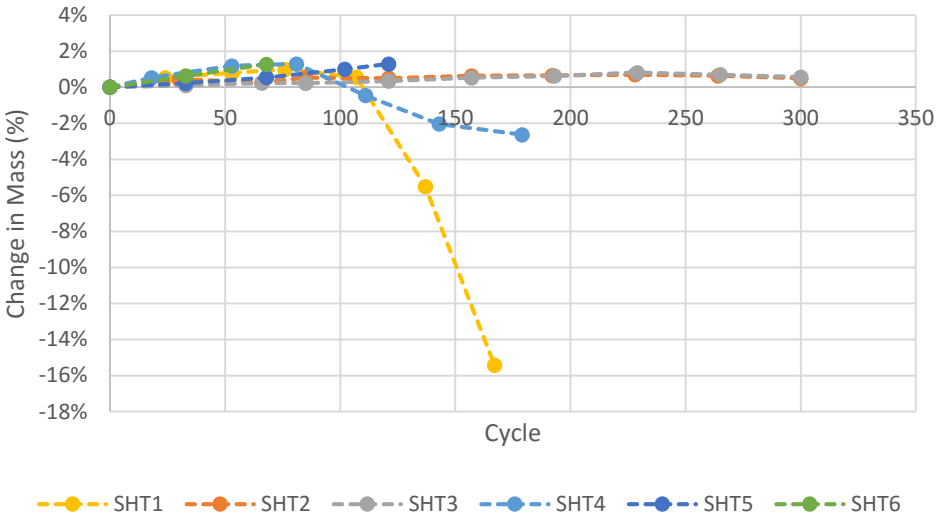


**Figure 5.9 Change in mass for the six sets of excised samples**

**Figure 5.10 Mass loss for saw-cut samples in freeze-thaw testing (SHT4)**

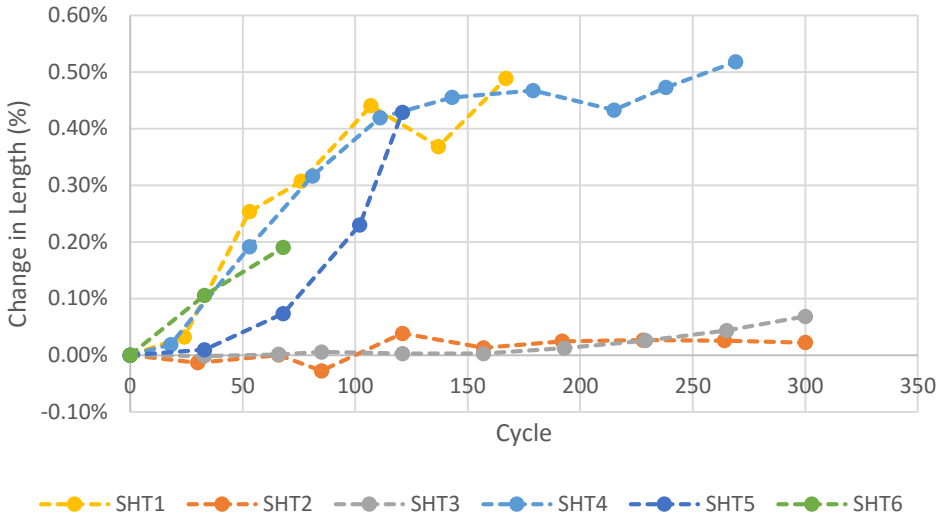


**Figure 5.11 Change in length for the six sets of excised samples**

In order to verify the effects of thermal diffusivity and saw-cutting through the wire, the set of samples excised from ties with non-prestressed wires and without wires were compared. Figure 5.12 shows the average change in mass for the various sets of samples excised from the cast-reinforced ties, but not prestressed and unreinforced ties, as compared to the companion cast prisms. The cast prisms and saw-cut samples made from the saw-cutting had a negligible effect compared to the presence of steel in the samples. This is significant when comparing air-entrained plain samples (NWA) to air-entrained non-prestressed samples (NPA) in terms of length change and RDME, as shown in Figure 5.13 and Figure 5.14, respectively.

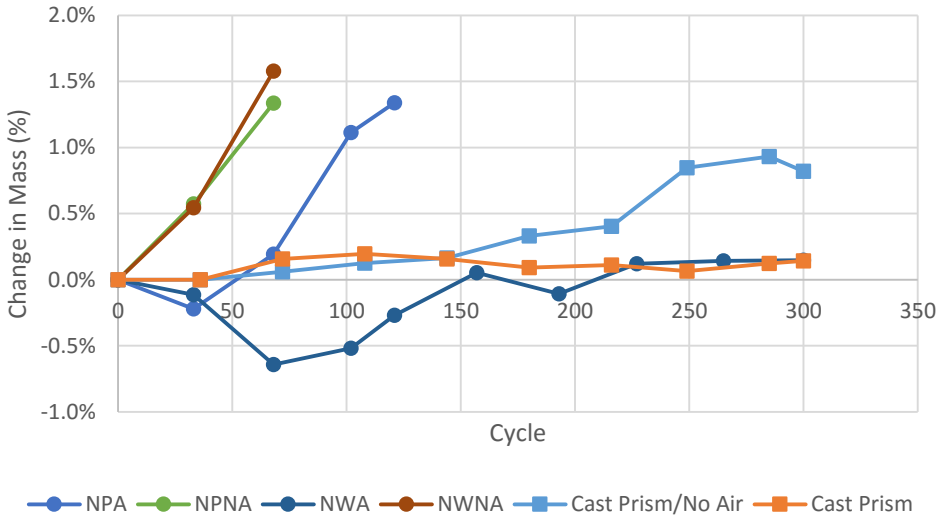


**Figure 5.12 Change in mass for the saw-cut non-prestressed, saw-cut plain, and cast prisms samples with and without air entrainment**

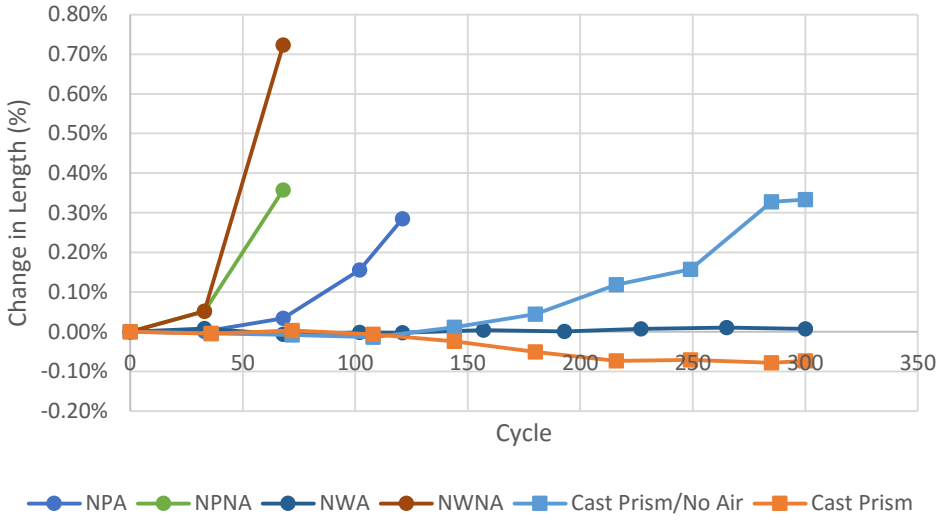


**Figure 5.13 Change in length for the saw-cut non-prestressed, saw-cut plain, and cast prisms samples with and without air entrainment**

Saw-cut plain samples (NWA) did not show deterioration over the 300 cycles of the freeze-thaw testing due to lack of additional thermal stresses in the reinforced samples. This occurred as

the micro-cracking from saw-cutting became more pronounced and relevant for the smaller samples. The non-air-entrained samples they acted as a control group for the air-entrained samples.

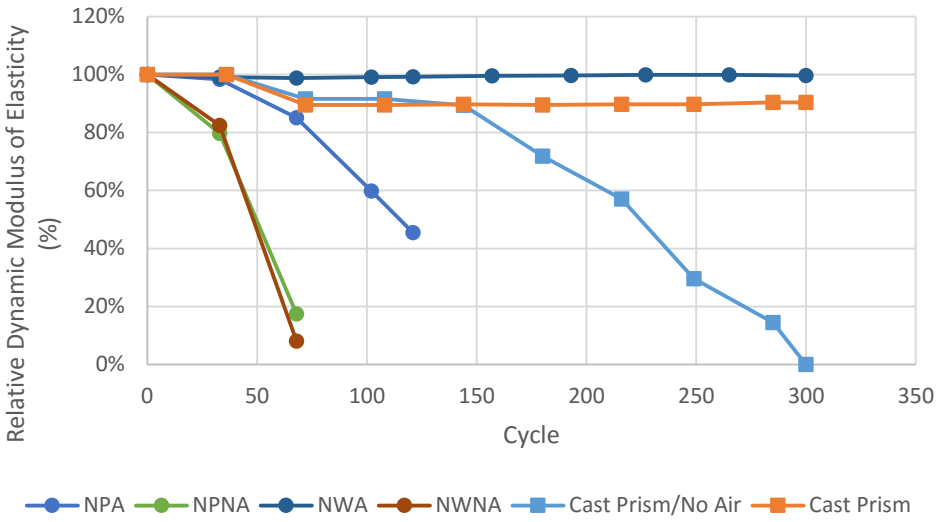


**Figure 5.14 Average RDME results for the saw-cut non-prestressed, saw-cut plain, and cast prisms samples with and without air entrainment**

Only one half tie (HT5) passed the freeze-thaw testing without significant deterioration. In addition, deterioration for half ties HT2, HT3, and HT4 was determined to be caused by cracking resulting from the saw-cutting process since propagation of the crack started from the saw-cut (epoxied) end. This deterioration due to saw-cutting is shown in Figure 5.15. Figure 5.16 shows that excised samples for freeze-thaw testing failed at a much faster rate compared to the ties from which they were excised. Meanwhile, two half ties showed excessive deterioration: the tie without air entrainment (HT6), which failed at 215 cycles, and HT1, which failed at 143 cycles. This excessive deterioration is shown in Figure 5.17. Deterioration for sample HT1 began at the tie end, not the middle of the tie saw-cut, after delivery to KSU. Deterioration of this tie was the result of a poor air void system, high degree of saturation, damage from wires during saw-cutting during

manufacturing, and faster freezing rates. A summary of all initial and final results after freeze-thaw testing are presented in Table 5.3.

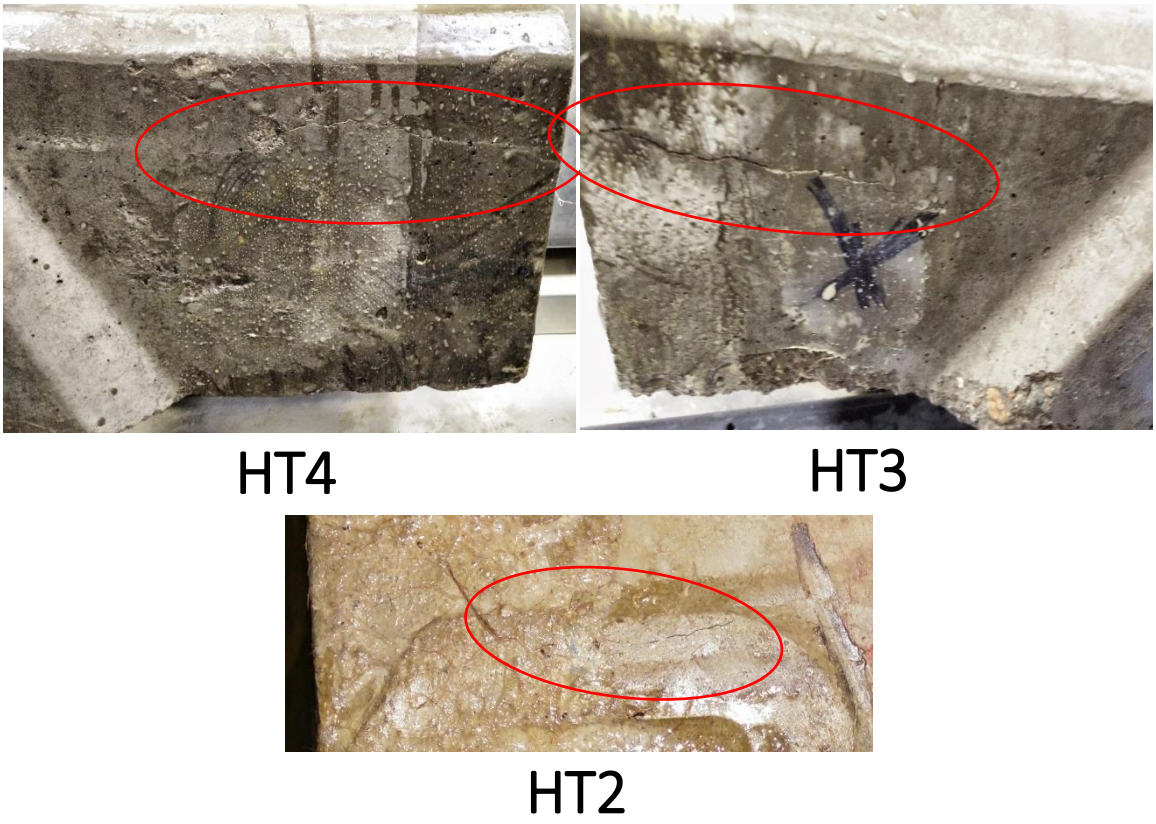


**Figure 5.15 Half ties that developed cracking from the saw-cut (epoxied) end**

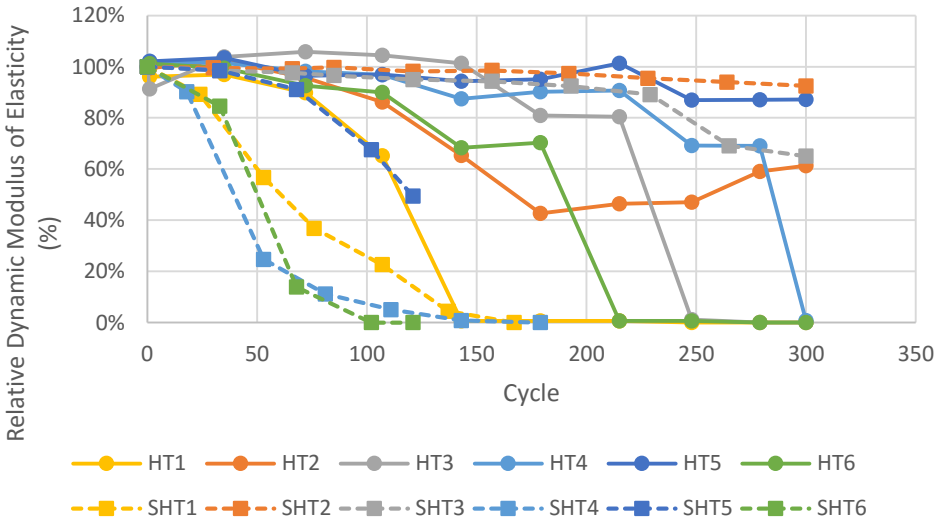

**Figure 5.16 Average RDME results for half ties as compared to excised samples from the same ties**


**Figure 5.17 Half ties with excessive deterioration (HT6 made with 0.9% fresh air content and no air-entraining agent)**

**Table 5.3 Summary of all results at failure compared to initial values**

| Sample | Failing Cycle | Initial Results | | | Results at Failure or at 300 Cycles | | | | |
|---|---|---|---|---|---|---|---|---|---|
| | | *Weight (lb)* | *Fundamental Frequency (Hz)* | *UPV (ft/s)* | *Weight (lb)* | *Length Change (%)* | *Fundamental Frequency (Hz)* | *UPV (ft/s)* | *RDME (%)* |
| **HT1** | 143 | 350.1 | - | 9974.4 | 350.2 | - | - | 817.4 | 0.7 |
| **HT2** | 179 | 351.9 | - | 9760.2 | 352.0 | - | - | 7510.3 | 42.6 |
| **HT3** | 248 | 339.2 | - | 7765.0 | 339.9 | - | - | 817.4 | 1.1 |
| **HT4** | 300 | 349.2 | - | 9213.0 | 351.7 | - | - | 817.4 | 0.8 |
| **HT5** | - | 481.3 | - | 9413.4 | 481.6 | - | - | 8788.9 | 87.2 |
| **HT6** | 215 | 500.4 | - | 9532.4 | 504.4 | - | - | 739.5 | 0.6 |
| **06-M1** | 76 | 5.0 | 4072.0 | - | 5.1 | 1.0 | 2806.0 | - | 47.5 |
| **06-M2** | 76 | 4.5 | 3638.0 | - | 4.5 | 0.2 | 1797.0 | - | 24.4 |
| **06-B** | 53 | 5.6 | 3765.0 | - | 5.7 | 0.2 | 2398.0 | - | 40.6 |
| **F-M1** | - | 5.1 | 3530.0 | - | 5.1 | 0.0 | 3520.0 | - | 99.4 |
| **F-M2** | - | 5.2 | 3477.0 | - | 5.2 | 0.0 | 3145.0 | - | 81.8 |

| | | | | | | | | | |
|---|---|---|---|---|---|---|---|---|---|
| **F-B** | - | 5.1 | 3574.0 | - | 5.1 | 0.0 | 3550.0 | - | 98.7 |
| **1-M1** | - | 3.7 | 2925.0 | - | 3.8 | 0.0 | 2878.0 | - | 96.8 |
| **1-M2** | - | 4.1 | 3008.0 | - | 4.2 | 0.0 | 2980.0 | - | 98.1 |
| **1-B** | 265 | 4.8 | 3467.0 | - | 4.9 | 0.1 | 1208.0 | - | 12.1 |
| **09-M1** | 53 | 3.3 | 2837.0 | - | 3.3 | 0.1 | 1953.0 | - | 47.4 |
| **09-M2** | 53 | 3.8 | 3066.0 | - | 3.8 | 0.1 | 1675.0 | - | 29.8 |
| **09-B** | 53 | 5.3 | 3633.0 | - | 5.4 | 0.3 | 1338.0 | - | 13.6 |
| **PA-1** | 121 | 4.3 | 3335.0 | - | 4.4 | 0.2 | 2529.0 | - | 57.5 |
| **PA-2** | 102 | 4.6 | 3438.0 | - | 4.7 | 0.5 | 2563.0 | - | 53.5 |
| **PA-W** | 102 | 5.6 | 3403.0 | - | 5.7 | 0.6 | 2642.0 | - | 60.0 |
| **PNA-1** | 68 | 4.6 | 3398.0 | - | 4.6 | 0.1 | 1787.0 | - | 27.7 |
| **PNA-2** | 68 | 5.3 | 3652.0 | - | 5.4 | 0.2 | 1367.0 | - | 14.0 |
| **PNA-W** | 68 | 5.3 | 3560.0 | - | 5.4 | 0.5 | 44.0 | - | 0.0 |
| **NPA-1** | 102 | 4.7 | 3467.0 | - | 4.8 | 0.2 | 2578.0 | - | 55.3 |
| **NPA-2** | 121 | 4.7 | 3335.0 | - | 4.8 | 0.3 | 2248.0 | - | 45.4 |
| **NPA-W** | 102 | 5.4 | 3599.0 | - | 5.4 | 0.1 | 2754.0 | - | 58.6 |
| **NPNA-1** | 68 | 5.0 | 3315.0 | - | 5.1 | 0.2 | 1016.0 | - | 9.4 |
| **NPNA-2** | 68 | 4.8 | 3301.0 | - | 4.9 | 0.5 | 1401.0 | - | 18.0 |
| **NPNA-W** | 68 | 5.7 | 3560.0 | - | 5.7 | 0.5 | 1777.0 | - | 24.9 |
| **NWA-1** | - | 4.5 | 3408.0 | - | 4.5 | 0.0 | 3394.0 | - | 99.2 |
| **NWA-2** | - | 4.5 | 3325.0 | - | 4.5 | 0.0 | 3311.0 | - | 99.2 |
| **NWA-W** | - | 5.4 | 3560.0 | - | 5.4 | 0.0 | 3569.0 | - | 100 |
| **NWNA-1** | 68 | 5.3 | 3540.0 | - | 5.4 | 0.7 | 1182.0 | - | 11.1 |
| **NWNA-2** | 68 | 4.6 | 3311.0 | - | 4.7 | 1.0 | 44.0 | - | 0.0 |
| **NWNA-W** | 68 | 5.2 | 3330.0 | - | 5.3 | 0.5 | 1201.0 | - | 13.0 |
| **C1-A** | - | 7.6 | 2008.0 | - | 7.6 | -0.1 | 1885.0 | - | 89.1 |
| **C4-A** | - | 7.7 | 2008.0 | - | 7.7 | -0.1 | 1904.0 | - | 91.6 |
| **C1-NA** | 249 | 7.6 | 1860.0 | - | 7.6 | 0.1 | 1162.0 | - | 39.1 |
| **C4-NA** | 180 | 7.6 | 2008.0 | - | 7.6 | 0.1 | 1387.0 | - | 47.7 |

## 5.6. Conclusions

The effects of relieving prestressing stresses and metal inclusion on freeze-thaw durability of excised concrete samples were measured. Results obtained from the saw-cut samples indicated that saw-cutting had a minimal effect on freeze-thaw durability of air-entrained concrete, while the presence of reinforcement in the saw-cut sections led to accelerated failure. Comparison of saw-cut reinforced concrete samples to cast sample revealed that the saw-cut samples failed at much faster rate and increased in mass and length. In addition, UPV data and mass of the sample did not suffer any drops or significant changes. Saw-cut prestressed samples showed deterioration not representative of half tie performance for the larger sample.

# Chapter 6 - Comparison of Methods Used to Measure Freeze-Thaw Durability Prestressed Concrete Ties

Durability of small concrete samples used in freeze-thaw testing is typically measured using the change in RDME calculated from the fundamental transverse frequency. Although this method is applicable to small cast or saw-cut samples that satisfy requirements of ASTM C666, its ability to capture deterioration in large-scale samples is still unproven. While in track, sole dependence on visual inspection in order to assess prestressed concrete tie conditions is not feasible. Non-destructive test (NDT) methods are needed that can be implemented in the field without disturbing the track or extracting ties for testing. In order to investigate freeze-thaw durability of these ties, a proper NDT method to measure deterioration must be selected and understood. A relationship between drop in the non-destructive evaluation (NDE) and freeze-thaw durability must be established for each method. Such a tool can help determine and assess the condition of ties in the field without excessive extraction and destructive testing. In order to determine the most adequate forensic NDT tool to investigate freeze-thaw durability of large prestressed concrete ties as a system, several methods were tested in this research. RF, UPV, and IE were used to quantify freeze-thaw deterioration in these ties.

## 6.1. Samples and Testing

Measurement of freeze-thaw durability of large-scale prestressed concrete ties was done using multiple NDT methods to determine the ability of each method in order to measure deterioration of prestressed concrete railroad ties undergoing freeze-thaw deterioration. These NDT methods included RF, UPV, IE, and mass change measurements. Figure 6.1 shows the various sizes and shapes subjected to testing.

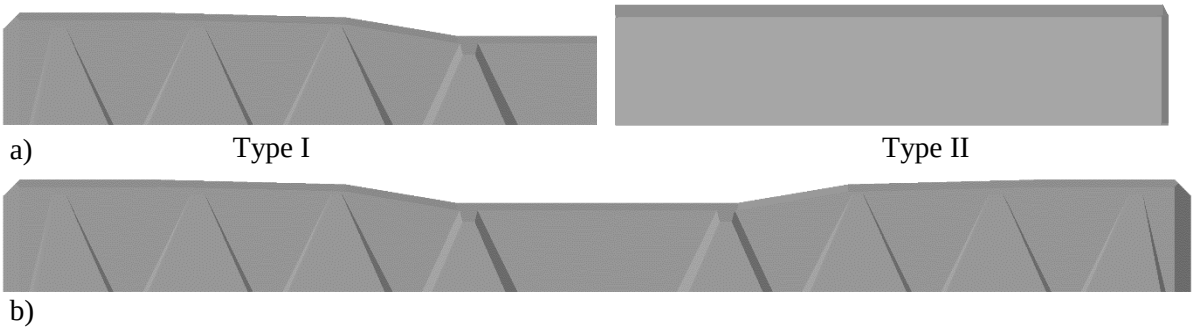


**Figure 6.1 Sizes and shapes of tested ties: a) half ties, b) full ties**

RF was performed on both types of half ties with a triaxial accelerometer that measured the impact wave 38 in. (965 mm) away. Impacting and measuring were conducted using the same mechanism implemented in the traverse fundamental frequency method. Then recorded acceleration was analyzed and the FFT algorithm was applied to the acceleration in order to obtain the frequency. Values equivalent to the RDME were calculated using Equation 6.1.

$$P_c = \left(\frac{n_c^2}{n^2}\right) x100 \qquad \textbf{Equation 6.1}$$

where $P_c$ is the RDME after $c$ cycles of freezing and thawing (%), $n$ is the RF at 0 cycles of freezing and thawing, and $n_c$ is the RF after $c$ cycles of freezing and thawing.

In addition to RF, the UPV and IE were performed on various half ties. UPV and IE readings were performed using an Olson Instruments NDE 360. UPV sensors were placed 38 in. apart on the top surface, and the IE sensor was placed on the rail seat, as shown in Figure 6.2. From the UPV measurement, the RDME was calculated by dividing the square of each cycle reading over the square of the initial reading, and change in thickness was obtained from the IE method. A list of all samples tested and types of tests performed on each sample are presented in Table 3.1. In addition, all samples were weighed regularly during testing with a 1,000-lb (454 kg) crane scale with a resolution of 0.1 lb (0.05 kg).

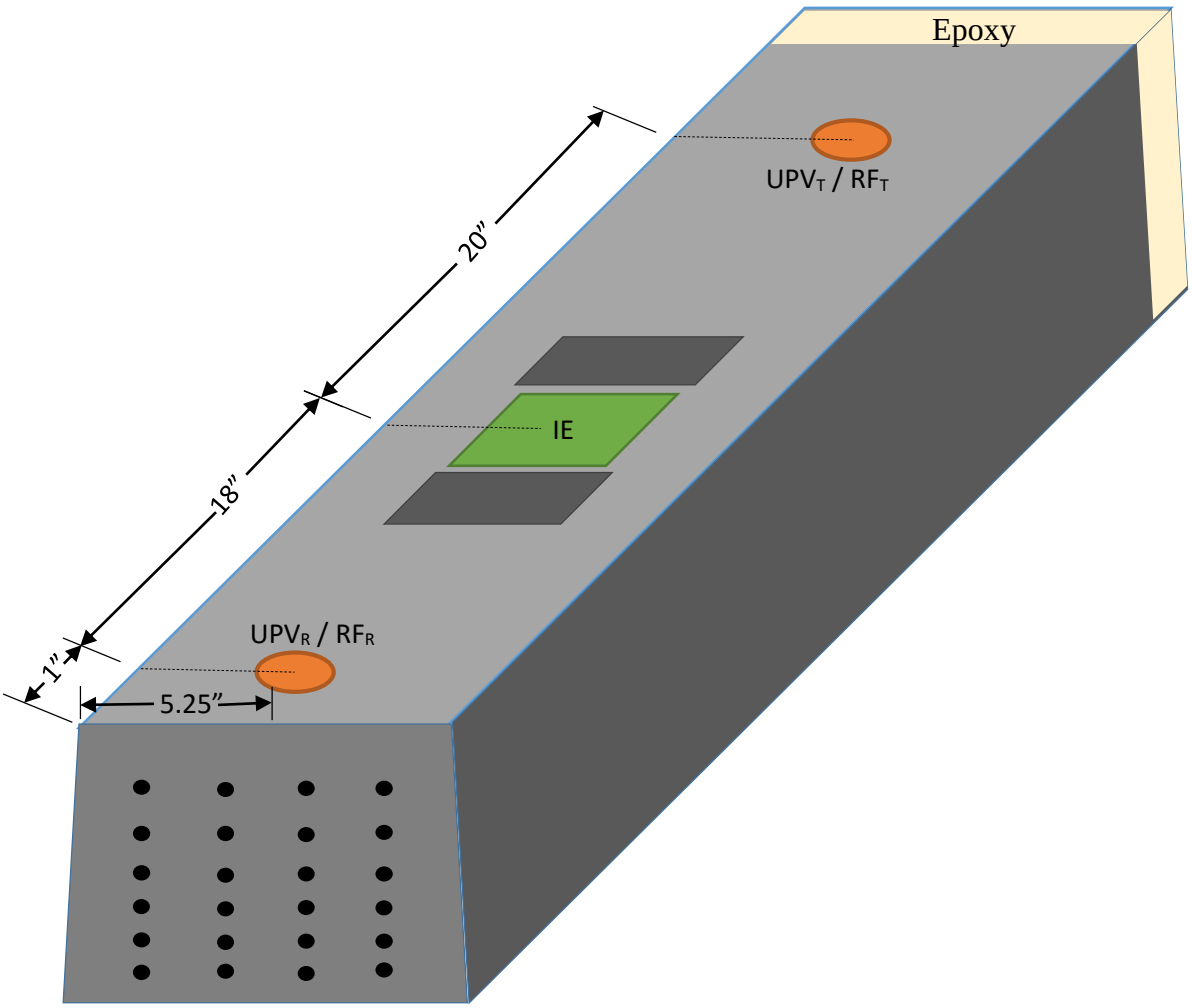


**Figure 6.2 Measurement locations on half ties (R represents the receiver and T represents the transmitter)**

**Table 6.1 Summary of all samples tested and types of tests performed**

| Sample | Type | Test | | | |
|---|---|---|---|---|---|
| | | RF | UPV | IE | Mass Chang |
| **1-053-C** | Full | | | | • |
| **2-05029-2** | Full | | | | • |
| **2-4386-B** | Full | | | | • |
| **1-4397-F** | Full | | | | • |
| **2-042-C** | Full | | | | • |
| **2-05103-2** | Full | | | | • |

| | | | | | |
|---|---|---|---|---|---|
| **1-05009-3** | Full | | | | ● |
| **HT1** | Half Type I | ● | ● | ● | ● |
| **HT2** | Half Type I | ● | ● | ● | ● |
| **HT3** | Half Type I | ● | ● | ● | ● |
| **HT4** | Half Type I | ● | ● | ● | ● |
| **HT5** | Half Type II | ● | ● | ● | ● |
| **HT6** | Half Type II | ● | ● | ● | ● |

Failure criteria for the RF and UPV were set to 60% RDME, similar to ASTM C666. IE failure criteria were set to a 40% change in thickness and any mass loss of 10% or more was considered a failure. Although these criteria were not used as a base for terminating the test, they were used to define the condition of the samples tested. Descriptions of freeze-thaw testing of the full ties and half ties were presented in Chapter 4 and Chapter 5, respectively.

## 6.2. Results and Analysis

For the half ties, UPV measurements identified deterioration in the ties, as shown in Figure 6.3. One of the ties (HT1), failed at 143 cycles, while the other ties failed at 179, 215, 248, and 300 for half ties HT2, HT6, HT3, and HT4, respectively. The drop in UPV values was consistent with the appearance of cracking in these half ties, as shown in Figure 6.4. Although some of the cracking may have been caused by the stress release resulting from the saw-cutting process, UPV measurements indicated a change in the condition of the half ties.

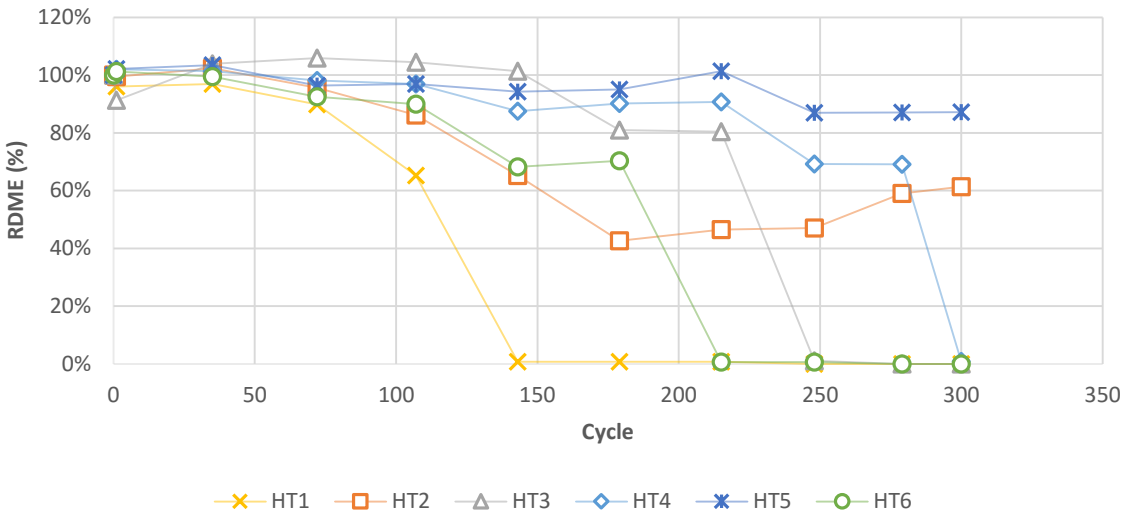


**Figure 6.3 RDMEs from UPV measurements of half ties using Olson Instruments NDE 360 UPV**

**Figure 6.4 Half tie (HT4) crack appearance at 248 cycles of freeze-thaw**

For IE measurements, thicknesses of two of the ties exceeded the 40% failure criteria set, as shown in Figure 6.5. The IE method detected failure in two ties with some variable measurements in order to simulate deterioration in the ties. Although the IE did not properly

represent freeze-thaw deterioration in all the ties, it can be used as a conjunction method to the UPV. The IE method was unable to detect failure in some of the samples because the IE method typically measures depth of the concrete section. Two main reasons can be attributed to the IE method's inability to detect failure in some of the ties. The first reason is that cracking in the ties did not propagate to reach the location measured in the tie. The second reason is that the IE was unable to detect micro-cracking in the ties. The IE device can only detect cracking between the accelerometer and the solenoid impactor, as demonstrated by HT2 in which the crack did not propagate in order to reach the testing location. In a recent study regarding detection limits of the IE method, the researcher concluded that only minimal dimension can be detected by the IE method [103]. This dimension was approximately 7 cm at a minimal detection depth of 4 to 5 cm [103]. The HT1 sample showed a significant decrease in detected thickness as a result of large splitting cracks observed in the sample. The only outlier for the IE method was the drop in thickness of HT5 from 10.4 in. to 6.45 in.

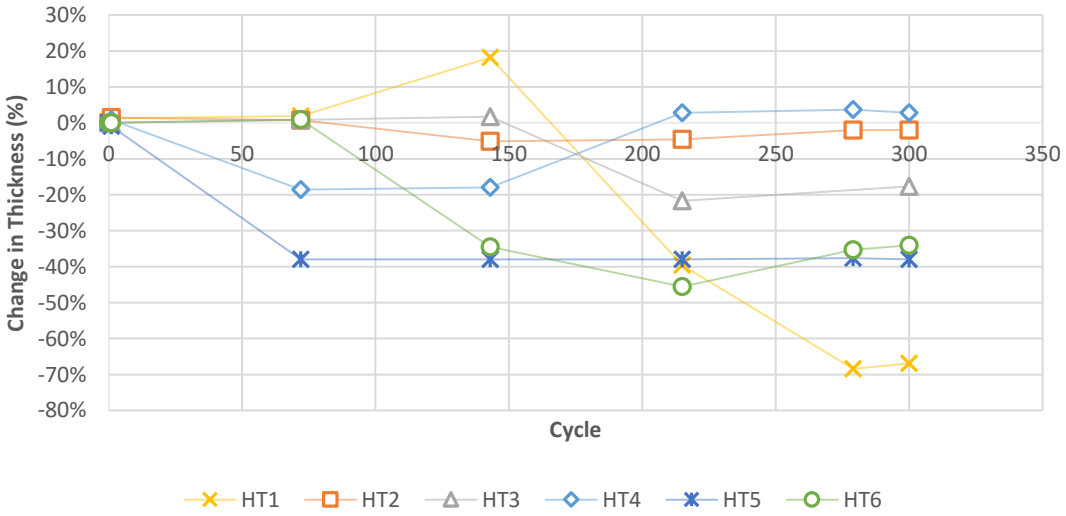


**Figure 6.5 IE measurements of half ties using Olson Instruments NDE 360 IE**

The RF method typically measures wave frequencies that lead to the highest amplitude after performing the FFT algorithm in order to convert acceleration to frequency. The primary difference between the two methods is the accelerometer used. In this study, the accelerometer used in RF measurements demonstrated high accuracy in the low frequencies (0.8 to 10,000 Hz). Regardless of this modification, the test was unable to detect deterioration in the ties, possibly due to the presence of prestressing wires and force. Half tie HT6 was the only sample that showed deterioration but no failure, as shown in Figure 6.6. Table 6.2 summarizes initial deterioration in each test compared to initial deterioration detected by visual inspection and deterioration location. At the onset of cracking, the RDME from UPV readings tended to drop below 70% in most of the samples. This can be used as a guideline when inspecting ties in the field. The main requirement for the railroad inspector is to have initial UPV readings before installation in track. Although this research did not cover factors that affect UPV readings, such as saturation and temperature, the tested ties were soaked for 7 days before freeze-thaw testing commenced to ensure saturation. Testing of UPV, IE, and RF were conducted at 40 $^{o}$F.

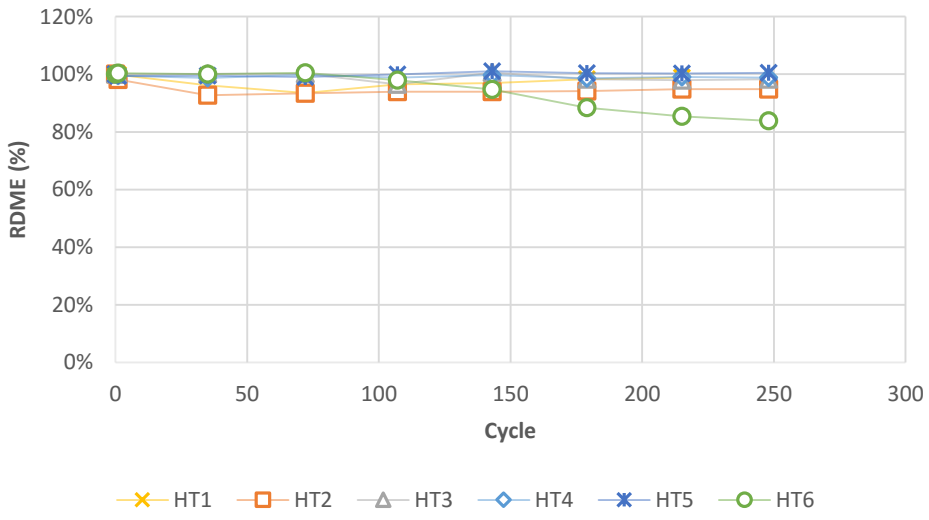


**Figure 6.6 RDME from RF measurements of half ties using the triaxial accelerometer**

**Table 6.2 Summary of half tie samples in terms of the cycle of initial deterioration for each test compared to visual inspection**

| Sample | Cycle of initial Deterioration for Each Test | | | | Location of the Deterioration |
|---|---|---|---|---|---|
| | RF | UPV | IE | Visual Inspection | |
| **HT1** | - | 72 | 215 | 107 | Cracking in the non-epoxied end |
| **HT2** | - | 143 | - | 143 | Cracking in the epoxied end |
| **HT3** | - | 179 | 215 | 107 | Cracking in the epoxied end |
| **HT4** | - | 248 | - | 248 | Cracking in the epoxied end |
| **HT5** | - | - | 72 | - | - |
| **HT6** | 197 | 143 | 143 | 107 | Fine cracking everywhere, especially at corners |

## 6.3. Conclusions

Due to absorption and evaporation of water content in the samples tested, the change in mass failed as a mechanism to assess freeze-thaw durability of prestressed concrete ties. Compared to RF, UPV was unable to identify deterioration of the samples because of the mechanism of how the UPV method works. UPV measures the velocity at which a fixed wave, with known frequency and amplitude travels through concrete. RF, however, determines wave frequencies that cause the highest amplitude in the concrete. Effects of the surroundings tend to be more significant and exaggerated when measuring low frequencies compared to large frequencies in the small samples. UPV had good correlation with deterioration seen in the visual inspection. Because the IE method captured only splitting cracking, that method should be used as a supplemental test to the UPV.

# Chapter 7 - Bursting Strains in Samples Excised from Prestressed Concrete Railroad Ties

Concrete railroad ties are often constructed as one continuous concrete structure in long-line prestressing beds and saw-cut into individual railroad ties. Indented strands or wires are used to prestress the concrete ties. Some distance along the length of the tie, called the transfer length, is required in order to fully transfer prestressing forces from the prestressing steel to the concrete. As forces spread out from the steel-concrete interface to the full concrete cross section, strains in the transverse direction are created. These strains are referred to as bursting strains. Short transfer lengths lead to large bursting strains. These bursting strains have been linked to splitting cracks in concrete railroad ties after saw-cutting a large prestressed concrete element into individual ties. A recent study measured bursting strains in prestressed concrete railroad ties with time in order to quantify their magnitude and growth.

## 7.1. Methodology

Vibration wire gauges were installed in six concrete railroad ties in a triaxial configuration as shown in Figure 7.1. These gauges (Geokon 4202x) were placed at 6.5 in. (165.1 mm) from both ends of the ties, leading to six gauges placed in each tie. The gauges were not attached to any prestressing wires but were suspended in the concrete between the wires as shown in Figure 7.2. The installation process was performed at a prestressed concrete manufacturing facility. Ties were made upside down in a long-line bed as shown in Figure 7.3. Separators with holes allowing the wires in a bed to pass were used on each tie end. Once the prestressing wires were, the concrete was placed into the forms. After the concrete hardened, the prestressing wires were saw-cut at each tie ends'. Two of the concrete railroad ties made were unreinforced. Figure 7.4 shows the unreinforced tie cover in plastic for curing. Another two were made with twenty-four 0.209 in.

(5.32 mm) diameter wires but not prestressed. The remaining two ties were made with the same twenty-four 0.209 in. (5.32 mm) diameter wires and were prestressed to 7000 lbs per wire. The prestressed and non-prestressed ties were made with two stirrups at each end for each tie. These wire stirrups fully encircled the prestressing wires, as shown in Figure 7.2. The manufactured ties were 8.5 ft (2.6 m) long, with a trapezoidal cross section 10 in. (254 mm) wide on top, 10.5 in. (267 mm) on the bottom and 10.5 in. (267 mm) in height.

**Figure 7.1 Vibration wire gauges inside the ties**

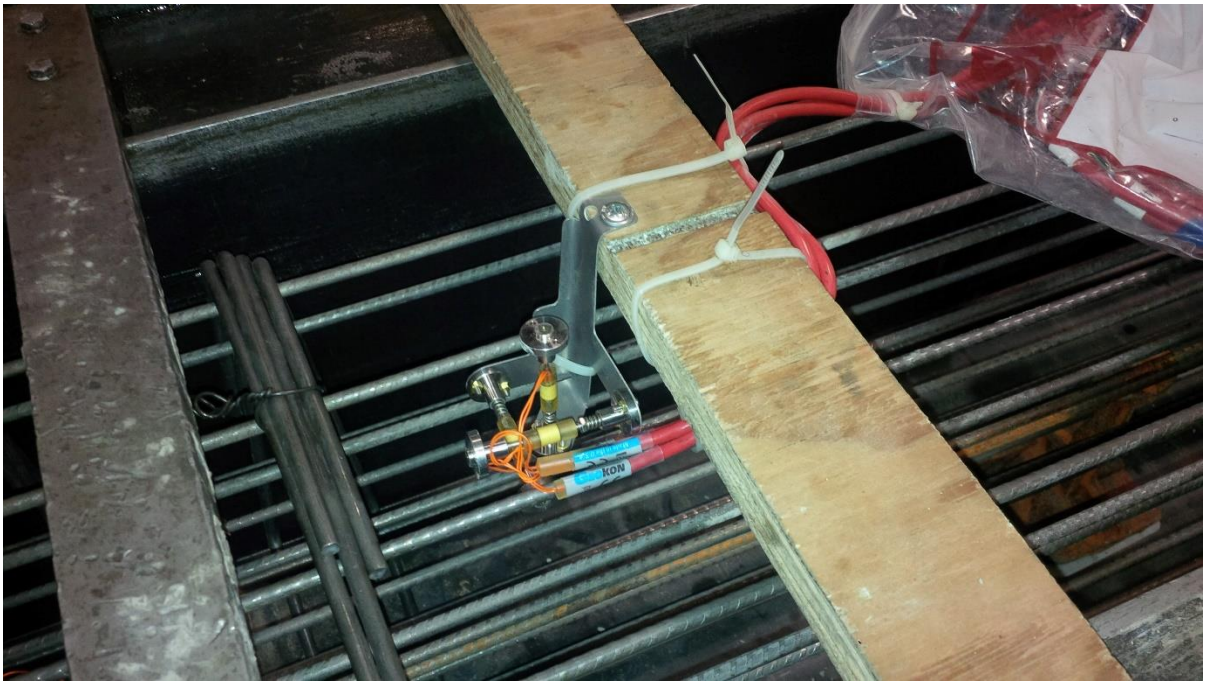

**Figure 7.2 Vibrating wire gages in the tie next to the two stirrups**

**Figure 7.3 Ties in a long-line bed form**

**Figure 7.4 Unreinforced tie covered in plastic**

A handheld vibrating wire gage reader (GK-404) was used to take strain and temperature readings; after hardening, after detensioning, after demolding and wires saw-cutting, after delivery to the K-State labs, after saw-cutting the ties in half and after excising the ASTM C666 samples. Unfortunately some of the delicate vertical and transverse gauges stopped working either after the concrete hardened or after detensioning. The locations of the cuts made and the gauge are shown in Figure 7.5.

Readings recorded from the handheld GK-404 device were from apparent strains ($\varepsilon_{ap}$) and had to be corrected in order to obtain actual strains ($\varepsilon_{actual}$). Equation 7.1 was used to correct for the temperature and to obtain actual strains.

$$\boldsymbol{\varepsilon_{actual} = \left(\left(\varepsilon_{ap}\right)_{current} - \left(\varepsilon_{ap}\right)_{initial}\right) B + (T_{current} - T_{initial})(C_s - C_c)} \qquad \textbf{Equation 7.1}$$

where $B$ is the batch calibration factor, $T_{current}$ is the current temperature, $T_{initial}$ is the initial temperature, $C_s$ is the steel coefficient of expansion, and $C_c$ is the concrete coefficient of expansion.

A list of all gauges used, the ties were installed in, and the types of ties they were installed in are presented in Table 7.1. Two types of concrete were utilized to make these ties: one with air entrainment agent and one without an air entrainment agent. Properties of these two types of concrete are presented in Table 7.2.

**Table 7.1 Summary of ties made and vibrating wire gauges used**

| Vibrating Wire Gage # | Type | | | | Tie/End |
|---|---|---|---|---|---|
| | Air Entrained | Prestressed | Not Prestressed | No Wire | |
| L 1 A | | | ● | | 1 / Dead End |
| T 2 A | | | ● | | |
| V 3 A | | | ● | | |
| L 4 A | | | ● | | 1 / Live End |
| T 5 A | | | ● | | |
| V 6 A | | | ● | | |
| L 7 A | ● | | ● | | 2 / Dead End |
| T 8 A | ● | | ● | | |
| V 9 A | ● | | ● | | |
| L 10 A | ● | | | ● | 3 |
| T 11 A | ● | | | ● | |
| V 12 A | ● | | | ● | |
| L 13 A | ● | | ● | | 2 / Live End |
| T 14 A | ● | | ● | | |
| V 15 A | ● | | ● | | |
| L 1 B | | | | ● | 4 |
| T 2 B | | | | ● | |
| V 3 B | | | | ● | |
| L 4 B | | ● | | | 5 / Dead End |
| T 5 B | | ● | | | |
| V 6 B | | ● | | | |
| L 7 B | | ● | | | 5 / Live End |
| T 8 B | | ● | | | |
| V 9 B | | ● | | | |
| L 10 B | ● | ● | | | 6 / Dead End |
| T 11 B | ● | ● | | | |
| V 12 B | ● | ● | | | |
| L 13 B | ● | ● | | | 6 / Live End |
| T 14 B | ● | ● | | | |
| V 15 B | ● | ● | | | |

**Table 7.2 Properties of concrete used**

| | Non-Air Entrained | Air Entrained |
|---|---|---|
| Temperature (°F) | 82.2 | 83.6 |
| Unit Weight (lb/ft3) | 148.4 | 138 |
| Fresh Air Content (%) | 0.9 | 7 |
| Compressive Strength at Release (psi) | 6850 | 6630 |
| Splitting Tensile Strength at Release (psi) | 410 | 560 |
| Compressive Strength at 28 days (psi) | 13570 | 12380 |
| Splitting Tensile Strength at 28 days (psi) | 740 | 760 |

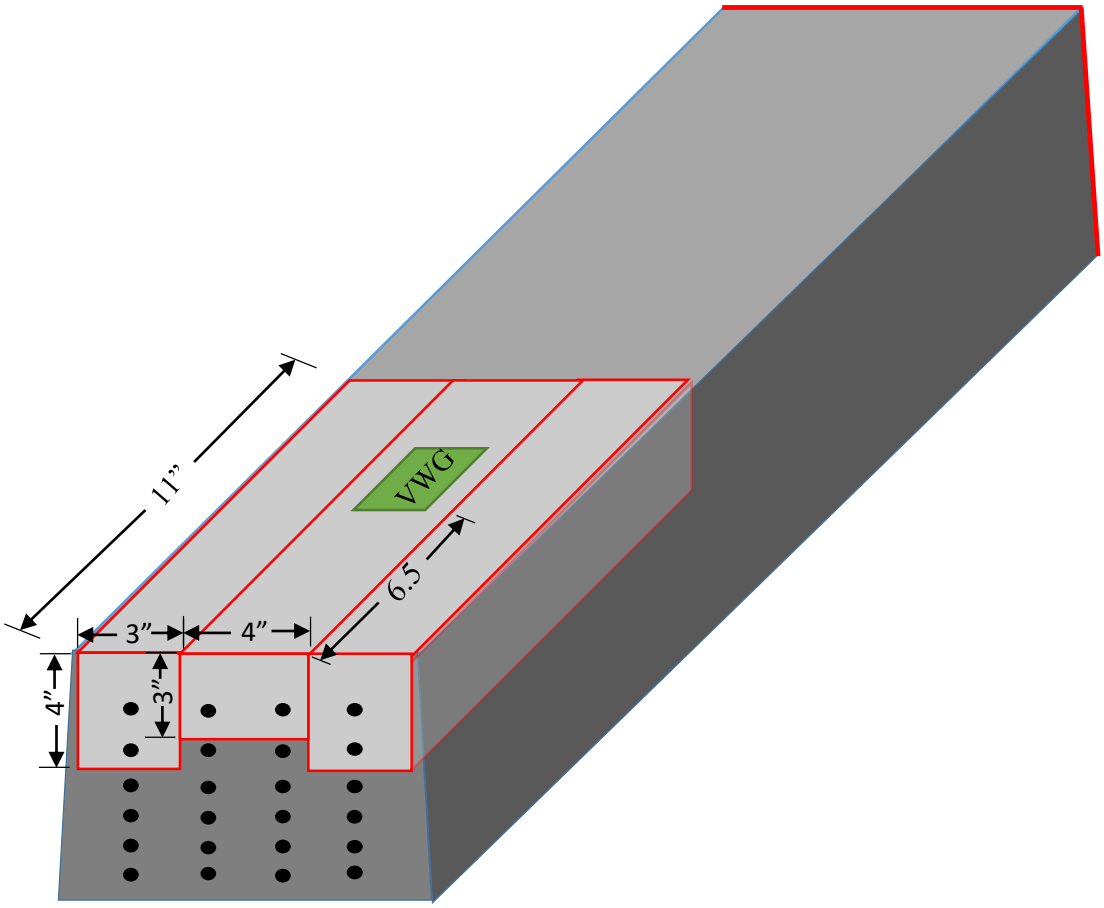


**Figure 7.5 Saw-cutting locations on ties (red) and saw-cutting locations on the gauge (VWG) (green)**

## 7.2. Results and Analysis

Table 7.3 includes a list of all the gauges that remained functional after concrete hardening. The large number of non-functional gages can be the result of either the strains going beyond limits of the gauge (4000 με) or the gauges were damaged during the placement or the hardening process. The results obtained shows that the ties in the longitudinal direction underwent compression as a result of the prestressing as shown in Figure 7.6. Furthermore, no apparent effects on the strains in the longitudinal direction were seen as a result of air entrainment, as expected. While one of the gauges in the non-air entrained samples failed after saw-cutting the tie in half, it is most likely that the strains jumped to values beyond the limits of the gages.

**Table 7.3 Vibrating wire gauges that remained operational after concrete hardening**

| Vibrating Wire Gage # | Functional | Vibrating Wire Gage # | Functional |
|---|---|---|---|
| L 1 A | | L 1 B | |
| T 2 A | | T 2 B | |
| V 3 A | | V 3 B | |
| L 4 A | ● | L 4 B | ● |
| T 5 A | | T 5 B | |
| V 6 A | | V 6 B | |
| L 7 A | ● | L 7 B | ● |
| T 8 A | | T 8 B | |
| V 9 A | | V 9 B | |
| L 10 A | ● | L 10 B | ● |
| T 11 A | ● | T 11 B | ● |
| V 12 A | ● | V 12 B | |
| L 13 A | ● | L 13 B | |
| T 14 A | ● | T 14 B | |
| V 15 A | ● | V 15 B | ● |

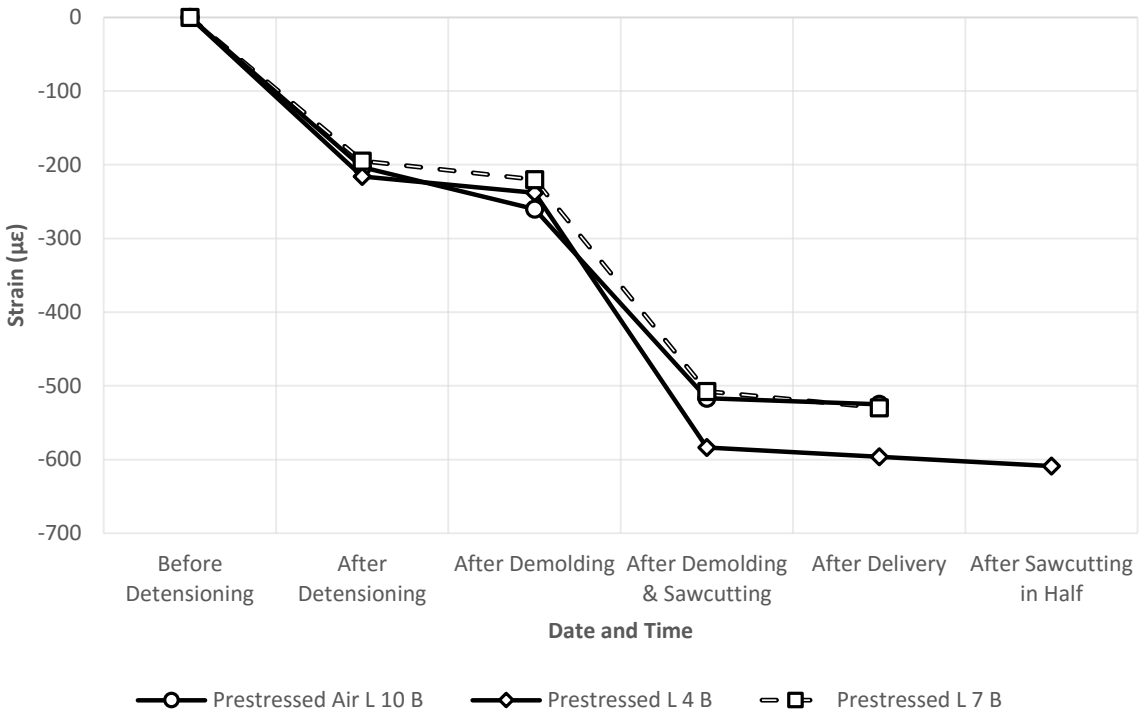


**Figure 7.6 Longitudinal strain development in non-air-entrained concrete samples versus air-entrained concrete**

When comparing the prestressed strains to the non-prestressed strains of non-air entrained concrete in the longitudinal direction in Figure 7.7 , it can be seen that there are compression strains even in the non-prestressed tie. While the longitudinal strains in the prestressed tie are three times that of the non-prestressed tie. The presence of these longitudinal strains in the non-prestressed tie can be the result of shrinkage and thermal stresses. The transverse strains recorded for the air entrained samples are presented in Figure 7.8. The transvers strains shows that the samples were under tension in the transverse direction resulting either from the prestressing force in the case of the prestressed sample or the shrinkage in the non prestressed samples.

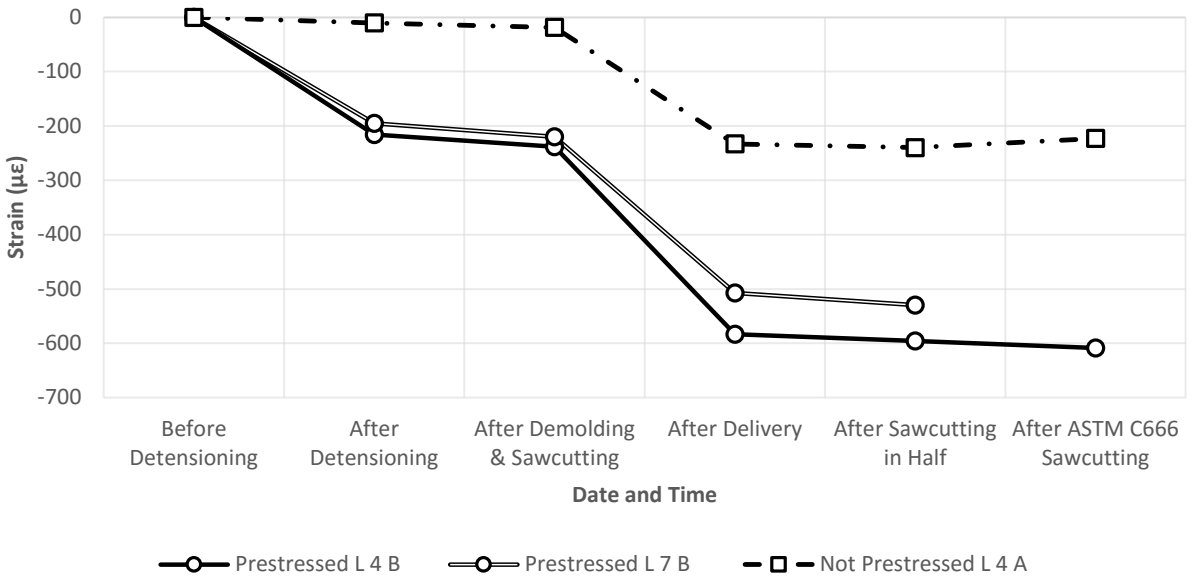


**Figure 7.7 Longitudinal strain development in non-air-entrained concrete samples**


**Figure 7.8 Transverse strain development in non-air-entrained concrete samples**

As for the air entrained concrete ties, the longitudinal strains in the non-prestressed and plain ties varied between +290 με and -50 με. These variation in compression and tension can be the result of variation in the thermal and shrinkage stresses inside the ties. These longitudinal

strains, in the non-prestressed and plain ties, remain smaller than that of the prestressed tie since the prestressed tie had the prestressing force on top of the thermal and shrinkage stresses. Figure 7.9 represent the variation in the longitudinal strains of the air entrained non-prestressed and plain concrete ties in comparison to the prestressed air-entrained tie. Similar to the non-air entrained concrete, the longitudinal strain in the prestressed tie tends to increase from one stage to the next. This increase was more prominent in the case of vibrating wire gage L 10 B which can be the result of gauge failure.

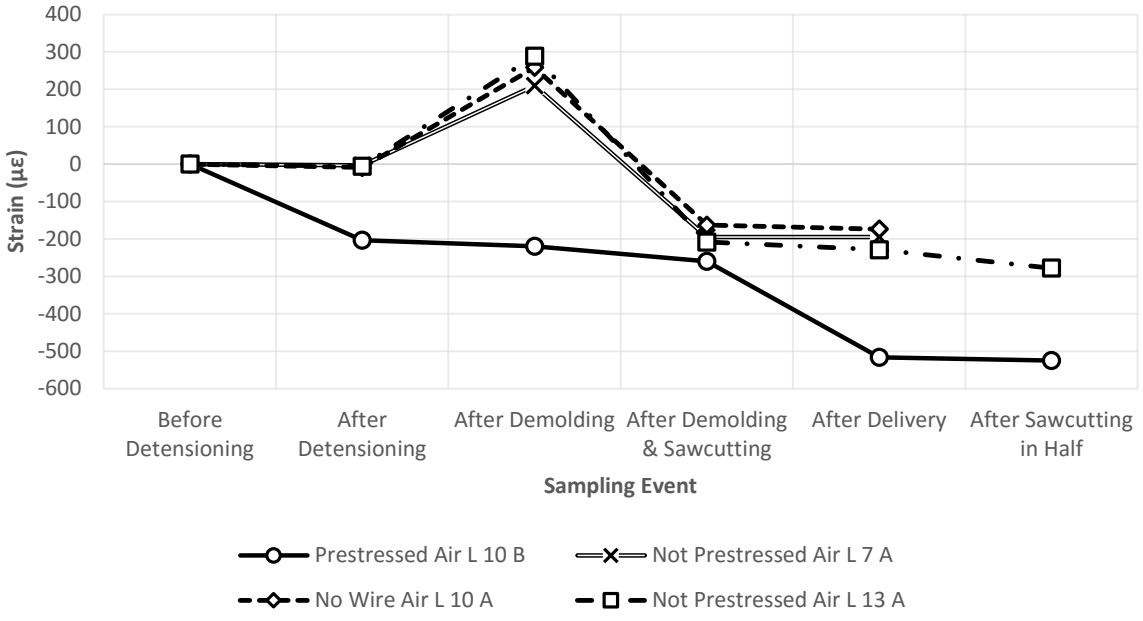


**Figure 7.9 Longitudinal strain development in air-entrained concrete samples**

While no transverse gauges remained working in the case of the air entrained concrete ties, the vertical gauges remained operational to a certain stage as shown in Figure 7.10. The recorded vertical strains in the case of the air entrained non-prestressed tie were higher than that of the air entrained prestressed and the plain tie. This can be the result of: shrinkage, creep, temperature variation between the concrete and the gauges. Concrete tends to shrink as its water content

diminishes and swells when it absorb water. These shrinkage and swelling lead to increases in the recorded strains which are not related to load or stress changes.

The bursting strain required to exceed the concrete tensile strength can be estimated using the concrete unit weight, compressive strength at release, splitting tensile strength, and ACI equation for elastic modulus as seen in Equation 7.2.

$$\boldsymbol{\varepsilon_{cracking}} = \frac{f_t}{w_c^{1.5} 33 \sqrt{f_c}} \qquad \textbf{Equation 7.2}$$

where $\varepsilon_{cracking}$ is the bursting strain required to cause cracking (με), $f_t$ is the concrete tensile strength (psi), $w_c$ is the concrete unit weight (lb/ft$^3$), and $f_c$ is the concrete compressive strength (psi), resulting in 83 and 128 με for non-air-entrained and air-entrained concrete mixtures, respectively. These strain values were easily exceeded in the vertical direction between saw-cutting and delivery. The ties instrumented included stirrups to prevent the ties from cracking during fabrication, which may explain why cracking was not seen in the ties until after saw-cutting small ASTM C666 samples.

All these increases in the strains in the various directions, but especially in the longitudinal direction, can be described as bursting strains. The effects of these bursting strains, increase in strains, can be very apparent when the saw-cut samples crack on their own without any freeze-thaw testing, as can be seen in Figure 7.11. It was noticed that many of the samples saw-cut to the small ASTM C666 compliant sample sizes tended to crack in a direction parallel to the prestressing wires. Even when increasing the concrete cover, which could only be increased to 0.75 in (19 mm) in the case of the tested ties, the concrete still cracked in some of the saw-cut samples. In addition, some of the wires in some of the samples slipped inside the concrete for 0.04 in (1 mm) indicating a new sample transfer length was created when the sample was saw-cut, creating stresses and

cracking. This cracking and reinforcing wire shrinkage could be exaggerated when the samples containing any of these outcomes of bursting strains are subjected to freeze-thaw cycles.

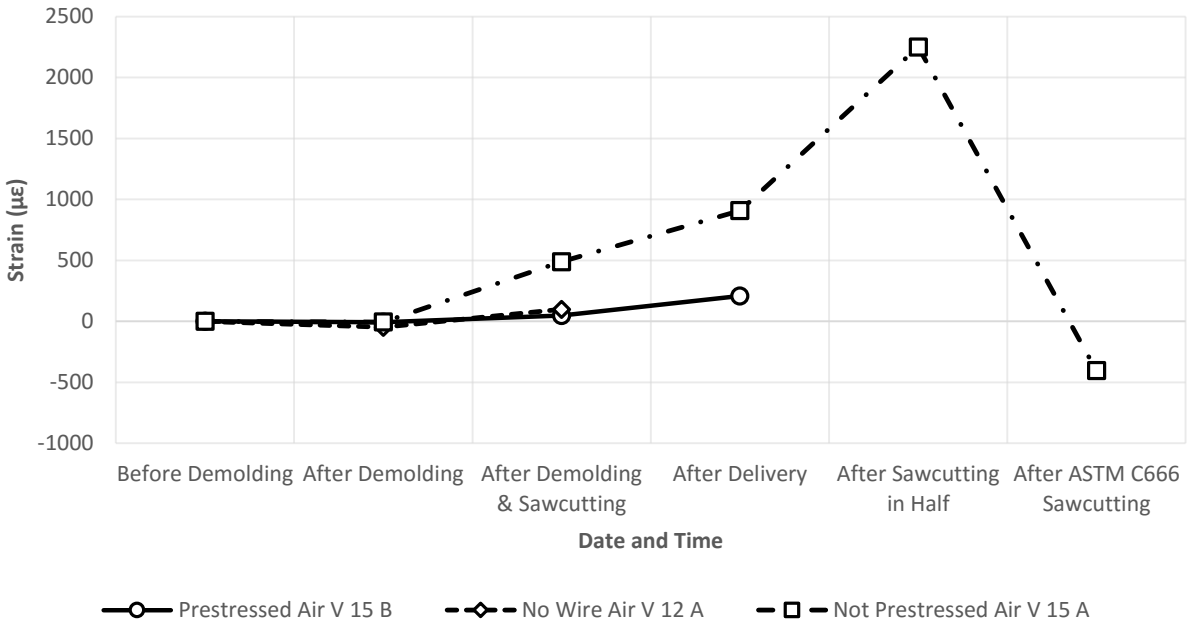


**Figure 7.10 Vertical strain development in air-entrained concrete samples**

**Figure 7.11 Cracking due to stress release from saw-cutting**

## 7.3. Conclusions

In order to understand what causes cracking in saw-cut samples that were not subjected to freeze-thaw testing, it is important to quantify the amount of strains inside these samples and how these strains increase due to the stress release caused by the saw-cutting process. These bursting strains were recorded after various stages using vibrating wire gages embedded in variously

reinforced ties with two types of concrete, air entrained and non-air entrained concrete. The strains in the prestressed non-air entrained concrete were tensile and close to calculated values for cracking. Additional stresses caused by saw-cutting samples for ASTM C666 testing was enough to cause cracking in the ties and could cause potentially misleading deterioration in freeze-thaw testing.

# Chapter 8 - Conclusions and Recommendations

## 8.1. Summary

This research had two initial objectives:

a) Determine the effect of concrete rheology and fabrication process on air content in concrete railroad ties, and

b) Determine effects of testing procedures on results of freeze-thaw quality control testing of prestressed concrete railroad ties.

In order to address the first objective, manufacturing processes at three concrete manufacturing plants were investigated. The primary goal of the investigation was to evaluate the effects of the manufacturing processes on the air void system in the concrete railroad ties. The investigation included testing the fresh concrete air content, slump, temperature, vibration, and rheology. Hardened concrete samples were also collected at various stages of manufacturing in order to quantify these effects in terms of air content, spacing, and distribution using image analysis.

In order to accomplish the second objective, three sets of ties were made with companion prisms that satisfied ASTM C666 standards. The three sets included two prestressed ties, two reinforced ties without prestressing, and two non-reinforced ties. Each set consisted of a tie with air content of 7% and a tie with air content of 0.9%. Saw-cutting small prestressed concrete samples to satisfy ASTM C666 led to insufficient transfer length, resulting in cracking that was parallel to the prestressing. In order to quantify the strain and stress release due to saw-cutting, vibrating wire gauges were embedded in these ties. Saw-cut samples from the three sets of ties and the cast prisms were tested in freeze-thaw conditions in order to investigate deterioration caused

by saw-cutting and prestressing. In addition, various investigation methods were compared in order to evaluate freeze-thaw deterioration of half and full ties.

## 8.2. Conclusions

The effects of concrete rheology and fabrication process on air content in concrete railroad ties were determined in this research, and the effects of testing procedures on results of freeze-thaw quality control testing of prestressed concrete railroad ties were investigated. The following conclusions were drawn:

1. Once the concrete left the mixer, each stage (after delivery and vibration) in the process decreased the air content.
2. Results showed correlation between concrete yield stresses and air loss from the fresh concrete during handling.
3. The concrete air void spacing factor increased significantly during handling with a more workable mixture and extended vibration. This was the result of air loss caused by the movement, concrete dropping from the mixer to the delivery buckets, and placement in the forms and vibration.
4. Observed variation in batch-to-batch concrete rheology could be attributed to small adjustments made to the mixture, variation in aggregate moisture content, and different air content.
5. Form-based vibrators induced high complexity of wave propagation for more time than was necessary to consolidate the concrete. This led to increased air loss and less adequate air system. Meanwhile, immersion vibrators vibrated the concrete for a shorter, more concentrated and effective period of time.

6. Whole concrete railroad ties did not experience significant deterioration as a result of slightly less severe freeze-thaw testing temperatures as compared to ASTM C666 temperature limits, leading to a less freezing distress in those ties.
7. Results of the saw-cut samples indicated that saw-cutting had a minimal effect on freeze-thaw durability, while the presence of reinforcement in the saw-cut sections led to accelerated failure. Saw-cut prestressed samples showed deterioration not representative of half tie performance observed in the large sample. This deterioration could be due to stress release caused by the saw-cutting combined with freeze-thaw cycles, which tends to cause expansion from micro-cracking.
8. Stresses caused by saw-cutting samples for ASTM C666 testing were sufficient to cause cracking in the ties, thereby potentially misrepresenting deterioration in freeze-thaw testing.
9. Samples placed on top of the vibrating bed showed comparable air content to the air content of the ties below. This can be used in quality control testing in order to calibrate samples subjected to the same vibration and freeze-thaw testing.
10. Although testing large-scale samples for freeze-thaw durability is not feasible, cast prisms made with the same concrete used to make the ties could be tested and subjected to the same levels of handling and vibration. This could be accomplished by bolting cast prisms forms to vibrating tie forms on various locations across the casting bed length. An alternative method would be use of a vibrator that is tuned to the same acceleration magnitude and frequency as the ties.
11. Freeze-thaw can be misidentified in the field as splitting cracking from bursting strains. This research revealed two types of freeze-thaw cracking: mesh cracking

and split cracking with freeze-thaw cracking. Fine cracking begins as micro level damage and spreads throughout the whole sample, while split cracking with freeze-thaw cracking is caused by excessive prestressing and loading. Misidentification of these freeze-thaw cases could lead to underestimation of freeze-thaw deterioration in the field.

12. Accurate correlation was found between the UPV measurement and deterioration observed in the half ties.

## 8.3. Recommendations for Future Research

Although several aspects and methods of freeze-thaw durability of prestressed concrete railroad ties were studied in this research, further research is needed in order to successfully propose a more feasible freeze-thaw testing mechanism. The following recommendations should be taken into account in any future research related to freeze-thaw durability of prestressed concrete ties:

- Test small excised samples in freeze-thaw conditions identical to conditions of half ties, such as rate of freezing and thawing.
- Determine the effects of using stirrups for preventing splitting cracking observed in half ties.
- Vibration time, frequency, and amplitude effect on the air system must be determined.

# References


[1] J. C. Zeman, J. R. Edwards, C. P. Barkan and D. A. Lange, "Failure Mode and Effect Analysis of Concrete Ties in North America," in *Proceedings of the 9th International Heavy Haul Conference*, Shanghai, China, 2009.

[2] H. Shang, Y. Song and J. Ou, "Behavior of Air-Entrained Concrete After Freeze-Thaw cycles," *Acta Mechanica Solida Sinica*, vol. 22, no. 3, June 2009.

[3] C. R. Duggan, C. J. Dalton and J. F. Scott, "Freeze-Thaw Tests on Concrete Ties," CN Rail Research Center, Montreal, Quebec, 1979.

[4] Delhi Metro Rail Corporation LTD., "Kerala High-speed Rail between Thiruvananthapuram and Ernakulam: Pre Feasibility Report," Delhi Metro Rail Corporation LTD, Delhi, 2011.

[5] A. N. Hanna, "Concrete Ties for U.S. Railroads -An Update," in *SP-93: Concrete in Transportation*, D. R. Morgan, Ed., American Concrete Institute (ACI), 1986, pp. 267-286, Document: SP93-13.

[6] R. L. Murphy, Determining the Transfer Length in Prestressed Concrete Railroad Ties Produced In the United States, Manhattan: Kansas State University, 2012.

[7] American Railway Engineering and Maintenance-of-Way Association, "AREMA Manual for Railway Engineering," American Railway Engineering and Maintenance-of-Way Association, Lanham, Maryland, 2007.

[8] R. H. Lutch, "Capacity Optimization of a Prestressed Concrete Railroad Tie," Michigan Technological University, Houghton, Michigan, 2009.

[9] E. G. Nawy, Prestressed Concrete : A Fundamental Approach, 5th edition ed., New Jersey: Prentice Hall, Inc., 2005.

[10] A. N. Hanna, "Prestressed Concrete Ties for North American Railroads," *PCI journal*, vol. 24, no. 5, p. 29, 1979.

[11] A. J. Reinschmidt, "Rail-seat abrasion: Cause and the search for the cure," *Railway Track and Structures*, vol. 87, no. 7, pp. 24-25, 1991.

[12] R. H. Lutch, D. K. Harris and T. M. Ahlborn, "Prestressed Concrete Ties in North America," in *Proceeding of AREMA Annual Conference*, Chicago, USA, 2009.

[13] G. P. Raymond, "Track Support Must be Right if Concrete Sleepers are to Survive," *Railway Gazette International,* vol. 140, no. 7, pp. 528-530, 1984.

[14] C. K. Nmai, "Freezing and Thawing," in *ASTM STP 169D: Significance of Tests and Properties of Concrete and Concrete-Making Materials*, Bridgeport, NJ, American Society for Testing and Materials, 2006, pp. 154-163.

[15] M. J. Setzer, R. Auberg, S. Kasparek, S. Palecki and P. Heine, "CIF-Test-Capillary suction, internal damage and freeze thaw test," *Materials and Structures,* vol. 34, no. 9, pp. 515-525, 2001.

[16] M. Pigeon and R. Pleau, Modern Concrete Technology 4: Durability of Concrete in Cold Climates, New York: CRC Press, 1995.

[17] Z. Sun and G. W. Scherer, "Effect of air voids on salt scaling and internal freezing," *Cement and Concrete Research,* vol. 40, no. 2, pp. 260-270, 2010.

[18] J. J. Valenza II and G. W. Scherer, "Mechanism for Salt Scaling," *Journal of the American Ceramic Society,* vol. 89, no. 4, p. 1161–1179, 2006.

[19] S. Mindess, J. F. Young and D. Darwin, Concrete, 2nd Edition ed., Upper Saddle River, NJ: Prentice Hall, 2003.

[20] S. Hamoush, M. Picornell-Darder, T. Abu-Lebdeh and A. Mohamed, "Freezing and Thawing Durability of Very High Strength Concrete," *American J. of Engineering and Applied Sciences,* vol. 4, no. 1, pp. 42-51, 2011.

[21] T. C. Powers and T. F. Willis, "The Air Requirement of Frost Resistant Concrete," in *29th Anual Highway Research Board,* Washington, D.C., December 13-16, 1949.

[22] J. Tanesi and R. Meininger, "Freeze-Thaw Resistance of Concrete With Marginal Air Content," FHWA Office of Infrastructure Research and Development, FHWA-HRT-06-117, McLean, VA, 2006.

[23] J. Cao, A study of effects of a new agricultural-based deicer on the properties of pavement concrete, Ames, Iowa: Iowa State University, 2014.

[24] P. Qiao, D. I. McLean and F. Chen, Concrete Performance Using Low-Degradation Aggregates, Pullman, WA: Washington State Department of Transportation, June 2012.

[25] C. L. Page and M. M. Page, Eds., Durability of Concrete and Cement Composites, Cambridge, England: Woodhead Publishing, 2007.

[26] ACI Committee 621, "Selection and Use of Aggregates for Concrete," *Journal of the American Concrete Institute,* vol. 58, no. 11, pp. 513-542, 1961.

[27] P. K. Mehta, "Durability of High-Strength Concrete," *ACI Special Publication,* vol. 122, pp. 19-27, 1990.

[28] R. D. Walker and T.-C. Hsieh, "Relationship Between Aggregate Pore Characteristics and Durability of Concrete Exposed to Freezing and Thawing," Highway Research Board, Washington, DC, 1968.

[29] D. S. Lane and R. C. Meininger, "Laboratory Evaluation of the Freezing and Thawing Durability of Marine Limestone coarse aggregate in concrete," *ACI Special Publication,* vol. 100, pp. 1311-1324, 1987.

[30] G. Verbeck and R. Landgren, "Influence of Physical Characteristics of Aggregates on the Frost Resis-tance of Concrete," *Proceedings of the American Society for Testing Materials ,* vol. 60, pp. 1063-1079, 1960.

[31] R. A. Helmuth, "Dimensional Changes of Hard-ened Portland Cement Pastes Caused by TemperatureChanges," in *Proceedings of the Fortieth Annual Meeting of the Highway Research Board,* Washington, D.C., 1961.

[32] J. S. SawanI, "Cracking Due to Frost Action in Portland Cement Concrete Pavements--A Literature Survey," *ACI Special Publication,* vol. 100, pp. 781-804, 1987.

[33] T. Powers, The Properties of Fresh Concrete, New York: John Wiley & Sons, 1968.

[34] L. Du and K. J. Folliard, "Mechanisms of air entrainment in concrete," *Cement and Concrete Research,* vol. 35, no. 8, pp. 1463-1471, 2005.

[35] R. C. Mielenz, V. E. Wolkodoff, J. E. Backstrom and H. L. Flack, "Origin, evolution, and effects of the air void system in concrete: Part 1," *ACI Journal Proceedings,* vol. 55, no. 7, pp. 95-121, 1958.

[36] T. C. Powers, "A Working Hypothesis for Further Studies of Frost Resistance of Concrete," *Journal of the American Concrete Institute,* vol. 16, no. 4, pp. 245-271, 1945.

[37] K. C. Hover, "Air Content and Density of Hardened Concrete," in *ASTM STP 169D: Significance of Tests and Properties of Concrete and Concrete-Making Materials,* J. F. Lamond and J. H. Pielert, Eds., Bridgeport, NJ, The American Society for Testing and Materials, 2006, pp. 288-308.

[38] S. H. Lamb, Hydrodynamics, 6th ed. ed., London: Cambridge University Press, 1993.

[39] D. Pomeroy, "Concrete durability: From basic research to practical reality," *ACI Special Publication,* vol. 100, pp. 111-130, 1987.

[40] D. Whiting and D. Stark, "Control of air content in concrete," Transportation Research Board, Washington, D.C., 1983.

[41] S. H. Kosmatka, B. Kerkhoff and W. C. Panarese, Design and Control of Concrete Mixtures, 14th ed., Skokie, Illinois, USA: Portland Cement Association, 2002.

[42] M. Nagi, "Evaluating Air-entraining Admixtures for Highway Concrete," Transportation Research Board, Washington, D.C., 2007.

[43] W. F. Perenchio and P. Klieger, "Further Laboratory Studies of Portland-Pozzolan Cements," Portland Cement Association, Skokie, IL, 1976.

[44] B. Łazniewska-Piekarczyk, "The influence of selected new generation admixtures on the workability, air-voids parameters and frost-resistance of self compacting concrete," *Construction and Building Materials,* vol. 31, p. 310–319, 2012.

[45] H. Kamal, K. H. Khayat and J. Assaad, "Air-void stability in self-consolidating concrete," *ACI Materials Journal,* vol. 99, no. 4, pp. 408-416, 2002.

[46] P. Plante, M. Pigeon and C. Foy, "The influence of water-reducers on the production and stability of the air void system in concrete," *Cement and Concrete Research,* vol. 19, no. 4, pp. 621-633, 1989.

[47] B. Łazniewska-Piekarczyk, "The type of air-entraining and viscosity modifying admixtures and porosity and frost durability of high performance self-compacting concrete," *Construction and Building Materials,* vol. 40, pp. 659-671, 2013.

[48] K. H. Khayat and J. Assaad, "Air-Void Stability in Self-Consolidating Concrete," *ACI Materials Journal,* vol. 99, no. 4, pp. 408-416, 2002.

[49] L. J. Struble and Q. Jiang, "Effects of Air Entrainment on Rheology," *ACI Materials Journal,* vol. 101, no. 6, pp. 448-456, 2004.

[50] W. L. Dolch, "Air-Entraining Admixtures," in *Concrete Admixtures Handbook: Properties, Science and Technology*, Ottawa, Canada, National Research Council Canada, 1996, pp. 518-537.

[51] E. W. J. Scripture and F. J. Litwinowicz, "Effects of Mixing Time, Size of Batch and Brand of Cement on Air Entrainment," *Journal of the American Concrete Institute,* vol. 45, no. 5, pp. 653-662, 1949.

[52] J. F. Barbee, "Effect of Mixing Time and Overloading on Concrete Produced by Stationary Mixers," Highway Research Board, Washington, D.C., 1961.

[53] K. C. Hover, "Vibration Tune-Up," *Concrete International,* vol. 23, no. 9, pp. 31-35, 2001.

[54] K. Hover, "Air in concrete: expect variability in gaining, losing, and measuring: part 2 of a two part series," *Concrete Construction,* vol. 48, no. 1, pp. 55-59, 2003.

[55] S. Tymkowicz and R. Steffes, "Vibration Study for Consolidation of Portland Cement Concrete," Iowa Department of Transportation, Ames, Iowa, 1999.

[56] R. S. Brewster, "Effect of Vibration Time upon Loss of Entrained Air from Concrete Mixes," Bureau of Reclamation, Denver, CO, 1949.

[57] D. C. Stark, "Effect of Vibration on the Air-System and Freeze-Thaw Durability of Concrete," Research and Development Bulletin RD092, Portland Cement Association, 1986.

[58] S. Tymkowicz and R. F. Steffes, "Vibration Study for Consolidation of Portland Cement Concrete," Iowa Department of Transportation, Ames, Iowa, 1996.

[59] E. C. Higginson, "Some Effects of Vibration and Handling on Concrete Containing Entrained Air," *ACI Journal Proceedings,* vol. 49, no. 9, pp. 1-12, 1952.

[60] P. H. Torrans and D. L. Ivey, "Review of Literature on Air-Entrained Concrete," Texas Transportation Institute, College Station, Texas, 1968.

[61] M. Kaneuji, "Correlation between Pore Size Distribution and Freeze Thaw Durability of Coarse Aggregate in Concrete: Interim Report," Publication FHWA/IN/JHRP-78/15. Joint Highway Research Project, Indiana Department of Transportation and Purdue University, West Lafayette, Indiana, 1978.

[62] M. Molero, S. Aparicio, G. Al-Assadi, M. J. Casati, M. Hernández and J. Anaya, "Evaluation of freeze–thaw damage in concrete by ultrasonic imaging," *NDT&E International,* vol. 52, pp. 86-94, 2012.

[63] ASTM Standard C666, "Standard Test Method for Resistance of Concrete to Rapid Freezing and Thawing," ASTM International, West Conshohocken, PA, 2008.

[64] UNE-CEN/TS12390-9:2008EX, "Testing hardened concrete—part 9: freeze-thaw resistance—scaling," AENOR, 2008.

[65] JISA1148:2010, "Method of test for resistance of concrete to freezing and thawing," Japanese Industrial Standards, Tokyo, 2010.

[66] L. Tang and P. E. Petersson, "Slab test-freeze/Thaw resistance of concrete - Internal deterioration," *Materials and Structures,* vol. 34, no. 9, pp. 526-531, 2001.

[67] P. Boos and Z. Giergiczny, "Testing the frost resistance of concrete with different cement types – experience from laboratory and practice," *Architecture Civil Engineering Environment,* no. 2, pp. 41-51, 2010.

[68] SIS/TK 185, "Concrete testing - hardened concrete - scaling at freezing," Swedish Standards Institution, Stockholm, Sweden, 2005.

[69] S. Popovics, Strength and Related Properties of Concrete: A Quantitative Approach, Hoboken, NJ: John Wiley & Sons, 1998.

[70] S. Popovics, Concrete Materials, 2nd Ed.: Properties, Specifications, and Testing, William Andrew, 2012.

[71] J. Marchand, M. Pigeon and M. Setzer, Freeze-Thaw Durability of Concrete: Volume 30 of RILEM proceedings, CRC Press, 2004.

[72] E. Siebel and T. Reschke, "Three different methods for testing the freeze-thaw resistance of concrete with and without de-icing salt," E and F Spon Limited, London, England, 1997.

[73] H. Kuosa, M. Ferreira and M. Leivo, "Freeze—thaw testing CSLA Projekct — Task 1. Literature Review," VTT Technical Research Centre of Finland, Finland, 2013.

[74] B. Kelly and P. Murphy, "Prediction of Freeze-thaw Resistance of Concrete," University College Dublin, Belfield, Dublin, Republic of Ireland, 2010.

[75] G. Fagerlund, "The critical degree of saturation method of assessing the freeze/thaw resistance of concrete," *Matériaux et Construction,* vol. 10, no. 4, pp. 217-229, 1977.

[76] A. Hassan and S. Jones, "Non-destructive testing of ultra high performance fibre reinforced concrete (UHPFRC): A feasibility study for using ultrasonic and resonant frequency testing techniques," *Construction and Building Materials,* vol. 35, pp. 361-367, 2012.

[77] V. Malhotra and N. J. Carino, Handbook on Nondestructive Testing of Concrete, Second Edition, West Conshohocken, PA: CRC Press, 2003.

[78] ASTM C215-14, "Standard Test Method for Fundamental Transverse, Longitudinal, and Torsional Resonant Frequencies of Concrete Specimens," ASTM International, West Conshohocken, PA, 2014.

[79] Z. Yang, Assessing cumulative damage in concrete and quantifying its influence on life cycle performance modeling, West Lafayette, IN: Purdue University, 2004.

[80] International Atomic Energy Agency (IAEA), Guidebook on non-destructive testing of concrete structures, Vienna, Austria: International Atomic Energy Agency, 2002.

[81] Y. Tinkey, L. D. Olson, R. Bedon and C. Lieberle, "Impact Echo Scanning Technology for Internal Grout Condition Evaluation in Post-Tensioned Bridge Ducts," in *International Symposium Non-Destructive Testing in Civil Engineering 2003*, 2003.

[82] F. E. Musleh, "The Effects of Freezing and Thawing on Pre-Stressed Concrete. Publication FHWA/IN/JHRP-59/04," Joint Highway Research Project, Indiana Department of Transportation and Purdue University, West Lafayette, Indiana, 1959.

[83] ASTM Standard C138, "Standard Test Method for Density (Unit Weight), Yield, and Air Content (Gravimetric) of Concrete," ASTM International, West Conshohocken, PA, 2013.

[84] ASTM Standard C173, "Standard Test Method for Air Content of Freshly Mixed Concrete by the Volumetric Method," ASTM International, West Conshohocken, PA, 2014.

[85] W.W Grainger, Inc., "Roll-a-Meter, Aluminum," [Online]. Available: http://www.grainger.com/product/RollAMeter-Air-Indicator-5ZPX1?Pid=search. [Accessed 18 March 2014].

[86] ASTM Standard C231, "Standard Test Method for Air Content of Freshly Mixed Concrete by the Pressure Method," ASTM International, West Conshohocken, PA, 2010.

[87] K. Y. Kim, T. S. Yun, J. Choo, D. H. Kang and H. S. Shin, "Determination of air-void parameters of hardened cement-based materials using X-ray computed tomography," *Construction and Building Materials*, vol. 37, pp. 93-101, 2012.

[88] K. Snyder, K. Natesaiyer and K. Hover, "The Stereological and Statistical Properties of Entrained Air Voids in Concrete: A Mathematical Basis for Air Void System Characterization," S. Mindess and J. Skalny, Eds., American Ceramic Society, Westerville, OH, 2001.

[89] ASTM Standard C457, "Standard Test Method for Microscopical Determination of Parameters of the Air-Void System in Hardened Concrete," ASTM International, West Conshohocken, PA, 2012.

[90] H. N. Walker, D. S. Lane and P. E. Stutzman, "Petrographic Methods of Examining Hardened Concrete: A Petrographic Manual," Federal Highway Administration, McLean, VA, 2006.

[91] K. H. Khayat and K. W. Nasser, "Comparison of Air Contents in Fresh and Hardened Concretes Using Different Airmeters," *Cement, Concrete, and Aggregates,* vol. 13, no. 1, pp. 18-24, 1991.

[92] C. Ozyildirim, "Comparison of the Air Contents of Freshly Mixed and Hardened Concretes," *Cement, Concrete, and Aggregates*, vol. 13, no. 1, pp. 11-17, 1991.

[93] S. Schlorholtz, "Image Analysis for Evaluating Air Void Parameters of Concrete," Iowa Department of Transportation, Ames, Iowa, 1998.

[94] T. D. Hanson, "Evaluation of the RapidAir 457 Air Void Analyzer," Iowa Department of Transportation, Ames, Iowa, 2012.

[95] K. Peterson, Air void analysis of hardened concrete via flatbed scanner, Houghton, MI: Unpuplished master's thesis, Michigan Technological University, 2001.

[96] K. W. Peterson, L. L. Sutter and T. J. Van Dam, "An Experiment with a High Resolution Flatbed Scanner to Examine Variability in ASTM C 457 Test Results from a Single Concrete Specimen," in *ASTM Cement Concrete Aggregates Symposium,* 2002.

[97] A. M. Ramezanianpour and R. D. Hooton, "Evaluation of Two Automated Methods for Air-Void Analysis of Hardened Concrete," *Journal of ASTM International,* vol. 7, no. 2, 2010.

[98] M. Radlinski, J. Olek, Q. Zhang and K. Peterson, "Evaluation of the Critical Air-Void System Parameters for Freeze-Thaw Resistant Ternary Concrete Using the Manual Point-Count and the Flatbed Scanner Methods," *Journal of ASTM International,* vol. 7, no. 4, 2010.

[99] ASTM C143 / C143M-12, "Standard Test Method for Slump of Hydraulic-Cement Concrete," ASTM International, West Conshohocken, PA, 2012.

[100] ASTM C1064 / C1064M-12, "Standard Test Method for Temperature of Freshly Mixed Hydraulic-Cement Concrete," ASTM International, West Conshohocken, PA, 2012.

[101] T. Woodhouse, "Multi-State Coarse Aggregate Freeze-Thaw Comparison," Michigan Deparment of Transportation, Research report R-1469, Lansing, MI, 2005.

[102] J. Chan, Thermal properties of concrete with different Swedish aggregate materials, Lund, Sweden: Lund University, 2013.

[103] D. Sekulic, D. Bjegović, D. Veza and N. Gucunski, "Experimental determination of detection limits of Impact echo method," in *MATEST 2011 International NDT Conference*, Split, Croatia, 2011.

[104] H. S. Mattimore, "Durability Test of Certain Portland Cements," *Highway Research Board Proceedings,* vol. 16, pp. 135-166, 1936.

[105] M. O. Withey, F. B. Hornibrook, H. S. Mattimore, H. F. Gonnerman, J. L. Miner, M. Hirschtal, J. E. Myers, P. Holland, F. V. Reagel, F. H. Jackson, H. H. Scofield, F. C. Lang, T. E. Stanton and G. H. Larson, "Progress Report, Committee on Durability of Concrete," *Highway Research Board Proceedings,* vol. 24, pp. 174-202, 1944.

[106] M. Pigeon, R. Gagné, P.-C. Aïtcin and N. Banthia, "Freezing and thawing tests of high-strength concretes," *Cement and Concrete Research,* vol. 21, no. 5, pp. 844-852, 1991.

[107] R. C. Kreisel, C. E. French and M. B. Snyder, "Freeze-thaw durability of high strength concrete," Minnesota Department of Transportation, Minneapolis, MN, 1998.

# Appendix A - Additional Whole-Tie Freeze-Thaw Results

The following figures represent additional data in terms of length change and RDME from whole-tie testing.

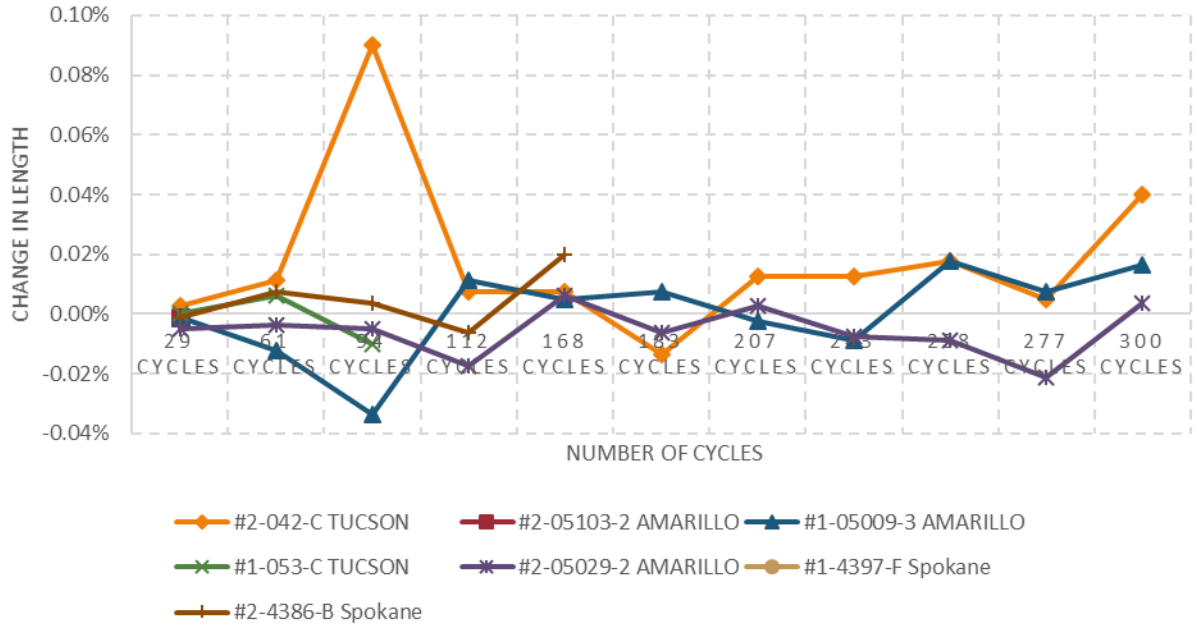


**Figure A-1: Length change in diagonal direction at the ID side**

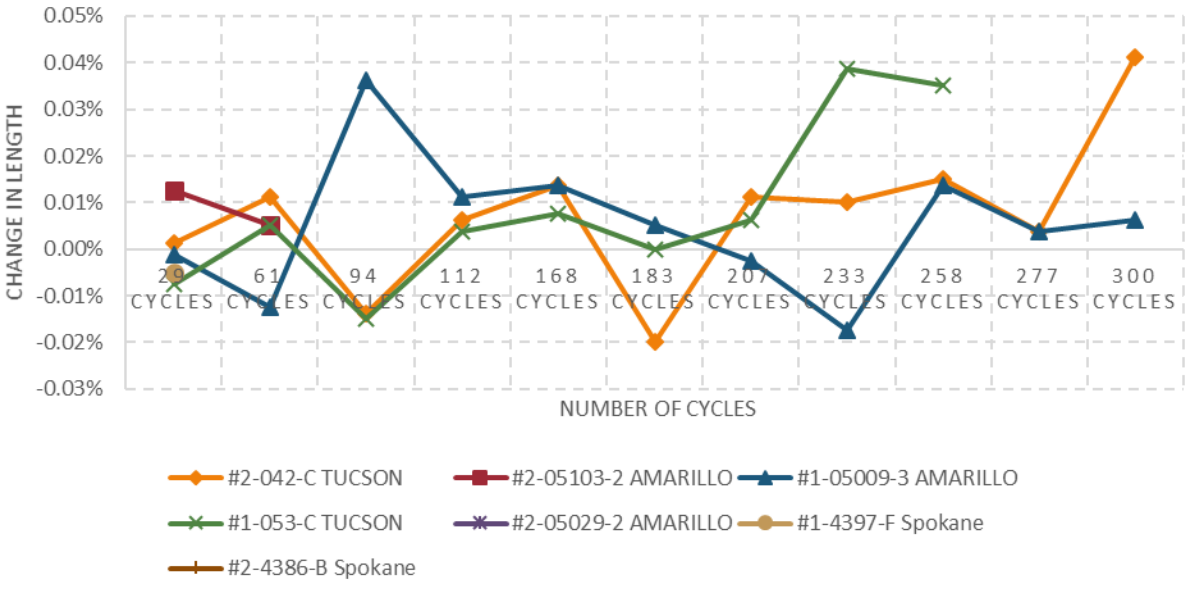


**Figure A-2: Length change in vertical direction at the ID side**

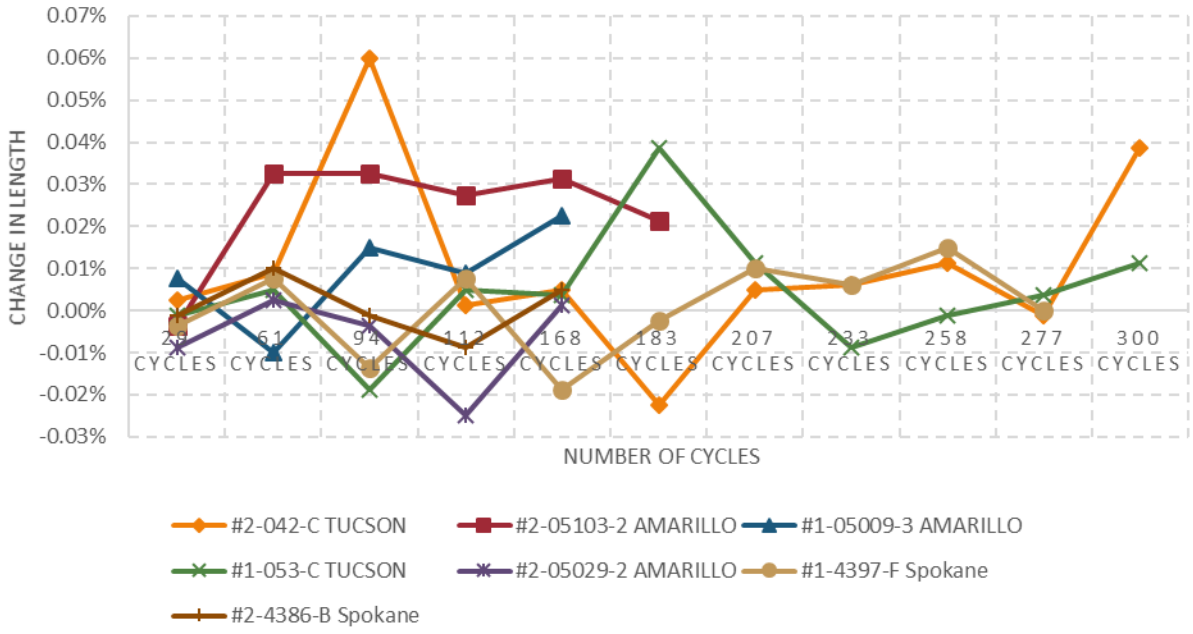


**Figure A-3: Length change in horizontal direction at the ID side**

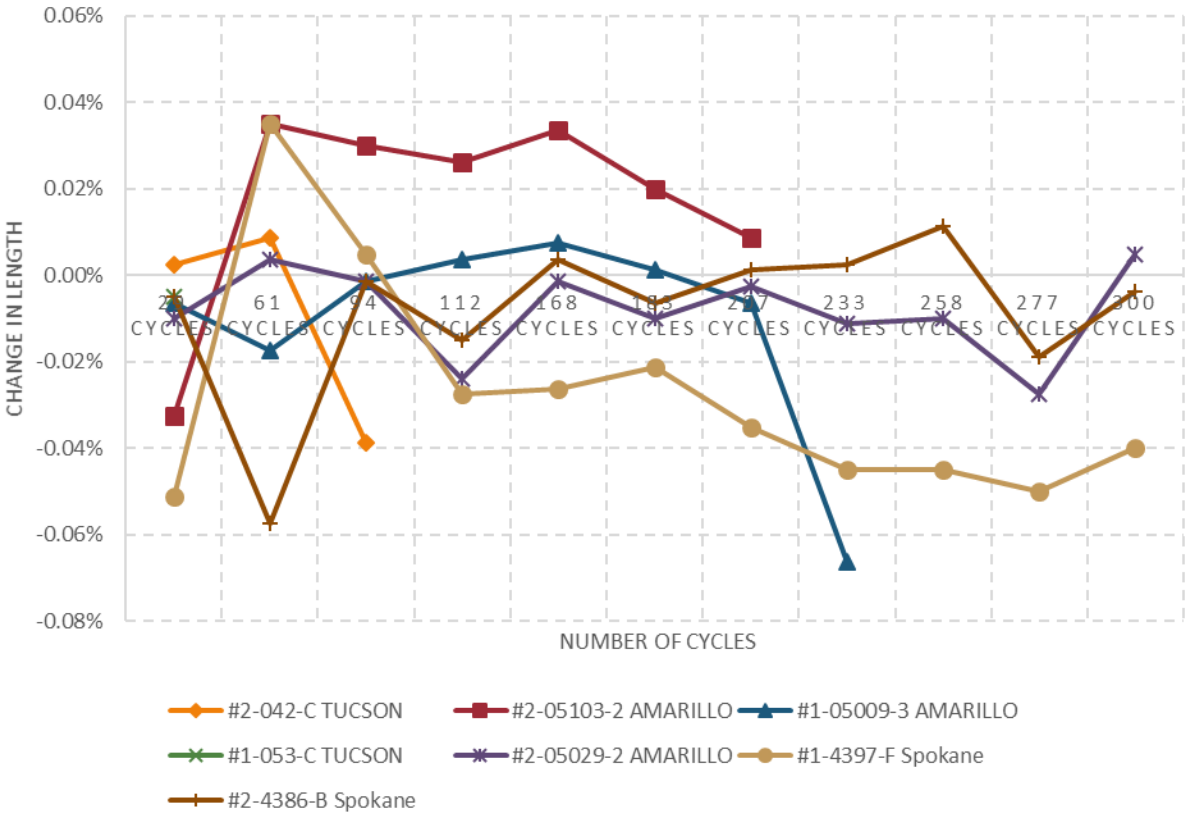


**Figure A-4: Length change in horizontal direction at the opposite side to ID**

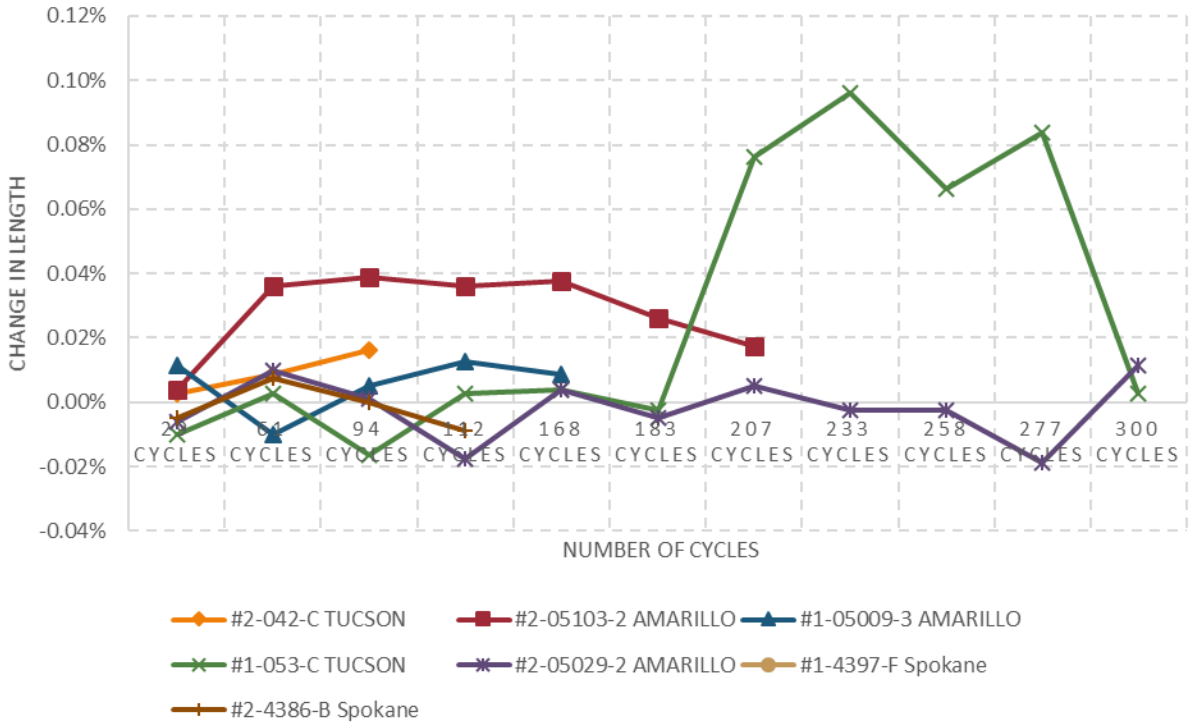


**Figure A-5: Length change in vertical direction at the opposite side to ID**

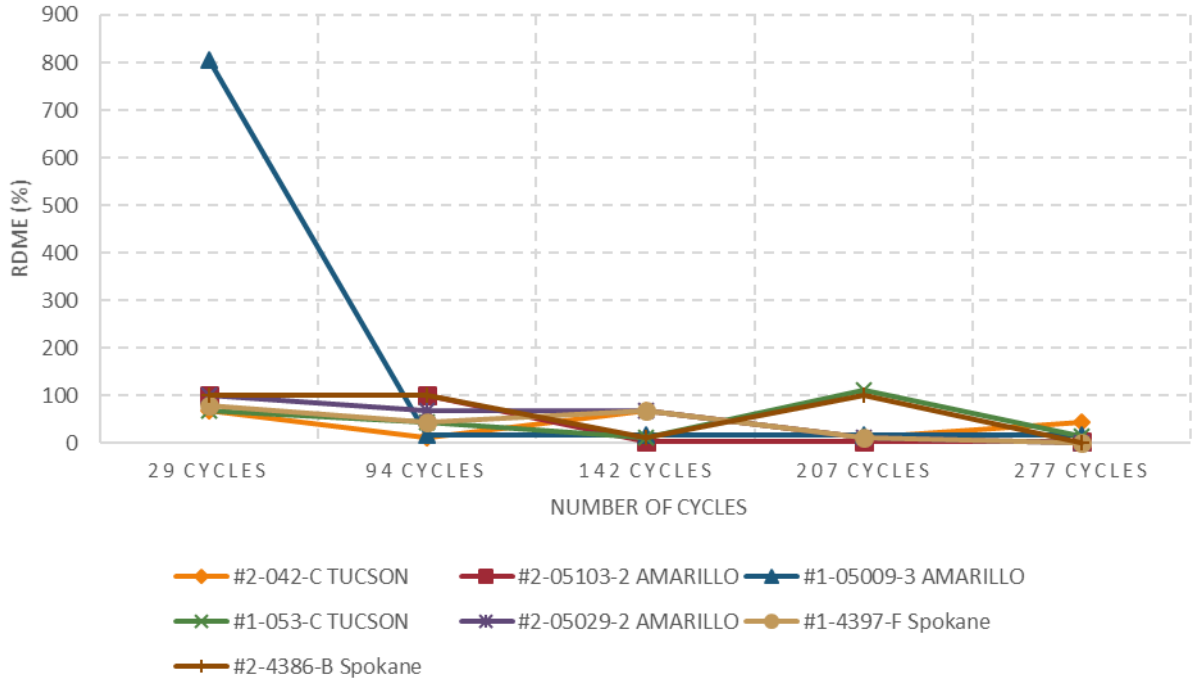


**Figure A-6: RDME values at the ID side for the top transverse direction of the tie**

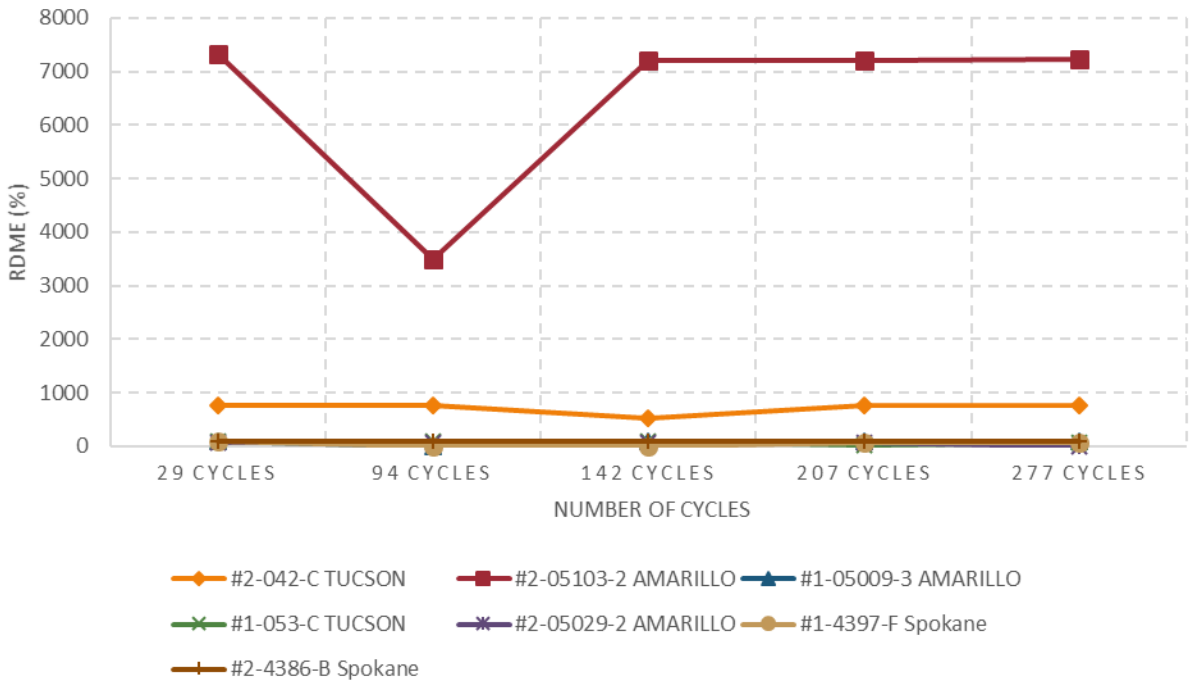


**Figure A-7: RDME values at the ID side for the short top longitudinal direction of the tie**

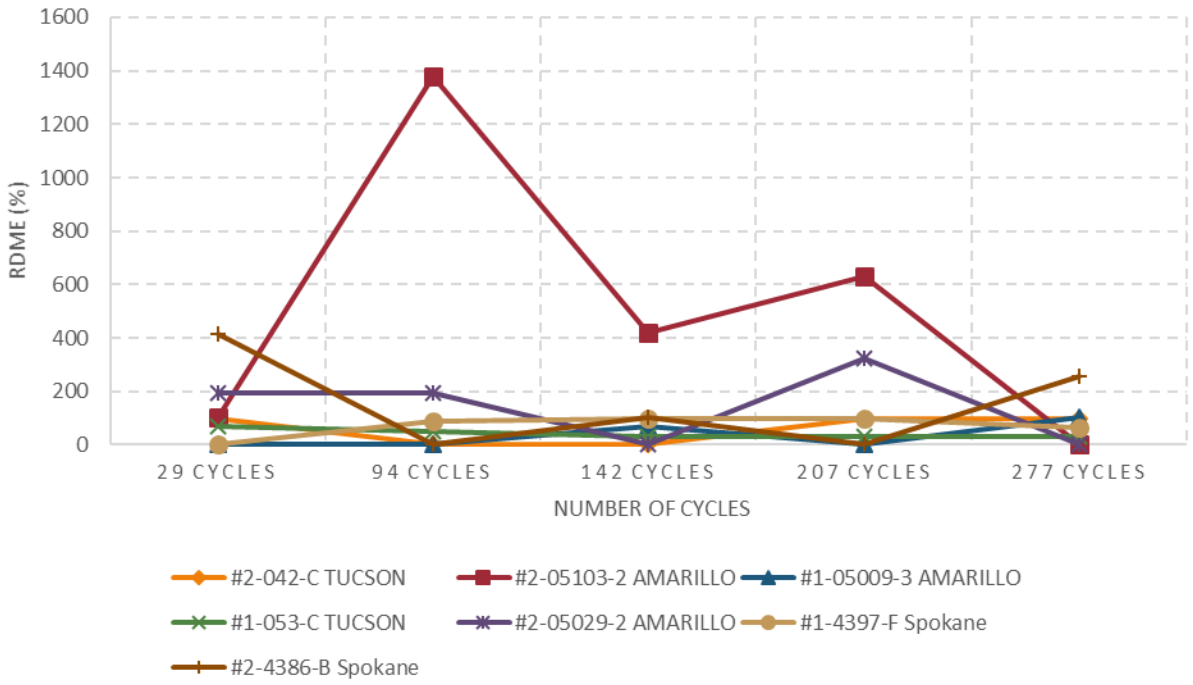


**Figure A-8: RDME values at the ID side for the side transverse direction of the tie**

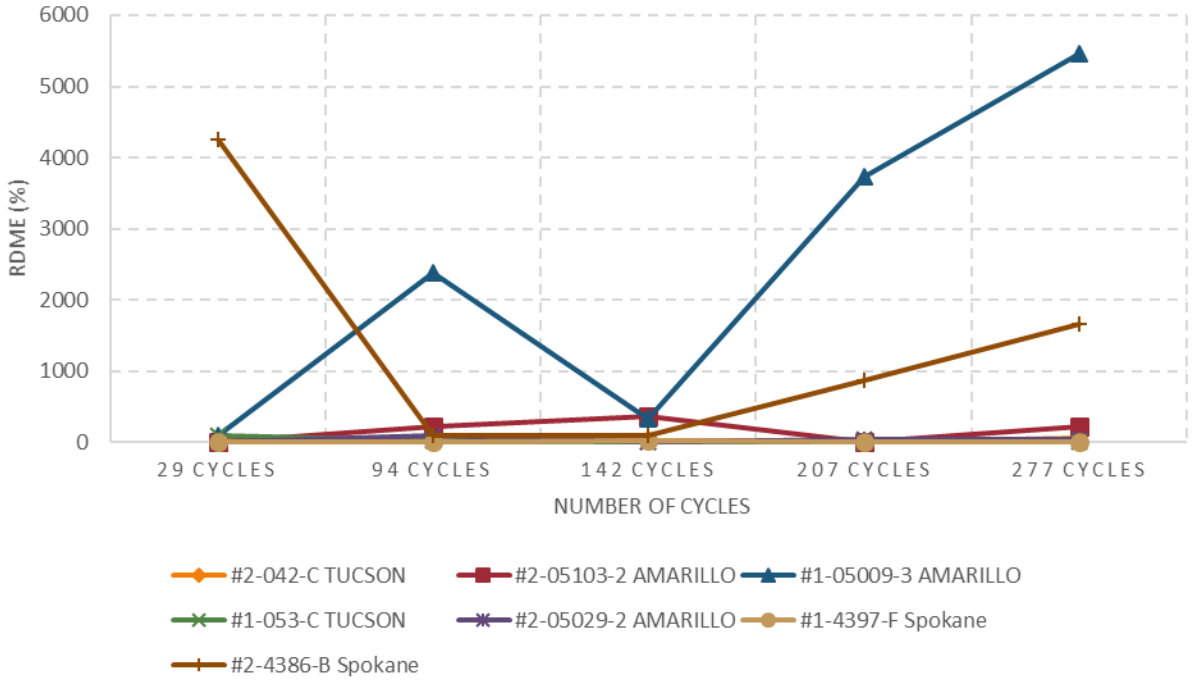


**Figure A-9: RDME values at the ID side for the side longitudinal direction of the tie**

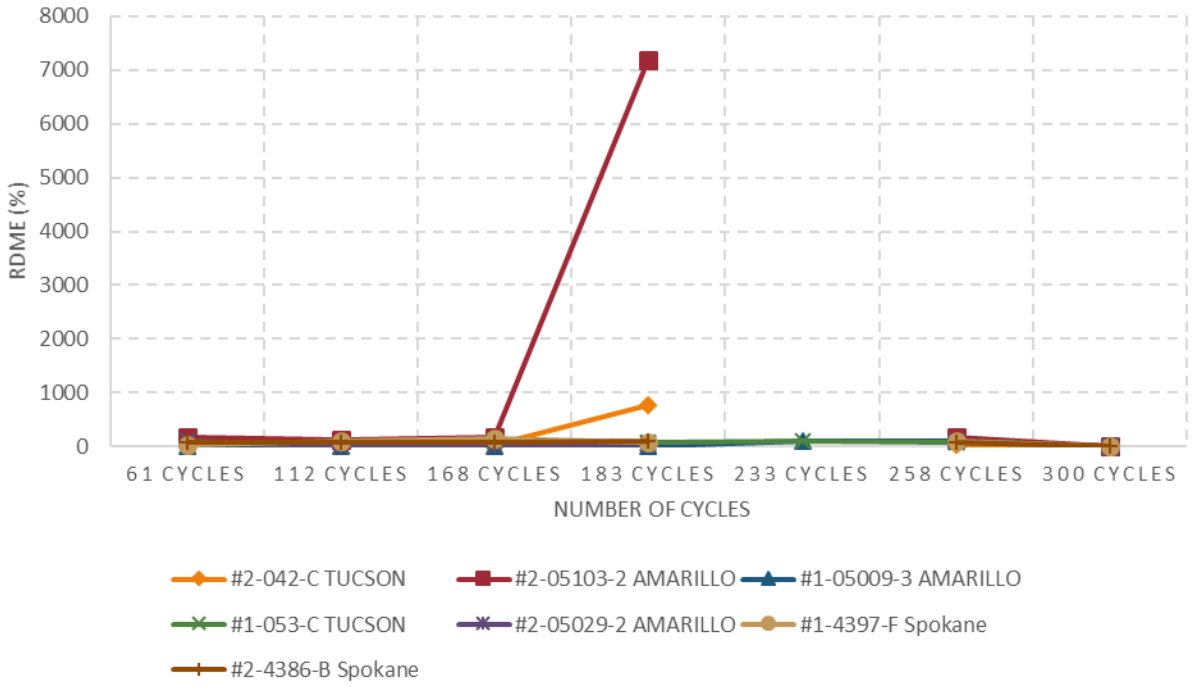


**Figure A-10: RDME values at the other side for the short top longitudinal direction of the tie**

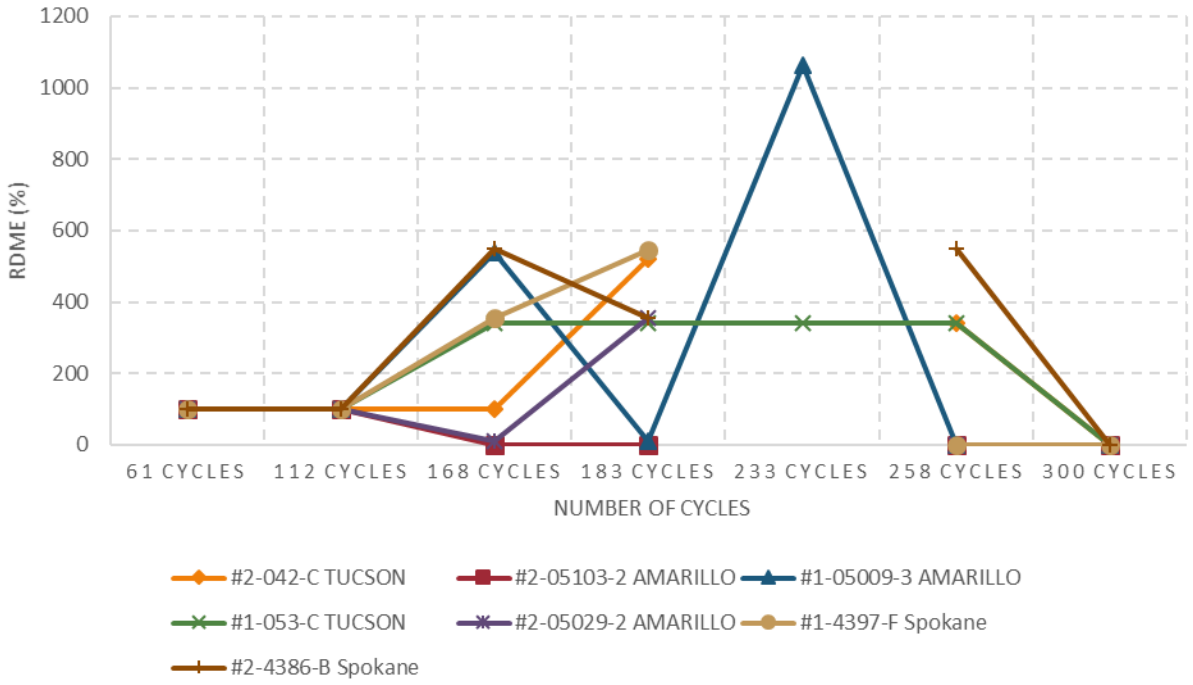


**Figure A-11: RDME values at the other side for the long top longitudinal direction of the tie**

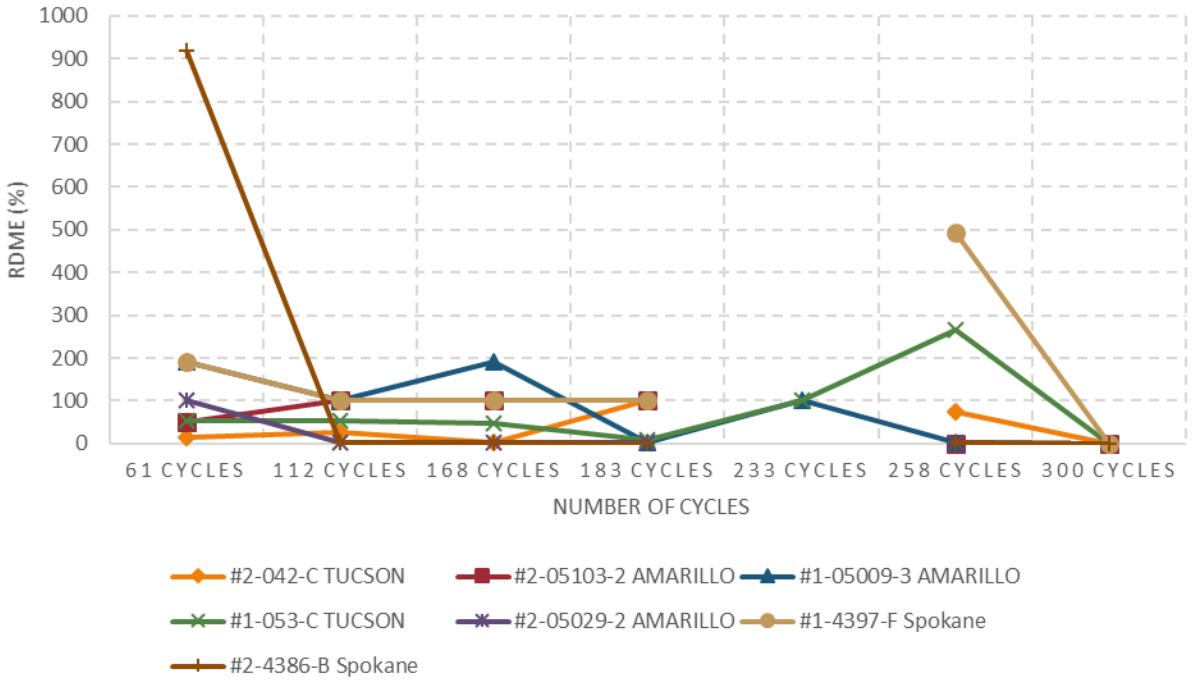


**Figure A-12: RDME values at the other side for the side transverse direction of the tie**

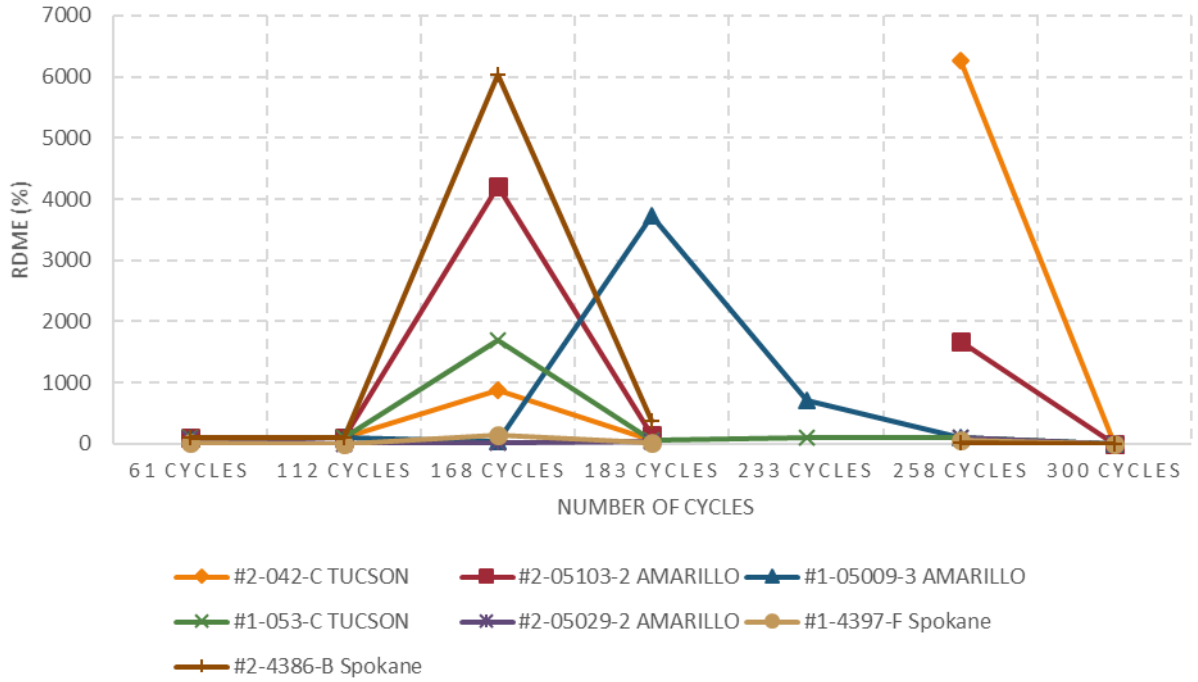


**Figure A-13: RDME values at the other side for the transverse longitudinal direction of the tie**

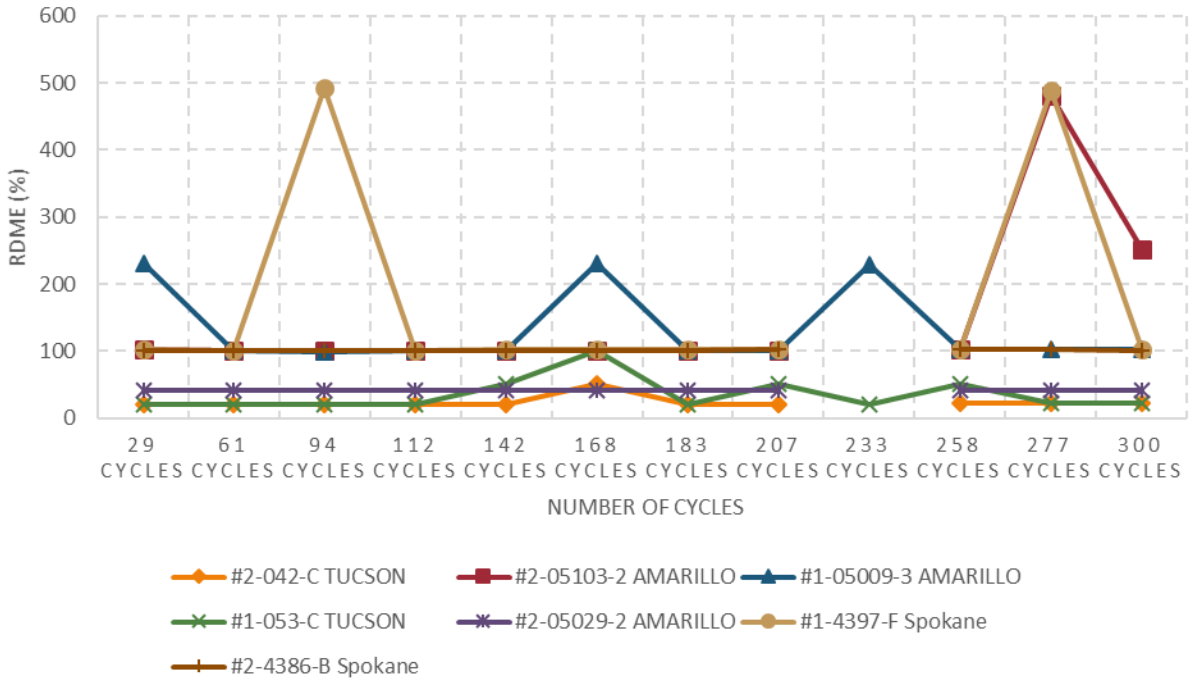


**Figure A-14: RDME values at the middle for the top transverse direction of the tie**

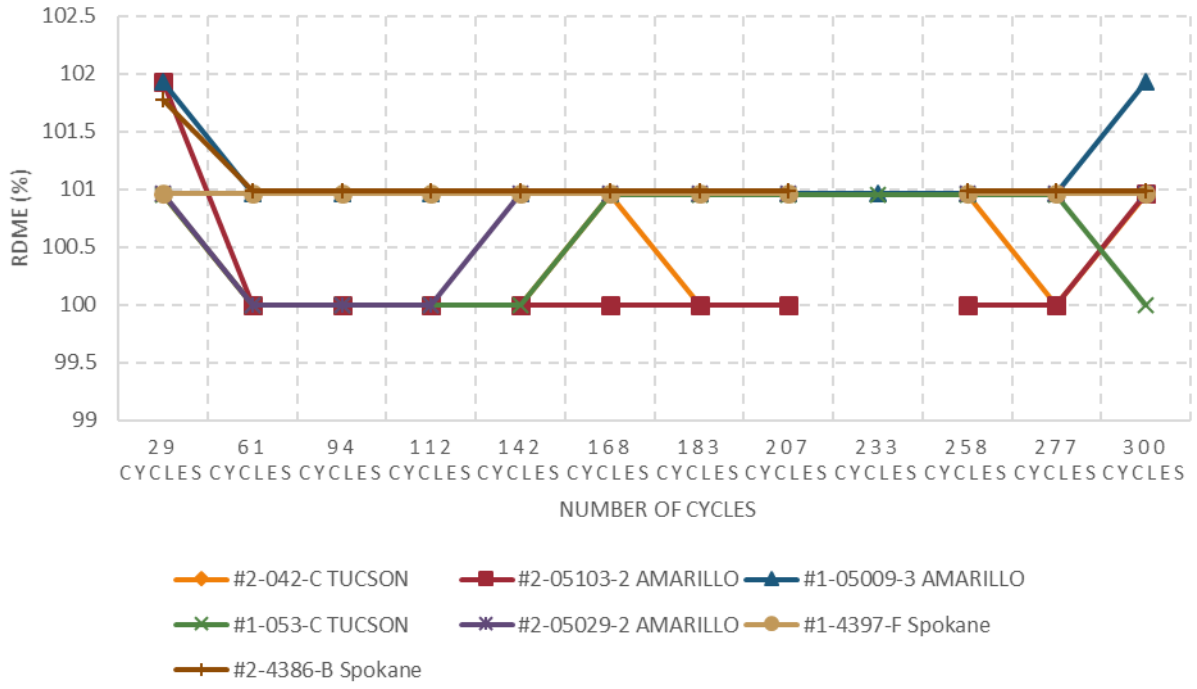


**Figure A-15: RDME values at the middle for the top longitudinal direction of the tie**

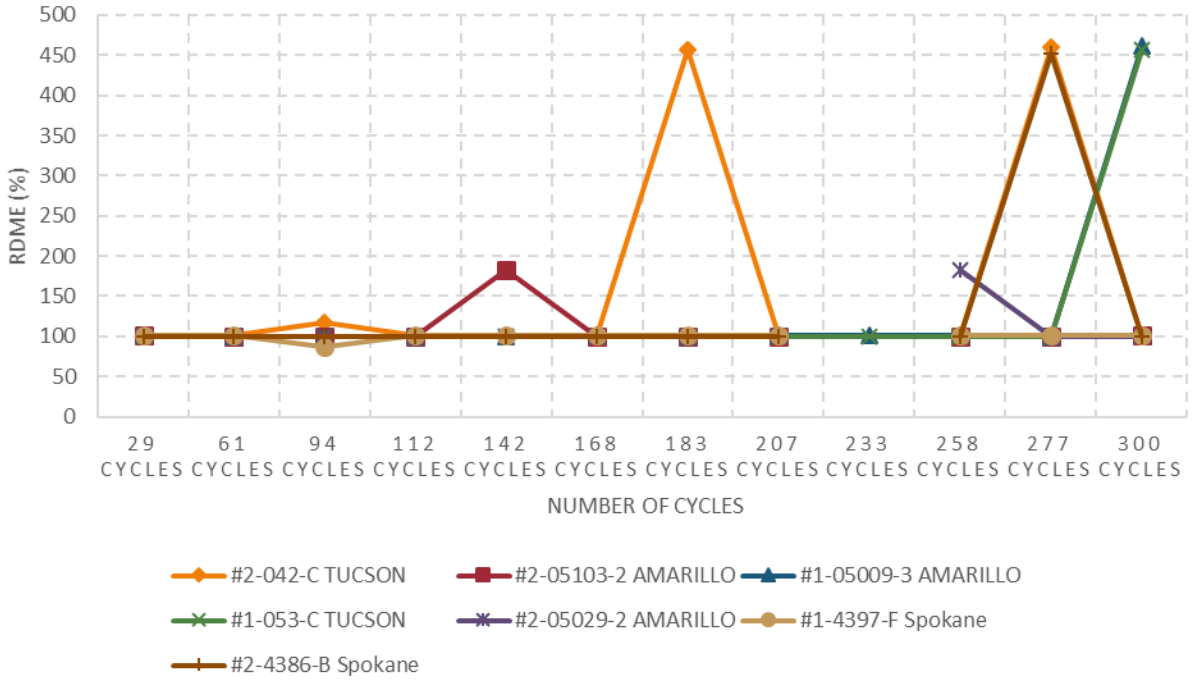


**Figure A-16: RDME values at the middle for the side transverse direction of the tie**

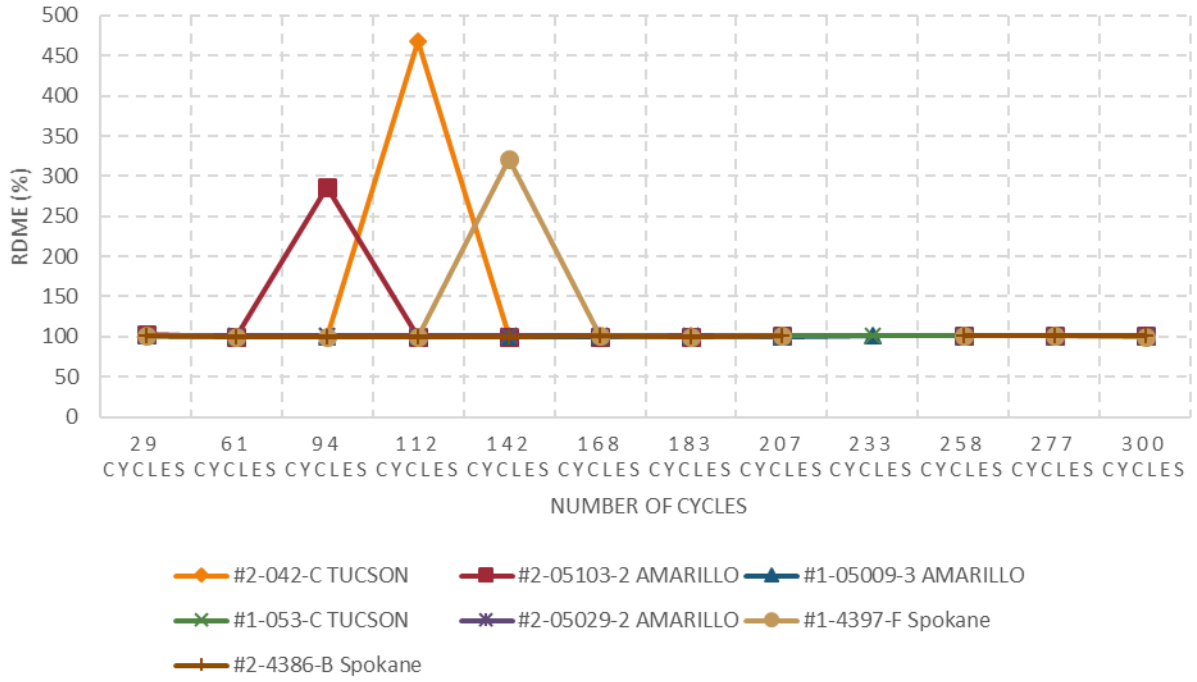


**Figure A-17: RDME values at the middle for the side longitudinal direction of the tie**

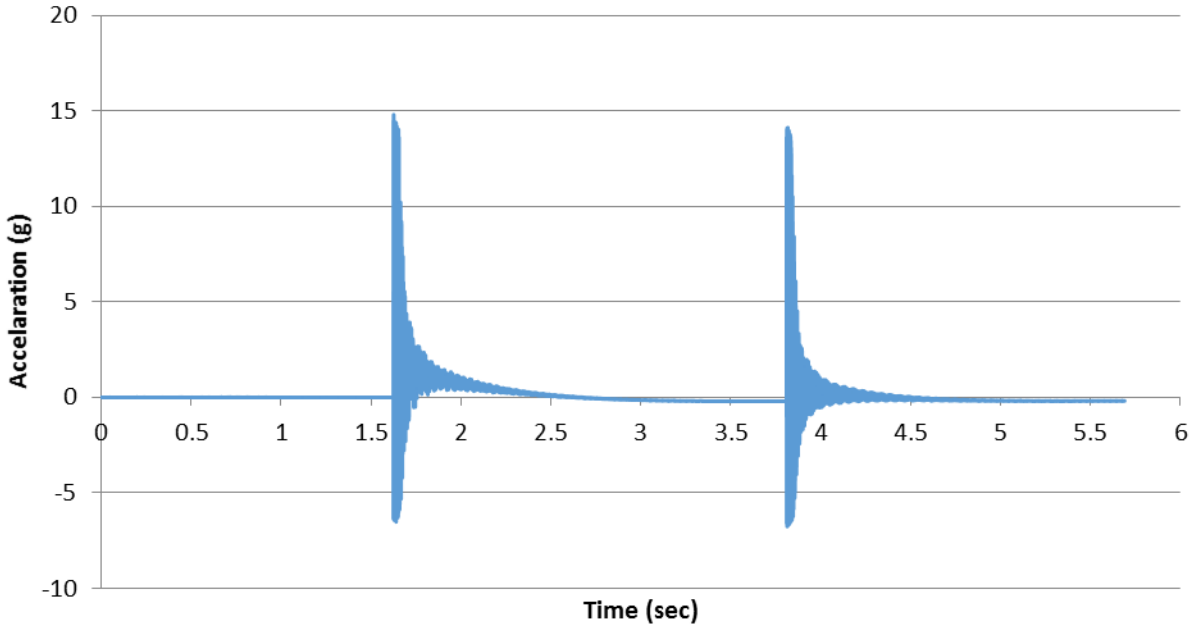


**Figure A-18: Impact acceleration measurements for Tie #2-05103-2 Plant C at the 258th cycle**

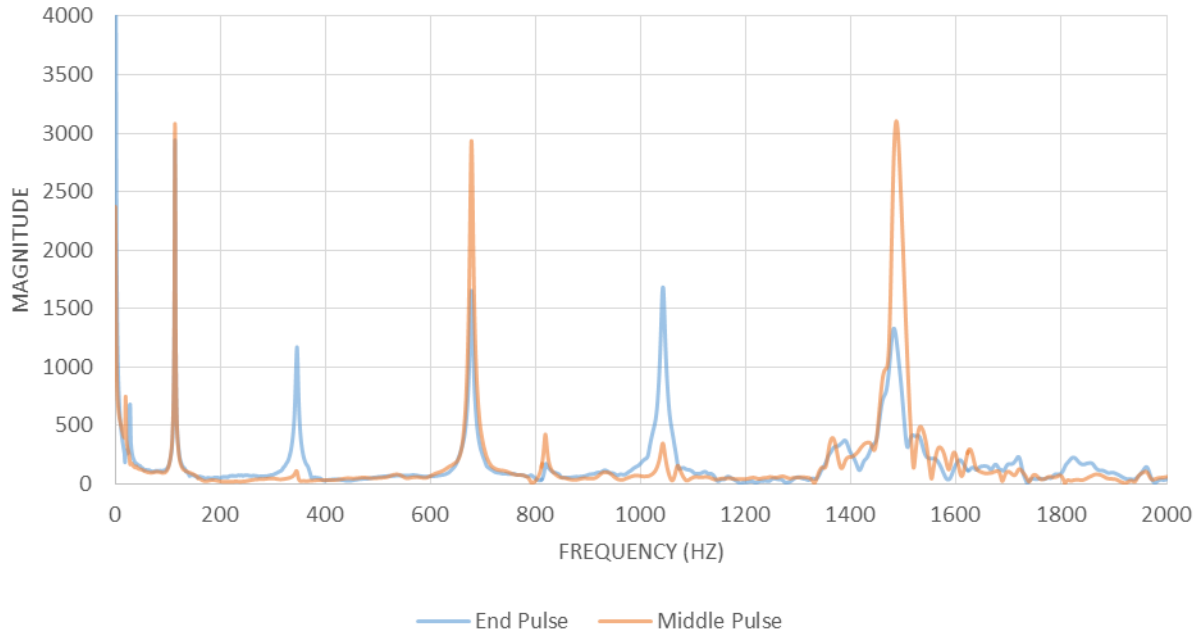


**Figure A-19: Frequency domain for Tie #2-05103-2 Plant C at the 258th cycle after impact**

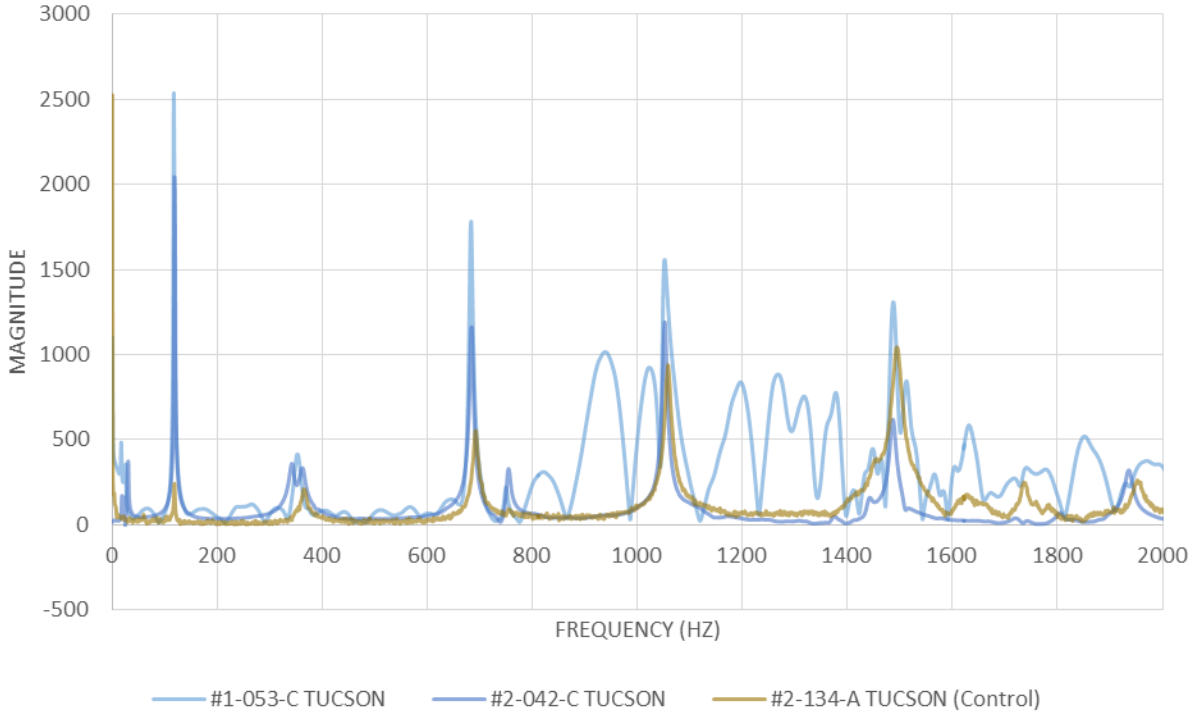


**Figure A-20: Tie end frequency domain for Plant B ties after the 277th cycle after impact**

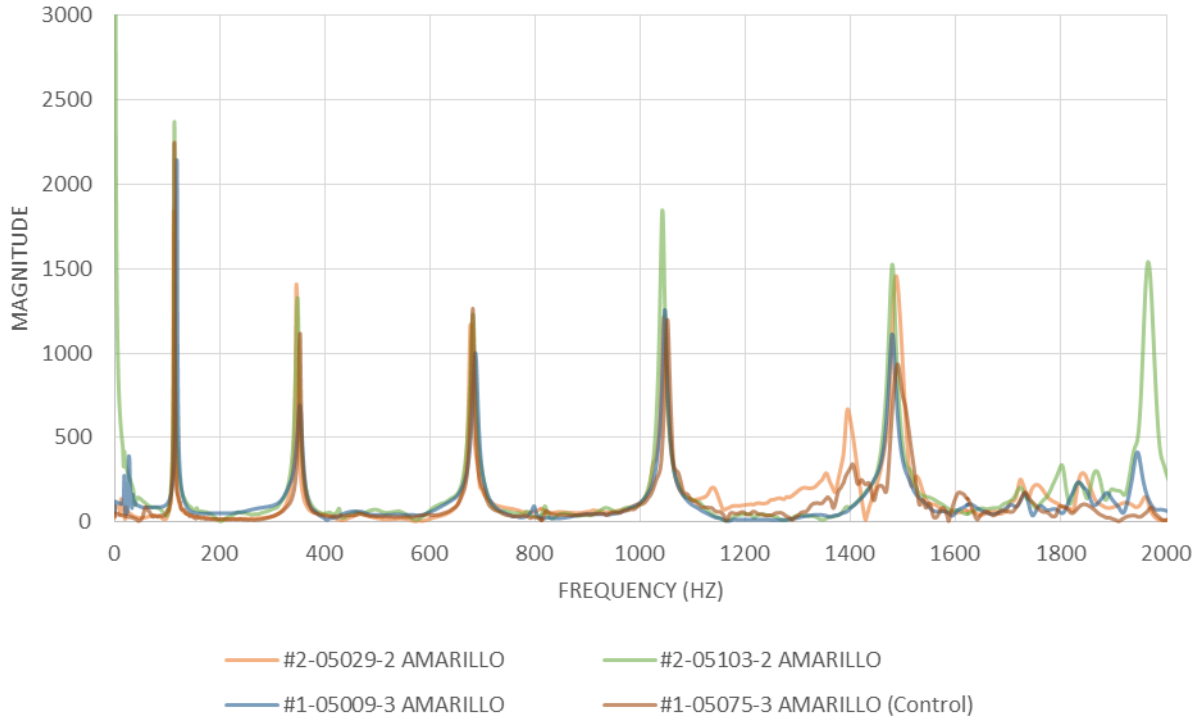


**Figure A-21: Tie end frequency domain for Plant C after the 277th cycle after impact**

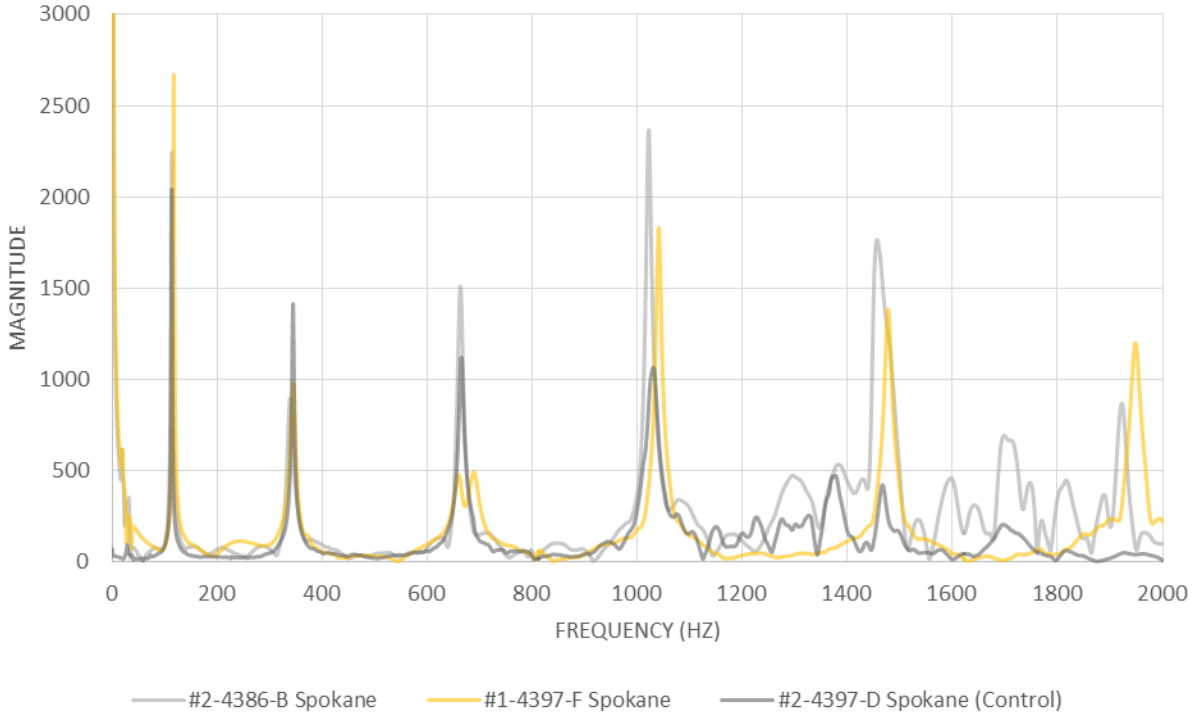


**Figure A-22: Tie end frequency domain for Plant A at the 277th cycle after impact**

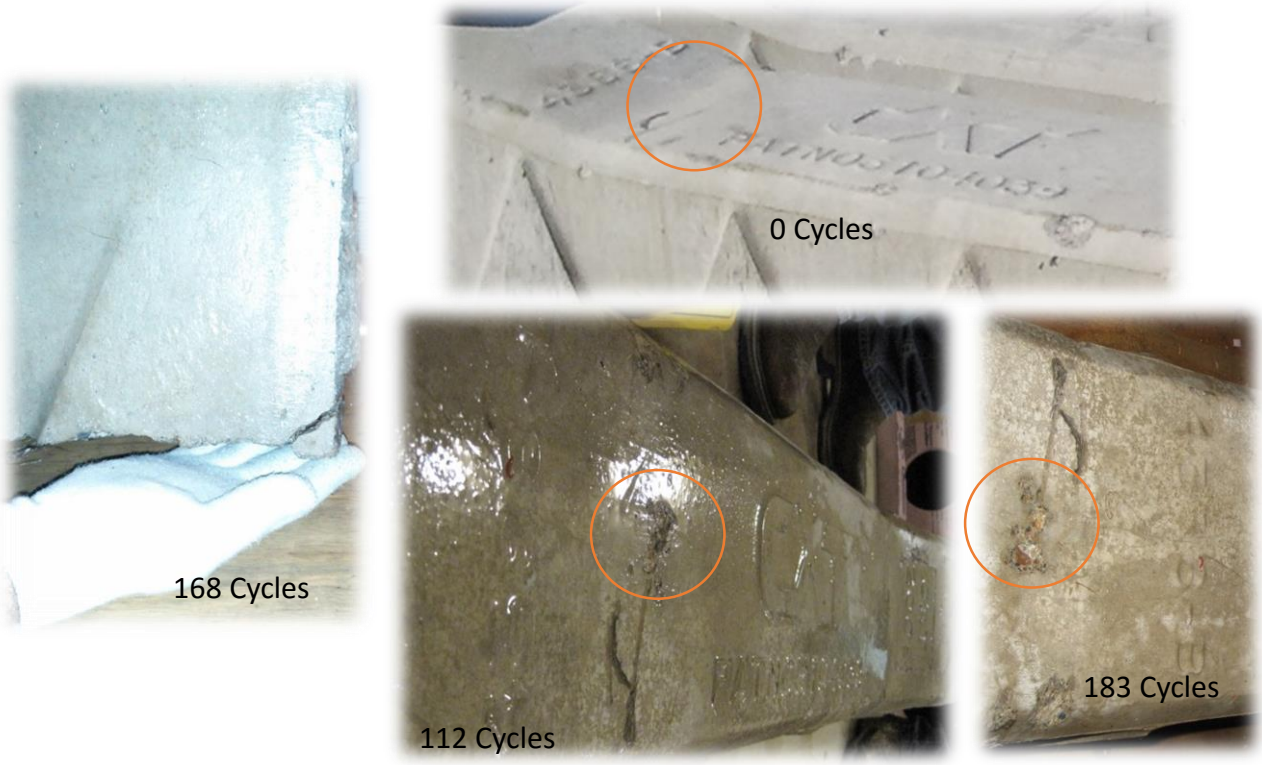


**Figure A-23: Tie #2-4386-B Plant A visual observations**


**Figure A-24: Tie #1-05009-3 Plant C visual observations**

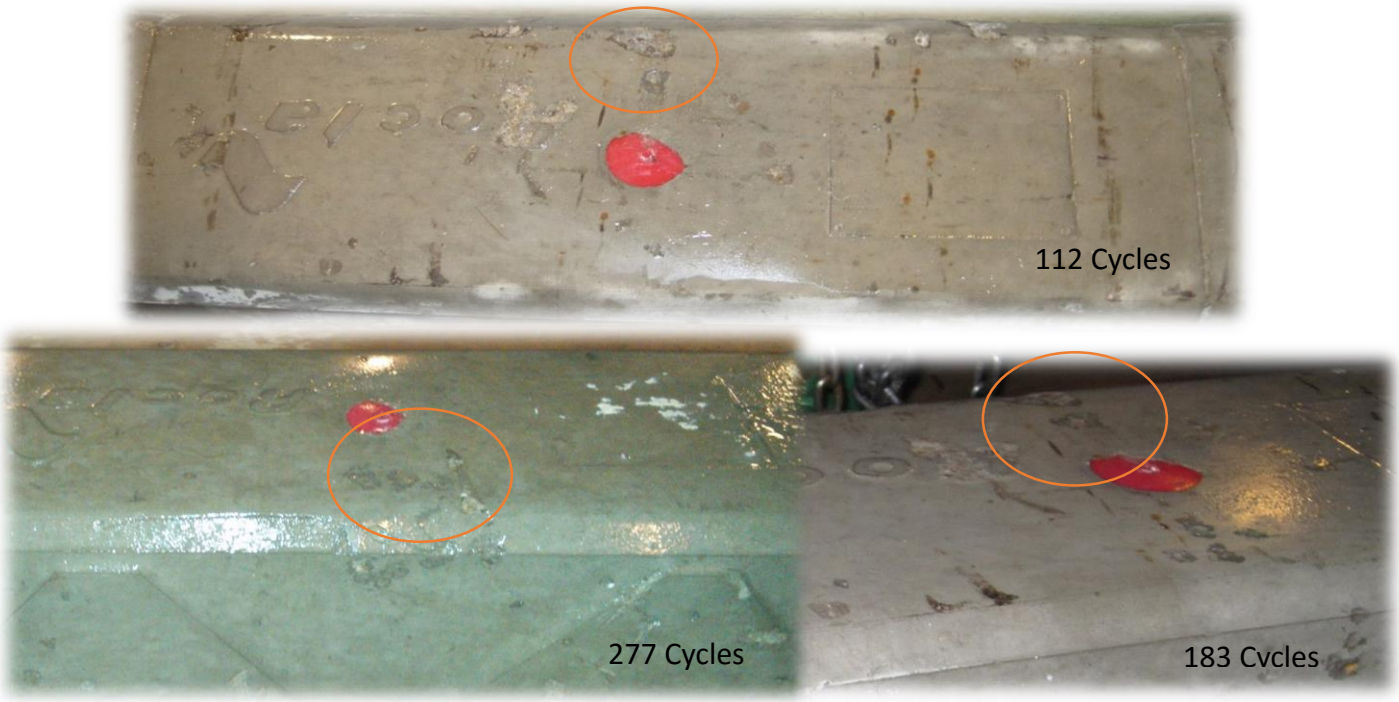


**Figure A-25: Tie #2-05103-2 Plant C visual observations**

# Appendix B - Reproduction Authorization

The following email represents reproduction authorization for Figure 2.2.

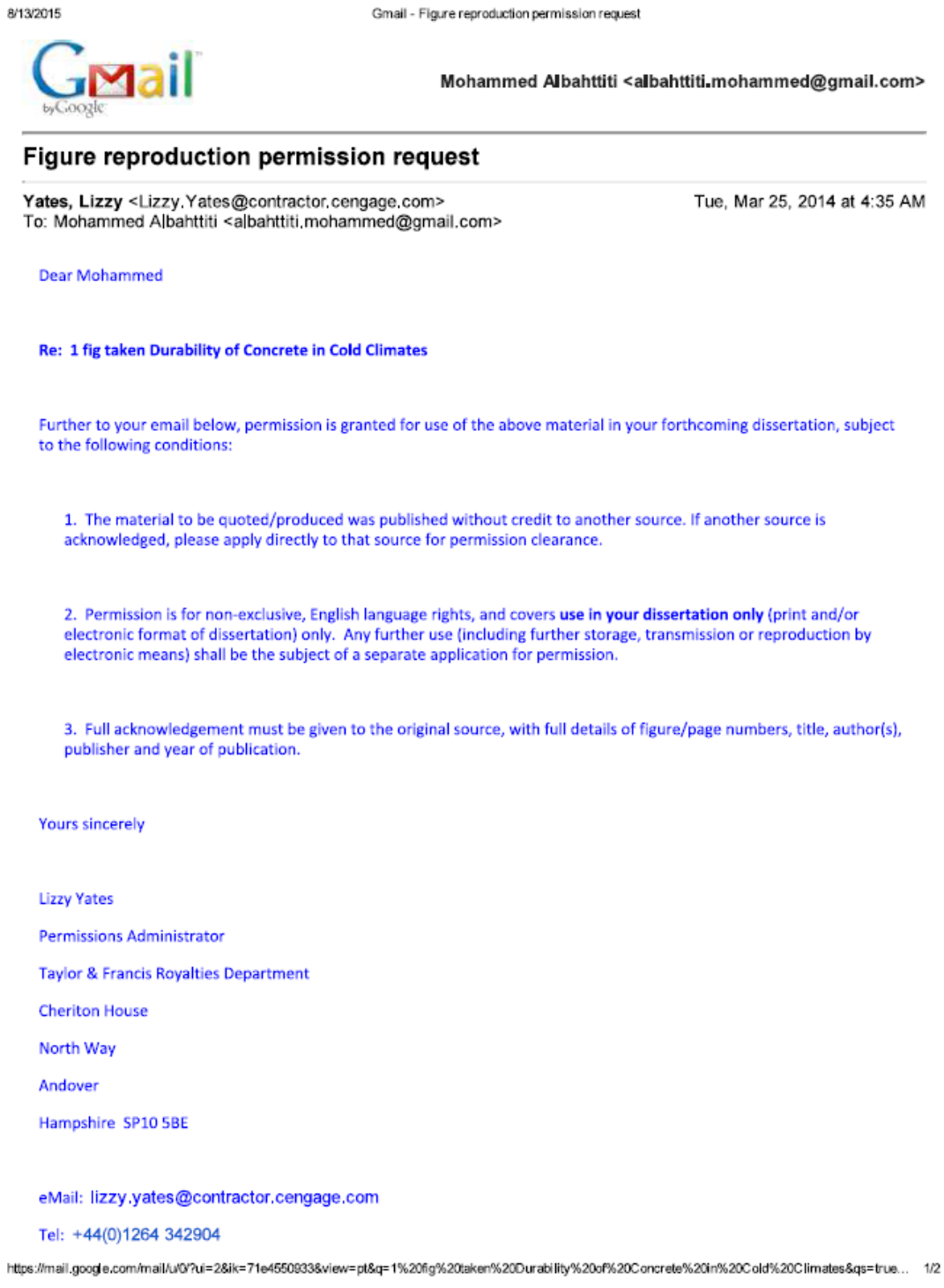

8/13/2015 Gmail - Figure reproduction permission request

Gmail

**Mohammed Albahttiti <albahttiti.mohammed@gmail.com>**

**Figure reproduction permission request**

**Yates, Lizzy** <Lizzy.Yates@contractor.cengage.com> Tue, Mar 25, 2014 at 4:35 AM
To: Mohammed Albahttiti <albahttiti.mohammed@gmail.com>

Dear Mohammed

**Re: 1 fig taken Durability of Concrete in Cold Climates**

Further to your email below, permission is granted for use of the above material in your forthcoming dissertation, subject to the following conditions:

1. The material to be quoted/produced was published without credit to another source. If another source is acknowledged, please apply directly to that source for permission clearance.

2. Permission is for non-exclusive, English language rights, and covers **use in your dissertation only** (print and/or electronic format of dissertation) only. Any further use (including further storage, transmission or reproduction by electronic means) shall be the subject of a separate application for permission.

3. Full acknowledgement must be given to the original source, with full details of figure/page numbers, title, author(s), publisher and year of publication.

Yours sincerely

Lizzy Yates

Permissions Administrator

Taylor & Francis Royalties Department

Cheriton House

North Way

Andover

Hampshire SP10 5BE

eMail: lizzy.yates@contractor.cengage.com

Tel: +44(0)1264 342904

https://mail.google.com/mail/u/0/?ui=2&ik=71e4550933&view=pt&q=1%20fig%20taken%20Durability%20of%20Concrete%20in%20Cold%20Climates&qs=true... 1/2

The following email represents reproduction authorization for Figure 2.9.



Gmail by Google

Mohammed Albahttiti <albahttiti.mohammed@gmail.com>

## Figures reproduction

**Hooper, Kathe** <khooper@astm.org> Tue, Mar 18, 2014 at 1:31 PM
To: Mohammed Albahttiti <bahttiti@ksu.edu>

Dear Mr. Albahttiti,

It was a pleasure to talk with you yesterday.

ASTM International grants a limited, non-exclusive license to reproduce Figure 1 form ASTM C231/C231M-10 in your PhD dissertation provided the following credit line is used:

"Reprinted, with permission, from C231/C231-10 Standard Test Method for Air Content of Freshly Mixed Concrete by the Pressure Method, copyright ASTM International, 100 Barr Harbor Drive, West Conshohocken, PA 19428. A copy of the complete standard may be obtained

from ASTM International, www.astm.org."

Thank you for your interest in ASTM Standards.

Kind regards,

Kathe

Kathe Hooper
ASTM International
100 Barr Harbor Drive, PO Box C700
West Conshohocken, PA 19428-2959
phone: *610-832-9634*
fax: *610-834-7018*
email: *khooper@astm.org*

**From:** Mohammed Albahttiti [mailto:bahttiti@ksu.edu]
**Sent:** Monday, March 17, 2014 4:35 PM
**To:** Hooper, Kathe
**Subject:** Figures reproduction

[Quoted text hidden]